ADVANCED NEUROIMAGING OF BRAIN METASTASES

EDITED BY: Behroze Adi Vachha, Susie Y. Huang and Tarik F. Massoud
PUBLISHED IN: Frontiers in Neurology

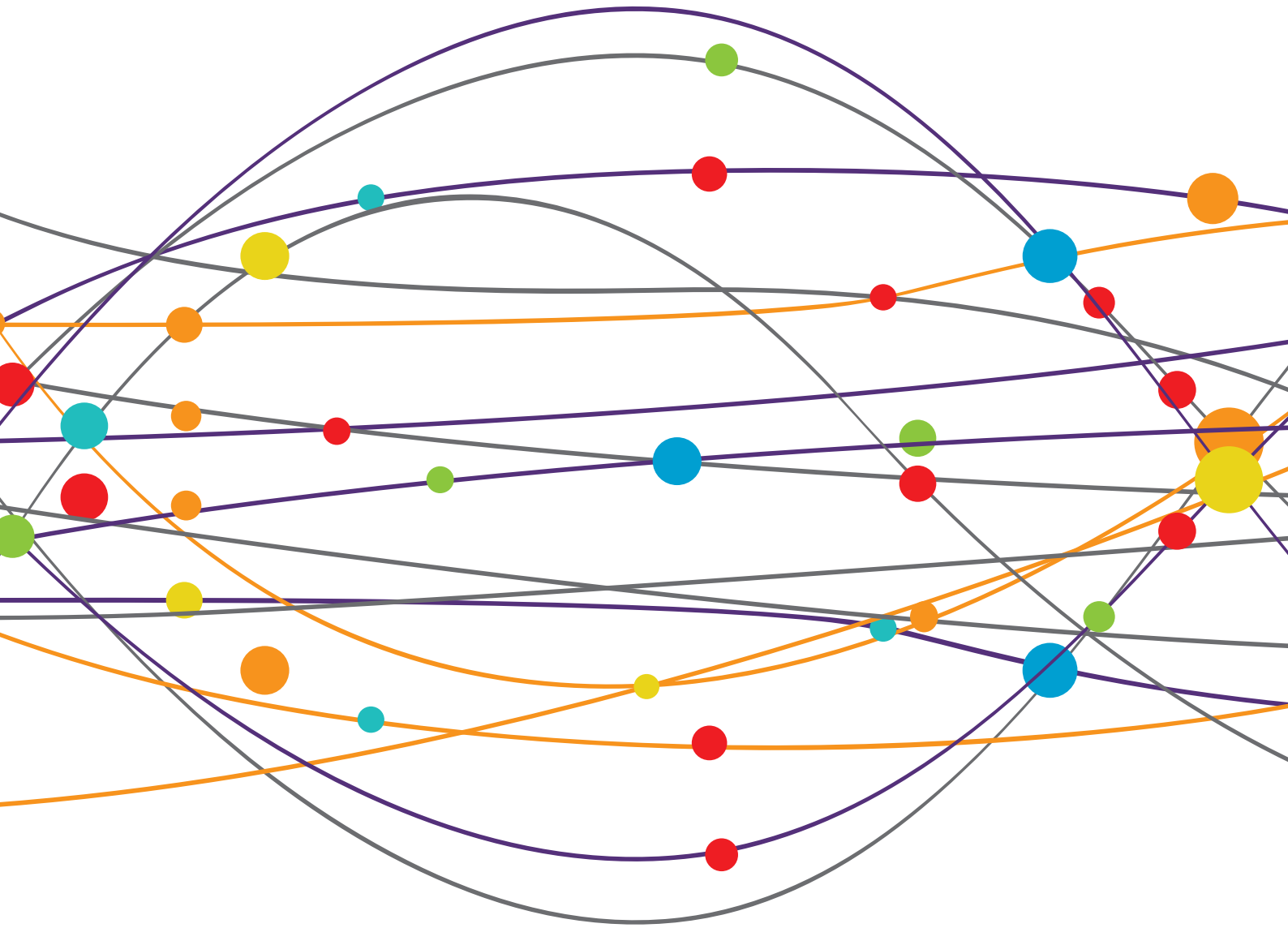

frontiers Research Topics

frontiers

ISSN 1664-8714
ISBN 978-2-88966-744-4
DOI 10.3389/978-2-88966-744-4

About Frontiers

Frontiers is more than just an open-access publisher of scholarly articles: it is a pioneering approach to the world of academia, radically improving the way scholarly research is managed. The grand vision of Frontiers is a world where all people have an equal opportunity to seek, share and generate knowledge. Frontiers provides immediate and permanent online open access to all its publications, but this alone is not enough to realize our grand goals.

Frontiers Journal Series

The Frontiers Journal Series is a multi-tier and interdisciplinary set of open-access, online journals, promising a paradigm shift from the current review, selection and dissemination processes in academic publishing. All Frontiers journals are driven by researchers for researchers; therefore, they constitute a service to the scholarly community. At the same time, the Frontiers Journal Series operates on a revolutionary invention, the tiered publishing system, initially addressing specific communities of scholars, and gradually climbing up to broader public understanding, thus serving the interests of the lay society, too.

Dedication to Quality

Each Frontiers article is a landmark of the highest quality, thanks to genuinely collaborative interactions between authors and review editors, who include some of the world's best academicians. Research must be certified by peers before entering a stream of knowledge that may eventually reach the public - and shape society; therefore, Frontiers only applies the most rigorous and unbiased reviews.
Frontiers revolutionizes research publishing by freely delivering the most outstanding research, evaluated with no bias from both the academic and social point of view. By applying the most advanced information technologies, Frontiers is catapulting scholarly publishing into a new generation.

What are Frontiers Research Topics?

Frontiers Research Topics are very popular trademarks of the Frontiers Journals Series: they are collections of at least ten articles, all centered on a particular subject. With their unique mix of varied contributions from Original Research to Review Articles, Frontiers Research Topics unify the most influential researchers, the latest key findings and historical advances in a hot research area! Find out more on how to host your own Frontiers Research Topic or contribute to one as an author by contacting the Frontiers Editorial Office: frontiersin.org/about/contact

ADVANCED NEUROIMAGING OF BRAIN METASTASES

Topic Editors:
Behroze Adi Vachha, Memorial Sloan Kettering Cancer Center, United States
Susie Y. Huang, Harvard Medical School, United States
Tarik F. Massoud, Stanford University, United States

Citation: Vachha, B. A., Huang, S. Y., Massoud, T. F., eds. (2021). Advanced Neuroimaging of Brain Metastases. Lausanne: Frontiers Media SA.
doi: 10.3389/978-2-88966-744-4

Table of Contents

frontiers in Neurology

EDITORIAL
published: 17 March 2021
doi: 10.3389/fneur.2021.668310

Editorial: Advanced Neuroimaging of Brain Metastases

Behroze A. Vachha[1]*, *Susie Y. Huang*[2] *and Tarik F. Massoud*[3]

[1] Department of Radiology, Memorial Sloan Kettering Cancer Center, New York, NY, United States, [2] Department of Radiology, Massachusetts General Hospital and Harvard Medical School, Boston, MA, United States, [3] Department of Radiology, Stanford University, Stanford, CA, United States

Keywords: brain metastases, advanced neuroimaging, radiomics, imaging biomarkers, SWI

Editorial on the Research Topic

Advanced Neuroimaging of Brain Metastases

Metastasis is the most common cause of brain cancer. Advanced magnetic resonance imaging (MRI) and positron emission tomography (PET) techniques are playing an increasingly important role in the surveillance, diagnosis, and management of patients with brain metastases as treatments for systemic cancers continue to improve. These advanced neuroimaging methods enable better delineation of metastatic lesions, while also providing a rich array of information regarding the microstructural, vascular, metabolic, and functional properties of metastases and the affected brain parenchyma. However, barriers remain in the widespread translation and adoption of these techniques. The challenges of imaging patients with brain metastases include the heterogeneity of primary tumors and the tumor microenvironment. The varied appearances of metastases before, during and after treatment, especially in the face of a growing arsenal of new cancer therapies, are further difficulties to contend with.

Advanced neuroimaging biomarkers promise to improve the non-invasive characterization, prognostication, and evaluation of treatment response and post-treatment effects related to brain metastases. Such biomarkers may aid in the differentiation of metastases from other entities and serve as valuable adjuncts to conventional imaging in distinguishing disease progression from treatment-related effects. The standardization and validation of advanced imaging biomarkers will need to be addressed to facilitate the adoption of such techniques in clinical trials and clinical practice. A survey of the available techniques will help to define more precisely the role of state-of-the-art imaging approaches in targeted problem-solving, as well as their broader utility in elucidating the underlying cancer biology.

This Research Topic provides a glimpse of current and emerging advanced neuroimaging techniques used in the care of patients with brain metastases. Tong et al. provide a comprehensive review of advanced MRI techniques for brain metastases. These techniques are useful for both diagnosis, including differentiating between types of malignancy, and assessment of treatment response, including distinguishing radiation necrosis from disease progression. These methods include: black blood MRI; magnetic resonance spectroscopy; quantitative magnetization transfer imaging; dynamic contrast-enhanced MRI to measure the transmembrane water exchange rate; chemical exchange saturation transfer measurement; perfusion imaging; and radiomics and artificial intelligence techniques.

Picking up on the radiomics theme, Lohmann et al. review radiomic techniques and features when applied to PET/MRI of brain metastases. They discuss the underlying rationale of radiomic analysis, which is to identify appropriate characteristic image features and to use these to generate predictive or prognostic mathematical models. Hence, radiomics of brain metastases can be considered as a tool to complement established imaging analysis methods and other clinical measures that can be jointly used to make treatment decisions or final diagnoses with improved confidence.

OPEN ACCESS

Edited and reviewed by:
Jan Kassubek,
University of Ulm, Germany

***Correspondence:**
Behroze A. Vachha
vachhab@mskcc.org

Specialty section:
This article was submitted to Applied Neuroimaging, a section of the journal Frontiers in Neurology

Received: *16 February 2021*
Accepted: *22 February 2021*
Published: *17 March 2021*

Citation:
Vachha BA, Huang SY and Massoud TF (2021) Editorial: Advanced Neuroimaging of Brain Metastases. Front. Neurol. 12:668310. doi: 10.3389/fneur.2021.668310

Goncalves Filho et al. studied a highly accelerated Wave-controlled aliasing in parallel imaging (Wave-CAIPI) post-contrast 3D T1 SPACE MRI sequence for brain metastases, and found that it provides equivalent visualization of lesions and an overall diagnostic quality, with three times reduced scan time compared to standard 3D T1 SPACE MRI.

Two articles present the role of susceptibility weighted imaging (SWI) MRI for brain metastases. Schwarz et al. review its role in early diagnosis, determination of type of malignancy, and treatment monitoring, and they discuss therapy-associated changes that can affect SWI. They also review recent insights on the role of "isolated SWI signals" and the controversy on the specificity of SWI for early detection of brain metastases. Ceballos-Ceballos et al. compared unenhanced SWI and gadolinium-enhanced SWI (SWI-Gd) to assess if the latter improves brain metastasis detection in combination with other MRI sequences. They found that SWI-Gd may improve the diagnostic yield of brain metastases.

Ari Wijetunga and Jonathan Yang provide useful insights into various aspects of diagnostic neuroimaging that radiation oncologists rely on for clinical decision-making, radiation treatment planning, and assessment of treatment response or complications of brain metastases. Also of relevance to radiation treatment of brain metastases, Swinburne et al. conducted a study to determine if early intratumoral changes in interstitial fluid pressure (IFP) and velocity (IFV), estimated from computational fluid modeling using dynamic contrast-enhanced MRI, can predict long-term outcomes of lung cancer brain metastases treated using stereotactic radiosurgery. They found that early post-treatment assessment of IFP and IFV can be used to predict long-term response of lung cancer brain metastases to radiosurgery, allowing timely treatment modifications.

Finally, Kalakoti et al. present an interesting analysis of morphometric and volumetric differences across anatomical brain regions in patients with metastases presenting with seizures. That information could provide useful biomarkers in the identification of seizure expression and could serve as a neuronal target for mitigation. Using brain segmentation of T1-MPRAGE MRI images, they found that certain brain regions, such as the pars orbitalis, supramarginal and temporal gyrus (middle, transverse), and the pre-cuneus contribute a maximal potential for differentiation of seizure from non-seizure patients.

Overall, this collection of research articles and up-to-date reviews might act as a useful platform of knowledge for scientists and clinicians grappling with the difficult management of brain metastasis patients. We believe that the next big challenges in management of these patients will be to scale up various efforts and tools in the field of advanced neuroimaging of brain metastases. For instance, this will require new strategies and advances in techniques that include diffusion, perfusion, spectroscopy, functional MRI, positron emission tomography, radiomics and machine learning, to name a few. Moreover, in this era of precision medicine, these advanced neuroimaging techniques will need to be integrated with molecular information to allow personalized targeting of each patient's unique type of metastatic tumor.

AUTHOR CONTRIBUTIONS

All authors contributed to manuscript revision, read, and approved the submitted version.

Conflict of Interest: The authors declare that the research was conducted in the absence of any commercial or financial relationships that could be construed as a potential conflict of interest.

frontiers in Neurology

REVIEW
published: 04 February 2020
doi: 10.3389/fneur.2020.00055

Clinical Value of Susceptibility Weighted Imaging of Brain Metastases

Daniel Schwarz[1]*, *Martin Bendszus*[1] and *Michael O. Breckwoldt*[1,2]*

[1] Neuroradiology Department, University Hospital Heidelberg, Heidelberg, Germany, [2] Clinical Cooperation Unit Neuroimmunology and Brain Tumor Immunology, German Cancer Research Center (DKFZ), Heidelberg, Germany

MRI is used for screening, initial diagnosis and follow-up of brain metastases. Multiparametric MRI protocols encompass an array of image sequences to depict key aspects of metastases morphology and biology. Given the recent safety concerns of Gd-administration and the retention of linear Gd-agents in the brain, non-contrast sequences are currently evaluated regarding their diagnostic value for brain imaging studies. Susceptibility weighted imaging has been established as a valuable clinical and research tool that is heavily used in clinical practice and utilized in diverse pathologies ranging from neuroinflammation, neurovascular disease to neurooncology. We review the value of SWI in the field of brain metastases with an emphasis on its role in early diagnosis, determination of the primary tumor entity, treatment monitoring and discuss therapy-associated changes that can affect SWI. We also review recent insights on the role of "isolated SWI signals" and the controversy on the specificity of SWI for the early detection of brain metastases.

Keywords: MRI, brain metastases, SWI, treatment monitoring, radiotherapy

OPEN ACCESS

Edited by:
Behroze Adi Vachha, Memorial Sloan Kettering Cancer Center, United States

Reviewed by:
Nicola Amoroso, University of Bari Aldo Moro, Italy
Andrea Bink, University Hospital Zürich, Switzerland
Chanon Ngamsombat, Harvard Medical School, United States

***Correspondence:**
Daniel Schwarz
daniel.schwarz@med.uni-heidelberg.de
Michael O. Breckwoldt
michael.breckwoldt@med.uni-heidelberg.de

Specialty section:
This article was submitted to Applied Neuroimaging, a section of the journal Frontiers in Neurology

Received: *29 November 2019*
Accepted: *15 January 2020*
Published: *04 February 2020*

Citation:
Schwarz D, Bendszus M and Breckwoldt MO (2020) Clinical Value of Susceptibility Weighted Imaging of Brain Metastases. Front. Neurol. 11:55. doi: 10.3389/fneur.2020.00055

INTRODUCTION

Brain metastases (BM) are highly relevant in solid cancer patients and contribute significantly to overall morbidity and mortality (1). MR imaging is the gold standard for early diagnosis and treatment monitoring of BM patients (2). Treatment of BM is mainly based on neurosurgical resection and radiotherapy with a limited role for systemic chemotherapy due to low efficacy (3, 4). Recent immunotherapeutic trials have shown promising results in a subset of BM patients and are currently tested in clinical practice (5, 6). All such therapeutic regimes require regular and standardized MRI follow-up for disease monitoring to detect changes in the tumor micromilieu (TME) that occur during therapy.

In general, brain metastases imaging has three major goals: (a) early detection, (b) determination of the primary tumor entity, and (c) tumor monitoring, including differentiation between tumor progression and treatment related effects. Susceptibility weighted imaging (SWI) can contribute to all three challenges and this review will highlight these different aspects. SWI has been first described in 1997 when it was introduced for venous imaging (7). After the original description SWI has been widely used in clinical and preclinical studies (8–10). In clinical practice SWI is used for the detection of iron, hemorrhage and microbleedings (11–14) but has also been widely investigated in the field of neurovascular disease (15), for clot detection in stroke (16), in neurooncology (17, 18), neurotrauma (19), and autoimmune disease (20–23). Also neurosurgical applications of SWI have been recently reviewed (24).

ORIGIN OF THE SWI CONTRAST

The SWI signal originates from varying intrinsic susceptibilities that are present between voxels and get out of phase at longer echo times, leading to signal loss in the respective voxel. Susceptibility is altered by paramagnetic and diamagnetic materials such as deoxygenized hemoglobin within veins, tissue calcifications or iron depositions. Susceptibility is further introduced through the distortion of the magnetic field, e.g. at tissue boundaries or by metal implants. A thorough derivation of the physics behind SWI is beyond the scope of this article and has been covered by previous reviews (25).

In brief, for the generation of SWI, phase images are high-pass-filtered and transformed to a phase mask which is then multiplied on the magnitude image to increase contrast (25). It is important to note that the resulting image contrast depends on the manufacturer and the post-processing used: In a right-handed system, paramagnetic phase signals (like hemosiderin and deoxyhemoglobin) are depicted as dark voxels while diamagnetic phase signals (like calcifications) are shown as bright voxels. In a left-handed system, the images produced follow the inverse greyscale.

Newer developments in SWI include quantitative susceptibility mapping (QSM) and susceptibility tensor imaging which allow the quantitative measurement of the susceptibility in a given voxel (26–31). Recently, the minimum size of histo-pathologically confirmed microhemorrhages that can be depicted by clinical SWI were established (32). In this work, MR-positive microbleeds were typically found to correspond to histopathological hemorrhages of 3.6 mm^3 whereas MR false-negative microbleeds were found to be significantly smaller in size with an average volume of 0.3 mm^3 on histopathology.

SWI FOR BRAIN TUMOR IMAGING

In the brain tumor field SWI has been recently reviewed for glioma imaging (17). It is important to note that recent studies have shown that SWI can aid in glioma grading because of its sensitivity for (micro-)hemorrhages and the microvasculature itself that correlates with tumor grade (33). In particular, several authors found that the amount and extent of SWI artifacts correlated well with the grading of gliomas with more artifacts being correlated to higher tumor grade and increased neoangiogenesis (34–36). This could further be confirmed by quantification of intratumoral SWI patterns using fractal image analysis (37).

For monitoring of brain metastases multiparametric anatomical imaging is performed in the routine clinical setting (38). Further advanced sequences including chemical exchange saturation transfer imaging (CEST), magnetization transfer (MT) imaging and MR spectroscopy (MRS) have also been assessed regarding their clinical value and have recently been reviewed (39). In the context of neurooncology MT imaging could differentiate glioblastoma from brain metastasis (40). Interestingly, magnetization transfer imaging showed subtle changes also in the normal appearing white matter of the contralateral site that did not show obvious changes on standard MRI sequences (41), indicating that MT imaging might be more sensitive to detect subtle, tumor-induced changes. CEST was shown to enable the detection of radiotherapy induced apoptosis (42, 43). MRS has been used to differentiate radiation necrosis from tumor progression albeit with limited specificity (44).

SWI FOR DIFFERENTIATION OF THE UNDERLYING TUMOR ENTITY

As SWI provides an image contrast that is different from conventional spin echo MR sequences, the susceptibility information can reveal additional features of the tumor microenvironment. The concept of "intratumoral susceptibility signals" (ITSS) was introduced as a semiquantitative parameter that is comprised of "low-signal tubular structures or dot-like structures with or without conglomeration within a tumor" (45) that are indicative of tumor microbleedings or neovessels and indicate highly malignant lesions.

Using this approach, it was shown that metastases could be differentiated from GBM due to higher ITSS numbers in GBM, as well as high-grade gliomas from lymphomas and non-tumorous brain lesions (46).

However, the exact grading-scheme remained relatively reader-subjective, so further efforts were made subsequently to achieve a more objective, less reader-dependent measure. Percentage-wise quantification of ITSS using binarized mask of the SWI map compared the three most common metastatic entities in the brain, namely bronchial carcinoma (BC), mamma carcinoma (MC), and malignant melanoma (MM) (47) (**Figure 1**). This approach could discriminate MM from MC [area under the receiver operating characteristic curve (AUC) of 0.96] or BC (AUC of 0.81) while there was no clear cut-off between MC and BC. Specifically, only 1/20 MC patients showed more than 8% ITSS in contrast to 10/15 patients with MM. This indicates that different brain metastatic entities have different growth behavior, neoangiogenesis induction and aggressiveness, which can be inferred by SWI.

An important addition to this observation was made by Franceschi et al. who reported a correlation of ITSS and metastatic size (49): while micrometastases (i.e., <0.1 cm^3) only rarely showed ITSS (10/342), ITSS drastically increased in macrometastases (i.e., >0.1 cm^3, in 410/610 metastases). In this latter subpopulation, a higher propensity of ITSS in MM compared to MC was confirmed (76.9 vs. 55.6%).

SWI FOR INITIAL DIAGNOSIS OF BRAIN METASTASES

While SWI thus appears as a promising imaging contrast to contribute to the determination of the primary tumor entity in BM, it remained controversial if SWI is helpful for initial, early diagnosis of BM. This seems even more important in light of the recent discussions on the significance of gadolinium depositions in brain tissue following the exposure to gadolinium-containing contrast agents (50). This question was addressed in a recent work on the diagnostic performance of different MR

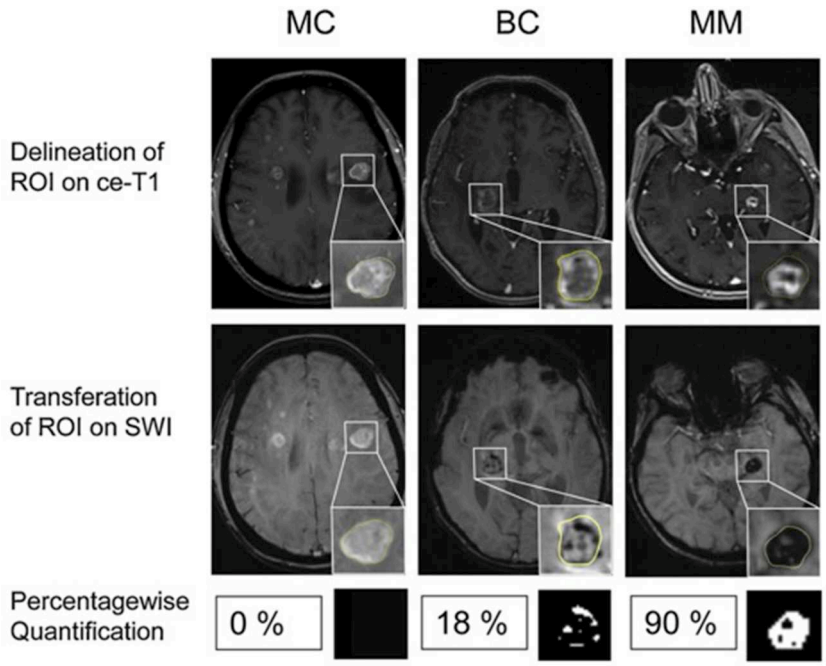

FIGURE 1 | Differentiation of brain metastases by ITSS. Examples of patients with MC, BC and MM. **(Upper)** Contrast enhanced T1-weighted images (ce-T1). **(Middle)** Contrast enhanced susceptibility weighted images (SWI). Insets: Delineation of the enhancing lesion on ce-T1 images and corresponding ROI on SWI. **(Lower)** Percentagewise ITSS quantification with corresponding binarized ITSS map. No ITSS (0%) in MC, minor ITSS (18%) in BC and subtotal ITSS (90%) in MM. Adapted from Radbruch et al. (48).

sequences in the early detection of melanoma brain metastases (38): In this work on a large retrospective cohort of more than 1200 patients, diagnostic sensitivity was compared between six different MR sequences, including SWI. The authors found that SWI did not reach the diagnostic sensitivity of contrast-enhanced T1-weighted imaging (64.7 vs. 99.7%). Interestingly, SWI also showed a lower sensitivity compared to FLAIR imaging (77.0%) but could outperform T2-weighted imaging (61.0%), non-contrast enhanced T1-weighted imaging (56.7%) and DWI (48.4%).

While data on other brain metastatic entities is currently lacking, it appears reasonable to assume that current SWI will not replace contrast-enhanced T1-weighted imaging for the early detection of metastatic brain disease because the underlying effects, namely the accumulation of paramagnetic ions and microbleedings, appear later than the early disruption of the blood brain barrier—which is delineated by ce-T1w-imaging.

SWI IN MELANOMA BRAIN METASTASES

Among malignant entities to metastasize to the brain, malignant melanoma plays a special role with regard to susceptibility effects. While SWI signal loss can relatively easily be attributed to (micro-)hemorrhage in other entities, melanin itself in MM may lead to susceptibility effects due to paramagnetic metal scavenging which is known to cause non-contrast-enhanced T1w-hyperintensity (51). This would imply that susceptibility-related signal losses could potentially indicate metastatic lesions which are not detectable in standard sequences. This was first reported by Gaviani et al. on T2*-weighted imaging in three malignant melanoma patients (52). However, later studies analyzing the fate of isolated cerebral SWI artifacts in larger patient cohorts over time could not confirm the hypothesis that such "isolated SWI signals" would eventually evolve into overt brain metastases (53, 54). Indeed, these studies showed that SWI signal losses without corresponding signal changes on standard sequences remained constant over time. On the other hand, it was reported that T1w-hyperintense melanotic metastases did not exhibit a higher frequency of SWI signal losses as compared to amelanotic metastases and the radiological presentation between cases could vary considerably (**Figure 2A**). Additionally, in another recent study significant differences in the susceptibility between melanotic and amelanotic brain metastases as measured by QSM could also not be demonstrated; nor could a correlation to T1-weighted signals be found, further underpinning that melanin *per se* does not account for a detectable paramagnetic effect *in vivo* (55) (**Figure 2B**).

SWI IN THE ASSESSMENT OF TREATMENT RESPONSES

Interestingly, Schwarz et al. found a significantly higher prevalence of isolated SWI artifacts among patients with

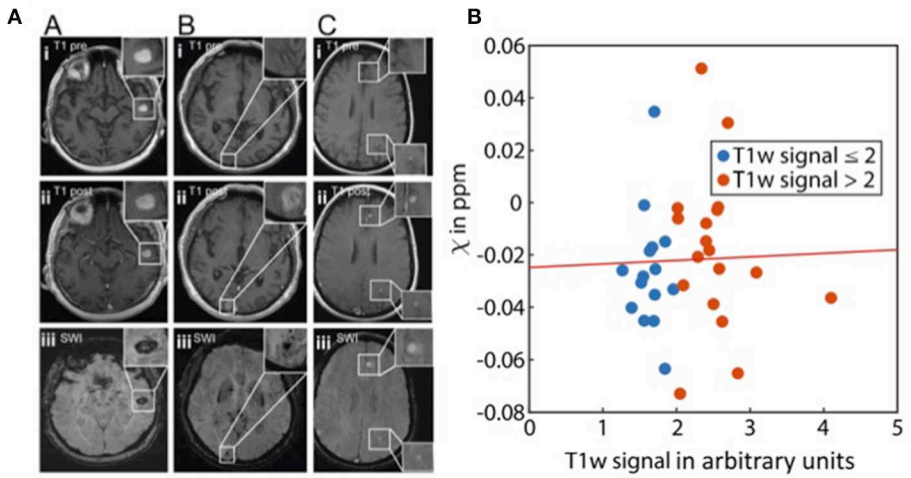

FIGURE 2 | Melanoma metastases and susceptibility. **(A)** Imaging findings in melanotic and amelanotic brain metastases. T1 pre-Gd-contrast (i), post-Gd-contrast administration (ii), and SWI (iii) images are shown for melanotic (A) and amelanotic (B) brain metastasis. (C) Examples of metastases with melanotic and amelanotic imaging features in a single patient. Adapted from Schwarz et al. (54). **(B)** Scatter plot showing the relation of susceptibility values (χ) and normalized T1w signal of melanoma metastases ($p = 0.87$). The line represents a linear fit. From Straub et al. (55).

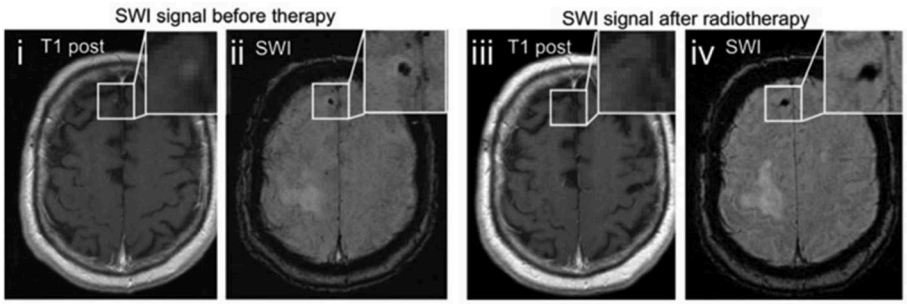

FIGURE 3 | Therapy related changes of SWI. Example images of a melanoma metastasis before (i, ii) and after radiotherapy (iii, iv). The punctuate contrast enhancement in the right frontal lobe (i) disappears after stereotactic radiotherapy (iii), being consistent with radiological remission. The SWI signal drop remains as a remnant of the preexisting metastasis (iv). Adapted from Schwarz et al. (54).

brain metastases as compared to melanoma patients without metastatic brain disease (54). Of those patients, only patients after radiotherapy showed an increased number of such artifacts indicating that these findings did not constitute vital tumor tissue but may rather represent either non-specific microbleedings or radiotherapy-related parenchymal damage (56) which are both well-known phenomena in patients after radiotherapy of the brain (57). As a third explanation of these findings the authors proposed the possibility of posttherapeutic remnants of former metastatic lesions because in cases of radiological remission of treated metastases, only an isolated SWI artifact persisted (**Figure 3**).

As many patients suffering from BM either receive stereotactic or whole-brain radiotherapy, it is crucial during tumor monitoring to differentiate between "pseudoprogression" following successful treatment and true recurrence of the disease (58, 59). Although not applied to brain metastases so far, R2*-mapping, another susceptibility-related imaging approach (60) has recently been introduced as a promising imaging marker to differentiate pseudoprogression from progressive disease in glioblastoma multiforme (61). The authors reported a rim of high R2* values with an accompanied SWI-hypointensity as indicative of pseudoprogression as well as a ratio of R2* in the contrast-enhancing to the non-contrast enhancing lesion close to 1. Conversely, a ratio of >1.3 was found in patients with true progression. According to this quantification a correct diagnosis was achieved in 9/9 patients. Similarly, promising results were reported in a preclinical model by the same group (62).

POTENTIAL FUTURE APPLICATIONS: TEXTURE ANALYSIS AND RADIOMICS

A number of methods have recently been introduced to extract multiple image features from MRI data to create high dimensional signatures of a given tumor. Such features of varying complexity can then, via a dedicated model, be used to predict certain target variables, in most cases histopathological or clinical

parameters possibly having an impact on treatment decisions and prognosis. This multi-step process is broadly referred to as "Radiomics" (63–65).

Expanding the input parameter space by adding complementary contrast with new information may provide new features and lead to a higher classification accuracy and reliability. SWI has just started to be incorporated into such models proving that it can indeed provide complementary discriminators, e.g., in the differentiation of glioblastoma and solitary brain metastases (66). It needs to be determined in future studies to which extent SWI will play a role for these applications.

SUMMARY AND OUTLOOK

SWI is a valuable image sequence that utilizes phase information to produce an image contrast different from standard anatomical MR sequences. It therefore provides complementary tissue information to further characterize brain lesions like brain metastases. While it does not appear to be usable as a sole image modality in metastatic brain disease lacking sensitivity and specificity, it can contribute important supplementary information on the underlying tumor entity and during treatment monitoring. In the future, quantitative susceptibility mapping may further refine tumor MR signatures, which could be used in texture and radiomic analysis to non-invasively support early detection and treatment monitoring of metastatic brain disease.

AUTHOR CONTRIBUTIONS

All authors listed have made a substantial, direct and intellectual contribution to the work, and approved it for publication.

FUNDING

MBr was supported by the Else Kröner-Fresenius Stiftung (2017-A25; 2019_EKMS.23). DS and MBe were supported by a physician-scientist fellowship of the Medical Faculty, University of Heidelberg. This work was further supported by the Deutsche Forschungsgemeinschaft (DFG, German Research Foundation, SFB 1389 and SFB 1118).

ACKNOWLEDGMENTS

We acknowledge financial support by the Baden-Württemberg Ministry of Science, Research and the Arts and by Ruprecht-Karls-Universität Heidelberg for open access publishing.

REFERENCES

1. Soffietti R, Abacioglu U, Baumert B, Combs SE, Kinhult S, Kros JM, et al. Diagnosis and treatment of brain metastases from solid tumors: guidelines from the European Association of Neuro-Oncology (EANO). *Neuro-Oncology*. (2017) 19:162–74. doi: 10.1093/neuonc/now241
2. Lin NU, Lee EQ, Aoyama H, Barani IJ, Barboriak DP, Baumert BG, et al. Response assessment criteria for brain metastases: proposal from the RANO group. *Lancet Oncol.* (2015) 16:e270–8. doi: 10.1016/S1470-2045(15)70057-4
3. Specht HM, Combs SE. Stereotactic radiosurgery of brain metastases. *J Neurosurg Sci.* (2016) 60:357–66. doi: 10.1007/s00066-016-0955-2
4. Kellner CP, D'Ambrosio AL. Surgical management of brain metastases. *Neurosurg Clin N Am*. (2011) 22:53–9– vi. doi: 10.1016/j.nec.2010.08.003
5. Tawbi HA, Forsyth PA, Algazi A, Hamid O, Hodi FS, Moschos SJ, et al. Combined nivolumab and ipilimumab in melanoma metastatic to the brain. *N Engl J Med*. (2018) 379:722–30. doi: 10.1056/NEJMoa1805453
6. Goldberg SB, Gettinger SN, Mahajan A, Chiang AC, Herbst RS, Sznol M, et al. Pembrolizumab for patients with melanoma or non-small-cell lung cancer and untreated brain metastases: early analysis of a non-randomised, open-label, phase 2 trial. *Lancet Oncol*. (2016) 17:976–83. doi: 10.1016/S1470-2045(16)30053-5
7. Reichenbach JR, Venkatesan R, Schillinger DJ, Kido DK, Haacke EM. Small vessels in the human brain: MR venography with deoxyhemoglobin as an intrinsic contrast agent. *Radiology*. (1997) 204:272–7. doi: 10.1148/radiology.204.1.9205259
8. Halefoglu AM, Yousem DM. Susceptibility weighted imaging: clinical applications and future directions. *World J Radiol*. (2018) 10:30–45. doi: 10.4329/wjr.v10.i4.30
9. Schweser F, Preda M, Zivadinov R. Susceptibility weighted MRI in rodents at 9.4 T. *Methods Mol Biol*. (2018) 1718:205–34. doi: 10.1007/978-1-4939-7531-0_13
10. Dusek P, Dezortova M, Wuerfel J. Imaging of iron. *Int Rev Neurobiol*. (2013) 110:195–239. doi: 10.1016/B978-0-12-410502-7.00010-7
11. Cheng AL, Batool S, McCreary CR, Lauzon ML, Frayne R, Goyal M, et al. Susceptibility-weighted imaging is more reliable than T2*-weighted gradient-recalled echo MRI for detecting microbleeds. *Stroke*. (2013) 44:2782–6. doi: 10.1161/STROKEAHA.113.002267
12. Goos JDC, van der Flier WM, Knol DL, Pouwels PJW, Scheltens P, Barkhof F, et al. Clinical relevance of improved microbleed detection by susceptibility-weighted magnetic resonance imaging. *Stroke*. (2011) 42:1894–900. doi: 10.1161/STROKEAHA.110.599837
13. Ghassaban K, Liu S, Jiang C, Haacke EM. Quantifying iron content in magnetic resonance imaging. *NeuroImage*. (2019) 187:77–92. doi: 10.1016/j.neuroimage.2018.04.047
14. Sehgal V, Delproposto Z, Haddar D, Haacke EM, Sloan AE, Zamorano LJ, et al. Susceptibility-weighted imaging to visualize blood products and improve tumor contrast in the study of brain masses. *J Magn Reson Imaging*. (2006) 24:41–51. doi: 10.1002/jmri.20598
15. Heyn C, Alcaide-Leon P, Bharatha A, Sussman MS, Kucharczyk W, Mandell DM. Susceptibility-weighted imaging in neurovascular disease. *Top Magn Reson Imaging.* (2016) 25:63–71. doi: 10.1097/RMR.0000000000000079
16. Radbruch A, Mucke J, Schweser F, Deistung A, Ringleb PA, Ziener CH, et al. Comparison of susceptibility weighted imaging and TOF-angiography for the detection of thrombi in acute stroke. *PLoS ONE*. (2013) 8:e63459. doi: 10.1371/journal.pone.0063459
17. Hsu CC-T, Watkins TW, Kwan GNC, Haacke EM. Susceptibility-weighted imaging of glioma: update on current imaging status and future directions. *J Neuroimaging*. (2016) 26:383–90. doi: 10.1111/jon.12360
18. Fahrendorf D, Schwindt W, Wölfer J, Jeibmann A, Kooijman H, Kugel H, et al. Benefits of contrast-enhanced SWI in patients with glioblastoma multiforme. *Eur Radiol*. (2013) 23:2868–79. doi: 10.1007/s00330-013-2895-x
19. Nisenbaum EJ, Novikov DS, Lui YW. The presence and role of iron in mild traumatic brain injury: an imaging perspective. *J Neurotrauma.* (2014) 31:301–7. doi: 10.1089/neu.2013.3102
20. Siemonsen S, Young KL, Bester M, Sedlacik J, Heesen C, Fiehler J, Stellmann JP. Chronic T2 lesions in multiple sclerosis are heterogeneous regarding phase MR imaging. *Clin Neuroradiol*. (2016) 26:457–64. doi: 10.1007/s00062-015-0389-8

21. Enzinger C, Barkhof F, Ciccarelli O, Filippi M, Kappos L, Rocca MA, et al. Nonconventional MRI and microstructural cerebral changes in multiple sclerosis. *Nat Rev Neurol*. (2015) 11:676–86. doi: 10.1038/nrneurol.2015.194
22. Eisele P, Fischer K, Szabo K, Platten M, Gass A. Characterization of contrast-enhancing and non-contrast-enhancing multiple sclerosis lesions using susceptibility-weighted imaging. *Front Neurol*. (2019) 10:515. doi: 10.3389/fneur.2019.01082
23. Absinta M, Sati P, Schindler M, Leibovitch EC, Ohayon J, Wu T, et al. Persistent 7-tesla phase rim predicts poor outcome in new multiple sclerosis patient lesions. *J Clin Invest*. (2016) 126:2597–609. doi: 10.1172/JCI86198
24. Di Ieva A, Lam T, Alcaide-Leon P, Bharatha A, Montanera W, Cusimano MD. Magnetic resonance susceptibility weighted imaging in neurosurgery: current applications and future perspectives. *J Neurosurg*. (2015) 123:1463–75. doi: 10.3171/2015.1.JNS142349
25. Haacke EM, Xu Y, Cheng Y-CN, Reichenbach JRR. Susceptibility weighted imaging (SWI). *Magn Reson Med*. (2004) 52:612–8. doi: 10.1002/mrm.20198
26. Haacke EM, Liu S, Buch S, Zheng W, Wu D, Ye Y. Quantitative susceptibility mapping: current status and future directions. *Magn Res Imaging*. (2015) 33:1–25. doi: 10.1016/j.mri.2014.09.004
27. Schweser F, Sommer K, Deistung A, Reichenbach JR. Quantitative susceptibility mapping for investigating subtle susceptibility variations in the human brain. *NeuroImage*. (2012) 62:2083–100. doi: 10.1016/j.neuroimage.2012.05.067
28. Liu S, Buch S, Chen Y, Choi H-S, Dai Y, Habib C, et al. Susceptibility-weighted imaging: current status and future directions. *NMR Biomed*. (2016) 30:e3552. doi: 10.1002/nbm.3552
29. Liu T, Surapaneni K, Lou M, Cheng L, Spincemaille P, Wang Y. Cerebral microbleeds: burden assessment by using quantitative susceptibility mapping. *Radiology*. (2012) 262:269–78. doi: 10.1148/radiol.11110251
30. Klohs J, Deistung A, Schweser F, Grandjean J, Dominietto M, Waschkies C, et al. Detection of cerebral microbleeds with quantitative susceptibility mapping in the ArcAbeta mouse model of cerebral amyloidosis. *J Cereb Blood Flow Metab*. (2011) 31:2282–92. doi: 10.1038/jcbfm.2011.118
31. Langkammer C, Liu T, Khalil M, Enzinger C, Jehna M, Fuchs S, Fazekas F, Wang Y, Ropele S. Quantitative susceptibility mapping in Multiple Sclerosis. *Radiology*. (2013) 267:551–9. doi: 10.1148/radiol.12120707
32. Haller S, Scheffler M, Salomir R, Herrmann FR, Gold G, Montandon M-L, Kövari E. MRI detection of cerebral microbleeds: size matters. *Neuroradiology*. (2019) 61:1209–13. doi: 10.1007/s00234-019-02267-0
33. Mohammed W, Xunning H, Haibin S, Jingzhi M. Clinical applications of susceptibility-weighted imaging in detecting and grading intracranial gliomas: a review. *Cancer Imaging*. (2013) 13:186–95. doi: 10.1102/1470-7330.2013.0020
34. Hori M, Ishigame K, Kabasawa H, Kumagai H, Ikenaga S, Shiraga N, et al. Precontrast and postcontrast susceptibility-weighted imaging in the assessment of intracranial brain neoplasms at 1.5 T. *Jpn J Radiol*. (2010) 28:299–304. doi: 10.1007/s11604-010-0427-z
35. Li C, Ai B, Li Y, Qi H, Wu L. Susceptibility-weighted imaging in grading brain astrocytomas. *EurJ Radiol*. (2010) 75:e81–5. doi: 10.1016/j.ejrad.2009.08.003
36. Pinker K, Noebauer-Huhmann IM, Stavrou I, Hoeftberger R, Szomolanyi P, Karanikas G, et al. High-resolution contrast-enhanced, susceptibility-weighted MR imaging at 3T in patients with brain tumors: correlation with positron-emission tomography and histopathologic findings. *Am J Neuroradiol*. (2007) 28:1280–6. doi: 10.3174/ajnr.A0540
37. Di Ieva A, Göd S, Grabner G, Grizzi F, Sherif C, Matula C, et al. Three-dimensional susceptibility-weighted imaging at 7 T using fractal-based quantitative analysis to grade gliomas. *Neuroradiology*. (2013) 55:35–40. doi: 10.1007/s00234-012-1081-1
38. Deike-Hofmann K, Thünemann D, Breckwoldt MO, Schwarz D, Radbruch A, Enk A, et al. Sensitivity of different MRI sequences in the early detection of melanoma brain metastases. *PLoS ONE*. (2018) 13:e0193946. doi: 10.1371/journal.pone.0193946
39. Mehrabian H, Detsky J, Soliman H, Sahgal A, Stanisz GJ. Advanced magnetic resonance imaging techniques in management of brain metastases. *Front Oncol*. (2019) 9:S192. doi: 10.3389/fonc.2019.00440
40. Garcia M, Gloor M, Bieri O, Radüe E-W, Lieb JM, Cordier D, Stippich C. Imaging of primary brain tumors and metastases with fast quantitative 3-dimensional magnetization transfer. *J Neuroimaging*. (2015) 25:1007–14. doi: 10.1111/jon.12222
41. Mehrabian H, Lam WW, Myrehaug S, Sahgal A, Stanisz GJ. Glioblastoma (GBM) effects on quantitative MRI of contralateral normal appearing white matter. *J Neurooncol*. (2018) 139:97–106. doi: 10.1007/s11060-018-2846-0
42. Desmond KL, Moosvi F, Stanisz GJ. Mapping of amide, amine, and aliphatic peaks in the CEST spectra of murine xenografts at 7 T. *Magn Reson Med*. (2014) 71:1841–53. doi: 10.1002/mrm.24822
43. Desmond KL, Mehrabian H, Chavez S, Sahgal A, Soliman H, Rola R, Stanisz GJ. Chemical exchange saturation transfer for predicting response to stereotactic radiosurgery in human brain metastasis. *Magn Reson Med*. (2017) 78:1110–20. doi: 10.1002/mrm.26470
44. Chuang M-T, Liu Y-S, Tsai Y-S, Chen Y-C, Wang C-K. Differentiating radiation-induced necrosis from recurrent brain tumor using MR perfusion and spectroscopy: a meta-analysis. *PLoS ONE*. (2016) 11:e0141438. doi: 10.1371/journal.pone.0141438
45. Park MJ, Kim HS, Jahng GH, Ryu CW, Park SM, Kim SY. Semiquantitative assessment of intratumoral susceptibility signals using non-contrast-enhanced high-field high-resolution susceptibility-weighted imaging in patients with gliomas: comparison with MR perfusion imaging. *Am J Neuroradiol*. (2009) 30:1402–8. doi: 10.3174/ajnr.A1593
46. Kim HS, Jahng GH, Ryu CW, Kim SY. Added value and diagnostic performance of intratumoral susceptibility signals in the differential diagnosis of solitary enhancing brain lesions: preliminary study. *Am J Neuroradiol*. (2009) 30:1574–9. doi: 10.3174/ajnr.A1635
47. Radbruch A, Wiestler B, Kramp L, Lutz K, Bäumer P, Weiler M, et al. Differentiation of glioblastoma and primary CNS lymphomas using susceptibility weighted imaging. *Eur J Radiol*. (2013) 82:552–6. doi: 10.1016/j.ejrad.2012.11.002
48. Radbruch A, Graf M, Kramp L, Wiestler B, Floca R, Baumer P, et al. Differentiation of brain metastases by percentagewise quantification of intratumoral-susceptibility-signals at Tesla. *Eur J Radiol*. (2012) 81:4064–8. doi: 10.1016/j.ejad.2012.06.016
49. Franceschi AM, Moschos SJ, Anders CK, Glaubiger S, Collichio FA, Lee CB, et al. Use of susceptibility-weighted imaging (SWI) in the detection of brain hemorrhagic metastases from breast cancer and melanoma. *J Comput Assist Tomogr*. (2016) 40:803–5. doi: 10.1097/RCT.0000000000000420
50. Kanda T, Ishii K, Kawaguchi H, Kitajima K, Takenaka D. High signal intensity in the dentate nucleus and globus pallidus on unenhanced T1-weighted MR images: relationship with increasing cumulative dose of a gadolinium-based contrast material. *Radiology*. (2014) 270:834–41. doi: 10.1148/radiol.13131669
51. Enochs WS, Petherick P, Bogdanova A, Mohr U, Weissleder R. Paramagnetic metal scavenging by melanin: MR imaging. *Radiology*. (1997) 204:417–23. doi: 10.1148/radiology.204.2.9240529
52. Gaviani P, Mullins ME, Braga TA, Hedley-Whyte ET, Halpern EF, Schaefer PS, et al. Improved detection of metastatic melanoma by T2*-weighted imaging. *Am J Neuroradiol*. (2006) 27:605–608.
53. Gramsch C, Göricke SL, Behrens F, Zimmer L, Schadendorf D, Krasny A, et al. Isolated cerebral susceptibility artefacts in patients with malignant melanoma: metastasis or not? *Eur Radiol*. (2013) 23:2622–7. doi: 10.1007/s00330-013-2857-3
54. Schwarz D, Niederle T, Münch P, Hielscher T, Hassel JC, Schlemmer H-P, et al. Susceptibility-weighted imaging in malignant melanoma brain metastasis. *J Magn Reson Imaging*. (2019) 16:e486. doi: 10.1002/jmri.26692
55. Straub S, Laun FB, Freitag MT, Kölsche C, Deimling von A, Denoix M, et al. Assessment of melanin content and its Influence on susceptibility contrast in melanoma metastases. *Clin Neuroradiol*. (2019) 1–8. doi: 10.1007/s00062-019-00816-x
56. Varon D, Simons M, Chiang F, Tedesqui G, Pacheco G, Martinez P, et al. Brain radiation-related black dots on susceptibility-weighted imaging. *Neuroradiol J*. (2014) 27:445–51. doi: 10.15274/NRJ-2014-10071
57. Lupo JM, Chuang CF, Chang SM, Barani IJ, Jimenez B, Hess CP, et al. 7-Tesla susceptibility-weighted imaging to assess the effects of radiotherapy on

normal-appearing brain in patients with glioma. *Int J Radiat Oncol Biol Phys*. (2012) 82:e493–500. doi: 10.1016/j.ijrobp.2011.05.046
58. Thust SC, van den Bent MJ, Smits M. Pseudoprogression of brain tumors. *J Magn Reson Imaging*. (2018) 48:571–89. doi: 10.1002/jmri.26171
59. Reardon DA, Weller M. Pseudoprogression: fact or wishful thinking in neuro-oncology? *Lancet Oncol*. (2018) 19:1561–3. doi: 10.1016/S1470-2045(18)30654-5
60. Deistung A, Schäfer A, Schweser F, Biedermann U, Turner R, Reichenbach JR. Toward in vivo histology: a comparison of quantitative susceptibility mapping (QSM) with magnitude-, phase-, and R2*-imaging at ultra-high magnetic field strength. *NeuroImage*. (2013) 65:299–314. doi: 10.1016/j.neuroimage.2012.09.055
61. Belliveau J-G, Bauman GS, Macdonald D, Macdonald M, Klassen LM, Menon RS. Apparent transverse relaxation (R_2^*) on MRI as a method to differentiate treatment effect (pseudoprogression) versus progressive disease in chemoradiation for malignant glioma. *J Med Imaging Radiat Oncol*. (2018) 62:224–31. doi: 10.1111/1754-9485.12694
62. Belliveau J-G, Jensen MD, Stewart JMP, Solovey I, Klassen LM, Bauman GS, et al. Prediction of radiation necrosis in a rodent model using magnetic resonance imaging apparent transverse relaxation. *Phys Med Biol*. (2018) 63:035010. doi: 10.1088/1361-6560/aaa034
63. Gillies RJ, Kinahan PE, Hricak H. Radiomics: images are more than pictures, they are data. *Radiology*. (2016) 278:563–77. doi: 10.1148/radiol.2015151169
64. Lambin P, Rios-Velazquez E, Leijenaar R, Carvalho S, van Stiphout RGPM, Granton P, et al. Radiomics: extracting more information from medical images using advanced feature analysis. *Eur J Cancer*. (2012) 48:441–6. doi: 10.1016/j.ejca.2011.11.036
65. Rizzo S, Botta F, Raimondi S, Origgi D, Fanciullo C, Morganti AG, et al. Radiomics: the facts and the challenges of image analysis. *Eur Radiol Exp*. (2018) 2:36. doi: 10.1186/s41747-018-0068-z
66. Petrujkić K, Milošević N, Rajković N, Stanisavljević D, Gavrilović S, DŽelebdŽić D, et al. Computational quantitative MR image features - a potential useful tool in differentiating glioblastoma from solitary brain metastasis. *Eur J Radiol*. (2019) 119:108634. doi: 10.1016/j.ejrad.2019.08.003

Conflict of Interest: The authors declare that the research was conducted in the absence of any commercial or financial relationships that could be construed as a potential conflict of interest.

frontiers in Neurology

REVIEW
published: 07 February 2020
doi: 10.3389/fneur.2020.00001

PET/MRI Radiomics in Patients With Brain Metastases

Philipp Lohmann[1,2*], *Martin Kocher*[1,2], *Maximillian I. Ruge*[2,3], *Veerle Visser-Vandewalle*[2], *N. Jon Shah*[1,4,5], *Gereon R. Fink*[1,6], *Karl-Josef Langen*[1,3,7] *and Norbert Galldiks*[1,3,6]

[1] *Institute of Neuroscience and Medicine (INM-3/-4/-11), Research Center Juelich, Jülich, Germany,* [2] *Department of Stereotaxy and Functional Neurosurgery, Faculty of Medicine and University Hospital Cologne, University of Cologne, Cologne, Germany,* [3] *Center of Integrated Oncology, Universities of Aachen, Bonn, Cologne, and Duesseldorf, Cologne, Germany,* [4] *JARA-BRAIN-Translational Medicine, Aachen, Germany,* [5] *Department of Neurology, Rheinisch-Westfälische Technische Hochschule (RWTH) Aachen University, Aachen, Germany,* [6] *Department of Neurology, Faculty of Medicine and University Hospital Cologne, University of Cologne, Cologne, Germany,* [7] *Department of Nuclear Medicine, Rheinisch-Westfälische Technische Hochschule (RWTH) Aachen University, Aachen, Germany*

Although a variety of imaging modalities are used or currently being investigated for patients with brain tumors including brain metastases, clinical image interpretation to date uses only a fraction of the underlying complex, high-dimensional digital information from routinely acquired imaging data. The growing availability of high-performance computing allows the extraction of quantitative imaging features from medical images that are usually beyond human perception. Using machine learning techniques and advanced statistical methods, subsets of such imaging features are used to generate mathematical models that represent characteristic signatures related to the underlying tumor biology and might be helpful for the assessment of prognosis or treatment response, or the identification of molecular markers. The identification of appropriate, characteristic image features as well as the generation of predictive or prognostic mathematical models is summarized under the term radiomics. This review summarizes the current status of radiomics in patients with brain metastases.

Keywords: artificial intelligence, machine learning, deep learning, brain tumors, textural features, amino acid PET, CT

OPEN ACCESS

Edited by:
Susie Y. Huang,
Massachusetts General Hospital,
Harvard Medical School,
United States

Reviewed by:
Niha Beig,
Case Western Reserve University,
United States
Marc Benayoun,
Wake Forest Baptist Medical Center,
United States

***Correspondence:**
Philipp Lohmann
p.lohmann@fz-juelich.de

Specialty section:
This article was submitted to Applied Neuroimaging, a section of the journal Frontiers in Neurology

Received: *15 November 2019*
Accepted: *02 January 2020*
Published: *07 February 2020*

Citation:
Lohmann P, Kocher M, Ruge MI, Visser-Vandewalle V, Shah NJ, Fink GR, Langen K-J and Galldiks N (2020) PET/MRI Radiomics in Patients With Brain Metastases. Front. Neurol. 11:1. doi: 10.3389/fneur.2020.00001

INTRODUCTION

Brain metastases are one of the most common neurological complications of extracranial cancer and account for more than half of all brain tumors (1). In patients with solid cancers, the risk to develop brain metastases depends on the type and initial stage of the primary tumor. It is in the range of 5–20% and may be increasing due to improvements in control of extracerebral disease by modern systemic treatment and the resulting increasing life expectancy, and technical advances in medical imaging for the detection of small brain metastases (1–3).

Lung cancer, breast cancer, and melanoma are the most common primary tumors that lead to the formation of brain metastases in adults and account for 67–80% of all cancers (1). In about 10% of patients with brain metastases, the primary tumor is unknown (cancer of unknown primary, CUP) (1, 4). Standard treatment for patients with oligometastatic brain disease includes surgical resection, radiotherapy (predominantly stereotactic radiosurgery), and combinations thereof (5). Whole-brain radiotherapy is frequently used in patients with multiple brain metastases. Furthermore,

modern systemic treatment options such as immunotherapy including checkpoint inhibitors and targeted therapy are increasingly used to control intra- and extracranial disease (6, 7). Importantly, some molecularly defined subgroups of patients have been identified which have an improved prognosis (8) and benefit from these recently developed agents, e.g., combined BRAF/MEK inhibition using the kinase inhibitors dabrafenib plus trametinib in patients with BRAF-mutant melanoma brain metastases (9).

Magnetic resonance imaging (MRI) is the method of choice to evaluate patients with brain lesions such as primary or metastatic brain tumors. MRI offers excellent soft tissue contrast and a high availability, but its specificity is low (10–12). For example, contrast-enhancing lesions during follow-up and signal alterations on T2 or fluid attenuated inversion recovery (FLAIR) MRI may be non-specific and can result from various causes other than tumor tissue such as infection, demyelination, inflammation, ischemia, or treatment-related changes after surgery, radiotherapy, or systemic therapy. Consequently, with the use of conventional MRI alone, important diagnostic challenges remain such as the differentiation of local brain metastasis relapse from radiation injury and the evaluation of response to treatment that included immunotherapy (13, 14). The latter may lead to the clinically important phenomenon of pseudoprogression, which is characterized by worsening imaging findings on conventional MRI during follow-up caused by treatment-related changes imitating tumor progression that spontaneously vanish during further follow-up without treatment (14). A false diagnosis of pseudoprogression carries the risk of a premature termination of an effective treatment with serious consequences for the patients (13–15).

Advanced MRI techniques have been introduced in the last years to overcome some of the aforementioned limitations of conventional MRI in patients with brain tumors. The advanced MRI techniques currently under investigation in neuro-oncology include, but are not limited to, diffusion-weighted imaging (DWI), perfusion-weighted imaging (PWI), and MR spectroscopy (MRS) (16–19). These techniques might complement conventional MRI by providing insights into additional tumor characteristics such as perfusion, angiogenesis, cellularity, pH, or metabolite concentrations beyond anatomical information.

Another advanced imaging method extensively evaluated in neuro-oncology is positron emission tomography (PET) with tracers other than the traditionally used 2-[^{18}F]-fluoro-2-deoxy-D-glucose (FDG) for the characterization of tumor metabolism. It has been emphasized by the Response Assessment in Neuro-Oncology (RANO) working group, the European Association for Neuro-Oncology (EANO), and the Society for Neuro-Oncology (SNO) that the additional clinical value of amino acid PET tracers such as [^{11}C]-methyl-L-methionine (MET), O-(2-[^{18}F]fluoroethyl)-L-tyrosine (FET), or 3,4-dihydroxy-6-[18F]-fluoro-L-phenylalanine (FDOPA) in patients with gliomas (11, 20, 21) and also brain metastases (4, 22) is outstanding and superior to FDG for various clinical indications.

Although a variety of imaging modalities are used or currently being investigated for patients with brain tumors including brain metastases, clinical image interpretation to date uses only a fraction of the underlying information. Importantly, the images contain complex, high-dimensional digital information that can be made accessible by means of advanced image analysis using machine learning techniques. The growing availability of high-performance computing allows the extraction of quantitative imaging features from medical images that are beyond human perception. Using machine learning techniques and advanced statistical methods, subsets of these imaging features are used to generate mathematical models that represent characteristic signatures related to the underlying tumor biology and might be helpful for the assessment of prognosis or treatment response, or the identification of molecular markers. The identification of appropriate, characteristic image features as well as the generation of predictive or prognostic mathematical models is summarized under the term radiomics (23–26).

Radiomics is usually applied in standard-of-care medical images from any imaging modality (e.g., CT, MRI, PET), thereby allowing additional data evaluation at low cost. The computed radiomics features, either predefined (feature-based radiomics) or generated by supervised learning (deep learning-based radiomics), are more reliable, robust, and reproducible compared to the visual interpretation of imaging features, because radiomics features are computed semi- or fully-automatically.

Another application of radiomics analysis, radiogenomics, aims at the prediction of molecular biomarkers such as genetic mutations, chromosome alterations, or methylation profiles from image data (27). Typically, such biomarkers require tissue samples obtained by stereotactic biopsy or tumor resection and are not accessible by conventional, qualitative image analysis. Consequently, radiogenomics as a non-invasive method to assess biomarkers in patients with brain tumors is of great scientific and clinical interest.

This review summarizes the current status of radiomics in patients with brain metastases.

RADIOMICS

Basically, radiomics can be subdivided into feature-based and deep learning-based radiomics. Feature-based radiomics uses mathematically predefined image features that are extracted and computed from preprocessed and segmented medical images. Using machine learning techniques, a subset of these features is selected for the generation of a predictive or prognostic model related to the research question.

Deep learning-based radiomics is fundamentally different as it does not require image segmentation or pre-defined features. In deep learning, artificial neural networks imitate the function of the human visual system and automatically extract high-dimensional features from the original images at different abstraction levels and such autonomously learn characteristic patterns and classify them. In the following section, the basic principles of feature- and deep learning-based radiomics image analysis are briefly introduced.

Feature-Based Radiomics

Pre-processing

Radiomics aims at the extraction of quantitative features from medical images (23–26). Consequently, the imaging data supposed to be analyzed have to be quantitative or at least semi-quantitative. In order to allow reproducible and comparable results, especially if data from different scanners or acquisition protocols are used, an upfront normalization procedure is necessary which may include intensity normalizations, spatial smoothing or re-sampling, other types or image filtering or corrections of MRI field inhomogeneities (24, 28–30).

Segmentation

For brain metastases, segmentation is usually performed manually on conventional MRI or CT. Although brain metastases are usually well-circumscribed contrast-enhancing lesions, the manual, three-dimensional segmentation is time-consuming. To overcome this issue, machine learning techniques are being developed for the automated detection and segmentation of brain metastases using deep learning (31, 32). However, these tools still have to prove their reliability and added value to ultimately become part of clinical routine.

Feature Extraction

Different kind of quantitative features can be extracted from medical images, which are usually grouped into the following subgroups:

- *Shape features*: Geometric properties of the segmented region of interest (ROI) or volume of interest (VOI) such as compacity, sphericity, volume, or maximum surface can be described by shape features.
- *Histogram-based features* (first-order statistics features): Histograms are used to characterize the distribution of individual voxel intensity values within the ROI or VOI without considering their spatial orientation. From the histogram, measures such as the mean, median, minimum, maximum, entropy (randomness), uniformity, asymmetry (skewness), or kurtosis (flatness) can be calculated.
- *Textural features* (second-order statistics features): The intratumoral heterogeneity can be quantified by means of textural feature analysis. Textural features represent statistical relationships between intensity of neighboring voxels and groups of voxels. Textural features are not directly calculated from the image, but from special matrices that already represent a certain aspect of intravoxel relationship; i.e., the gray-level co-occurrence matrix (GLCM) represents the incidence of voxels with the same intensity values at a certain distance along a fixed direction. Another frequently used matrix, the gray-level size-zone matrix (GLSZM), represents the distribution of groups of voxels with the same intensity. Several other matrices exist from which a number of different textural features can be calculated (33).
- *Higher-order statistics features*: Features extracted by statistical methods after the application of mathematical transformations (filters) for, e.g., edge enhancement, noise suppression, or the identification of repeating patterns or histogram-oriented gradients are considered higher-order statistics features. Such mathematical transformations or filters include Laplacian transforms of Gaussian-filtered images (Laplacian-of-Gaussian, LoG), wavelet transforms, fractal analysis, or Minkowski functionals.

In this way, hundreds to thousands of quantitative features can be extracted from a single medical image.

Feature Selection and Model Generation

As mentioned above, hundreds to thousands of features can be easily extracted from a single medical image, which is why the relevant parameters from the large number of available features have to be extracted. This essential step is called feature selection (26).

Once a subset of important features is identified, a mathematical model can be generated that predicts the known, underlying ground truth such as a certain genotype or a better prognosis. Commonly used machine learning algorithms for model generation in radiomics are decision trees (e.g., random forests), linear or logistic regression, support vector machines, and k-nearest neighbors. These algorithms are tested for classification accuracy in a subset of data (training dataset). Then, in order to assess the robustness of the model, the best-performing model is applied to another subset of data that were not used during the process of model generation (validation dataset). Ideally, the model is finally applied to a third dataset (test dataset) including imaging data acquired from different institutions using different scanners and different acquisition protocols in order to evaluate the generalizability of the model. However, these steps require large amounts of data (e.g., 70% of images for training/validation and 30% for testing).

In cases in which the number of patients is small and no reasonable and balanced data splitting into a training and a test cohort can be performed prior to model generation, statistical methods such as cross-validation can be applied to estimate the model performance without the availability of a test dataset. The available datasets are partitioned into k subsets of equal size, and one subset is retained as testing data, while the remaining k-1 datasets are used as training data. Afterwards, the process is repeated k-times with each subset used once as testing data. The model performance estimators from each k iteration can then be averaged to produce a single estimation of model performance.

Deep Learning-Based Radiomics

Deep learning as another sub-category of machine learning or artificial intelligence uses artificial neural networks that simulate the neural structure of the brain for classification of high-dimensional non-linear data or pattern recognition (34).

Conventional machine learning algorithms require a workflow involving image preprocessing, segmentation of the ROI, and definition of the inherent features using feature selection techniques followed by model generation and validation. Artificial neural networks automatically extract high-dimensional features from the original or preprocessed images at different scaling and abstraction levels, and autonomously learn the patterns and classify them (35). A cascaded system

of single layer neural networks is trained to identify and learn relevant structures within the image data that are useful for classification without any prior definition or selection. These complex structures are then combined to generate features with a higher level of abstraction. The output from the very last layer of the network is then used to fit a prediction model.

However, artificial neural networks strongly depend on the input data and usually require large amounts of image for the identification of robust and representative features which limits its applicability in neuro-oncological research, where the number of available datasets usually is small. One technique to overcome this issue is called transfer learning, wherein an artificial neural network is utilized that was already trained for a different, but similar task; e.g., a neural network that has been used for the classification of glioma subtypes might also be useful for the classification of brain metastases (36). Thereby, the amount of data necessary for training the network can be reduced since the network already has some prior knowledge about brain lesions.

RADIOMICS IN PATIENTS WITH BRAIN METASTASES

Radiomics in patients with brain metastases is mainly based on the analysis of conventional MRI data. The majority of studies investigated the usefulness of radiomics to differentiate treatment-related changes from brain metastases recurrence after radiotherapy, which is one of the most important indications in the field. Some studies have also evaluated the value of radiomics for the prediction of brain metastases origin and the differentiation of brain metastases from glioblastoma. Furthermore, radiomics in patients with brain metastases was used for treatment response assessment. In the following, the key findings of radiomics-based research in patients with brain metastases are summarized. An overview of the discussed studies and the main results is provided in **Table 1**.

Differentiation of Treatment-Related Changes From Brain Metastases Recurrence

Patients with brain metastases are increasingly treated with stereotactic radiosurgery. Not infrequently, radiation injury (e.g., radiation necrosis) may occur after radiosurgery and is often indistinguishable from actual tumor progression using conventional MRI alone.

Peng et al. (37) evaluated the usefulness of MRI radiomics for this important question. Sixty-six patients with 82 lesions treated with stereotactic radiosurgery and imaging findings on contrast-enhanced T1 and FLAIR sequences suspicious for tumor recurrence were included in the study. Fifty-one radiomics features (3 shape features, 14 histogram-based features, and 34 textural features) were extracted for each lesion on each MRI contrast. Models were generated using the IsoSVM algorithm which performs both feature selection and classification (49). No separate dataset was available for model testing. However, cross-validation was performed to assess overall model performance. The model reached an area under the receiver operating characteristic curve (AUC) of 0.81 with a specificity of 65% and a sensitivity of 87%. On the contrary, experienced radiologists could only classify 73% of the cases with a sensitivity of 97% and a specificity of only 19%.

Similarly, Zhang et al. (38) used pre- and post-contrast T1-weighted MR images, T2 and FLAIR from 87 patients to calculate 285 radiomics features. Interestingly, imaging data from two time points were available so that the authors also investigated feature reproducibility to identify a feature subset with reproducible values. Changes in radiomics features (so-called "delta radiomics") from one follow-up time point to the other were evaluated and used for differentiation of radiation necrosis and tumor progression. The final model generated by an ensemble classifier had an overall predictive accuracy of 73% and an AUC of 0.73 after cross-validation. Again, no separate dataset for testing was available.

Besides MRI, also amino acid PET images have been used to evaluate radiomics for the differentiation of treatment-related changes from brain metastases recurrence. It has been demonstrated that the evaluation of the time-activity-curves (TAC) that represent the tracer uptake over time is helpful for differentiation of treatment-related changes from brain metastases recurrence (50). However, this requires a time-consuming dynamic FET PET scan of at least 40 min acquisition time or more. Therefore, Lohmann et al. (39) calculated 62 textural parameters on static FET PET scans from 47 patients with MRI findings suspicious for tumor recurrence after radiosurgery. The goal of the study was to investigate whether FET PET radiomics in combination with conventional FET PET parameters could contribute to an improved diagnosis of recurrent tumor. Parameter combinations were investigated using ROC analysis without prior feature selection. The diagnostic accuracy of conventional FET PET parameters was in the range of 81–83% and could be slightly increased to 85% when combined with textural features. Such, FET PET radiomics in combination with conventional PET parameters may have the potential to increase the diagnostic accuracy without the need for a more time-consuming, dynamic FET PET scan. However, no dataset for validation or testing was available.

In a subsequent study, Lohmann et al. (40) investigated the value of combining FET PET and MRI radiomics for the differentiation of treatment-related changes from brain metastases recurrence. Fifty-two patients with newly or progressively contrast-enhancing lesions on MRI after radiotherapy were additionally investigated using FET PET. Prior to feature extraction, images were filtered using three-dimensional wavelet transformation and the LoG filter to enhance edges. Forty-two features were extracted from filtered and unfiltered MR images as well as from summed FET PET images (20–40 min post injection). After feature selection, logistic regression models limited to a maximum of five parameters to avoid over-fitting were generated for the combined PET/MRI features and for each modality separately and validated using cross-validation; no test dataset was available. The highest diagnostic accuracy of 89% (specificity, 96%; sensitivity, 85%) was achieved by the combination of MRI and FET PET features,

TABLE 1 | Radiomics based on MRI and/or PET in patients with brain metastases.

Study	No. of patients (patients/ lesions)	Purpose	PET tracer	MRI contrast(s)	Classification method	Validation method	Model applied to a separate test dataset?	Highest accuracy /Most important result
Peng et al. (37)	66/82	Differentiation of TRC from BM recurrence	n.a.	T1-CE, FLAIR	Support vector machines	LOOCV	No	0.81 (AUC)
Zhang et al. (38)	87/97	Differentiation of TRC from BM recurrence by delta radiomics	n.a.	T1, T1-CE, T2, FLAIR	Ensemble trees	LOOCV	No	0.73 (AUC)
Lohmann et al. (39)	47/54	Differentiation of TRC from BM recurrence	FET	n.a.	ROC analysis	n.a.	No	85%
Lohmann et al. (40)	52/52	Differentiation of TRC from BM recurrence	FET	T1-CE, T2, FLAIR	Logistic regression	5-fold CV, 10-fold CV, LOOCV	No	89%
Hotta et al. (41)	41/44	Differentiation of TRC from BM recurrence	MET	n.a.	Random forest	10-fold CV	No	0.98 (AUC)
Ortiz-Ramon et al. (42)	30/50	Prediction of BM origin	n.a.	T1	Naive Bayes	Nested CV	No	0.95 (AUC)
Ortiz-Ramon et al. (43)	38/67	Prediction of BM origin	n.a.	T1	Random forest	Nested CV	No	0.96 (AUC)
Kniep et al. (44)	189/658	Prediction of BM origin	n.a.	T1, T1-CE, FLAIR	Random forest	Model-external 5-fold CV	Yes	0.82 (AUC)
Qian et al. (45)	412/412	Differentiation of BM from GBM	n.a.	T1-CE	Support vector machines	5-fold CV	Yes	0.90 (AUC)
Artzi et al. (46)	439/439	Differentiation of BM from GBM	n.a.	T1-CE	Support vector machines	5-fold CV	Yes	0.96 (AUC)
Cha et al. (35)	89/110	Prediction of treatment response to SRS	n.a.	CT only	Ensemble model (CNN)	Validation dataset	Yes	0.86 (AUC)
Della Seta et al. (47)	48/48	Prediction of treatment response to SRS	n.a.	T1-CE	Cox regression	n.a.	Yes	Enhancing tumor volume associated with a 2.1-fold longer OS ($p = 0.005$)
Bhatia et al. (48)	88/196	Prediction of treatment response to immune checkpoint inhibitors	n.a.	T1-CE	Cox regression	n.a.	Yes	Radiomics features associated with prolonged OS ($p = 0.001$)

AUC, area under the receiver operating characteristic (ROC) curve; BM, brain metastasis; CNN, convolutional neural network; CT, computed tomography; CV, cross-validation; FET: O-(2-[^{18}F]fluoroethyl)-L-tyrosine; FLAIR, fluid attenuated inversion recovery; GBM, glioblastoma; HR, hazard ratio; LOOCV, leave-one-out CV; n.a., not available; OS, overall survival; ROC, receiver operating characteristic; SRS, stereotactic radiosurgery; T1-CE, contrast-enhanced T1-weighted MRI; TRC, treatment-related changes.

suggesting that the combined FET PET/MRI radiomics analysis encoded more diagnostic information than either modality alone.

Hotta et al. (41) developed a random forest classifier to differentiate recurrent brain tumor from radiation necrosis based on MET PET in a mixed cohort of 41 patients with brain metastasis ($n = 21$) or glioma ($n = 20$). All patients had been treated with radiotherapy and presented one or more tumor-like lesions on MRI. Forty-two features including conventional and textural features were calculated on summed MET PET images (20–30 min post injection). Afterwards, a random forest classifier was trained to separate radiation necrosis from recurrent brain tumor. The results from the optimized classifier were evaluated using 10-fold cross-validation; no test dataset was available. The most relevant features for classification were identified by using the Gini index (51). The highest diagnostic accuracy with an AUC of 0.98 (specificity, 94%; sensitivity, 90%) was achieved by the radiomics model and outperformed the conventional MET PET parameter evaluation (AUC, 0.73; specificity, 73%; sensitivity, 61%). However, the mixed cohort of gliomas and brain metastases complicates the interpretation of the results.

Prediction of Brain Metastases Origin

In ∼10% of cases, patients are diagnosed with brain metastases without knowing the site of the underlying primary tumor. Conventional MRI usually does not aid the identification of the primary cancer.

The usefulness of radiomics for the prediction of brain metastases origin was investigated by Ortiz-Ramon and colleagues (42). Based on conventional contrast-enhanced T1-weighted MR images of 30 patients with 50 lesions with known primary cancer (27 lung cancer; 23 melanoma), a total of 43 features (3 histogram-based and 40 textural features) were extracted in 2D and 3D, and five predictive models were evaluated using a nested cross-validation scheme. Due to the relatively small number of datasets, no independent test set was available. The highest diagnostic accuracy with an AUC of 0.95 for the differentiation of brain metastases from lung cancer and melanoma was achieved using a model generated by the probabilistic naive Bayes classifier.

In another study of the same group (43), the same question was addressed with a higher number of patients. Contrast-enhanced MRI scans from 38 patients with 67 brain metastases with known primary cancer (27 lung cancer; 23 melanoma; 17 breast cancer) were analyzed. Again, 43 features (3 histogram-based and 40 textural features) were extracted in 2D and 3D. A z-score normalization was performed prior to feature selection and a random forest classification within a nested cross-validation structure was applied. The diagnostic accuracy for differentiation of the three primary cancer types had an AUC of 0.87 using 3D texture features. Higher accuracies could be achieved for a one-by-one classification: AUC, 0.96 (lung cancer vs. breast cancer); AUC, 0.96 (lung cancer vs. melanoma). Interestingly, the classification of breast cancer and melanoma brain metastases was unsatisfactory with an AUC of only 0.61. The authors concluded that the volumetric (3D) evaluation of textural features encodes more information and is of higher value for the identification of the primary cancer than 2D features. However, no further model validation was performed.

Kniep et al. (44) also addressed the question of predicting the tumor type in patients with unknown primary lesion at the time of brain metastases diagnosis using MRI radiomics. In that study, 658 brain metastases from 189 patients with known primary cancer were included (151 small cell lung cancer; 225 non-small cell lung cancer; 50 gastrointestinal cancer; 89 melanoma; 143 breast cancer). Imaging data comprised contrast-enhanced and native T1-weighted MRI as well as FLAIR images. Of note, the MR images had been acquired at different MR scanners, thus, the cohort contained heterogenous imaging data. Basic clinical data were combined with 1,423 quantitative image features and evaluated using random forest classification. The final model was validated with model-external cross-validation using an independent training and validation dataset. Furthermore, the results from the classifier were compared with predictions based on conventional image reading by two radiologists. The final model accuracy for classification of all five primary cancer types ranged between an AUC of 0.64 for non-small cell lung cancer brain metastases and an AUC of 0.82 for melanoma brain metastases. The prediction performance was superior to the classification made by two radiologists.

Differentiation of Brain Metastases From Glioblastoma

Brain metastases and glioblastomas are the two most common malignant brain tumors in adults (52, 53). Importantly, glioblastomas and brain metastases often present similar clinical and imaging characteristics on conventional MRI, resulting in difficult differential diagnosis based on the clinical presentation on standard MRI alone.

Qian et al. (45) addressed this important question using MRI radiomics. A large group of patients ($n = 412$) with untreated brain metastases ($n = 170$) and treatment naive, newly diagnosed glioblastomas ($n = 242$) was divided into a training ($n = 227$) and a test cohort ($n = 180$). Tumors were segmented manually and 1,303 radiomic features were calculated on contrast-enhanced MR images prior to feature selection and model generation. The best classifier that showed a high predictive performance in the test cohort (AUC, 0.90) was a support vector machine algorithm that used least absolute shrinkage and selection operator (LASSO) for feature selection. Also, the classifier showed a better performance than experienced neuroradiologists.

Artzi et al. (46) extracted 760 radiomics features from contrast-enhanced MR images of 439 patients with brain metastases ($n = 227$) or glioblastoma ($n = 212$). After image preprocessing and semi-automatic tumor segmentation using a region-growing algorithm, feature selection, and model generation were performed. Prior to model generation, the datasets were divided into a training and a test cohort in a ratio of 80/20. Interestingly, the authors identified the same support vector machine algorithm as the study by Qian et al. described above, to have the highest predictive performance in the test cohort

(AUC, 0.96) for the differentiation of brain metastases from glioblastoma.

Although these studies demonstrated the model performance in an independent test cohort, further external validation is required. However, these two studies nicely demonstrate that radiomics analyses on routinely acquired imaging data already allow the differentiation between brain metastases and glioblastoma with a higher accuracy than experienced neuroradiologists.

Prediction of Treatment Response

Stereotactic radiosurgery is increasingly used in patients with a limited number and size of brain metastases. However, the treatment response may depend not only on the size but also on the structure of the metastasis which may contain tumor cells and tissue compartments of differing radiosensitivity even within the same histologic type.

Cha et al. (35) tried to predict the response to stereotactic radiosurgery in 89 patients with 110 brain metastases using a deep learning-based radiomics approach by utilizing a convolutional neural networks ensemble radiomics model based on planning CT images. Prior to model generation and evaluation, datasets were randomly assigned to a training, validation, and test cohort. The convolutional neural network learned the classification using training images and labels. The final model was able to predict treatment outcome in the independent test dataset with a high accuracy (AUC, 0.86). The study demonstrates the feasibility of CT-based convolutional neural network radiomics models for the prediction of response to stereotactic radiosurgery also for smaller patient cohorts.

Della Seta et al. (47) demonstrated that sometimes complex radiomics models can be outperformed by a single, conventional imaging feature. Pretreatment contrast-enhanced MR images of 48 patients with singular brain metastases treated with stereotactic radiosurgery were investigated. The subgroup of patients with non-small cell lung cancer brain metastases ($n = 27$) was used to find the ideal cut-off to predict treatment response and the subgroup of patients with melanoma brain metastases were used as validation cohort ($n = 21$). After three-dimensional segmentation of the lesions, tumor volumes and enhancing tumor volumes were determined and the percentage of enhancing tumor volume was calculated. Patients with an enhancing tumor volume of more than 68.6% survived significantly longer (4.9 vs. 10.2 months; $p = 0.005$) and showed significantly longer progression-free survival rates compared to patients with a lower proportion of contrast enhancement. Therefore, the percentage of enhancing tumor volume may be a prognostic imaging marker in patients with singular brain metastases.

Besides stereotactic radiosurgery, immunotherapy has become a valuable treatment option in patients with brain metastases. For example, the advent of immune checkpoint inhibition by antibodies against the programmed cell death protein 1 (PD1; pembrolizumab and nivolumab) or the cytotoxic T lymphocyte antigen 4 (CTLA-4; ipilimumab) resulted in an outcome improvement of patients with melanoma brain metastases. However, there is a subset of patients that do not respond to the immune checkpoint inhibitors and have a poor prognosis. To provide additional diagnostic information over and above what can be derived from anatomical MRI, further imaging biomarkers for the early stratification of patients with melanoma brain metastases according to therapy response are needed.

Bhatia et al. (48) hypothesized that the radiomics analysis of MR images could identify imaging features associated with survival in patients with melanoma brain metastases treated with immune checkpoint inhibitors. Twenty-one radiomics features were extracted from contrast-enhanced MRI scans of 88 patients with 196 melanoma brain metastases. Following manual segmentation, univariate Cox regression was performed for each radiomic feature followed by LASSO regression for dimensionality reduction and multivariate analysis. Several features were found to be associated with an increased overall survival and the mean LoG edge feature best explained the variation in outcome (hazard ratio, 0.68; $p = 0.001$). Unfortunately, no further details about overall survival times were provided. However, no radiomics feature remained statistically significant in the multivariate analysis. Surprisingly, the mean LoG edge feature was confirmed to be a significant predictor of an improved survival in an independent test dataset.

CONCLUSIONS

Taken together, it has to be emphasized that radiomics should be considered as an additional tool to complement established imaging analysis methods and other clinical measures that can be jointly used to make a treatment decision or a final diagnosis with maximum confidence. However, although promising results using radiomics analysis in the field of brain metastases have already been achieved, most studies lack a further validation of the initial results. External validation of the generated models is of high importance and great value to translate radiomics analyses into clinical routine. Another important aspect is the need of standardization of radiomics analysis. In particular, currently self-developed radiomics analysis tools or highly specialized algorithms are predominantly used that may prevent other investigators to reproduce the findings and furthermore limits comparability of the results. In addition, the influence of different scanners and imaging protocols as well as the different preprocessing parameters on the radiomics signatures and the computed models is still not well-understood and needs more attention in future research in order to further promote the translation of radiomics analysis into the clinical workflow.

Notwithstanding, radiomics has a great potential to add valuable additional diagnostic information to many clinical important questions in the field of brain cancer. To overcome the above-mentioned obstacles, respective efforts are currently ongoing.

AUTHOR CONTRIBUTIONS

All authors listed have made a substantial, direct and intellectual contribution to the work, and approved it for publication.

FUNDING

Funded by the Deutsche Forschungsgemeinschaft (DFG, German Research Foundation)–Projektnummer 428090865.

REFERENCES

1. Nayak L, Lee EQ, Wen PY. Epidemiology of brain metastases. *Curr Oncol Rep*. (2012) 14:48–54. doi: 10.1007/s11912-011-0203-y
2. Barnholtz-Sloan JS, Sloan AE, Davis FG, Vigneau FD, Lai P, Sawaya RE. Incidence proportions of brain metastases in patients diagnosed. (1973 to 2001) in the Metropolitan Detroit Cancer Surveillance System. *J Clin Oncol*. (2004) 22:2865–72. doi: 10.1200/JCO.2004.12.149
3. Schouten LJ, Rutten J, Huveneers HA, Twijnstra A. Incidence of brain metastases in a cohort of patients with carcinoma of the breast, colon, kidney, and lung and melanoma. *Cancer*. (2002) 94:2698–705. doi: 10.1002/cncr.10541
4. Galldiks N, Langen KJ, Albert NL, Chamberlain M, Soffietti R, Kim MM, et al. PET imaging in patients with brain metastasis-report of the RANO/PET group. *Neuro Oncol*. (2019) 21:585–95. doi: 10.1093/neuonc/noz003
5. Soffietti R, Abacioglu U, Baumert B, Combs SE, Kinhult S, Kros JM, et al. Diagnosis and treatment of brain metastases from solid tumors: guidelines from the European Association of Neuro-Oncology. (EANO). *Neuro Oncol*. (2017) 19:162–74. doi: 10.1093/neuonc/now241
6. Rick JW, Shahin M, Chandra A, Dalle Ore C, Yue JK, Nguyen A, et al. Systemic therapy for brain metastases. *Crit Rev Oncol Hematol*. (2019) 142:44–50. doi: 10.1016/j.critrevonc.2019.07.012
7. Venur VA, Karivedu V, Ahluwalia MS. Systemic therapy for brain metastases. *Handb Clin Neurol*. (2018) 149:137–53. doi: 10.1016/B978-0-12-811161-1.00011-6
8. Ramakrishna N, Temin S, Chandarlapaty S, Crews JR, Davidson NE, Esteva FJ, et al. Recommendations on disease management for patients with advanced human epidermal growth factor receptor 2-positive breast cancer and brain metastases: ASCO Clinical Practice Guideline Update. *J Clin Oncol*. (2018) 36:2804–7. doi: 10.1200/JCO.2018.79.2713
9. Davies MA, Saiag P, Robert C, Grob J-J, Flaherty KT, Arance A, et al. Dabrafenib plus trametinib in patients with BRAFV600-mutant melanoma brain metastases. (COMBI-MB): a multicentre, multicohort, open-label, phase 2 trial. *Lancet Oncol*. (2017) 18:863–73. doi: 10.1016/S1470-2045(17)30429-1
10. Langen KJ, Galldiks N. Update on amino acid PET of brain tumours. *Curr Opin Neurol*. (2018) 31:354–61. doi: 10.1097/WCO.0000000000000574
11. Langen KJ, Galldiks N, Hattingen E, Shah NJ. Advances in neuro-oncology imaging. *Nat Rev Neurol*. (2017) 13:279–89. doi: 10.1038/nrneurol.2017.44
12. Pope WB. Brain metastases: neuroimaging. *Handb Clin Neurol*. (2018) 149:89–112. doi: 10.1016/B978-0-12-811161-1.00007-4
13. Lin NU, Lee EQ, Aoyama H, Barani IJ, Barboriak DP, Baumert BG, et al. Response assessment criteria for brain metastases: proposal from the RANO group. *Lancet Oncol*. (2015) 16:e270–8. doi: 10.1016/S1470-2045(15)70057-4
14. Okada H, Weller M, Huang R, Finocchiaro G, Gilbert MR, Wick W, et al. Immunotherapy response assessment in neuro-oncology: a report of the RANO working group. *Lancet Oncol*. (2015) 16:e534–e42. doi: 10.1016/S1470-2045(15)00088-1
15. Camidge DR, Lee EQ, Lin NU, Margolin K, Ahluwalia MS, Bendszus M, et al. Clinical trial design for systemic agents in patients with brain metastases from solid tumours: a guideline by the Response Assessment in Neuro-Oncology Brain Metastases working group. *Lancet Oncol*. (2018) 19:e20–e32. doi: 10.1016/S1470-2045(17)30693-9
16. Salama GR, Heier LA, Patel P, Ramakrishna R, Magge R, Tsiouris AJ. Diffusion weighted/tensor imaging, functional MRI and perfusion weighted imaging in glioblastoma-foundations and future. *Front Neurol*. (2017) 8:660. doi: 10.3389/fneur.2017.00660
17. Luypaert R, Boujraf S, Sourbron S, Osteaux M. Diffusion and perfusion MRI: basic physics. *Eur J Radiol*. (2001) 38:19–27. doi: 10.1016/S0720-048X(01)00286-8
18. Buonocore MH, Maddock RJ. Magnetic resonance spectroscopy of the brain: a review of physical principles and technical methods. *Rev Neurosci*. (2015) 26:609–32. doi: 10.1515/revneuro-2015-0010
19. Henning A. Proton and multinuclear magnetic resonance spectroscopy in the human brain at ultra-high field strength: a review. *Neuroimage*. (2018) 168:181–98. doi: 10.1016/j.neuroimage.2017.07.017
20. Albert NL, Weller M, Suchorska B, Galldiks N, Soffietti R, Kim MM, et al. Response assessment in neuro-oncology working group and european association for neuro-oncology recommendations for the clinical use of PET imaging in gliomas. *Neuro Oncol*. (2016) 18:1199–208. doi: 10.1093/neuonc/now058
21. Langen KJ, Watts C. Neuro-oncology: Amino acid PET for brain tumours - ready for the clinic? *Nat Rev Neurol*. (2016) 12:375–6. doi: 10.1038/nrneurol.2016.80
22. Galldiks N, Kocher M, Ceccon G, Werner JM, Brunn A, Deckert M, et al. Imaging challenges of immunotherapy and targeted therapy in patients with brain metastases: response, progression, and pseudoprogression. *Neuro Oncol*. (2019) 22:17–30. doi: 10.1093/neuonc/noz147
23. Gillies RJ, Kinahan PE, Hricak H. Radiomics: images are more than pictures, they are data. *Radiology*. (2016) 278:563–77. doi: 10.1148/radiol.2015151169
24. Lambin P, Rios-Velazquez E, Leijenaar R, Carvalho S, van Stiphout RG, Granton P, et al. Radiomics: extracting more information from medical images using advanced feature analysis. *Eur J Cancer*. (2012) 48:441–6. doi: 10.1016/j.ejca.2011.11.036
25. Aerts HJ, Velazquez ER, Leijenaar RT, Parmar C, Grossmann P, Carvalho S, et al. Decoding tumour phenotype by noninvasive imaging using a quantitative radiomics approach. *Nat Commun*. (2014) 5:4006. doi: 10.1038/ncomms5644
26. Rizzo S, Botta F, Raimondi S, Origgi D, Fanciullo C, Morganti AG, et al. Radiomics: the facts and the challenges of image analysis. *Eur Radiol Exp*. (2018) 2:36. doi: 10.1186/s41747-018-0068-z
27. Mazurowski MA. Radiogenomics: what it is and why it is important. *J Am Coll Radiol*. (2015) 12:862–6. doi: 10.1016/j.jacr.2015.04.019
28. Kumar V, Gu Y, Basu S, Berglund A, Eschrich SA, Schabath MB, et al. Radiomics: the process and the challenges. *Magn Reson Imaging*. (2012) 30:1234–48. doi: 10.1016/j.mri.2012.06.010
29. Yip SS, Aerts HJ. Applications and limitations of radiomics. *Phys Med Biol*. (2016) 61:R150–66. doi: 10.1088/0031-9155/61/13/R150
30. Zhou M, Scott J, Chaudhury B, Hall L, Goldgof D, Yeom KW, et al. Radiomics in brain tumor: image assessment, quantitative feature descriptors, and machine-learning approaches. *AJNR Am J Neuroradiol*. (2018) 39:208–16. doi: 10.3174/ajnr.A5391
31. Charron O, Lallement A, Jarnet D, Noblet V, Clavier JB, Meyer P. Automatic detection and segmentation of brain metastases on multimodal MR images with a deep convolutional neural network. *Comput Biol Med*. (2018) 95:43–54. doi: 10.1016/j.compbiomed.2018.02.004
32. Grovik E, Yi D, Iv M, Tong E, Rubin D, Zaharchuk G. Deep learning enables automatic detection and segmentation of brain metastases on multisequence MRI. *J Magn Reson Imaging*. (2019) 51:175–82. doi: 10.1002/jmri.26766
33. Haralick RM, Shanmugam K, Dinstein I. Textural features for image classification. *IEEE Transact Syst Man Cybernet*. (1973) Smc3:610–21. doi: 10.1109/TSMC.1973.4309314
34. Krizhevsky A, Sutskever I, Hinton GE. Imagenet classification with deep convolutional neural networks. *Adv Neural Inform Proc Syst*. (2012) 1:1097–1105.
35. Cha YJ, Jang WI, Kim MS, Yoo HJ, Paik EK, Jeong HK, et al. Prediction of response to stereotactic radiosurgery for brain metastases

using convolutional neural networks. *Anticancer Res*. (2018) 38:5437–45. doi: 10.21873/anticanres.12875
36. Tan C, Sun F, Kong T, Zhang W, Yang C, Liu C. A Survey on Deep Transfer learning. *arXiv [Pre-print]* (2018). Available online at: https://ui.adsabs.harvard.edu/abs/2018arXiv180801974T (accessed August 01, 2018).
37. Peng L, Parekh V, Huang P, Lin DD, Sheikh K, Baker B, et al. Distinguishing true progression from radionecrosis after stereotactic radiation therapy for brain metastases with machine learning and radiomics. *Int J Radiat Oncol Biol Phys*. (2018) 102:1236–43. doi: 10.1016/j.ijrobp.2018.05.041
38. Zhang Z, Yang J, Ho A, Jiang W, Logan J, Wang X, et al. A predictive model for distinguishing radiation necrosis from tumour progression after gamma knife radiosurgery based on radiomic features from MR images. *Eur Radiol*. (2018) 28:2255–63. doi: 10.1007/s00330-017-5154-8
39. Lohmann P, Stoffels G, Ceccon G, Rapp M, Sabel M, Filss CP, et al. Radiation injury vs. recurrent brain metastasis: combining textural feature radiomics analysis and standard parameters may increase. (18)F-FET PET accuracy without dynamic scans. *Eur Radiol*. (2017) 27:2916–27. doi: 10.1007/s00330-016-4638-2
40. Lohmann P, Kocher M, Ceccon G, Bauer EK, Stoffels G, Viswanathan S, et al. Combined FET PET/MRI radiomics differentiates radiation injury from recurrent brain metastasis. *Neuroimage Clin*. (2018) 20:537–42. doi: 10.1016/j.nicl.2018.08.024
41. Hotta M, Minamimoto R, Miwa K. 11C-methionine-PET for differentiating recurrent brain tumor from radiation necrosis: radiomics approach with random forest classifier. *Sci Rep*. (2019) 9:15666. doi: 10.1038/s41598-019-52279-2
42. Ortiz-Ramon R, Larroza A, Arana E, Moratal D. A radiomics evaluation of 2D and 3D MRI texture features to classify brain metastases from lung cancer and melanoma. *Conf Proc IEEE Eng Med Biol Soc*. (2017) 2017:493–6. doi: 10.1109/EMBC.2017.8036869
43. Ortiz-Ramon R, Larroza A, Ruiz-Espana S, Arana E, Moratal D. Classifying brain metastases by their primary site of origin using a radiomics approach based on texture analysis: a feasibility study. *Eur Radiol*. (2018) 28:4514–23. doi: 10.1007/s00330-018-5463-6
44. Kniep HC, Madesta F, Schneider T, Hanning U, Schonfeld MH, Schon G, et al. Radiomics of brain MRI: utility in prediction of metastatic tumor type. *Radiology*. (2019) 290:479–87. doi: 10.1148/radiol.2018180946
45. Qian Z, Li Y, Wang Y, Li L, Li R, Wang K, et al. Differentiation of glioblastoma from solitary brain metastases using radiomic machine-learning classifiers. *Cancer Lett*. (2019) 451:128–35. doi: 10.1016/j.canlet.2019.02.054
46. Artzi M, Bressler I, Ben Bashat D. Differentiation between glioblastoma, brain metastasis and subtypes using radiomics analysis. *J Magn Reson Imaging*. (2019) 50:519–28. doi: 10.1002/jmri.26643
47. Della Seta M, Collettini F, Chapiro J, Angelidis A, Engeling F, Hamm B, et al. A 3D quantitative imaging biomarker in pre-treatment MRI predicts overall survival after stereotactic radiation therapy of patients with a singular brain metastasis. *Acta Radiol*. 60:1496–503. doi: 10.1177/0284185119831692
48. Bhatia A, Birger M, Veeraraghavan H, Um H, Tixier F, McKenney AS, et al. MRI radiomic features are associated with survival in melanoma brain metastases treated with immune checkpoint inhibitors. *Neuro-Oncology*. (2019) 21:1578–86. doi: 10.1093/neuonc/noz141
49. Spitzer M, Lorkowski S, Cullen P, Sczyrba A, Fuellen G. IsoSVM–distinguishing isoforms and paralogs on the protein level. *BMC Bioinform*. (2006) 7:110. doi: 10.1186/1471-2105-7-110
50. Ceccon G, Lohmann P, Stoffels G, Judov N, Filss CP, Rapp M, et al. Dynamic O-(2–18F-fluoroethyl)-L-tyrosine positron emission tomography differentiates brain metastasis recurrence from radiation injury after radiotherapy. *Neuro Oncol*. (2017) 19:281–8. doi: 10.1093/neuonc/now149
51. Breiman L. Random forests. *Machine Learn*. (2001) 45:5–32. doi: 10.1023/A:1010933404324
52. Ohgaki H, Kleihues P. Epidemiology and etiology of gliomas. *Acta Neuropathol*. (2005) 109:93–108. doi: 10.1007/s00401-005-0991-y
53. Platta CS, Khuntia D, Mehta MP, Suh JH. Current treatment strategies for brain metastasis and complications from therapeutic techniques: a review of current literature. *Am J Clin Oncol*. (2010) 33:398–407. doi: 10.1097/COC.0b013e318194f744

Conflict of Interest: The authors declare that the research was conducted in the absence of any commercial or financial relationships that could be construed as a potential conflict of interest.

frontiers in Neurology

BRIEF RESEARCH REPORT
published: 11 February 2020
doi: 10.3389/fneur.2020.00005

Recognition of Brain Metastases Using Gadolinium-Enhanced SWI MRI: Proof-of-Concept Study

Joel Ceballos-Ceballos[1], Diego A. Loza-Gallardo[1], Marco A. Barajas-Romero[2], Carlos Cantú-Brito[3] and Sergio Iván Valdés-Ferrer[3,4,5]**

[1] Division of Neuroradiology, Department of Radiology, Hospital San Javier, Guadalajara, Mexico, [2] Department of Surgical Neurology, Hospital San Javier, Guadalajara, Mexico, [3] Department of Neurology, Instituto Nacional de Ciencias Médicas y Nutrición Salvador Zubirán, Mexico City, Mexico, [4] Department of Infectious Diseases, Instituto Nacional de Ciencias Médicas y Nutrición Salvador Zubirán, Mexico City, Mexico, [5] Center for Biomedical Science, Feinstein Institute for Medical Research, Manhasset, NY, United States

Background and purpose: SWI MRI, a T2*-dominant MRI sequence with T1 *shine-through* effect, uses intrinsic structural susceptibility to create enhancement among brain structures. We evaluated whether gadolinium-enhanced SWI (SWI-Gd) improves brain metastasis detection in combination with other MRI sequences.

Materials and methods: MRI images of 24 patients (46 studies) were prospectively acquired using a 1.5-T scanner. T1-weighted, unenhanced SWI (SWI-U) and SWI-Gd were evaluated blindly to clinical features by two board-certified radiologists.

Results: SWI-Gd revealed more significant metastatic lesions than either T1-Gd or SWI-U ($p = 0.0004$ for either comparator sequence). Moreover, SWI-Gd revealed more lesions only for those patients with ≤5 lesions on T1-Gd ($n = 30$ studies from 16 patients; $p = 0.046$). Performing SWI-Gd added <5 min of scanning time with no further additional risk.

Conclusions: Our findings suggest that, when added to T1-Gd and other common sequences, SWI-Gd may improve the diagnostic yield of brain metastases with only a few extra minutes of scanning time and no further risk than that of a regular gadolinium-enhanced MRI.

Keywords: brain metastasis, MRI, SWI, susceptibility-weighted image, gadolinium, metastasis diagnosis

OPEN ACCESS

Edited by:
Susie Y. Huang, Massachusetts General Hospital, Harvard Medical School, United States

Reviewed by:
Ranliang Hu, Emory University, United States
Chanon Ngamsombat, Athinoula A. Martinos Center for Biomedical Imaging, Harvard Medical School, United States

****Correspondence:***
Joel Ceballos-Ceballos
drjoelceballos@yahoo.com.mx
Sergio Iván Valdés-Ferrer
sergio.valdesf@incmnsz.mx

Specialty section:
This article was submitted to Applied Neuroimaging, a section of the journal Frontiers in Neurology

Received: *21 September 2019*
Accepted: *06 January 2020*
Published: *11 February 2020*

Citation:
Ceballos-Ceballos J, Loza-Gallardo DA, Barajas-Romero MA, Cantú-Brito C and Valdés-Ferrer SI (2020) Recognition of Brain Metastases Using Gadolinium-Enhanced SWI MRI: Proof-of-Concept Study. Front. Neurol. 11:5. doi: 10.3389/fneur.2020.00005

INTRODUCTION

Cerebral metastases are the most common form of brain tumors in adults (1, 2), are a significant source of morbidity and mortality, and have direct implications on the treatment and prognosis of the primary tumor (3, 4).

Contrast-enhanced magnetic resonance imaging (MRI) is the standard for diagnosing brain metastases (5); however, there is no one-size-fits-all MRI protocol for their evaluation (6). Treatment of brain metastases depends on a number of tumor and host factors, as well as lesion location and surgical accessibility, for which an adequate MRI staging is crucial (5). Taking advantage of already established MRI methods–with simple modifications–can potentially result in earlier detection of metastatic lesions.

Susceptibility-weighted imaging (SWI) is an MRI technique that takes advantage of intrinsic magnetic susceptibility differences between adjacent tissues (7), leading to a better distinction

of inter- and intratissue characteristics (8, 9). SWI is routinely performed without the use of gadolinium contrast enhancement and is used clinically to evaluate a number of neurological conditions (10, 11).

Although SWI is a T2*-dominant sequence, there is also a so-called *T1 shine-through* effect, in which lesions preserve on SWI the characteristics expected on T1-weighted images (12). Hence, gadolinium can hypothetically enhance lesions on SWI and, by creating further intratissue contrast, unmask small lesions early in the course of metastatic seeding.

Gadolinium enhancement has been used experimentally in SWI for evaluating primary gliomas, where it has shown promising results on staging, grading, and even determining the aggressiveness of primary brain tumors (13). SWI-Gd has been recently shown to be helpful for the detection of blood–brain barrier dysfunction in patients with multiple sclerosis (14), suggesting that it can also improve the imaging assessment of brain metastases. Hence, gadolinium enhancement in SWI (SWI-Gd) can potentially reveal certain characteristics of cerebral metastases not observed otherwise. The present study was therefore designed to investigate if SWI-Gd can improve identifying metastatic brain lesions in comparison to the usual (T1-Gd and SWI-U) MRI sequences.

METHODS

Ethics

The study was approved by the Institutional Ethics Review Board of Hospital San Javier, Guadalajara, Mexico. All patients signed the informed consent.

Study Design and Selection of Participants

This study was designed as a prospective one. All participants were adults (≥18 years old) with a histologically confirmed systemic tumor who came for MRI evaluation either in search of cerebral metastases or to evaluate previously determined metastatic disease. Demographic data, as well as specific details about the diagnosis of the primary and metastatic tumor, and other diagnostic data were acquired retrospectively from hospital records.

MRI Protocol

MRI studies were acquired on a 1.5-T scanner (Achieva; Philips Healthcare, Best, The Netherlands) using a 16-channel coil. After signing the informed consent, participants underwent a standard unenhanced MRI protocol [T1-, T2-, diffusion-weighted, and fluid-attenuated inversion recovery (FLAIR)], followed by T1-GD images (duration of acquisition: 3'17") and SWI-Gd (duration of acquisition: 3'26"), instead of only acquiring the routine T1-Gd images. The order of sequence acquisition postcontrast infusion was as follows: (1) Perfusion-weighted (duration: 1'11"); (2) T1-weighted (duration: 3'17"); SWI (duration: 3'26"). Therefore, gadolinium-enhanced T1-weighted images were acquired 1'11" post-infusion, while SWI-Gd were acquired 4'38" post-infusion. Lesions of interest were defined *a priori* as follows: in SWI-U, as single or multiple, hypointense or hyperintense lesions, as previously reported (15). In gadolinium-enhanced sequences, lesions show nodular or ring enhancement. MRI studies were performed from September 2017 to August 2018. Studies that had artifacts interfering with the interpretation or those suggestive of an alternative diagnosis were excluded from the study.

Contrast-enhanced with fast field echo (FFE) T1-weighted images were acquired using the following parameters: slice thickness 0.55 mm; FOV 230 × 183 × 142 mm^3; matrix 256 × 159; TR/TE/TI 11,000/130/2,800 ms; and acquisition time 5 min and 8 s. SWI images were acquired with a flow-compensated 3D gradient-echo method using the following parameters: FOV, 230 × 187 × 130 mm^3; matrix, 244 × 186 mm^3; voxel size, 1.0 × 1.0 × 2.0 mm^3; voxel volume, 2 mm^3; TR/TE, 51/60 ms; slice thickness, 1 mm; flip angle = 20°; acquisition time, 3 min and 26 s. For image reconstruction on SWI, we used raw data, as well as minimum intensity projection (MinIP). Gadolinium-enhanced SWI and T1-weighted images were repeated after intravenous administration of 0.2 ml/kg (0.1 mmol/kg) of gadoterate meglumine (Dotarem®; Guerbet; Paris, France), which was infused as a bolus at a rate of 2.0 ml/s. The order of imaging acquisition was consistent between participants. SWI images were reviewed simultaneously in phase and magnitude; phase was used to detect the paramagnetic/diamagnetic signal that is suggestive of blood or calcium content. All images were analyzed blindly to patient information by two radiologists; one of them (JC-C) is a neuroradiologist with 30 years of diagnostic experience, while the second one (DAL-G) has 3 years of neuroimaging diagnostic experience. Images were analyzed jointly by both reviewers, and individual lesions, as well as lesion burden, were determined by consensus.

Statistical Analysis

Statistical analysis was performed using Prism version 6 (GraphPad Software, San Diego, CA). Images were analyzed independently by two observers, and the number of metastatic lesions was counted manually on unenhanced SWI and T1-weighted followed by Gd-enhanced sequences. Continuous data such as means and standard deviations were obtained. *Student t* and one-way ANOVA tests were used to compare differences between groups, and $p < 0.05$ were considered statistically significant.

RESULTS

Sample

Thirty-five patients agreed to participate; however, six did not sign the informed consent and were therefore excluded from the study; of the 29 remaining patients, five patients had to be excluded due to technical reasons. Our final sample included 24 patients (19 female, 5 male), with a total of 58 MRI studies, of which 12 studies were excluded from the analysis due to movement artifacts, leaving us with 46 MRI studies that were considered of good quality for analysis (on average, 1.9 studies/patient).

Demographic and Tumor-Specific Baseline Characteristics

Patients presented with a wide variety of clinical manifestations, but the presence of headache, altered mental status, and focal neurological signs were the most commonly recorded (**Table 1**).

The mean age at diagnosis of the primary tumor was 56.4 ± 16.1 years, while the age at diagnosis of metastatic disease was 57.8 ± 16.5 years. The mean time from diagnosis of the primary tumor to metastatic brain disease was 372 ± 519 days. The most common tumor was breast cancer ($n = 11$; 45.8%) followed by lung ($n = 7$; 29.5%), and colon ($n = 2$; 8.3%) cancer; there was one patient each with pancreatic, kidney, melanoma, or hematopoietic cancer.

MRI Findings

Burden of Metastatic Brain Disease

In T1-Gd, we observed an average of 5.61 ± 10.02 brain metastases; in SWI-U, we observed an average of 6.22 ± 11.61 brain metastases. In contrast, in the SWI-Gd, we observed, on average, 12.52 ± 21.95 brain metastases. SWI-Gd was statistically superior to either reference sequence (one-way ANOVA, $p = 0.0009$; intergroup Student's t-test, $p = 0.0004$) (**Figure 1A**).

A sub-analysis of MRI studies independently of the burden of metastasis showed that, in 24 out of 46 sets of images obtained from 14 patients, SWI-Gd revealed one or more enhancing lesions that had not been observed in T1-Gd; in comparison, T1-Gd revealed more enhancing lesions than those seen by SWI-Gd in only one case. We observed no difference in the number of metastatic lesions in the remaining studies.

We then wondered if SWI-Gd would result in an improved ability to determine the number of brain lesions in patients with a smaller burden of metastatic disease (**Figure 2**). First, we reviewed MRI scans from patients with ≤5 brain metastases in T1-Gd. A total of 30 MRIs from 16 patients were analyzed. In this group, T1-Gd revealed a mean of 2.13 ± 1.0 metastases; SWI-U, 1.47 ± 1.46 metastases; while SWI-Gd, 3.03 ± 2.71 metastases. Here, we also observed that SWI-Gd was statistically superior (one-way ANOVA, $p = 0.003$; intergroup Student's t-test, $p = 0.046$ vs. T1-Gd and $p = 0.0003$ vs. SWI-U) (**Figure 1B**).

Finally, we reviewed MRI scans from patients with ≤2 brain metastases in T1-Gd. A total of 20 MRIs from 11 patients were

TABLE 1 | Clinical manifestations of brain metastases (patients had in general more than one clinical manifestation).

Tumor ($N = 24$)	Frequency (%)
Asymptomatic/incidental ($n = 3$)	12.5
Headache ($n = 10$)	41.6
Altered mental status ($n = 5$)	20.8
Focal signs ($n = 4$)	16.7
Seizures ($n = 3$)	
• Status epilepticus ($n = 1$)	12.5
Cerebellar/ataxia: ($n = 3$)	12.5
Cranial nerve signs ($n = 2$)	8.3
Pain/sensory loss ($n = 2$)	8.3
Vertigo/dizziness ($n = 2$)	8.3
Visual disturbances ($n = 2$)	8.3
Gait disorders ($n = 2$)	8.3
Intracranial hypertension ($n = 2$)	8.3

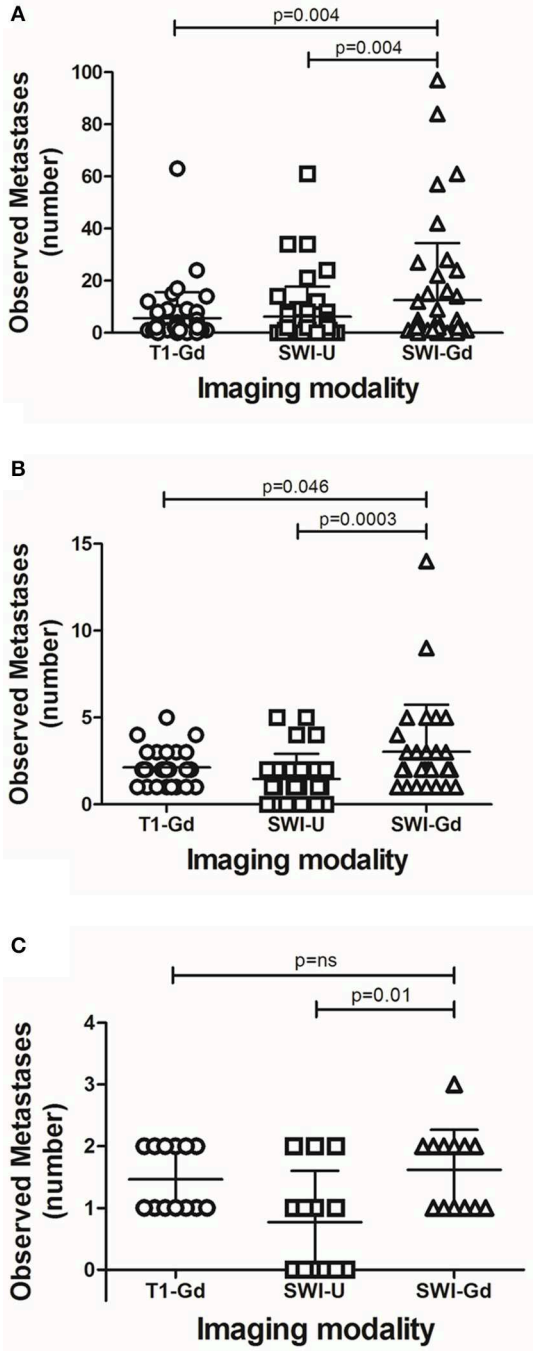

FIGURE 1 | Detection of metastatic brain lesions by different MRI sequences. The number of detected metastases by each of the analyzed MRI sequences with all cases **(A)**; those with five or fewer lesions **(B)**; or those with two or fewer lesions **(C)**. Each dot represents a patient. Error bars represent median ± interquartile range. Statistical values represent differences between groups, and a value of $p \leq 0.05$ was considered statistically significant.

analyzed. In this group, T1-Gd revealed 1.6 ± 0.5 metastases; SWI-U, 1.0 ± 0.86 metastases; and SWI-Gd, 1.85 ± 0.93 metastases. At this level (two or fewer lesions or visible on T1-Gd), SWI-Gd was superior to SWI-U (Student's *t*-test, $p = 0.01$), but not statistically different to T1-Gd (**Figure 1C**).

Non-oncologic Findings

Images suggestive of microbleeds were observed in three scans using SWI-U and four scans using SWI-Gd ($p =$ ns). Microbleeds were concurrent on SWI-U and SWI-Gd in two patients with breast cancer metastases and one patient with hematopoietic cancer metastases. The differing case occurred in one patient with malignant melanoma metastases. Six patients had non-specific white matter intensities suggestive of microangiopathy; three had dilated perivascular spaces; two patients had intrasellar arachnoidocele; and one had leukoaraiosis associated with radiotherapy. As expected, non-oncological findings were consistent between studies.

DISCUSSION

Here, we present compelling preliminary evidence suggesting that SWI-Gd MRI increases the ability to recognize brain metastases from extracerebral tumors (**Figure 2**).

Ever since its inception in the clinical arena, brain MRI changed the way intracranial metastases are diagnosed (16). Among the common MRI sequences available, SWI takes advantage of intrinsic tissue magnetic characteristics to generate intrinsic contrast. SWI generates invaluable information about cerebral vasculature, deoxyhemoglobin in veins, hemorrhage and microbleeds, iron, and calcium deposition, and neovascularization, all without the need for contrast agents (17–19). SWI is therefore used routinely to evaluate a number of neurological conditions, including diffuse axonal injury, stroke, multiple sclerosis, or cerebral amyloid angiopathy, to name a few (10, 11). Recent evidence suggests that gadolinium can be useful in susceptibility-weighted MRI (14) hypothetically by taking advantage of the so-called *T1 shine-through* effect (12),

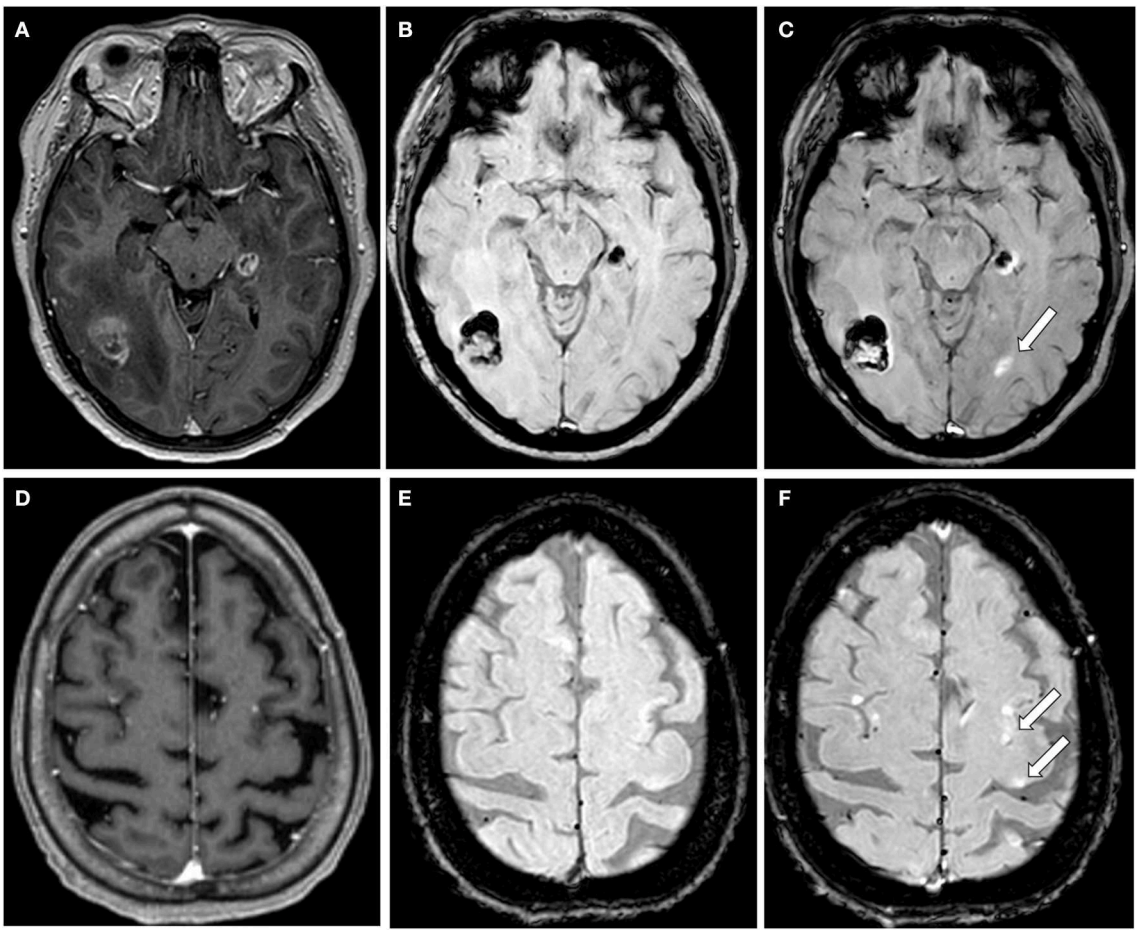

FIGURE 2 | Illustrative cases of lesions seen only with SWI-Gd. **(A–C)** MRI from a 45 years old female patient diagnosed with breast cancer and preexisting metastases on the right parieto-occipital region and a second one on the fifth left temporal gyrus. T1-Gd shows heterogeneous enhancement on both lesions **(A)** that were heterogeneous but predominantly hypointense on SWI-U **(B)**. SWI-Gd showed annular enhancement and edema of the previously described lesions, as well as an otherwise not seen lesion (arrow) in the left occipital lobe with annular enhancement **(C)**. **(D–F)** MRI from a 58 years old female with pancreatic cancer. T1-Gd shows three small enhancing lesions: two in the right frontal lobe; another in the left frontal lobe **(D)**, that were not observed with SWI-U **(E)**. SWI-Gd shows the lesions observed in T1-Gd, as well as two previously unseen lesions (arrows) **(F)**.

potentially leading to improved detection of brain metastases, lesions know to be small, complex, and heterogeneous.

The diagnostic sensitivity of different MRI sequences (including T1-Gd and SWI-U) for the detection of brain metastases has been addressed before. In the case of brain metastases from systemic melanoma or breast cancer, T1-Gd has been shown to be better than other modalities (15, 20). Moreover, in direct comparison with T1-Gd for detecting melanoma metastases, SWI-U has shown no diagnostic advantage (21). To our knowledge, the present study is the first one to prospectively evaluate the added value of SWI-Gd for the potential detection of brain metastases. Here, we observed that SWI-Gd reveals more lesions with a greater level of detail than the usual sequences. This held true across the whole sample, as well as when we selected those participants with $\leq$5 lesions. However, we failed to observe differences when only those with $\leq$2 were considered, probably reflecting that SWI-Gd has no role at the lower burden of metastatic disease, but may also reflect a lack of power to detect differences due to the small sample size. Interestingly, some lesions that were visible in SWI-U became clearer after contrast administration; however, others were only observable only in SWI-Gd, even with a side-by-side unblinded comparison with SWI-U or T1-Gd. As expected, we did not observe improved detection of hemorrhagic lesions between SWI-U and SWI-Gd. This may be also due to the small sample size, as we observed microhemorrhages on a very small subset (three patients on SWI-U; four patients on SWI-Gd).

SWI-Gd has been evaluated for primary brain tumors with mixed results. In gliomas, SWI is useful in determining certain characteristics of the tumor, including growth potential (low- and high-grade) (22), intratumor vasculature (23, 24), and treatment response (25, 26). To our knowledge, our study is the first to analyze SWI-Gd for metastatic brain disease; its utility in the diagnosis of primary gliomas suggests that it can be a useful addition to the standard MRI protocol for evaluating brain metastases.

In the present study, the interval between gadolinium infusion and SWI acquisition was around 5 min. The timing between infusion of gadolinium and MRI acquisition can critically interfere with image enhancement, where delayed postcontrast acquisition ($\sim$20 min) may theoretically result in improved rates of lesion detection (27). However, shorter intervals (as in the present study, in which the delay was 4'38") have shown minimal, if any, impact on image quality or detection ability (28).

Due to the non-invasive nature of the present study, while all primary tumors were histologically confirmed, we did no obtain histological confirmation from the observed metastatic lesions. However, preclinical evidence derived from animal models of tumor metastases suggests that gadolinium-enhancing lesions correspond to metastatic seeding (29).

Our study has several limitations. First of all, we have a relatively small sample size due to the exploratory (proof-of-concept) design; therefore, our findings will have to be replicated or rejected in future studies. Other important limitations include a mixture of primary tumors, analysis of parenchymal (but not leptomeningeal) lesions, as well as expected differences in tumor biology among participants. Also, we did not perform a concordance analysis between MRI evaluators. While some patients were scanned only once, some others were scanned as many as four times during the duration of the present study, and we did not perform an intrasubject analysis. Those limitations, inherent to a proof-of-concept study, will, therefore, need to be validated in larger, tumor-specific, cohorts.

The study has also some technical limitations. In every case, T1-Gd was acquired before SWI-Gd; while the span between both was short, it is possible that the observed advantage of SWI-Gd was due in part to delayed enhancement. We plan to evaluate this in a follow-up study. Also, we used a 1.5-T scanner, something that can be seen as a limitation as well as an advantage: a limitation as it is known that more powerful scanners have better sensibility and require half the dose of gadolinium to achieve similar results; on the opposite end, 1.5-T scanners are widely available, making the results more easily generalizable.

In conclusion, here we observe for the first time that SWI-Gd can be a valuable addition to the detection of brain metastases. By taking advantage of gadolinium contrast, SWI-Gd may improve the detection of brain metastases when added to the standard contrast-enhanced MRI sequences without further risk (as the patient is already receiving gadolinium) and with only a few extra minutes of scanning.

DATA AVAILABILITY STATEMENT

All datasets generated for this study are included in the article/supplementary material.

ETHICS STATEMENT

The studies involving human participants were reviewed and approved by Institutional Ethics Review Board of Hospital San Javier, Guadalajara, Mexico. The patients/participants provided their written informed consent to participate in this study.

AUTHOR CONTRIBUTIONS

JC-C, DL-G, and SV-F conceived the study. Data was collected by JC-C, DL-G, and MB-R. Data were analyzed by SV-F and JC-C. The manuscript was written by SV-F, CC-B, and JC-C. All authors reviewed and approved the final version.

FUNDING

Covered by institutional funds from Hospital San Javier and Instituto Nacional de Ciencias Médicas y Nutrición Salvador Zubirán. Further funding was obtained from Consejo Nacional de Ciencia y Tecnología de México (grant FOSISS-289788 to SV-F), and Pfizer Scientific Institute (to SV-F).

REFERENCES

1. Nayak L, Lee EQ, Wen PY. Epidemiology of brain metastases. *Curr Oncol Rep.* (2012) 14:48–54. doi: 10.1007/s11912-011-0203-y
2. Barnholtz-Sloan JS, Sloan AE, Davis FG, Vigneau FD, Lai P, Sawaya RE. Incidence proportions of brain metastases in patients diagnosed (1973 to 2001) in the Metropolitan Detroit Cancer Surveillance System. *J Clin Oncol.* (2004) 22:2865–72. doi: 10.1200/JCO.2004.12.149
3. Mcneill KA. Epidemiology of brain tumors. *Neurol Clin NA.* (2016) 34:981–98. doi: 10.1016/j.ncl.2016.06.014
4. Sankowski R, Mader S, Valdés-Ferrer SI. Systemic inflammation and the brain: novel roles of genetic, molecular, and environmental cues as drivers of neurodegeneration. *Front Cell Neurosci.* (2015) 9:28. doi: 10.3389/fncel.2015.00028
5. Soffietti R, Abacioglu U, Baumert B, Combs SE, Kinhult S, Kros JM, et al. Diagnosis and treatment of brain metastases from solid tumors: guidelines from the European Association of neuro-oncology (EANO). *Neuro Oncol.* (2017) 19:162–74. doi: 10.1093/neuonc/now241
6. Zoccatelli G, Alessandrini F, Beltramello A, Talacchi A. Advanced magnetic resonance imaging techniques in brain tumours surgical planning. *J Biomed Sci Eng.* (2013) 06:403–17. doi: 10.4236/jbise.2013.63A051
7. Reichenbach JR, Venkatesan R, Schillinger DJ, Kido DK, Haacke EM. Small vessels in the human brain: MR venography with deoxyhemoglobin as an intrinsic contrast agent. *Radiology.* (2014) 204:272–7. doi: 10.1148/radiology.204.1.9205259
8. Haacke EM, Xu Y, Cheng Y-CN, Reichenbach JR. Susceptibility Weighted Imaging (SWI). *Magn Reson Med.* (2004) 52:612–8. doi: 10.1002/mrm.20198
9. Haacke E, Mittal S, Wu Z, Neelavalli J, Cheng Y-C. Susceptibility-weighted imaging: technical aspects and clinical applications, part 1. *Am J Neuroradiol.* (2009) 30:19–30. doi: 10.3174/ajnr.A1400
10. Mittal S, Wu Z, Neelavalli J, Haacke EM. Susceptibility-weighted imaging: technical aspects and clinical applications, part 2. *Am J Neuroradiol.* (2009) 30:232–52. doi: 10.3174/ajnr.A1461
11. Santhosh K, Kesavadas C, Thomas B, Gupta AK, Thamburaj K, Kapilamoorthy TR. Susceptibility weighted imaging: a new tool in magnetic resonance imaging of stroke. *Clin Radiol.* (2009) 64:74–83. doi: 10.1016/j.crad.2008.04.022
12. Hsu CCT, Haacke EM, Heyn CC, Watkins TW, Krings T. The T1 shine through effect on susceptibility weighted imaging: an under recognized phenomenon. *Neuroradiology.* (2018) 60:235–7. doi: 10.1007/s00234-018-1977-5
13. Trattnig S, Pinker K, Ba-Ssalamah A, Nöbauer-Huhmann IM. The optimal use of contrast agents at high field MRI. *Eur Radiol.* (2006) 16:1280–7. doi: 10.1007/s00330-006-0154-0
14. Do Amaral LLF, Fragoso DC, Nunes RH, Littig IA, Da Rocha AJ. Gadolinium-enhanced susceptibility-weighted imaging in multiple sclerosis: optimizing the recognition of active plaques for different MR imaging sequences. *Am J Neuroradiol.* (2019) 40:614–9. doi: 10.3174/ajnr.A5997
15. Deike-Hofmann K, Thünemann D, Breckwoldt MO, Schwarz D, Radbruch A, Enk A, et al. Sensitivity of different MRI sequences in the early detection of melanoma brain metastases. *PLoS ONE.* (2018) 13:e0193946. doi: 10.1371/journal.pone.0193946
16. Fink K, Fink J. Imaging of brain metastases. *Surg Neurol Int.* (2013) 4:S209–19. doi: 10.4103/2152-7806.111298
17. Liu S, Buch S, Chen Y, Choi HS, Dai Y, Habib C, et al. Susceptibility-weighted imaging: current status and future directions. *NMR Biomed.* (2017) 30:e3552. doi: 10.1002/nbm.3552
18. Boeckh-Behrens T, Lutz J, Lummel N, Burke M, Wesemann T, Schöpf V, et al. Susceptibility-weighted angiography (SWAN) of cerebral veins and arteries compared to TOF-MRA. *Eur J Radiol.* (2012) 81:1238–45. doi: 10.1016/j.ejrad.2011.02.057
19. Shams S, Martola J, Cavallin L, Granberg T, Shams M, Aspelin P, et al. SWI or T2∗: which MRI sequence to use in the detection of cerebral microbleeds? The Karolinska Imaging Dementia Study. *Am J Neuroradiol.* (2015) 36:1089–95. doi: 10.3174/ajnr.A4248
20. Franceschi AM, Moschos SJ, Anders CK, Glaubiger S, Collichio FA, Lee CB, et al. Use of Susceptibility-Weighted Imaging (SWI) in the detection of brain hemorrhagic metastases from breast cancer and melanoma. *J Comput Assist Tomogr.* (2016) 40:803–5. doi: 10.1097/RCT.0000000000000420
21. Schwarz D, Niederle T, Münch P, Hielscher T, Hassel JC, Schlemmer H, et al. Susceptibility-weighted imaging in malignant melanoma brain metastasis. *J Magn Reson Imaging.* (2019) 50:1251–9. doi: 10.1002/jmri.26692
22. Warmuth C, Günther M, Zimmer C. Quantification of blood flow in brain tumors: comparison of arterial spin labeling and dynamic susceptibility-weighted Contrast-enhanced MR imaging. *Radiology.* (2003) 228:523–32. doi: 10.1148/radiol.2282020409
23. Li C, Ai B, Li Y, Qi H, Wu L. Susceptibility-weighted imaging in grading brain astrocytomas. *Eur J Radiol.* (2010) 75:e81–5. doi: 10.1016/j.ejrad.2009.08.003
24. Di Ieva A, Göd S, Grabner G, Grizzi F, Sherif C, Matula C, et al. Three-dimensional susceptibility-weighted imaging at 7 T using fractal-based quantitative analysis to grade gliomas. *Neuroradiology.* (2013) 55:35–40. doi: 10.1007/s00234-012-1081-1
25. Law M, Oh S, Babb JS, Wang E, Inglese M, Zagzag D, et al. Low-grade gliomas: dynamic susceptibility-weighted contrast-enhanced perfusion MR imaging—prediction of patient clinical purpose. *Radiology.* (2006) 238:658–67. doi: 10.1148/radiol.2382042180
26. Hori M, Mori H, Aoki S, Abe O, Masumoto T, Kunimatsu S, et al. Three-dimensional susceptibility-weighted imaging at 3 T using various image analysis methods in the estimation of grading intracranial gliomas. *Magn Reson Imaging.* (2010) 28:594–8. doi: 10.1016/j.mri.2010.01.002
27. Essig M, Anzalone N, Combs SE, Dörfler A, Lee SK, Picozzi P, et al. MR imaging of neoplastic central nervous system lesions: review and recommendations for current practice. *Am J Neuroradiol.* (2012) 33:803–17. doi: 10.3174/ajnr.A2640
28. Cohen-Inbar O, Xu Z, Dodson B, Rizvi T, Durst CR, Mukherjee S, et al. Time-delayed contrast-enhanced MRI improves detection of brain metastases: a prospective validation of diagnostic yield. *J Neurooncol.* (2016) 130:485–94. doi: 10.1007/s11060-016-2242-6
29. Heyn C, Ronald JA, Ramadan SS, Snir JA, Barry AM, MacKenzie LT, et al. *In vivo* MRI of cancer cell fate at the single-cell level in a mouse model of breast cancer metastasis to the brain. *Magn Reson Med.* (2006) 56:1001–10. doi: 10.1002/mrm.21029

Conflict of Interest: The authors declare that the research was conducted in the absence of any commercial or financial relationships that could be construed as a potential conflict of interest.

frontiers in Neurology

REVIEW
published: 15 April 2020
doi: 10.3389/fneur.2020.00270

Advanced Imaging of Brain Metastases: From Augmenting Visualization and Improving Diagnosis to Evaluating Treatment Response

Elizabeth Tong[1]*, *Kassie Lyn McCullagh*[2] and *Michael Iv*[1]

[1] Stanford University Medical Center, Stanford, CA, United States, [2] Neuroradiology, Stanford University Medical Center, Stanford, CA, United States

OPEN ACCESS

Edited by:
Susie Y. Huang,
Harvard Medical School,
United States

Reviewed by:
Vaios Hatzoglou,
Memorial Sloan Kettering Cancer Center, United States
Ina Ly,
Harvard Medical School,
United States
John W. Chen,
Harvard Medical School,
United States
Marc Benayoun,
Wake Forest Baptist Medical Center,
United States

***Correspondence:**
Elizabeth Tong
liztong@gmail.com

Specialty section:
This article was submitted to Applied Neuroimaging, a section of the journal Frontiers in Neurology

Received: 30 October 2019
Accepted: 24 March 2020
Published: 15 April 2020

Citation:
Tong E, McCullagh KL and Iv M (2020) Advanced Imaging of Brain Metastases: From Augmenting Visualization and Improving Diagnosis to Evaluating Treatment Response. Front. Neurol. 11:270. doi: 10.3389/fneur.2020.00270

Early detection of brain metastases and differentiation from other neuropathologies is crucial. Although biopsy is often required for definitive diagnosis, imaging can provide useful information. After treatment commences, imaging is also performed to assess the efficacy of treatment. Contrast-enhanced magnetic resonance imaging (MRI) is the traditional imaging method for the evaluation of brain metastases, as it provides information about lesion size, morphology, and macroscopic properties. Newer MRI sequences have been developed to increase the conspicuity of detecting enhancing metastases. Other advanced MRI techniques, that have the capability to probe beyond the anatomic structure, are available to characterize micro-structures, cellularity, physiology, perfusion, and metabolism. Artificial intelligence provides powerful computational tools for detection, segmentation, classification, prediction, and prognosis. We highlight and review a few advanced MRI techniques for the assessment of brain metastases–specifically for (1) diagnosis, including differentiating between malignancy types and (2) evaluation of treatment response, including the differentiation between radiation necrosis and disease progression.

Keywords: cube, neural network, MRS, quantitative magnetization transfer (qMT), trans-membrane water exchange, chemical exchange saturation transfer (CEST), radiomic, artificial intelligence

INTRODUCTION

Early detection of brain metastases (BM) and accurate differentiation from other neuropathologies is crucial. Early diagnosis affects prognosis and outcome (1). Separating metastases from other etiologies such as primary brain tumors, infection, demyelination, infarction, and hemorrhage is important because the respective treatments are vastly different. Although biopsy is often required for definitive diagnosis, imaging can provide useful information.

Recent improvements in local procedures combined with newer systemic treatments, including targeted therapeutics, have substantially modified the prognosis and survival of patients with brain metastases. Primary approaches to the treatment of brain metastases include surgery, stereotactic radiosurgery (SRS), and whole brain radiation therapy (WBRT). One key determinant in informing treatment decisions is the number of metastases present. Convergent data suggest SRS to the surgical cavity is preferable to WBRT in most patients with up to four brain metastases (2, 3),

providing similar intracranial disease control with less risk of neurocognitive decline. Treatment for patients with multiple (>4) brain metastases has yet to be determined (4). Although expert opinion on the limit on number and size varies, there is no question that accurate accounting of the number of brain metastases is necessary.

Besides detection and tallying, imaging is also performed to assess treatment effects. According to the Response Assessment in Neuro-Oncology Brain Metastases (RANO-BM) working group's proposal, the size of metastases is an important criteria for assessing treatment response (5). Indeed, the four categories of response (complete response, partial response, progressive disease, and stable disease), are defined based on the lesion size. Another crucial task for clinicians and radiologists after radiotherapy is the distinction between radiation necrosis and tumor progression, which is challenging because of their overlapping features on conventional MRI sequences. Recent advances in the treatment of brain metastases (e.g., immunotherapy and targeted therapies) have also posed challenges for the interpretation of MRIs, specifically with regard to the question of pseudoprogression or radiation necrosis vs. true disease progression.

Traditionally, contrast-enhanced magnetic resonance imaging (MRI) is the preferred imaging study for the diagnosis of brain metastases (6, 7). The two most commonly used MRI sequences for assessing brain metastases are contrast-enhanced T1-weighted (CET1W) and T2-weighted FLAIR, which provide information about size, morphology and macroscopic structures. Newer MRI sequences have been developed to increase the conspicuity of enhancing metastases. More recently, advanced MRI techniques that have moved beyond anatomical imaging are available to characterize microstructures, cellularity, physiology, perfusion, and metabolism. Changes in these attributes may supersede perceivable macroscopic anatomic changes and can serve as potential biomarkers for monitoring treatment effect, recurrence, and disease progression (8).

The recent interest of artificial intelligence has transformed the field of medicine. Radiomics and deep learning are deployed to unveil discernible and grossly indiscernible features within radiological images, which can assist with decision-making in oncology (9, 10). Radiomics use sophisticated computational methods to extract quantitative features from medical images, which can be beyond human visual perception (9). A vast amount of computational data are generated, which are then mined by using various machine-learning algorithms to develop models that may potentially improve diagnostic, prognostic, and predictive accuracy (9). On the other hand, deep learning uses multilayer artificial neural networks to learn imperceptible features directly from data, without the constraints of predefined equations and is a powerful tool for classification, detection, and segmentation tasks (11).

Here, we highlight and review the utility of advanced MRI techniques, including new imaging sequences, quantitative methods, and artificial intelligence to evaluate brain metastases–specifically for (1) diagnosis, including differentiating between malignancy types and (2) evaluation of treatment response, including the differentiation between radiation necrosis and disease progression.

BLACK BLOOD MR IMAGING

A clinically dedicated brain metastasis MRI protocol typically consists of pre-contrast (i.e., diffusion-weighted, T2-weighted, T1-weighted) and post-contrast (i.e., T1-weighted, FLAIR) sequences. The critical sequence is the postcontrast 3D T1-weighted sequence, which is a high-resolution sequence acquired by either 3D volumetric Fast Spoiled Gradient-Echo (FSPGR) or Fast Spin-Echo (FSE) technique.

3D volumetric gradient echo imaging (e.g., BRAVO, GE Healthcare; MPRAGE, Siemens Healthcare; 3D TFE; Philips Healthcare) is employed broadly because of the excellent gray-white matter differentiation provided by the technique. 3D volumetric FSE imaging (e.g., CUBE, GE Healthcare; SPACE, Siemens Healthcare; VISTA, Phillips Healthcare) is a relatively newer technique that is also optimal for high-resolution imaging. T1-weighted, T2-weighted, PD-weighted, or FLAIR images can be obtained with the FSE technique. One important distinguishing feature between both of these techniques is the appearance of the vessels. Specifically, the vasculature appears bright on post-contrast 3D T1 FSPGR but appears dark ("black blood") on post-contrast 3D T1 FSE. As a result of the "bright blood" appearance on post-contrast FSPGR, it can sometimes be difficult to distinguish enhancing parenchymal metastases or leptomeningeal carcinomatosis (**Figure 1**) from background vascular enhancement (12). On the contrary, post-contrast FSE provides inherent background vascular suppression, yielding a higher contrast-to-noise ratio (CNR) of lesions, making enhancing parenchymal, and leptomeningeal metastases more conspicuous (13).

Detection of Brain Metastases

To make metastases even more perceptible, thick-section maximum intensity projection (MIP) images can be reconstructed from post-contrast 3D T1 FSE. Reconstruction with slice overlapping can further help to reduce artifacts from partial volume averaging and improve visualization of lesions (**Figure 2**) (14). The use of MIP images is standard practice for detecting pulmonary nodules in chest imaging (15), because discrete lesions are accentuated from the background. Yoon et al. used a similar technique and demonstrated better and faster detection of brain metastases using MIP images constructed from overlapping post-contrast T1-weighted CUBE (oCUBE-MIP). They compared oCUBE-MIP images with more conventional imaging techniques–source post-contrast 3D T1 FSPGR, source post-contrast 3D T1 CUBE, and non-overlapping CUBE MIPs (nCUBE-MIP) (14). As expected, the CNR was highest on oCUBE-MIP and lowest on FSPGR, for both small (<4 mm) and large lesions (>4 mm). The sensitivity for lesion detection was highest with oCUBE-MIP (0.96). oCUBE-MIP had a slightly higher false-positive rate than FSPGR, which they attributed to erroneous diagnosis of tiny vascular segments as punctate metastases. However, the false-positive rate of oCUBE-MIP was improved when source CUBE images were provided along with

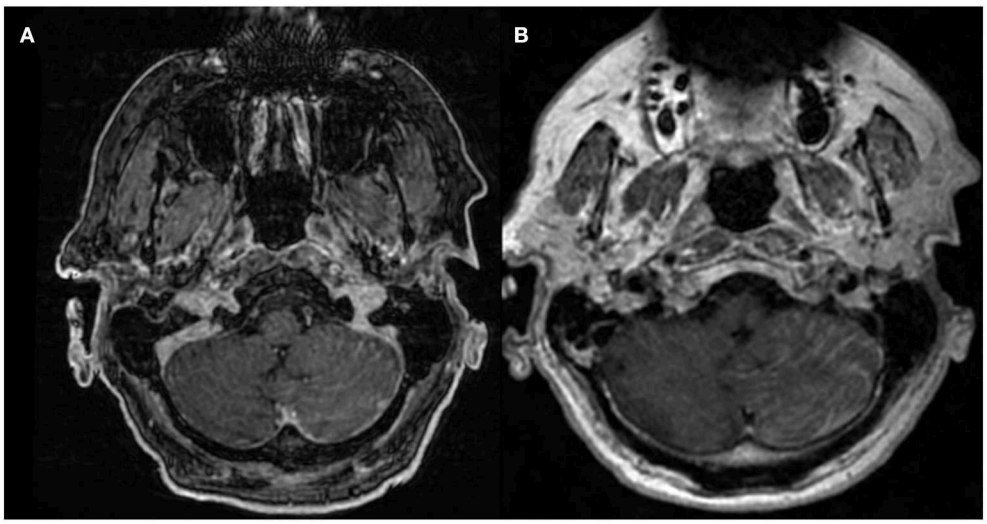

FIGURE 1 | 68-years-old patient with primary lung adenocarcinoma and leptomeningeal carcinomatosis. Diffuse nodular leptomeningeal enhancement is seen over the left cerebellar surface on **(A)** post-contrast 3D T1 FSPGR and **(B)** post-contrast 3D T1 CUBE, compatible with leptomeningeal carcinomatosis. Conspicuity of enhancement is increased in **(B)** compared to **(A)**.

oCUBE-MIP images for cross-referencing purposes, because vessels can be more accurately traced on source CUBE images. The mean interpretation time with oCUBE-MIP was 94.7 +/– 36.5 s, which was significantly lower than with source CUBE (173.5 +/– 67.7 s) and source BRAVO (195 +/– 64.8 s) alone, providing an average saving of at least 100 s per case.

Taking advantage of the higher CNR on CUBE images, Oh et al. demonstrated significantly better diagnostic accuracy for detection of leptomeningeal carcinomatosis in 78 subjects with post-contrast 3D T1 CUBE images ($p < 0.05$). Highest sensitivity was achieved on post-contrast CUBE (97.43%), followed by post-contrast 2D T1-weighted spin-echo (66.67%), and post-contrast T1 FSPGR (64.1%). There were no significant differences in specificities among the three imaging techniques (16).

Clinical Implication

Post-contrast 3D T1 CUBE, particularly with overlapping thick-section MIP reconstruction, is a clinically available imaging technique that offers high contrast-to-noise ratios of enhancing lesions within the brain and allows for fast and sensitive detection of brain metastases (**Table 1**).

MAGNETIC RESONANCE SPECTROSCOPY (MRS)

Protons of different molecules resonate at slightly different frequencies secondary to the local magnetic field generated by the electron cloud surrounding them. Magnetic resonance spectroscopy (MRS) detects tissue metabolites by their characteristic resonant frequencies (17). In oncologic applications, the metabolites of interest are products or byproducts of malignancy-related pathways (17, 18). The most common metabolites are N-acetylaspartate (NAA), choline (Cho), lipid (Lp), and creatine (Cr). NAA is a neurotransmitter, which is abundant in neurons, and is a marker for neuronal health (19). Its concentration is related to the extent of neuronal destruction (20). Choline is involved in the manufacturing of phospholipids, which is an integral component of cell membranes (21). Higher levels of choline are associated with higher cell membrane turnover, presumably from cell damage. Lipid is a byproduct associated with cellular necrosis and is often seen in the setting of glioblastoma or metastases. Creatine is involved in intracellular metabolic processes. Creatine concentration is higher in areas with higher energy metabolism (22). The concentration of these metabolites can be measured on MRS and can help to determine the underlying pathophysiology of a lesion.

There are many spectroscopic acquisition techniques, with commonly used methods being "PRESS" (23) and "STEAM" (24). While technical details of MRS are beyond the scope of this article, MRS can be acquired with either short or long echo-time (TE), with typical short TE values ranging between 18 and 45 ms and long TE values ranging between 120 and 288 ms. Different TE values highlight different aspects of the spectra. For example, on short TE MRS, the spectra tend to have an irregular fluctuating baseline, and NAA may overlap with the glutamine/glutamate peak. On long TE MRS, lipids may not be detected, and there may be an artifactual elevation of the Cho/Cr ratio (25). The optimal TE for brain malignancy MRS is still under discussion (25). MRS is acquired by using a single voxel technique, with a small voxel size of a few cubic centimeters, or with a (2D or 3D) multi-voxel technique, which provides larger coverage of a target lesion at a higher spatial resolution. However, both methods are limited in spatial resolution and coverage, making MRS susceptible to partial volume effects. Diagnostic accuracy of MRS can also be limited by sampling error, especially with heterogeneous lesions

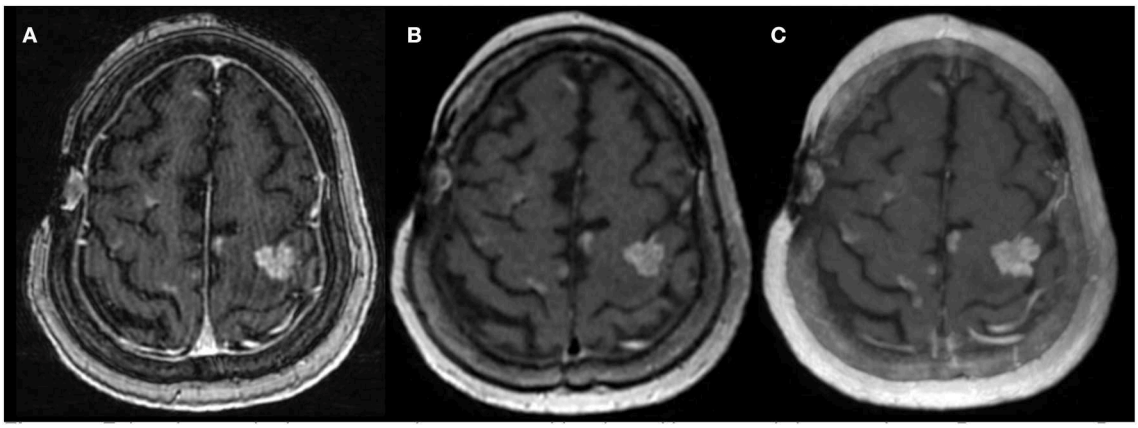

FIGURE 2 | Enhancing cerebral metastases in a 78-years-old patient with metastatic lung carcinoma. Postcontrast 3D T1-weighted **(A)** FSPGR, **(B)** CUBE, and **(C)** overlapping CUBE maximum intensity projection (oC-MIP) images demonstrate enhancing metastatic lesions. The lesions appear most conspicuous with overlapping CUBE MIPs **(C)**. The contrast-to-noise ratio of lesions is also highest for oC-MIP **(C)**.

TABLE 1 | Summary of imaging techniques, features, and potential applications.

Technique	Features	Potential applications
Overlapping post-contrast 3D T1-weighted CUBE (oCUBE-MIP)	High contrast-to-noise ratio of enhancing lesions	• Fast and sensitive detection of brain parenchymal and leptomeningeal metastases • Clinically available and easy to implement
Magnetic resonance spectroscopy	Detects tumoral metabolites	• Lipids detected in metastases and glioblastomas • Higher NAA/Cr in metastases than in primary gliomas • Higher Cho/Cr and Cho/NAA with tumor progression than with radiation necrosis • Clinically available but more difficult and complex to implement; complementary to structural imaging • Standardization across different MRI vendors is needed
Quantitative magnetization transfer	Characterizes magnetization transfer ratio (MTR), macromolecular concentration (F), exchange rate between the bound protons and free water protons (kf)	• Peritumoral MTR lowest in meningioma compared to glioblastoma and metastases • Macromolecular fraction in the non-contrast-enhancing region of tumor highest in metastases • Largely investigational at this time • No standardized post-processing software
Trans-membrane water exchange	Measures transmembrane intra-extracellular water exchange rate constant (kIE) which is sensitive to apoptosis	• kIE higher in responders (to radiosurgery) than non-responders • Largely investigational at this time
Chemical exchange saturation transfer	Measures metabolites of neoplasm milieu	• Higher MTR_{Amide} and NOE with tumor progression than with radiation necrosis. • Promising and rapidly developing molecular-imaging tool • More studies in humans and standardized techiques to improve the specificity are needed
Perfusion imaging	Relative cerebral blood volume and cerebral blood flow	• Peritumoral rCBV and rCBF higher in glioblastomas than metastases • Intratumoral rCBV can help to distinguish infection from tumor • Higher intratumoral and peritumoral ASL-rCBF in glioblastomas than in metastases. • Higher rCBV, higher rPH, lower PSR, higher Ktrans in recurrent tumor; lower rCBV, lower rPH, higher PSR, lower Ktrans in radiation necrosis • Clinically available with different acquisition and post-processing methods, limiting its universal adoption; complementary to structural imaging
Radiomics and textural analysis	Computes quantitative patterns and inter-pixel relationships of tumors	• Some textural parameters can distinguish glioblastomas from metastases Some textural parameters can classify the primary origins of brain metastases • Largely investigational at this time; large multicenter datasets are needed for validation

(8). In general, a multi-voxel technique is recommended for evaluation of heterogeneous tumors or multiple lesions in order to minimize sampling error from a specific area of a lesion (26). Moreover, voxels should be positioned away from fat, bone, air, ventricles, vessels, and cerebrospinal fluid in order to avoid contamination of the spectra.

Differentiate Malignancy Types

Similar to glioblastoma, brain metastases express elevated lipid signal (presumably as a result of cellular necrosis) on MRS. The lipid peak, therefore, has been used to differentiate these two tumor types from other brain neoplasms (27). Ishimaru et al. studied 11 patients with anaplastic gliomas, 20 patients with glioblastomas, and 25 patients with brain metastases using single-voxel MRS to differentiate between the three malignancy types (27). They measured the levels of lipids, NAA, Cho, and Cr. Metastases and glioblastomas showed definite lipid peak or lipid/lactate mixture peak, but no lipid signal was detected in anaplastic gliomas. Absence of the lipid signal precluded metastases. A strong Cho peak was detected in all tumors. No definite Cr peak was detected in 21 of the 25 metastases. Therefore, the presence of a Cr peak was suggestive of glioma, whereas the absence of a Cr peak was more suggestive of metastasis. The NAA/Cr ratio was shown to be higher in brain metastases (NAA/Cr = 1.58 ± 0.56), as compared to anaplastic gliomas (NAA/Cr = 0.70 ± 0.23) and glioblastomas (NAA/Cr = 0.76 ± 0.40) (27).

Similar results were reported in another study investigating 32 patients with high-grade gliomas, 14 patients with low-grade gliomas, and 14 patients with brain metastases using multi-voxel 2D MRS on 3T (28). Both NAA/Cr and Cho/Cr ratios within the tumors were higher in brain metastases (NAA/Cr = 4.43 ± 4.5, Cho/Cr = 4.88 ± 7.0), than in low-grade gliomas (NAA/Cr = 1.68 ± 0.9, Cho/Cr = 2.7 ± 2.1), and high-grade gliomas (NAA/Cr = 1.04 ± 0.6, Cho/Cr = 3.4 ± 1.7). In the peritumoral regions, NAA/Cr and Cho/Cr ratios were highest in low-grade gliomas (NAA/Cr = 3.73 ± 2.61, Cho/Cr = 4.62 ± 6.95), followed by brain metastases (NAA/Cr = 2.53 ± 1.13, Cho/Cr = 2.72 ± 2.55), and lowest in high-grade gliomas (NAA/Cr = 1.49 ± 0.83, and Cho/Cr = 2.49 ± 2.02) (28). Higher lipids were measured in high-grade gliomas (Lipids = 118.2 ± 215.9), which could help to discriminate them from metastases (Lipids = 35.48 ± 48.22). However, lipid levels in low-grade gliomas were similar to that of metastases and were therefore not useful to discriminate between the two (28). Lactate signal was also significantly different in high-grade gliomas (Lactate = 94.62 ± 123), with respect to low-grade gliomas (Lactate = 50.02 ± 97.89), and metastases (Lactate = 15.07 ± 16.74). Of note, the reported standard deviations in metabolite measurements were quite large and overlapped between tumor types. Therefore, further studies with larger populations are needed to better determine if MRS is useful for differentiating brain metastases from different glioma types.

Evaluate Treatment Effect

Sjobakk et al. used single voxel MRS to study lipid peak in 21 patients with brain metastases before treatment to predict outcome. Patients with a higher lipid signal at baseline had a higher 5-months survival rate. Four patients in the cohort underwent repeat MRS after treatment, which demonstrated decreased lipid signal. The two patients with a larger drop in lipid signal survived longer than the other two (16 vs. 3 months) (29).

MRS has also been used to differentiate radiation necrosis from tumor progression in brain metastases. Weybright et al. evaluated MRS in 29 patients with brain metastases after radiotherapy. Metastases that progressed showed significantly higher ratios of Cho/Cr and Cho/NAA compared to radiation necrosis (30). Schlemmer et al. also used MRS to differentiate radiation necrosis from disease progression in 56 patients (6 metastases, 2 meningiomas, 50 grade I to IV astrocytomas). Higher Cho/Cr and Cho/NAA ratios ($p < 0.0001$) were observed in tumor progression ($n = 34$) compared with radiation necrosis or stable disease ($n = 32$) and contralateral normal brain ($n = 33$). Using Cho/Cr and Cho/NAA ratios to classify a lesion as progressive tumor yielded 82 and 81% accuracy, respectively (31).

These findings were further interrogated in a meta-analysis of 13 studies, encompassing 397 lesions, that showed higher Cho/Cr and Cho/NAA ratios in tumors than in radiation necrosis (22). There was a significant difference in Cho/Cr ratio between recurrent tumor and radiation necrosis (0.77, 95%CI = 0.57 to 0.98, $p = 0.001$). There was also a significant difference in ratios of Cho/NAA between recurrent tumor and radiation necrosis (1.02, 95%CI = 0.03 to 2.00, $p = 0.044$). However, there was a large overlap in the values between the two groups.

These promising studies suggest that the concentrations and ratios of metabolites in tumor milieu detected by MRS may be useful in distinguishing between the following groups: neoplastic and non-neoplastic brain lesions, progressive disease and radiation necrosis, and treatment responders and non-responders.

Clinical Implication

MRS is a clinically available technique that provides information on tumoral metabolites in the treatment naïve and post-treatment setting (**Figures 3**, **4**). However, given overlapping features with different tumor types and subtypes and other metabolically active disease processes, prospective studies with larger sample sizes are needed to further investigate its potential diagnostic capabilities (**Table 1**). Partial volume effects and limited coverage are some of the reasons why MRS is replaced by other whole-brain techniques such as perfusion. Standardization across sites and different vendors of acquisition and analysis techniques is also needed before MRS can be widely adopted as clinical tool (32).

QUANTITATIVE MAGNETIZATION TRANSFER (qMT)

Magnetic transfer describes the phenomenon where net magnetization of free water hydrogen protons is exchanged with that of restricted hydrogen protons (those bound to macromolecules) (33). Such macromolecules include lipids constituted in myelin and cell membranes. Magnetization transfer imaging (MTI) applies radiofrequency energy (MT pulses) to the bound protons, which is then transferred to the free water pool (34). Depending on the degree of coupling between these pools, the free water pool becomes partially saturated. When imaged, this saturation effect (secondary to magnetization transfer) manifests as signal loss. Quantitative magnetization transfer imaging (qMT) characterizes the

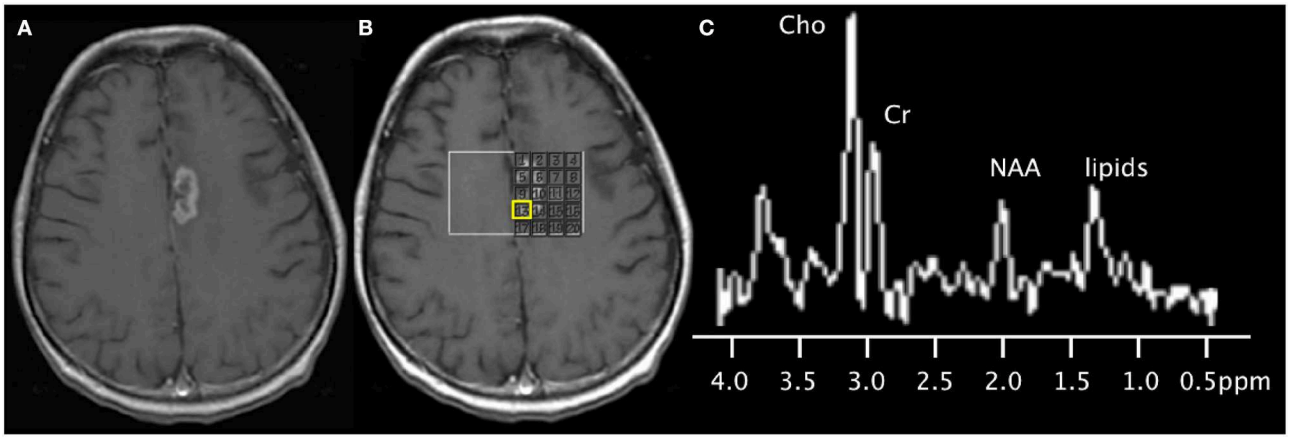

FIGURE 3 | 67-years-old patient with a left medial frontal lobe brain metastasis from primary lung cancer treated with stereotactic radiosurgery. **(A)** Post-contrast T1-weighted image shows the treated enhancing lesion. **(B)** Multi-voxel 2D magnetic resonance spectroscopy acquired at 3T with grid placed on the lesion. **(C)** Spectra (from the voxel highlighted in yellow) shows findings of disease progression, with the presence of a lipid peak (indicative of necrosis), high Cho peak, and increased Cho/NAA and Cho/Cr ratios. Subsequent short-term follow-up MRI showed growth of the lesion (not shown), supporting the diagnosis of disease progression.

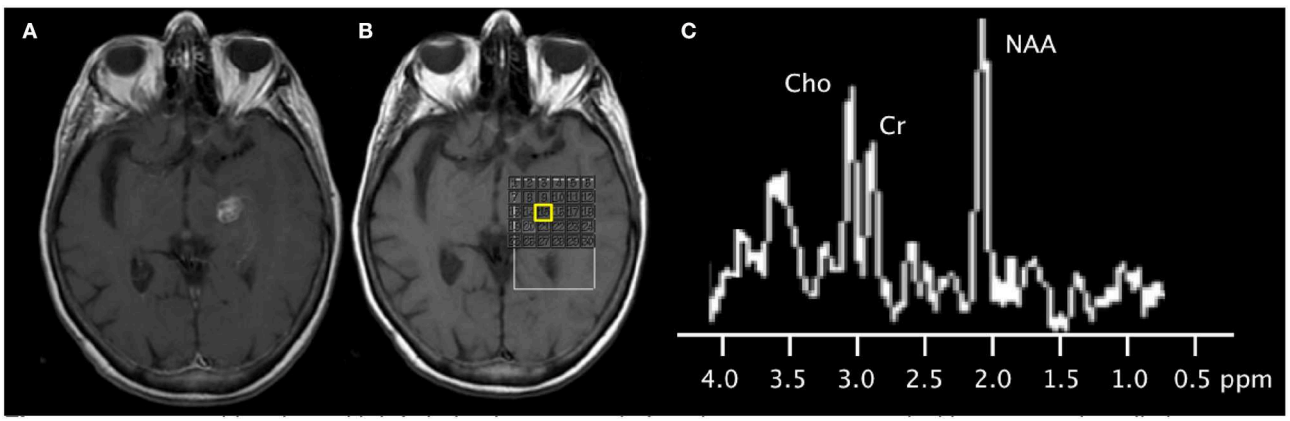

FIGURE 4 | 79-years-old patient with left thalamic metastasis from lung cancer treated with stereotactic radiotherapy. **(A)** Post-contrast T1-weighted image shows the treated enhancing lesion. **(B)** Multi-voxel 2D magnetic resonance spectroscopy acquired at 3T with grid placed on the lesion. **(C)** Spectra (from the voxel highlighted in yellow) shows mild elevation of the choline peak, slightly increased Cho/Cr ratio, slightly increased Cho/NAA ratio, and normal NAA/Cr ratio. Subsequent follow-up MRI showed shrinkage of the contrast-enhancing mass (not shown), supporting the diagnosis of radiation necrosis.

magnetization transfer ratio (MTR), the macromolecular concentration (F), the exchange rate between the bound protons and free water protons (kf), as well as the relaxation times (T1, T2) of the bound and free proton pools (34). MTR of each voxel is computed as: MTR = (So – SMT)/So, where So is the magnitude of tissue signal before the MT pulse and SMT is the signal after applying MT pulse.

Differentiate Malignancy Types

Garcia et al. used magnetization transfer ratio (MTR) and qMT parameters to differentiate brain metastases from other brain tumors in 26 patients (35). (**Figure 5**) Significant differences were found in the MTR and qMT parameters (on both the tumor rim and core) of glioblastoma, meningiomas, and brain metastases (35). MTR on the non-contrast-enhancing region of tumor was highest in metastases (MTR = 35.1% ± 0.5), followed by glioblastoma (MTR = 33.8% ± 1.2 and meningiomas (MTR = 28.9% ± 1.6), and was capable of separating metastases from meningiomas. MTR on the contrast-enhancing region was highest in meningiomas (MTR = 30.5% ± 1.2), followed by metastases (MTR = 27.4% ± 1.0) and glioblastoma (MTR = 25.2% ± 0.6), and could separate glioblastoma from meningiomas. MT exchange rate on the contrast-enhancing region of the tumor (k_f = 0.8 ± 0.1, 1.1 ± 0.1, 0.6 ± 0.0 for brain metastases, meningiomas, and glioblastomas, respectively) and macromolecular fraction on the non-contrast-enhancing region of the tumor (F = 7.2 ± 0.7, 5.6 ± 0.2, 3.6± 0.7 for brain metastases, meningiomas, and glioblastomas,

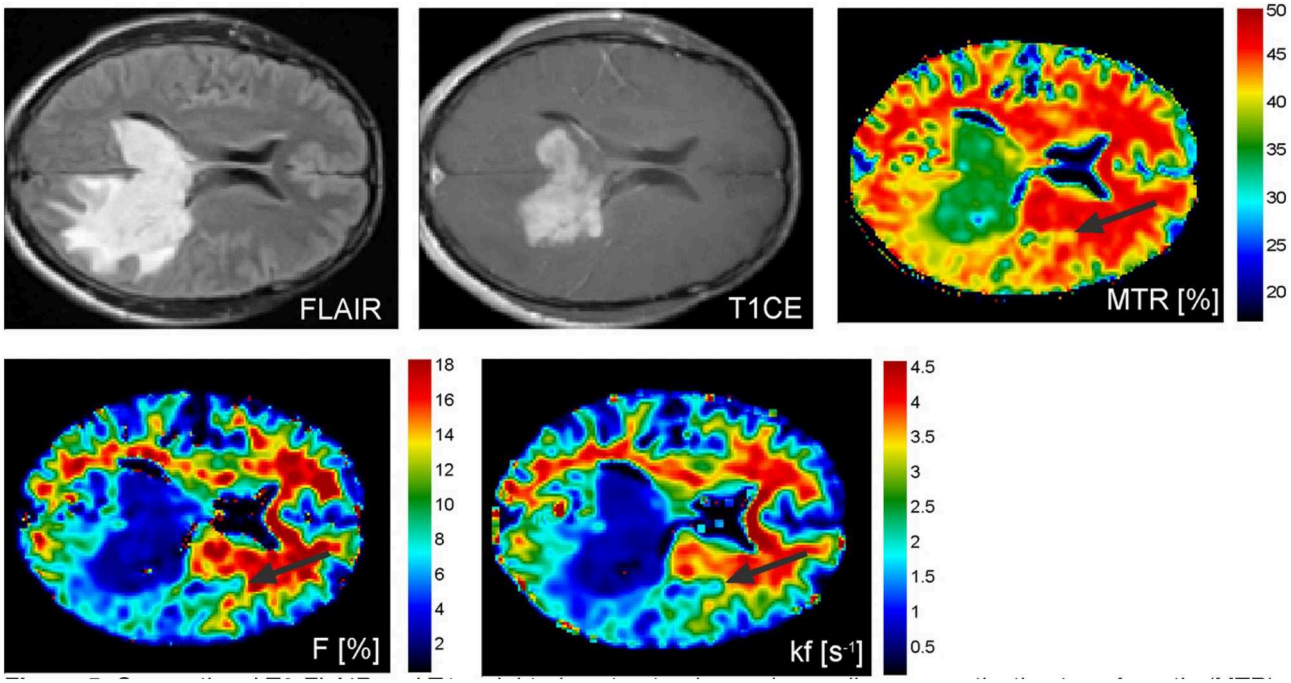

FIGURE 5 | Conventional T2-FLAIR and T1-weighted contrast-enhanced as well as magnetization transfer ratio (MTR), macromolecular concentration (F), and exchange rate between the bound protons and free water protons (kf) images of a patient with a malignant pleomorphic glial tumor in the left temporal and occipital lobes showing contralateral tumor extension via the splenium of the corpus callosum. Abnormal MTR values can be discerned ventrally and laterally to the altered looking tissue on conventional MRI (black arrows). Reproduced, with permission, from Garcia et al. (35).

respectively) could distinguish between all three tumor types (35).

Clinical Implication

Quantitative magnetization transfer imaging is largely research-based at this time. More and larger clinical studies are needed to validate its use in the clinical setting (**Table 1**). Currently, there are no FDA approved or standardized software to post-process the acquired data or display the results.

TRANS-MEMBRANE WATER EXCHANGE

Biologic tissue can be grossly divided into three compartments–vascular, intracellular, and extracellular extra-vascular, with different physiochemical properties. Water molecules move between these two non-vascular compartments constantly. The exchange rate of water molecules between intracellular and extracellular compartments depends on the permeability of the cell membrane as well as on the size and shape of the cell (36). Transmembrane intra-to-extracellular water exchange rate constant (kIE) is very sensitive to structure damage such as apoptosis. During apoptosis, cells are disfigured, shrunken, and have higher cell membrane permeability (36, 37), leading to an increase in kIE. It has been shown that kIE increases significantly within days after inducing apoptosis (38, 39).

Evaluate Treatment Effect

Mehrabian et al. developed a water exchange quantification technique for dynamic contrast-enhanced MRI, to measure the transmembrane water exchange rate (kIE) (39). Since the transmembrane intra-to-extracellular water exchange rate constant (kIE) is sensitive to apoptosis, and assuming effective treatment destroys malignant cells by apoptosis, kIE can be used to distinguish responders from non-responders to therapy. The authors investigated the change in transmembrane water exchange rate (kIE) between pre-treatment and 1-week post-treatment scans, and correlated measurements with treatment efficacy in 19 patients with brain metastases undergoing stereotactic radiosurgery (39). Trans-membrane water exchange rate constant is significantly increased in responders, as determined according to RANO-BM criteria (5), than non-responders within 1 week after treatment ($p < 0.001$). In addition, the increase in transmembrane water exchange rate (kIE) correlated with tumor shrinkage at 1 month after treatment ($R = -0.76$, $p < 0.001$). This ability to differentiate responders from non-responders at such early post-treatment stage can potentially help to inform treatment plans.

Clinical Implication

Multi-center trials complying with criteria of evidence-based medicine have not yet been completed, therefore transmembrane water exchange imaging is primarily investigational at this time (**Table 1**).

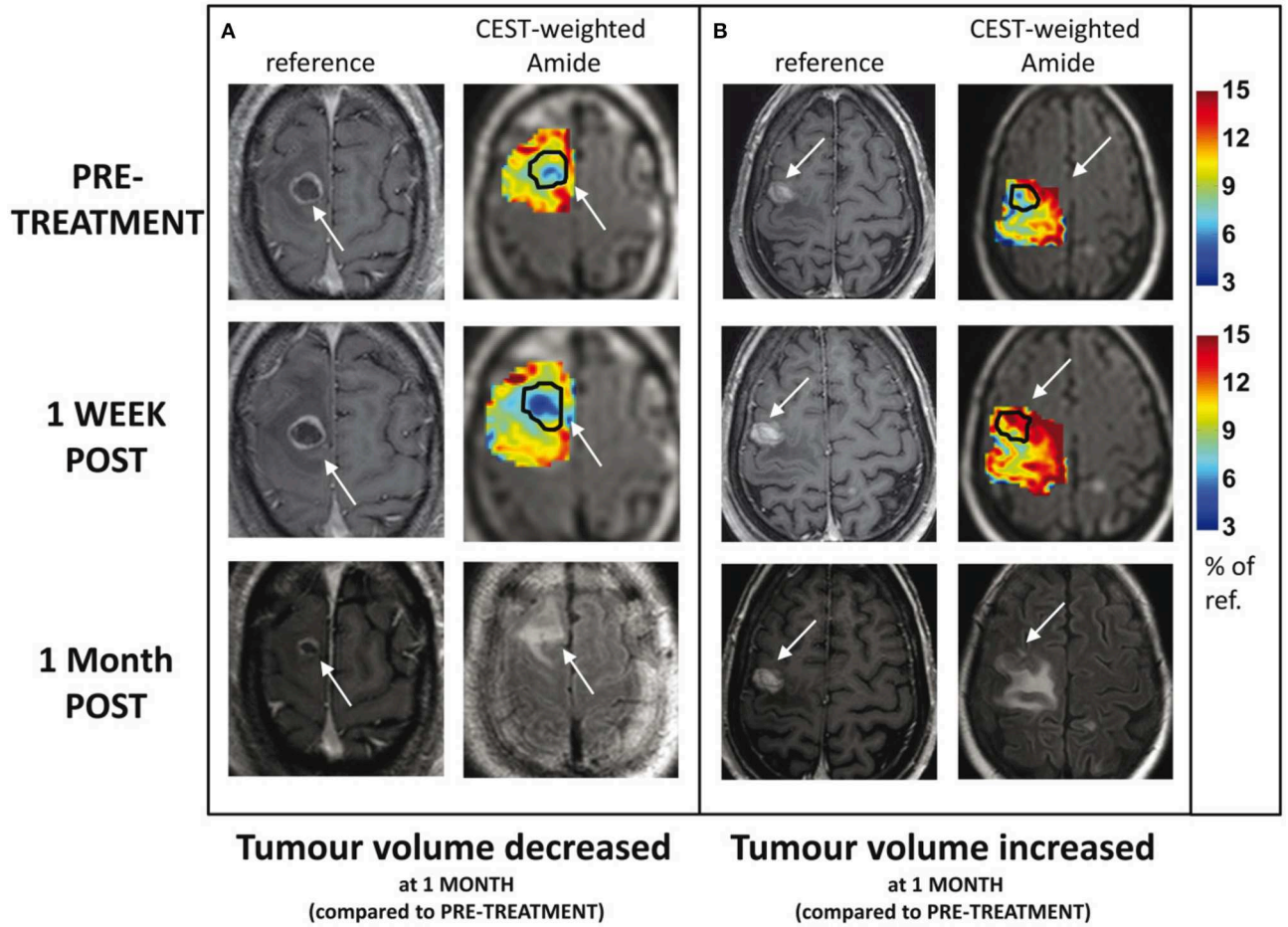

FIGURE 6 | Example CEST amide effect maps within the tumor and immediately surrounding tissue, including edema, at baseline and 1 week post-treatment for 2 patients: **(A)** tumor volume decreased 1 month post-therapy and **(B)** tumor volume increased 1 month post-therapy. The margins of the enhancing tumor are indicated with an arrow and outlined in black on the CEST maps. The corresponding slice from the high resolution, contrast-enhanced T1-weighted volume is shown for comparison. Contrast-enhanced T1-weighted and FLAIR images at 1 month follow-up are shown in the third row. Reproduced, with permission, from Desmond et al. (48).

CHEMICAL EXCHANGE SATURATION TRANSFER (CEST)

Chemical exchange saturation transfer MRI (CEST) is a novel MR technique that detects the chemical shift between exchanging protons of the metabolites with the local electron cloud (40). CEST can image certain compounds at concentrations that are too low to be detected by standard MR imaging or MRS (40–42). CEST is sensitive to the exchange of labile protons (including amide protons), rapid exchange of hydroxyl protons, and intramolecular transfer of magnetization from aliphatic (-CH) protons to labile protons, termed as relayed nuclear Overhauser effect (rNOE) (43). These protons are found in metabolites such as glutamate, lactate, myo-inositol and glucose, which are common constituents in a neoplastic milieu (44). The most commonly used CEST metrics in cancer are amide proton transfer (APT) (45), magnetization transfer ratio for amide (MTR_{Amide}), and nuclear Overhauser effect (NOE) (46). NOE is the transfer of nuclear spin polarization from one nuclear spin population to another via dipolar cross-relaxation (47).

Evaluation of Treatment Effect

Desmond et al. applied endogenous CEST-MRI to determine response of 25 patients with brain metastases within 1 week after stereotactic radiosurgery (SRS) treatment (48). Reduced CEST signal in responders and increased CEST in non-responders were observed (**Figure 6**). Furthermore, changes in CEST signals at 1-week post treatment correlated with the change in tumor volume measured at 1 month post-treatment. In particular, the width of the NOE peak in tumor (correlation coefficient, $r = -0.55$, $p = 0.028$) and amplitude of NOE peak on the normal-appearing white matter ($r = 0.69$, $p = 0.002$) yielded the highest correlations (48). The amplitude of the NOE peak in the contralateral normal-appearing white matter (NAWM) at baseline (before SRS) was inversely correlated with the degree of tumor volume change at

1 month post-treatment ($r = -0.69$, $p = 0.002$), which may be an indicator of tumor aggressiveness (48).

Mehrabian et al. used CEST to differentiate radiation necrosis from tumor progression in 16 patients with brain metastases, with nine confirmed radiation necrosis and seven tumor progression (49). Both MTR_{Amide} and NOE were able to differentiate progressive tumors from radiation necrosis with high accuracy ($p < 0.0001$) (49). Higher MTR_{Amide} was measured in tumor progression ($MTR_{Amide} = 12.0 \pm 1.9$), compared to radiation necrosis ($MTR_{Amide} = 8.2 \pm 1.0$). Higher NOE was measured in tumor progression (NOE $= 12.6 \pm 1.6$), compared to radiation necrosis (NOE $= 8.9 \pm 0.9$).

Clinical Implication

Chemical exchange saturation transfer shows promise as a tool for molecular imaging of CNS malignancy. Although CEST is largely a research tool currently, there are rapid development in CEST techniques for improving the acquisition speed and spatial coverage (50). More studies in humans and standardized techniques to improve the specificity of the methods will be needed in order to translate into the clinical setting (50) (**Table 1**).

PERFUSION IMAGING

The most commonly used techniques for assessing tumor perfusion are dynamic susceptibility contrast (DSC), dynamic contrast-enhanced (DCE), and arterial spin labeling (ASL) imaging (**Figure 7**). Different perfusion parameters are derived from each technique. For CNS tumor imaging, cerebral blood volume (CBV) and cerebral blood flow (CBF) are commonly studied metrics. CBV measures the amount of blood per volume of tissue. CBF measures the amount of blood per volume of tissue per unit of time. Both CBV and CBF reflect tumor vascularity. In addition to measuring absolute values, CBV and CBF are often measured relative to an internal control (typically the contralateral normal parenchyma). The ratios are often referred to as relative cerebral blood volume (rCBV) and relative cerebral blood flow (rCBF), respectively. In contrast to DSC and DCE imaging, ASL is a non-contrast method for determining CBF.

Differentiation of Malignancy Types

Server et al. measured DSC perfusion parameters within the tumor and peritumoral regions to differentiate glioblastomas ($n = 40$) from metastases ($n = 21$) (51). The rCBV and rCBF within the peritumoral region were significantly higher in glioblastomas (rCBV $= 1.8 \pm 0.7$, rCBF $= 2.1 \pm 1.4$) than metastases (rCBV $= 0.6 \pm 0.1$, rCBF $= 0.7 \pm 0.5$). An rCBV threshold of 0.8 yielded 95% sensitivity and 92% specificity for differentiating glioblastomas from metastasis. Other similar studies showed high negative predictive value and high specificity for detecting metastases with a peritumoral rCBV cutoff of 1.0 (52, 53).

Interestingly, the rCBV and rCBF within the tumor were not significantly different between glioblastomas and metastases (51). However, studies have shown that neoplasms (rCBV $= 4.28 \pm 2.11$) have higher rCBV than infectious lesions (rCBV $= 0.63 \pm 0.49$), and intratumoral rCBV can be helpful to distinguish infectious lesions from neoplasms (54).

Sunwoo et al. performed qualitative and quantitative analyses on ASL-CBF in 128 patients with glioblastoma ($n = 89$) and brain metastases ($n = 39$) (55). Intratumoral and peritumoral rCBF were assessed. Both qualitatively and quantitatively, glioblastomas demonstrated higher intratumoral and peritumoral rCBF than metastases. They report an area under the curve (AUC) of 0.835 for differentiating the two with peritumoral rCBF (55).

Evaluation of Treatment Effect

Tumor recurrences typically develop increased abnormal vasculature, which is represented by increased rCBV. Relative peak height (rPH), which is the maximum change in signal during the passage of contrast agent, correlates with tumor capillary blood volume. Tumor recurrences will also have relatively higher rPH (56). Percentage of signal-intensity recovery (PSR), an indicator of blood-brain-barrier integrity, reflects the degree of contrast agent leakage caused by alteration of capillary permeability. Tumor recurrences often have increased permeability due to abnormally formed vessels, which allow more gadolinium to leak into and remain in the extracellular space, leading to persistent gadolinium effects of decreasing signal and consequently decreased PSR. In contrast, in radiation necrosis, the vasculature is damaged, with resulting decreased blood flow, which is represented by decreased rCBV. Also, as there is less leakage of contrast into the extracellular space, the PSR will be higher in radiation necrosis (56).

Barajas et al. used DSC perfusion imaging to aid in the diagnosis of tumor recurrence vs. radiation necrosis; the authors assessed a total of 30 lesions in 27 patients with brain metastases, which were enlarging after SRS. They showed that rCBV and rPH were statistically higher and PSR was lower in recurrent tumor than in cases of radiation necrosis. Additionally, they demonstrated that PSR was the best indicator of radiation necrosis when a cutoff value of >76.3% was used, yielding a sensitivity of 95.65% and a specificity of 100% (56).

Ktrans, derived from DCE, reflects the permeability of the tissue. An increased Ktrans suggests tumor recurrence. Morabito et al. demonstrated similar accuracy of DCE compared to DSC in distinguishing between tumor recurrence and radiation necrosis in a total of 28 patients (total of 72 lesions) in both primary brain tumors (15 cases) and metastatic lesions (57 lesions) treated with SRS. The rCBV values for DSC and the Ktrans values for DCE were compared and showed similar accuracy in differentiation radiation necrosis from tumor progression (57).

Clinical Implication

MR perfusion imaging is a widely available clinical technique used for assessing tumor vascularity, for differentiating between tumor types, and for differentiating tumor recurrence from treatment effect (**Table 1**). However, widespread adoption has been limited by lack of imaging acquisition and post-processing standardization across multiple and different institutions.

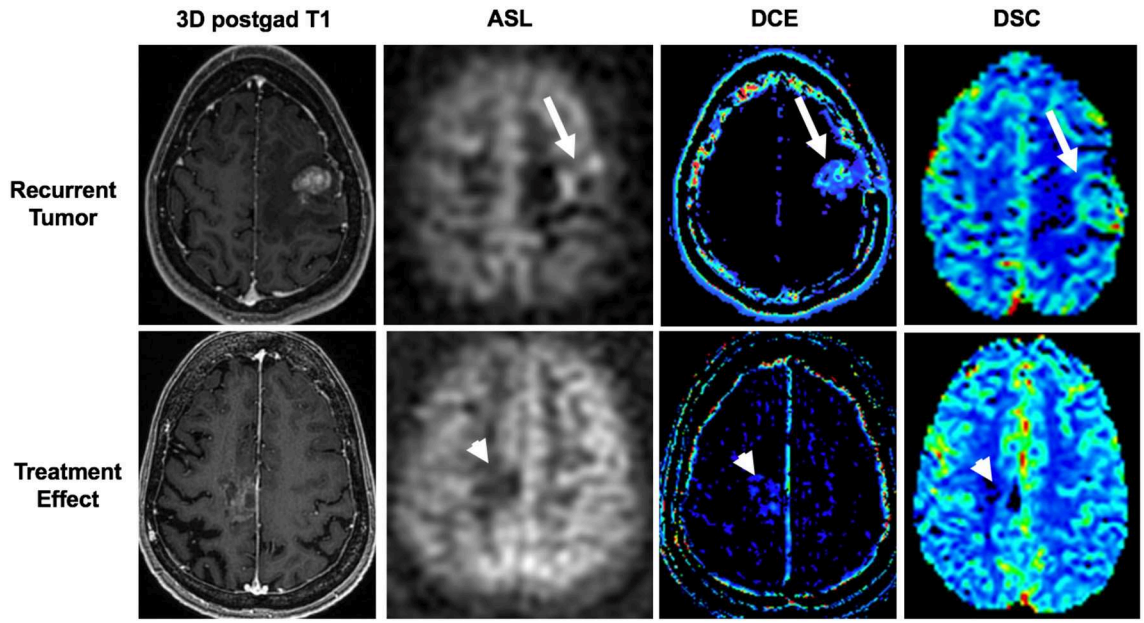

FIGURE 7 | Utility of arterial spin labeling (ASL), dynamic contrast enhancement (DCE), and dynamic susceptibility contrast (DSC) perfusion MRI to differentiate between recurrent tumor and treatment effect. Top panel shows recurrent tumor in a 34-years-old female with a left frontal breast cancer metastasis that was previously resected and treated with stereotactic radiosurgery. ASL, DCE, and DSC images demonstrate high cerebral blood flow, Ktrans, and cerebral blood volume (arrows), respectively, associated with the contrast-enhancing lesion. Tumor was confirmed on histopathology from subsequent re-resection. Bottom panel shows treatment effect in a 65-years-old female with a right frontal lung cancer metastasis who was previously resected and treated with stereotactic radiosurgery. ASL, DCE, and DSC images demonstrate low cerebral blood flow, Ktrans, and cerebral blood volume (arrowheads), respectively, associated with the mildly enhancing lesion. Treatment effect was confirmed with negative PET/MRI (not shown) and a stable 3-months follow-up MRI (not shown).

RADIOMICS AND ARTIFICIAL INTELLIGENCE

Treatment and prognosis for patients with primary CNS malignancies and different types of metastases are different, which makes distinguishing between them important. However, these neoplastic brain lesions have overlapping features on conventional MRI, such as enhancement, surrounding edema and central necrosis. More sophisticated features, beyond standard morphometric features, are needed to distinguish them.

Texture analysis, a common radiomics approach, uses high-order statistical methods to extract quantitative patterns and inter-pixel relationships within an image. The generated computational data are then mined by using various machine-learning algorithms to develop models that may potentially improve diagnostic, prognostic, and predictive accuracy (9). Texture analysis can characterize tumor heterogeneity by evaluating relationships of gray pixels/voxels to each other using mathematical techniques such as gray-level co-occurrence matrix (GLCM), gray-level run-length matrix (GLRLM), etc. Texture analysis has been used to distinguish brain metastases from various primary malignancies (58–60).

Differentiation of Malignancy Types

Petrujkic et al. performed texture analysis on 30 patients with glioblastomas and 25 patients with solitary metastases on T2-weighted, susceptibility weighted, and post-contrast MPRAGE (CET1) images (61). Five textural parameters were calculated– Angular second moment (S_{ASM}), Inverse difference moment (S_{IDM}), Contrast (S_{CON}), correlation (S_{COR}), and Entropy (S_{ENT}). Compared to glioblastomas, metastases had higher S_{ENT}, S_{COR}, and S_{CON}, and lower S_{ASM} and S_{IDM} (61). All five textural parameters from T2-weighted imaging were significantly different between glioblastoma and metastasis. Inverse difference moment (S_{IDM}) on T2-weighted imaging was most useful for differentiating the two (sensitivity = 83.3%). On CET1 images, four textural parameters (S_{ASM}, S_{IDM}, S_{CON}, S_{ENT}) were significantly different, with Inverse difference moment (S_{IDM}) being most specific (specificity = 84%). Performance was better when multi-sequence textural parameters were combined, achieving an AUC of 0.908, with 86.7% sensitivity and 80.0% specificity (61).

Similar results were reported in another study using perfusion imaging by Mouthuy et al. (62). Other investigators explored tumor heterogeneity by means of both 2D and 3D texture analysis in search for structural differences between brain metastases originating from different systemic cancers (63). Ortiz-Ramon et al. used random forest machine-learning approach based on texture analysis in 38 patients, to classify the primary origins of three brain metastases– lung cancer, melanoma, and breast cancer (64). Forty-three rotation-invariant 3D and 2D texture features were examined. Overall, 3D texture features were more discriminative than 2D features. A random forest classifier, using four 3D texture features, was accurate in differentiating lung

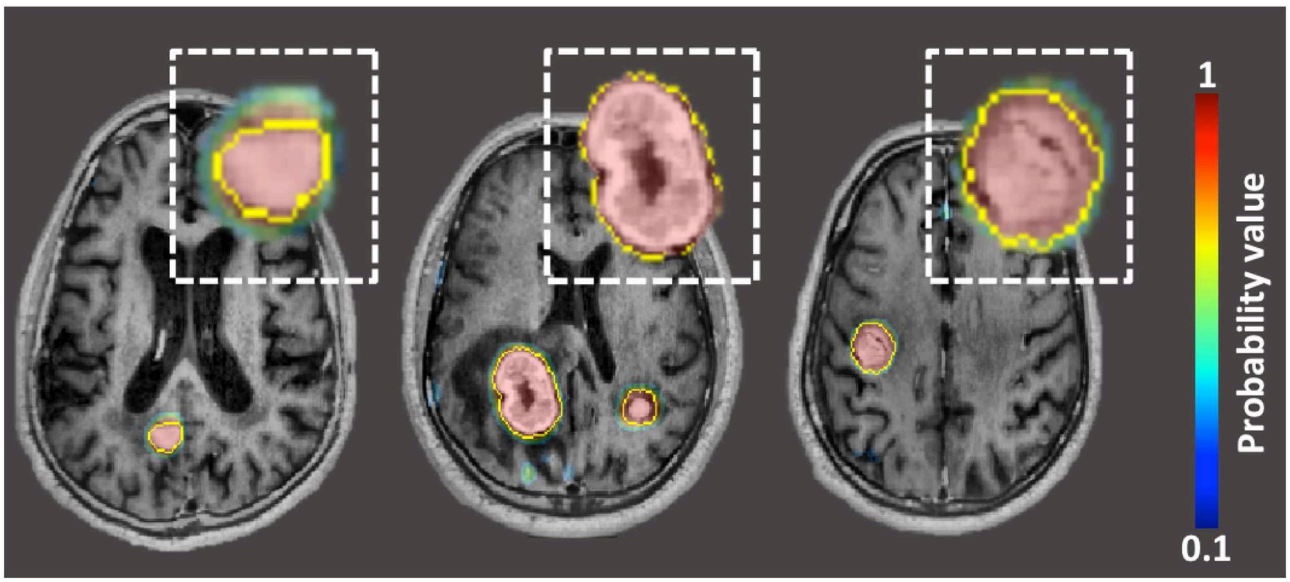

FIGURE 8 | Probability maps, generated by neural-network, overlaid on post-contrast BRAVO image in patient with three lung carcinoma metastases. The yellow outline represents "ground-truth" segmentation manually drawn by neuroradiologists.

cancer metastases from breast cancer metastases (AUC = 0.963 ± 0.054). Another random forest classifier, using eight 3D texture features, was very good in differentiating lung cancer metastases from melanoma metastases (AUC = 0.936 ± 0.070). However, none of their random forest classifiers were able to differentiate breast cancer metastases from melanoma metastases (AUC = 0.607 ± 0.180), presumably because of a limited small dataset. Nonetheless, texture analysis is a promising tool for classifying brain neoplasms.

Automatic Detection and Segmentation

Typical planning in stereotactic radiosurgery (SRS) requires accurate detection and meticulous segmentation of each target lesion. Both steps are time-consuming and subject to interobserver variation. Artificial intelligence is well-suited for tackling manually tedious and repetitive tasks that require high-precision, such as brain metastases detection and segmentation. Several deep learning (DL) algorithms have been developed to detect and segment primary brain metastases, by learning from voxel-wise labeled MRI data (65–67).

Grovik et al. designed a convolution neural network (CNN) for automatic detection and segmentation of brain metastases using multisequence (pre-contrast T1-weighted CUBE, post-contrast T1-weighted CUBE, post-contrast T1-weighted BRAVO, and 3D CUBE FLAIR) MRI data as input (68). Ground truth segmentations of the metastases were manually outlined on each slice depicting the lesion on post-contrast BRAVO images. The network's input was a slab of seven slices from each of the four sequences (pre-contrast T1-weighted CUBE, post-contrast T1-weighted CUBE, post-contrast T1-weighted BRAVO, and 3D CUBE FLAIR). The center slice of the slab was selected at the center of the metastasis. The CNN was based on the GoogLeNet architecture and was trained using TensorFlow. The output was a probability map (ranging between 0 and 1) of whether the voxel represented a metastasis (**Figure 8**). Voxel-wise detection accuracy was 0.98 +/– 0.04, corresponding to 94% sensitivity and 97% specificity. According to subgroup analysis and based on disease burden, the ability to detect metastatic voxels was better in patients with few (1–3) metastases than in those with more than four. Segmentation performance, as measured by the Dice coefficient, was slightly better for patients with 4–10 metastases. Using the optimal probability threshold, on a lesion-by-lesion basis, the sensitivity was 83 +/– 22%, with a false positive rate of 8.3 lesions per cases. False positive lesions were found primarily near vascular structures at the skull base such as the venous sinuses or over the cortex. Overall, the CNN performed best on patients with few metastases, both in terms of sensitivity and the number of FPs.

Other groups, using different variations of neural networks and imaging sequences as input, have reported comparable results (65–67). In essence, the CNNs have the potential to integrate detection, segmentation, and quantification of brain metastases using a streamlined process. The output of the CNN can also potentially be used as masks for radiotherapy planning.

Evaluate Treatment Effect

Larroza et al. used texture analysis and Support Vector Machine classification (a type of machine-learning classification technique) to differentiate between brain metastases and radiation necrosis on contrast-enhanced T1-weighted images (69). A total of 179 texture features were extracted from 115 lesions from 73 patients (60 untreated lesions, 23 SRS-treated lesions, and 32 radiation necrosis). A support vector machine was used to find a subset of features that attained best classification

performance. The highest classification accuracy was achieved by a machine trained with treated metastases, using a subset of 10 features (AUC = 0.94 ± 0.07). The second best performer was a machine trained with both treated and untreated metastases, using a subset of seven features and tested on treated metastases (AUC = 0.93 ± 0.02). Texture analysis on conventional MRI seems to be capable of differentiating between brain metastasis and radiation necrosis with high accuracy.

Clinical Implication

Studies using radiomics and machine learning in all fields of medicine are rapidly growing; however, validation with large multicenter and heterogeneous datasets is needed to confirm performance accuracy before deployment in the clinical neuro-oncology setting (**Table 1**).

CONCLUSION

Treatment of brain metastases has become increasingly individualized as surgical and radiosurgical techniques have evolved over the past several decades. Accurate diagnosis and assessment of brain metastases in patients with systemic cancers has important implications for patient prognosis and treatment strategy. Newer anatomic imaging techniques such as "black-blood" MR imaging accentuate detection of enhancing brain parenchymal metastases and has been reported to have more sensitivity for the detection of leptomeningeal carcinomatosis. Overlapping CUBE-MIP images make identifying brain metastases easier and quicker. Advanced MRI techniques that penetrate beyond macrostructures of brain metastases, such as MRS, MR perfusion, CEST, and qMT, provide quantitative parameters that are sensitive to underlying tissue microstructure and pathophysiology. These parameters may hold promise as imaging biomarkers for monitoring disease progression and predicting treatment outcome. However, it is important to note that some of the MRI techniques highlighted in this review are still largely research-based tools and have not been integrated into clinical practice. Systematic validation using standardized protocols in the clinical setting is needed before any potential efficacy or utility of these methods is realized.

Artificial intelligence can enhance assessment of brain metastases. Texture analysis computes a large amount of intrinsic features for quantitative comparisons. Various machine-learning algorithms can be applied in tandem to extract useful features for classification. Deep Learning, utilizing neural networks, can automate detection and segmentation with high accuracy and precision.

These important advancements are helpful for promoting individualized risk-stratification, tumor characterization, and treatment decisions. However, further investigations are needed to standardize these advanced techniques and measurements. Larger multicenter clinical trials are also imperative to fully evaluate the clinical utility of these various techniques and image data.

AUTHOR CONTRIBUTIONS

ET was the first author and was responsible for the design, draft, figures, and review of the article. KM was the second author and was responsible for the draft and review of the article. MI was the senior author and was responsible for the design and review of the article.

REFERENCES

1. Lam TC, Sahgal A, Chang EL, Lo SS. Stereotactic radiosurgery for multiple brain metastases. *Expert Rev Anticancer Ther.* (2014) 14:1153–72. doi: 10.1586/14737140.2014.940325
2. Soliman H, Das S, Larson DA, Sahgal A. Stereotactic radiosurgery (SRS) in the modern management of patients with brain metastases. *Oncotarget.* (2016) 7:12318–30. doi: 10.18632/oncotarget.7131
3. Tsao M, Xu W, Sahgal A. A meta-analysis evaluating stereotactic radiosurgery, whole-brain radiotherapy, or both for patients presenting with a limited number of brain metastases. *Cancer.* (2012) 118:2486–93. doi: 10.1002/cncr.26515
4. Sahgal A, Ruschin M, Ma L, Verbakel W, Larson D, Brown PD. Stereotactic radiosurgery alone for multiple brain metastases? A review of clinical and technical issues. *Neuro Oncol.* (2017) 19:ii2–15. doi: 10.1093/neuonc/nox001
5. Lin NU, Lee EQ, Aoyama H, Barani IJ, Barboriak DP, Baumert BG, et al. Response assessment in neuro-oncology, response assessment criteria for brain metastases: proposal from the RANO group. *Lancet Oncol.* (2015) 16:e270–8. doi: 10.1016/S1470-2045(15)70057-4
6. Schaefer PW, Budzik RF Jr, Gonzalez RG. Imaging of cerebral metastases. *Neurosurg Clin N Am.* (1996) 7:393–423. doi: 10.1016/S1042-3680(18)30369-3
7. Sze G, Milano E, Johnson C, Heier L. Detection of brain metastases: comparison of contrast-enhanced MR with unenhanced MR enhanced CT. *AJNR Am J Neuroradiol.* (1990) 11:785–91.
8. Mehrabian H, Detsky J, Soliman H, Sahgal A, Stanisz GJ. Advanced magnetic resonance imaging techniques in management of brain metastases. *Front Oncol.* (2019) 9:440. doi: 10.3389/fonc.2019.00440
9. Gillies RJ, Kinahan PE, Hricak H. Radiomics: images are more than pictures, they are data. *Radiology.* (2016) 278:563–77. doi: 10.1148/radiol.2015151169
10. Yip SS, Aerts HJ. Applications and limitations of radiomics. *Phys Med Biol.* (2016) 61:R150–66. doi: 10.1088/0031-9155/61/13/R150
11. Akkus Z, Galimzianova A, Hoogi A, Rubin DL, Erickson BJ. Deep learning for brain MRI segmentation: state of the art and future directions. *J Digit Imaging.* (2017) 30:449–59. doi: 10.1007/s10278-017-9983-4
12. Bae YJ, Choi BS, Lee KM, Yoon YH, Sunwoo L, Jung C, Kim JH. Efficacy of maximum intensity projection of contrast-enhanced 3d turbo-spin echo imaging with improved motion-sensitized driven-equilibrium preparation in the detection of brain metastases. *Korean J Radiol.* (2017) 18:699–709. doi: 10.3348/kjr.2017.18.4.699
13. Majigsuren M, Abe T, Kageji T, Matsuzaki K, Takeuchi M, Iwamoto S, et al. Comparison of brain tumor contrast-enhancement on T1-CUBE and 3D-SPGR images. *Magn Reson Med Sci.* (2016) 15:34–40. doi: 10.2463/mrms.2014-0129
14. Yoon BC, Saad AF, Rezaii P, Wintermark M, Zaharchuk G, Iv M. Evaluation of thick-slab overlapping MIP images of contrast-enhanced 3D T1-weighted cube for detection of intracranial metastases: a pilot study for comparison of lesion detection, interpretation time, sensitivity with non-overlapping CUBE MIP. CUBE, inversion-recovery-prepared fast-spoiled gradient recalled brain volume. *AJNR Am J Neuroradiol.* (2018) 39:1635–42. doi: 10.3174/ajnr.A5747
15. Valencia R, Denecke T, Lehmkuhl L, Fischbach F, Felix R, Knollmann F. Value of axial and coronal maximum intensity projection (MIP) images in the detection of pulmonary nodules by multislice spiral CT: comparison with axial 1-mm and 5-mm slices. *Eur Radiol.* (2006) 16:325–32. doi: 10.1007/s00330-005-2871-1

16. Oh J, Choi SH, Lee E, Shin DJ, Jo SW, Yoo RE, et al. Application of 3D fast spin-echo T1 black-blood imaging in the diagnosis and prognostic prediction of patients with leptomeningeal carcinomatosis. *AJNR Am J Neuroradiol.* (2018) 39:1453–59. doi: 10.3174/ajnr.A5721
17. Toft PB, Leth H, Lou HC, Pryds O, Henriksen O. Metabolite concentrations in the developing brain estimated with proton MR spectroscopy. *J Magn Reson Imaging.* (1994) 4:674–80. doi: 10.1002/jmri.1880040510
18. Mori N, Wildes F, Takagi T, Glunde K, Bhujwalla ZM. The tumor microenvironment modulates choline and lipid metabolism. *Front Oncol.* (2016) 6:262. doi: 10.3389/fonc.2016.00262
19. Burri R, Steffen C, Herschkowitz N. N-acetyl-L-aspartate is a major source of acetyl groups for lipid synthesis during rat brain development. *Dev Neurosci.* (1991) 13:403–11. doi: 10.1159/000112191
20. Magalhaes A, Godfrey W, Shen Y, Hu J, Smith W. Proton magnetic resonance spectroscopy of brain tumors correlated with pathology. *Acad Radiol.* (2005) 12:51–7. doi: 10.1016/j.acra.2004.10.057
21. Wehrl HF, Schwab J, Hasenbach K, Reischl G, Tabatabai G, Quintanilla-Martinez L, et al. Multimodal elucidation of choline metabolism in a murine glioma model using magnetic resonance spectroscopy and 11C-choline positron emission tomography. *Cancer Res.* (2013) 73:1470–80. doi: 10.1158/0008-5472.CAN-12-2532
22. Chuang MT, Liu YS, Tsai YS, Chen YC, Wang CK. Differentiating radiation-induced necrosis from recurrent brain tumor using mr perfusion and spectroscopy: a meta-analysis. *PLoS ONE.* (2016) 11:e0141438. doi: 10.1371/journal.pone.0141438
23. Bottomley PA. Spatial localization in NMR spectroscopy *in vivo*. *Ann N Y Acad Sci.* (1987) 508:333–48. doi: 10.1111/j.1749-6632.1987.tb32915.x
24. Frahm J, Merboldt DK, Hänicke W. Localized proton spectroscopy using stimulated echoes. *J Magn Reson.* (1989) 72:502–8. doi: 10.1016/0022-2364(87)90154-5
25. Cianfoni A, Law M, Re TJ, Dubowitz DJ, Rumboldt Z, Imbesi SG. Clinical pitfalls related to short and long echo times in cerebral MR spectroscopy. *J Neuroradiol.* (2011) 38:69–75. doi: 10.1016/j.neurad.2010.10.001
26. Oz G, Alger JR, Barker PB, Bartha R, Bizzi A, Boesch C, et al. Clinical proton MR spectroscopy in central nervous system disorders. *Radiology.* (2014) 270:658–79. doi: 10.1148/radiol.13130531
27. Ishimaru H, Morikawa M, Iwanaga S, Kaminogo M, Ochi M, Hayashi K. Differentiation between high-grade glioma and metastatic brain tumor using single-voxel proton MR spectroscopy. *Eur Radiol.* (2001) 11:1784–91. doi: 10.1007/s003300000814
28. Caivano R, Lotumolo A, Rabasco P, Zandolino A, D'Antuono F, Villonio A, et al. 3 Tesla magnetic resonance spectroscopy: cerebral gliomas vs. metastatic brain tumors. Our experience and review of the literature. *Int J Neurosci.* (2013) 123:537–43. doi: 10.3109/00207454.2013.774395
29. Sjobakk TE, Johansen R, Bathen TF, Sonnewald U, Kvistad KA, Lundgren S, et al. Metabolic profiling of human brain metastases using *in vivo* proton MR spectroscopy at 3T. *BMC Cancer.* (2007) 7:141. doi: 10.1186/1471-2407-7-141
30. Weybright P, Sundgren PC, Maly P, Hassan DG, Nan B, Rohrer S, et al. Differentiation between brain tumor recurrence and radiation injury using MR spectroscopy. *AJR Am J Roentgenol.* (2005) 185:1471–6. doi: 10.2214/AJR.04.0933
31. Schlemmer HP, Bachert P, Herfarth KK, Zuna I, Debus J, van Kaick G. Proton MR spectroscopic evaluation of suspicious brain lesions after stereotactic radiotherapy. *AJNR Am J Neuroradiol.* (2001) 22:1316–24.
32. Horska A, Barker PB. Imaging of brain tumors: MR spectroscopy and metabolic imaging. *Neuroimaging Clin N Am.* (2010) 20:293–310. doi: 10.1016/j.nic.2010.04.003
33. Wolff SD, Balaban RS. Magnetization transfer contrast (MTC) and tissue water proton relaxation *in vivo*. *Magn Reson Med.* (1989) 10:135–44. doi: 10.1002/mrm.1910100113
34. Henkelman RM, Stanisz GJ, Graham SJ. Magnetization transfer in MRI: a review. *NMR Biomed.* (2001) 14:57–64. doi: 10.1002/nbm.683
35. Garcia M, Gloor M, Bieri O, Radue EW, Lieb JM, Cordier D, et al. Imaging of primary brain tumors and metastases with fast quantitative 3-dimensional magnetization transfer. *J Neuroimaging.* (2015) 25:1007–14. doi: 10.1111/jon.12222
36. Bailey C, Giles A, Czarnota GJ, Stanisz GJ. Detection of apoptotic cell death *in vitro* in the presence of Gd-DTPA-BMA. *Magn Reson Med.* (2009) 62:46–55. doi: 10.1002/mrm.21972
37. Darzynkiewicz Z, Juan G, Li X, Gorczyca W, Murakami T, Traganos F. Cytometry in cell necrobiology: analysis of apoptosis and accidental cell death (necrosis). *Cytometry.* (1997) 27:1–203.
38. Bailey C, Moosvi F, Stanisz GJ. Mapping water exchange rates in rat tumor xenografts using the late-stage uptake following bolus injections of contrast agent. *Magn Reson Med.* (2014) 71:1874–87. doi: 10.1002/mrm.24847
39. Mehrabian H, Desmond KL, Chavez S, Bailey C, Rola R, Sahgal A, et al. Water exchange rate constant as a biomarker of treatment efficacy in patients with brain metastases undergoing stereotactic radiosurgery. *Int J Radiat Oncol Biol Phys.* (2017) 98:47–55. doi: 10.1016/j.ijrobp.2017.01.016
40. Wu B, Warnock G, Zaiss M, Lin C, Chen M, Zhou Z, et al. An overview of CEST MRI for non-MR physicists. *EJNMMI Phys.* (2016) 3:19. doi: 10.1186/s40658-016-0155-2
41. van Zijl PCM, Lam WW, Xu J, Knutsson L, Stanisz GJ. Magnetization transfer contrast and chemical exchange saturation transfer mrfeatures i, analysis of the field-dependent saturation spectrum. *Neuroimage.* (2018) 168:222–41. doi: 10.1016/j.neuroimage.2017.04.045
42. Zhou J, Wilson DA, Sun PZ, Klaus JA, van Zijl PC. Quantitative description of proton exchange processes between water and endogenous and exogenous agents for WEX, CEST, APT experiments. *Magn Reson Med.* (2004) 51:945–52. doi: 10.1002/mrm.20048
43. van Zijl PC, Yadav NN. Chemical exchange saturation transfer (CEST): what is in a name and what isn't? *Magn Reson Med.* (2011) 65:927–48. doi: 10.1002/mrm.22761
44. deBrosse C, Nanga RP, Bagga P, Nath K, Haris M, Marincola F, et al. Lactate chemical exchange saturation transfer (latest) imaging *in vivo* A biomarker for LDH activity. *Sci Rep.* (2016) 6:19517. doi: 10.1038/srep21813
45. Zhou J, Tryggestad E, Wen Z, Lal B, Zhou T, Grossman R, et al. Differentiation between glioma and radiation necrosis using molecular magnetic resonance imaging of endogenous proteins and peptides. *Nat Med.* (2011) 17:130–4. doi: 10.1038/nm.2268
46. Mehrabian H, Myrehaug S, Soliman H, Sahgal A, Stanisz GJ. Evaluation of glioblastoma response to therapy with chemical exchange saturation transfer. *Int J Radiat Oncol Biol Phys.* (2018) 101:713–23. doi: 10.1016/j.ijrobp.2018.03.057
47. Lundström P. Nuclear overhauser effect. In: Roberts GCK, editor. *Encyclopedia of Biophysics.* Berlin, Heidelberg: Springer Berlin Heidelberg (2013). p. 1753–9. doi: 10.1007/978-3-642-16712-6_308
48. Desmond KL, Mehrabian H, Chavez S, Sahgal A, Soliman H, Rola R,et al. Chemical exchange saturation transfer for predicting response to stereotactic radiosurgery in human brain metastasis. *Magn Reson Med.* (2017) 78:1110–20. doi: 10.1002/mrm.26470
49. Mehrabian H, Desmond KL, Soliman H, Sahgal A, Stanisz GJ. Differentiation between radiation necrosis and tumor progression using chemical exchange saturation transfer. *Clin Cancer Res.* (2017) 23:3667–75. doi: 10.1158/1078-0432.CCR-16-2265
50. Kogan F, Hariharan H, Reddy R. Chemical Exchange Saturation Transfer (CEST) imaging: description of technique and potential clinical applications. *Curr Radiol Rep.* (2013) 1:102–14. doi: 10.1007/s40134-013-0010-3
51. Server A, Orheim TE, Graff BA, Josefsen R, Kumar T, Nakstad PH. Diagnostic examination performance by using microvascular leakage, cerebral blood volume, blood flow derived from 3-T dynamic susceptibility-weighted contrast-enhanced perfusion MR imaging in the differentiation of glioblastoma multiforme and brain metastasis. *Neuroradiology.* (2011) 53:319–30. doi: 10.1007/s00234-010-0740-3
52. Blasel S, Jurcoane A, Franz K, Morawe G, Pellikan S, Hattingen E. Elevated peritumoural rCBV values as a mean to differentiate metastases from high-grade gliomas. *Acta Neurochir.* (2010) 152:1893–9. doi: 10.1007/s00701-010-0774-7
53. Bulakbasi N, Kocaoglu M, Farzaliyev A, Tayfun C, Ucoz T, Somuncu I. Assessment of diagnostic accuracy of perfusion MR imaging in primary and metastatic solitary malignant brain tumors. *AJNR Am J Neuroradiol.* (2005) 26:2187–99.
54. Floriano VH, Torres US, Spotti AR, Ferraz-Filho JR, Tognola WA. The role of dynamic susceptibility contrast-enhanced perfusion MR imaging in differentiating between infectious and neoplastic focal brain lesions:

results from a cohort of 100 consecutive patients. *PLoS ONE.* (2013) 8:e81509. doi: 10.1371/journal.pone.0081509
55. Sunwoo L, Yun TJ, You SH, Yoo RE, Kang KM, Choi SH, et al. Differentiation of glioblastoma from brain metastasis: qualitative and quantitative analysis using arterial spin labeling mr imaging. *PLoS ONE.* (2016) 11:e0166662. doi: 10.1371/journal.pone.0166662
56. Barajas RF, Chang JS, Sneed PK, Segal MR, McDermott MW, Cha S. Distinguishing recurrent intra-axial metastatic tumor from radiation necrosis following gamma knife radiosurgery using dynamic susceptibility-weighted contrast-enhanced perfusion MR imaging. *AJNR Am J Neuroradiol.* (2009) 30:367–72. doi: 10.3174/ajnr.A1362
57. Morabito R, Alafaci C, Pergolizzi S, Pontoriero A, Iati G, Bonanno L, et al. DCE and DSC perfusion MRI diagnostic accuracy in the follow-up of primary and metastatic intra-axial brain tumors treated by radiosurgery with cyberknife. *Radiat Oncol.* (2019) 14:65. doi: 10.1186/s13014-019-1271-7
58. Ng F, Kozarski R, Ganeshan B, Goh V. Assessment of tumor heterogeneity by CT texture analysis: can the largest cross-sectional area be used as an alternative to whole tumor analysis? *Eur J Radiol.* (2013) 82:342–8. doi: 10.1016/j.ejrad.2012.10.023
59. Yoon SH, Park CM, Park SJ, Yoon JH, Hahn S, Goo JM. Tumor heterogeneity in lung cancer: assessment with dynamic contrast-enhanced MR imaging. *Radiology.* (2016) 280:940–8. doi: 10.1148/radiol.2016151367
60. Kim JH, Ko ES, Lim Y, Lee KS, Han BK, Ko EY, et al. Breast cancer heterogeneity: MR imaging texture analysis and survival outcomes. *Radiology.* (2017) 282:665–75. doi: 10.1148/radiol.2016160261
61. Petrujkic K, Milosevic N, Rajkovic N, Stanisavljevic D, Gavrilovic S, Dzelebdzic D, et al. Computational quantitative MR image features–a potential useful tool in differentiating glioblastoma from solitary brain metastasis. *Eur J Radiol.* (2019) 119:108634. doi: 10.1016/j.ejrad.2019.08.003
62. Mouthuy N, Cosnard G, Abarca-Quinones J, Michoux N. Multiparametric magnetic resonance imaging to differentiate high-grade gliomas and brain metastases. *J Neuroradiol.* (2012) 39:301–7. doi: 10.1016/j.neurad.2011.11.002
63. Li Z, Mao Y, Li H, Yu G, Wan H, Li B, et al. Differentiating brain metastases from different pathological types of lung cancers using texture analysis of T1 postcontrast MR. *Magn Reson Med.* (2016) 76:1410–9. doi: 10.1002/mrm.26029
64. Ortiz-Ramon R, Larroza A, Ruiz-Espana S, Arana E, Moratal D. Classifying brain metastases by their primary site of origin using a radiomics approach based on texture analysis: a feasibility study. *Eur Radiol.* (2018) 28:4514–23. doi: 10.1007/s00330-018-5463-6
65. Charron O, Lallement A, Jarnet D, Noblet V, Clavier JB, Meyer P. Automatic detection and segmentation of brain metastases on multimodal MR images with a deep convolutional neural network. *Comput Biol Med.* (2018) 95:43–54. doi: 10.1016/j.compbiomed.2018.02.004
66. Liu Y, Stojadinovic S, Hrycushko B, Wardak Z, Lau S, Lu W, et al. A deep convolutional neural network-based automatic delineation strategy for multiple brain metastases stereotactic radiosurgery. *PLoS ONE.* (2017) 12:e0185844. doi: 10.1371/journal.pone.0185844
67. Liu Y, Stojadinovic S, Hrycushko B, Wardak Z, Lu W, Yan Y, et al. Automatic metastatic brain tumor segmentation for stereotactic radiosurgery applications. *Phys Med Biol.* (2016) 61:8440–61. doi: 10.1088/0031-9155/61/24/8440
68. Grovik E, Yi D, Iv M, Tong E, Rubin D, Zaharchuk G, et al. Deep learning enables automatic detection and segmentation of brain metastases on multisequence MRI. *J Magn Reson Imaging.* (2019) 51:175–82. doi: 10.1002/jmri.26766
69. Larroza A, Moratal D, Paredes-Sanchez A, Soria-Olivas E, Chust ML, Arribas LA, et al. Support vector machine classification of brain metastasis and radiation necrosis based on texture analysis in MRI. *J Magn Reson Imaging.* (2015) 42:1362–8. doi: 10.1002/jmri.24913

Conflict of Interest: The authors declare that the research was conducted in the absence of any commercial or financial relationships that could be construed as a potential conflict of interest.

frontiers in Neurology

ORIGINAL RESEARCH
published: 28 May 2020
doi: 10.3389/fneur.2020.00402

Computational Modeling of Interstitial Fluid Pressure and Velocity in Non-small Cell Lung Cancer Brain Metastases Treated With Stereotactic Radiosurgery

Nathaniel Swinburne[1], Eve LoCastro[2], Ramesh Paudyal[2], Jung Hun Oh[2], Neil K. Taunk[3], Akash Shah[1], Kathryn Beal[4], Behroze Vachha[1], Robert J. Young[1], Andrei I. Holodny[1], Amita Shukla-Dave[2†] and Vaios Hatzoglou[1†]*

[1] Department of Radiology, Memorial Sloan Kettering Cancer Center, New York, NY, United States, [2] Department of Medical Physics, Memorial Sloan Kettering Cancer Center, New York, NY, United States, [3] Department of Radiation Oncology, Hospital of the University of Pennsylvania, Philadelphia, PA, United States, [4] Department of Radiation Oncology, Memorial Sloan Kettering Cancer Center, New York, NY, United States

OPEN ACCESS

Edited by:
Tarik F. Massoud,
Stanford University, United States

Reviewed by:
Bo Gao,
Affiliated Hospital of Guizhou Medical University, China
Ali Alaraj,
University of Illinois at Chicago, United States

***Correspondence:**
Vaios Hatzoglou
hatzoglv@mskcc.org

[†]These authors have contributed equally to this work and share senior authorship

Specialty section:
This article was submitted to Applied Neuroimaging, a section of the journal Frontiers in Neurology

Received: 29 January 2020
Accepted: 17 April 2020
Published: 28 May 2020

Citation:
Swinburne N, LoCastro E, Paudyal R, Oh JH, Taunk NK, Shah A, Beal K, Vachha B, Young RJ, Holodny AI, Shukla-Dave A and Hatzoglou V (2020) Computational Modeling of Interstitial Fluid Pressure and Velocity in Non-small Cell Lung Cancer Brain Metastases Treated With Stereotactic Radiosurgery. Front. Neurol. 11:402. doi: 10.3389/fneur.2020.00402

Background: Early imaging-based treatment response assessment of brain metastases following stereotactic radiosurgery (SRS) remains challenging. The aim of this study is to determine whether early (within 12 weeks) intratumoral changes in interstitial fluid pressure (IFP) and velocity (IFV) estimated from computational fluid modeling (CFM) using dynamic contrast-enhanced (DCE) MRI can predict long-term outcomes of lung cancer brain metastases (LCBMs) treated with SRS.

Methods: Pre- and post-treatment T_1-weighted DCE-MRI data were obtained in 41 patients treated with SRS for intact LCBMs. The imaging response was assessed using RANO-BM criteria. For each lesion, extravasation of contrast agent measured from Extended Tofts pharmacokinetic Model (volume transfer constant, K^{trans}) was incorporated into a computational fluid model to estimate tumor IFP and IFV. Estimates of mean IFP and IFV and heterogeneity (skewness and kurtosis) were calculated for each lesion from pre- and post-SRS imaging. The Wilcoxon rank-sum test was utilized to assess for significant differences in IFP, IFV, and IFP/IFV change (Δ) between response groups.

Results: Fifty-three lesions from 41 patients were included. Median follow-up time after SRS was 11 months. The objective response (OR) rate (partial or complete response) was 79%, with 21% demonstrating stable disease (SD) or progressive disease (PD). There were significant response group differences for multiple posttreatment and Δ CFM parameters: post-SRS IFP skewness (mean −0.405 vs. −0.691, $p = 0.022$), IFP kurtosis (mean 2.88 vs. 3.51, $p = 0.024$), and IFV mean (5.75e-09 vs. 4.19e-09 m/s, $p = 0.027$); and Δ IFP kurtosis (mean −2.26 vs. −0.0156, $p = 0.017$) and IFV mean (1.91e-09 vs. 2.38e-10 m/s, $p = 0.013$). Posttreatment and Δ thresholds predicted non-OR with high sensitivity (sens): post-SRS IFP skewness (−0.432, sens 84%), kurtosis (2.89, sens 84%), and IFV mean (4.93e-09 m/s, sens 79%); and Δ IFP kurtosis (−0.469, sens 74%) and IFV mean (9.90e-10 m/s, sens 74%).

Conclusions: Objective response was associated with lower post-treatment tumor heterogeneity, as represented by reductions in IFP skewness and kurtosis. These results suggest that early post-treatment assessment of IFP and IFV can be used to predict long-term response of lung cancer brain metastases to SRS, allowing a timelier treatment modification.

Keywords: Stereotactic radiosurgery (SRS), brain metastases from lung cancer, perfusion MRI, computational fluid modeling, interstitial fluid pressure, treatment response

INTRODUCTION

Brain metastases (BMs) represent the largest category of intracranial malignant tumors with an annual incidence 3–10 times greater than primary brain malignancies (1, 2). Occurring in up to 40% of patients with systemic cancer (3), BMs represent a major source of morbidity and mortality in this population. In particular, the most frequent source are primary lung malignancies, which comprise up to 36–64% of brain metastases (4).

Radiation therapy (RT) is the standard of care for patients in whom complete surgical resection is not possible due to surgically inaccessible lesion locations, disqualifying comorbidities, or uncontrolled systemic disease. Stereotactic radiosurgery (SRS), which employs single high-dose targeted treatment using stereotactic image guidance, has shown comparable efficacy to whole brain radiation therapy (WBRT) in controlling oligometastatic intracranial disease, achieving >80–90% local control while decreasing the risks of toxicities, such as neurocognitive decline (5–8).

Identification of eventual non-response in the early post-SRS time period is difficult. Surveillance MRI, which represents the standard for assessing brain metastasis treatment response, may be confounded in the early post-treatment setting by the tendency of up to one-third of BMs to transiently increase in size following SRS (9). The ability to predict SRS failure has major clinical importance, as it would potentially allow non-responsive tumors to undergo treatment intensification or prompt modifications to systemic therapy regimens.

The limitations of traditional size-based treatment response assessment following locoregional therapies, such as SRS, have driven the development of advanced MR imaging techniques, such as dynamic contrast-enhanced (DCE) perfusion MRI, that go beyond anatomic visualization to characterize tumor physiology. The extended Tofts pharmacokinetic model (ETM) is one such paradigm that quantifies surrogate measures of vascular permeability (i.e., volume transfer constant, K^{trans} [min^{-1}]). Interstitial pressures within the tumor affect the extravasation of medications into the interstitium and influence the response and outcome to radiotherapy (10–12).

The disorganized and tortuous architecture of blood vessels results in altered fluid dynamics across the vasculature and in the interstitium. The resulting elevated interstitial fluid pressure (IFP) effectively reduces the hydrostatic pressure differential that normally exists between vasculature and extracellular extravascular spaces, which can adversely impact the successful delivery of anti-tumor therapy (13–15). IFP returns to normal levels in the healthy tissues surrounding the tumor. The precipitous drop in IFP at the tumor periphery results in a zone where the interstitial fluid velocity (IFV) is increased and directed outward, causing rapid exudate flux of interstitial fluid from regions of high to low pressure (16), further diminishing the effectiveness of drug delivery and therapy.

To support this model, the direct invasive measurement of intralesional IFP in cervical cancer using modified wick-in-needle (WIN) probes has shown mid–radiation therapy IFP to be significantly different between patients with complete and partial responses at 1 month post-treatment (17). Fyles et al. reported high IFP measurement to be associated with a negative prognosis in cervical cancer (18). However, the invasive measurement of IFP and interstitial fluid velocity (IFV), which can be derived from the IFP gradient (19), is not feasible in many settings, especially where a tumor cannot be easily or safely accessed. Additionally, single-point WIN probing of tumor does not provide insight into the internal spatial variation of IFP. Therefore, non-invasive computational fluid modeling (CFM) to provide estimates of tumor IFP using the volume transfer constant (K^{trans}) obtained from ETM (20, 21) is a desirable alternative. K^{trans} is incorporated into an observable CFM equation to modulate the net pressure developed in tissue, including trans-capillary hydrostatic pressure, for the delivery of fluid, which is taken into consideration by conventional DCE-derived pharmacokinetic models.

Previously, we investigated the ability of ETM parameters to predict long-term local tumor control in the early post-SRS setting for patients with lung cancer brain metastases. We showed that K^{trans} standard deviation (SD) was highly sensitive (89%) for predicting disease progression vs. no progressive disease (22). This result was not surprising, as K^{trans} SD is considered a marker of tumor vascular heterogeneity (22, 23), and tumors are known to recruit disorganized and heterogeneous microvasculature.

In the present study, we have aimed to investigate whether non-invasive IFP and IFV estimates of global tissue physiology can predict the long-term response of lung cancer brain metastases treated within 12 weeks of SRS. The patient cohort is from our previous work that utilized more conventional DCE-derived parameters. These novel imaging biomarkers may further our ability to optimize patient management by demonstrating changes in tumor physiology.

MATERIALS AND METHODS

Patients and Treatment

This retrospective investigation was performed at a tertiary cancer center following institutional review board approval and in accordance with the Health Insurance Portability and Accountability Act. Patients treated between 2012 and 2015 that met the following inclusion criteria were included in this analysis:

- Histopathologic diagnosis of non-small cell lung cancer (NSCLC).
- Treatment of one or more intact (non-resected) brain metastases with SRS.
- No history of WBRT prior to SRS.
- DCE perfusion MRI scans, including coverage of the treated lesion(s) obtained both pre-treatment and within 12 weeks following SRS treatment.

Patient demographic and treatment data collected included patient age, histologic tumor subtype, three-dimensional lesion size, lesion location, and SRS treatment dose(s). All treatments employed single-fraction SRS. Our study population consisted of 41 patients who were previously included in a study analyzing DCE-MRI parameters (22).

MR Perfusion Imaging Acquisition

Patients were scanned on 1.5T or 3T scanners (Signa Excite, HDx and Discovery 750, GE Healthcare) using an 8-channel head coil. Standard T1-weighted, T2-weighted, diffusion-weighted, fluid-attenuated inversion recovery, susceptibility-weighted, and contrast T1-weighted images were acquired in multiple planes. T1-weighted DCE data were acquired using an axial 3D spoiled gradient-echo sequence (repetition time [TR], 4–5 ms; echo time [TE], 1–2 ms; section thickness, 5 mm; flip angle [FA], 25 degrees; field of view, 24 cm; matrix, 256 × 128). Ten phases were acquired pre-injection followed by another 30 phases during the dynamic injection of intravenous contrast. This was followed by a 40-mL saline flush. The time between phases (temporal resolution) was 5–6 s. Matching contrast T1-weighted (TR/TE, 600/8 ms; thickness, 5 mm; matrix, 256 × 224) spin-echo images were obtained. Ten to twelve slices were obtained to cover the entire volume of each lesion. Gadopentetate dimeglumine (Magnevist; Bayer HealthCare Pharmaceuticals, Berlin, Germany) was power-injected via an intravenous catheter (18–21 gauge) at doses standardized by patient body weight (0.2 mL/kg body weight, maximum 20 mL) at 2–3 mL/s. High resolution 3D T1-weighted contrast-enhanced images in the axial plane with a slice thickness of 1 mm and no gaps between slices were routinely acquired for SRS planning and follow-up after therapy.

DCE MRI Pharmacokinetic Modeling

The two-compartment extended Tofts model (ETM) accounts for vascular space (v_p) and extravascular extracellular space [EES], (v_e). The ETM expression for modeling $C_t(t)$ is given (24):

$$C_t(t) = K^{trans} \int_0^t e^{-k_{ep}(t-\tau)} C_p(\tau) d\tau + v_p C_p(t) \quad (1)$$

where, K^{trans} (min^{-1}) is the volume transfer constant of CA, $C_p(t)$ is the delivery time-course of plasma CA concentration (or arterial input function, AIF), and v_e and v_p are the volume fractions of the EES and blood plasma, respectively. CA transfer from EES back into the vascular space is defined as $k_{ep} = K^{trans}/v_e$. A detailed calculation of tissue contrast concentration C_t from DCE signal is given elsewhere (25).

AIF for each patient was selected from a sagittal sinus voxel in the imaging time course (25, 26). Brain metastasis volumes-of-interest (VOIs) were manually segmented by an attending neuroradiologist on late phases of the T_1w DCE images using ITK-SNAP (27).

In the absence of multi-flip angle pre-contrast T_1 images, T_{10} values were set to either 0.8 or 1s (dependent on magnetic field strength) for each voxel in determination of ΔR_1. Tissue concentration time course, $C_t(t)$ [Equation. (1)], was calculated using non-linear fitting to minimize the sum of squared errors (SSE) between model fit and data. The fitting procedure estimates the values of K^{trans}, v_e and v_p, for each voxel. Parameter estimation bound limits were set: K^{trans} ε [0, 5] (min^{-1}), v_e, and v_p ε [0, 1]. All DCE data analysis was performed using in-house MRI-QAMPER software (Quantitative Analysis Multi-Parametric Evaluation Routines) written in MATLAB (The MathWorks, Inc., Natick, MA).

Interstitial Fluid Pressure Simulation

CFM Mathematical Model

The fluid mechanics of a system are given by the Navier-Stokes hydrodynamic mass-balance equation (28). The extracellular matrix is modeled as a porous medium. We assumed the case of an incompressible fluid, ignoring friction within fluid, and exchange of momentum between fluid and solid phases. Fluid movement through EES is approximated with low-Reynolds Number flow (29) and modeled under assumption of steady-state velocity. We applied the well-known Darcy's Law to describe bulk fluid movement, expressing the product of gradient in IFP (∇p_i) and the hydraulic conductivity of the porous medium, K_H as the interstitial fluid velocity, **u**:

$$\mathbf{u} = -K_H \nabla p_i \quad (2)$$

A dynamic system can then be modeled as follows: fluid enters EES via the vascular compartment. In the human brain, there is no established lymphatic system of clearance, and we take the lymphatic drainage function to be zero in both normal and tumor tissue.

The full derivation for the continuity equation [Equation. 3] is presented in the **Appendix**. The final form is given in terms of the dependent variable interstitial pressure, p_i:

$$-K_H \nabla^2 p_i = \frac{K^{trans}}{\langle K^{trans} \rangle} \left[L_p \frac{S}{V} \left(p_V - p_i - \sigma_T (\pi_V - \pi_i) \right) \right] - \frac{L_{pL} S_L}{V} \left(p_i - p_L \right) \quad (3)$$

where $\langle K^{trans} \rangle$ represents mean K^{trans} values within the tumor; this term is used to account for heterogeneous fluid leakiness in

the tumor (30), L_P is the hydraulic conductivity of the capillary wall (or vessel permeability), S/V is microvascular surface area per unit volume, p_V is the blood pressure in the microvessel, and p_i is interstitial fluid pressure; π_V is osmotic pressure in microvasculature, π_i is osmotic pressure in interstitial space, and σ_T is the osmotic reflection coefficient. The lymphatic clearance term, $L_{pL}S_L/V$, is assumed to be zero in the brain. Estimates for physical parameters were selected in agreement with previous literature on modeling IFP in brain tumors (21, 31–34).

Computational Fluid Modeling

The continuity partial differential equation (PDE) was implemented using the COMSOL CFM simulation PDE module. Solving [Equation. 7] provides the basis for estimation of $p-_i$ and 3D parametric maps of IFP and IFV.

The 3D physiological mesh model was generated from each patient's T_1w DCE tumor images. ROIs for tumor in the simulation domain were resliced to be 1 mm^3-isotropic in MATLAB using the NIfTI Toolbox (35) and converted to stereolithography (STL) file format. STL files were imported into the simulation software and interpreted as boundary meshes for the model.

ETM-estimated K^{trans} maps were co-registered to match the simulation mesh space. K^{trans} maps were incorporated in COMSOL as a scalar field over the simulation domain and numerical values for physical constants in normal and tumor tissue were defined in the appropriate regions of the 3D STL domain mesh, as listed in **Table 1**. A stationary solution of Equation 13 was computed on the 3D extended domain ROI, and pressure at the simulation boundary was set to zero to agree with pressure conditions in normal brain tissue.

Simulation was conducted using the general coefficient form PDE module in a commercial multiphysics software package (COMSOL Inc., Stockholm, Sweden) using the finite element method to solve PDE computations.

Data Analysis

We analyzed IFP and IFV parameters as follows. For each metric, we computed the mean and descriptive statistics such as standard deviation (SD), kurtosis, and skewness, leading to a set of eight features. We generated three sets of these eight features: pre-RT, post-RT, and the change of values (denoted as Δ) between pre-RT and post-RT. For each imaging feature, an average value was computed across multiple slices on each lesion. Univariate analysis was performed using the Wilcoxon rank-sum test to find the degree of differences in these features between patients with an objective response (either partial or complete response, OR) vs. non-OR (either stable disease or progressive disease). A receiver operating characteristic (ROC) curve analysis was performed to find the best cutoffs on these features using Youden's index.

For clinical data, local control was assessed by the modified Response Assessment in Neuro-Oncology Brain Metastases (RANO-BM) criteria using conventional MRI (40), with additional information from surgical resection if performed after SRS. The modification we made to standard RANO-BM criteria was to lower the minimum size limit of measurable disease to 5 mm. We chose to lower the limit because we routinely treat BMs measuring between 5 and 10 mm with SRS at our institution. Local relapse-free survival was calculated from day of treatment to most recent imaging. Failure was determined by progressive disease defined by RANO-BM or surgical resection indicating viable tumor. All statistical analysis was performed using R language version 3.5.2 and MATLAB version R2018b.

RESULTS

Forty-one patients with 53 BMs were included in the analysis (**Table 2**). Thirty-two patients had a single brain metastasis, seven patients had two metastases, and two patients had three or more metastases. Median SRS treatment dose was 21 Gy (range, 18–22 Gy).

TABLE 2 | Patient characteristics.

Characteristic		*N* (%)
Number	Patients	41
	Lesions	53
Sex	Male	21 (51.2)
	Female	20 (48.8)
Age (y)	Median (range)	52 (36–71)
Histologic subtype (by patient)	Adenocarcinoma	35 (85.4)
	Squamous cell	3 (7.3)
	Large cell	1 (2.4)
	Poorly differentiated/not otherwise specified	2 (4.9)
Number of lesions	Single	29 (70.7)
	Multiple	12 (29.3)
Location	Supratentorial	46 (86.8)
	Infratentorial	7 (13.2)
Radiation dose	Median (range)	21 Gy (18–22)

TABLE 1 | List of assigned physical parameters in the CFM simulation.

Parameter	Description	Units	Normal tissue	Tumor tissue	References
K_H	Interstitial hydraulic conductivity	$\frac{m^2}{Pa \cdot s}$	5.65×10^{-15}	4.9×10^{-13}	(21, 36, 37)
L_p	Vascular hydraulic conductivity	$\frac{m^2}{Pa \cdot s}$	8×10^{-14}	6.4×10^{-13}	(21, 38, 39)
S/V	Vessel exchange area	m^{-1}	10,000	20,000	(21, 31)
P_{eff}	Effective pressure	Pa	400	1,550	(21, 31)

No patients received concurrent systemic therapy with SRS. Per our institution's general practice, most patients ($n = 39$) had a washout period before and following SRS: at least 2 weeks for systemic therapies and at least 1 week for targeted systemic therapies.

Post-treatment imaging was obtained 7–8 weeks ($n = 19$), 9–10 weeks ($n = 16$), or 11–12 weeks ($n = 18$) following SRS. Median duration of post-treatment follow-up was 11 months (range, 3.7–8.3 months), including 73% of patients who were followed until death. Following SRS, one patient subsequently underwent resection for a growing mass and was found to have viable tumor. Eight patients were treated with WBRT after SRS for control of non-index metastases. Local control at 1-year post-treatment was 85% as determined by subsequent histopathologic sampling, where available, or RANO-BM imaging criteria. Rates of complete response, partial response, stable disease, and progressive disease were 9, 49, 21, and 21%, respectively (**Table 3**).

Univariate analysis using Wilcoxon rank-sum test (**Table 4**) showed a significant difference between lesions showing OR vs. non-OR: post-SRS IFP skewness (mean −0.405 vs. −0.691, $p = 0.022$), IFP kurtosis (mean 2.88 vs. 3.51, $p = 0.024$), and IFV mean (5.75e-09 vs. 4.19e-09 m/s, $p = 0.027$); and Δ IFP kurtosis (mean −2.26 vs. −0.0156, $p = 0.017$) and IFV mean (1.91e-09 vs. 2.38e-10 m/s, $p = 0.013$). Using the Youden index, balanced thresholds for differentiating non-OR vs. OR were determined: post-SRS IFP skewness −0.432 (sensitivity 84%, specificity 59%), IFP kurtosis 2.89 (sensitivity 84%, specificity 63%), and IFV mean 4.93e-09 m/s (sensitivity 79%, specificity 67%); and Δ IFP kurtosis −0.469 (sensitivity 74%, specificity 59%) and IFV mean 9.90e-10 m/s (sensitivity 74%, specificity 74%). SRS dose was not significantly correlated with RANO-BM treatment response.

Figure 1A shows representative pre-SRS and post-SRS anatomic MR images and corresponding lesion K^{trans}, IFP, and IFV color maps. **Figure 1B** exhibits representative histograms showing the distribution of intratumoral voxel values for IFP in two patients who experienced OR vs. non-OR. The left-shift in the IFP values (kPa) of the histogram for the patient who experienced OR shows a decrease in pressure after treatment. In contrast, the histogram of a patient who experienced non-OR shows a subtle upward shift in mean IFP values and has many voxels with the same IFP value, resulting in a skew distribution. Receiver operating characteristic areas-under-curve for post-SRS IFP skewness (0.70), IFP kurtosis (0.70), and IFV mean (0.69); and Δ IFP kurtosis (0.71) and IFV mean (0.72) are shown in **Figures 2**, **3**.

TABLE 3 | Summary of RANO-BM response categories.

	RANO-BM category	Number of lesions
OR	CR	5 (9%)
	PR	26 (49%)
Non-OR	SD	11 (21%)
	PD	11 (21%)

OR, objective response; CR, complete response; PR, partial response; SD, stable disease; PD, progression of disease.

DISCUSSION

We investigated whether non-invasive estimates of intratumoral IFP and IFV in the early post-treatment setting using ETM-derived K^{trans} can predict the long-term response of lung cancer brain metastases to SRS. IFP and IFV parameters estimated from CFM were able to accurately predict long-term response using both isolated post-treatment values (IFP kurtosis, IFP skewness, and IFV mean) and changes between post- and pre-treatment values (Δ IFP kurtosis and Δ IFV mean). Our results support the use of these biomarkers as early post-SRS predictors of long-term treatment response in LCBMs. These parameters may enable the earlier identification of LCBM non-responders, allowing more timely treatment intensification or modifications to systemic therapies.

A major cause of elevated IFP within tumors is aberrant microvasculature resulting in altered fluid dynamics (41). Radiation therapy causes early and sustained damage to vasculature (42–44), which tends to lower intratumoral microvascular heterogeneity (45). In our cohort, IFP kurtosis and skewness, measures of tumoral IFP heterogeneity, showed

TABLE 4 | Univariate analysis using the Wilcoxon rank-sum test.

	Parameter (Units)	Non-OR mean	OR mean	*P*
Pre-SRS	IFP mean (kPa)	1.44	1.44	0.784
	IFP SD (kPa)	0.0139	0.0257	0.752
	IFP skewness	−0.698	−6.33	0.430
	IFP kurtosis	3.53	4.93	0.644
	IFV mean (m/s)	3.95e-09	3.80e-09	0.774
	IFV SD (m/s)	2.56e-09	2.44e-09	0.518
	IFV skewness	1.79	1.72	0.926
	IFV kurtosis	9.39	8.95	0.782
Post-SRS	IFP mean (kPa)	1.40	1.42	0.705
	IFP SD (kPa)	0.0145	0.0178	0.186
	IFP skewness	−0.691	−0.405	**0.0216**
	IFP kurtosis	3.51	2.88	**0.0243**
	IFV mean (m/s)	4.19e-09	5.75e-09	**0.0272**
	IFV SD (m/s)	2.61e-09	3.10e-09	0.265
	IFV skewness	1.61	1.28	0.135
	IFV kurtosis	8.24	6.47	0.228
Change	IFP mean (kPa)	−0.0475	−0.0154	0.428
	IFP SD (kPa)	5.91e-04	−9.55e-03	0.441
	IFP skewness	0.00614	0.357	0.255
	IFP kurtosis	−0.0156	−2.26	**0.0170**
	IFV mean (m/s)	2.38e-10	1.91e-09	**0.0132**
	IFV SD (m/s)	5.33e-11	5.80e-10	0.177
	IFV skewness	−0.179	−0.577	0.141
	IFV kurtosis	−1.16	−3.12	0.188

OR, objective response; IFP, interstitial fluid pressure; IFV, interstitial fluid velocity; SD, standard deviation. Bolded values represent statistically significant P-values ($P < 0.05$).

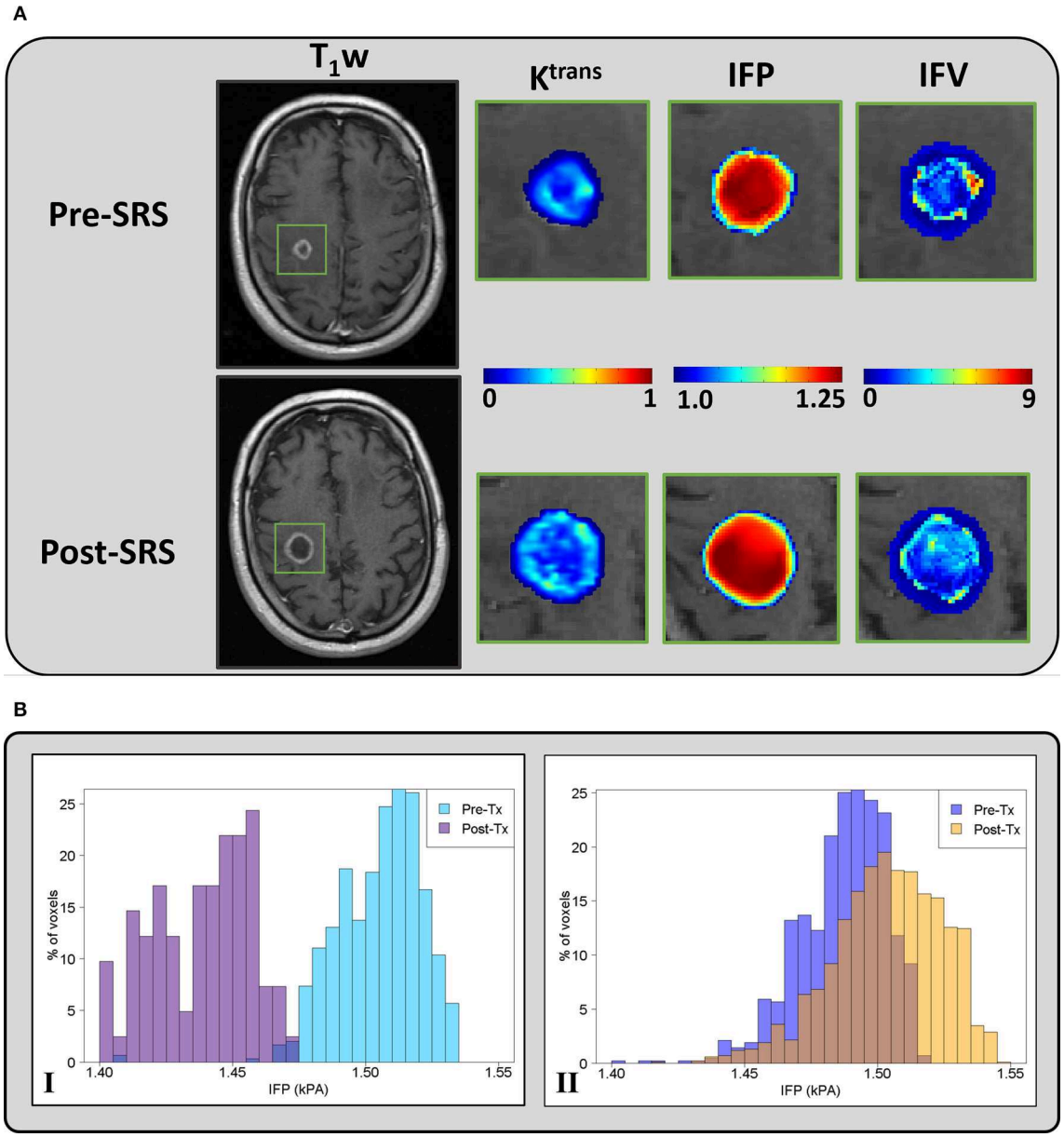

FIGURE 1 | (A) - Representative pre-SRS and post-SRS T1-weighted post-contrast MR images of a patient (59 years, male) with brain metastases who experienced progressive disease (PD). The green rectangle delineates the ROI at the metastatic lesion. K^{trans} (min^{-1}), IFP (kPa), and IFV (10^{-9} m/s) maps are zoomed at the location of the ROI. **(B)** - Histograms of percentage (%) voxel-wise IFP values at pre- and post-SRS treatment from representative patients who experienced (I) OR (male, 73 years old) and (II) non-OR (male, 47 years old).

early decreases in patients who ultimately showed objective response to SRS. This is intuitive, since post-treatment necrosis would be expected to smooth tumoral IFP distribution, resulting in decreased heterogeneity. Furthermore, Smith et al. showed that a necrotic tumor core, which lacks functioning vasculature necessary for fluid resorption, results in decreased pressure decay within the core and thus promotes increased IFV (31). This may provide a framework to explain why IFV mean was both significantly higher following SRS and showed greater relative increases from baseline in patients with objective response. Conversely, the correlation between poor outcomes and persistent intratumoral hypertension following treatment may be related to previous observations that high IFP in extracranial tumors decreases the uptake of chemotherapy drugs (41, 46) and promotes the outward flow of tumor-promoting growth factors and chemoreceptor ligands (47, 48).

To the best of our knowledge, ours is the first study to assess the predictive capabilities of non-invasively estimated IFP and IFV parameters for brain metastases that have been treated with SRS. A prior investigation successfully used these

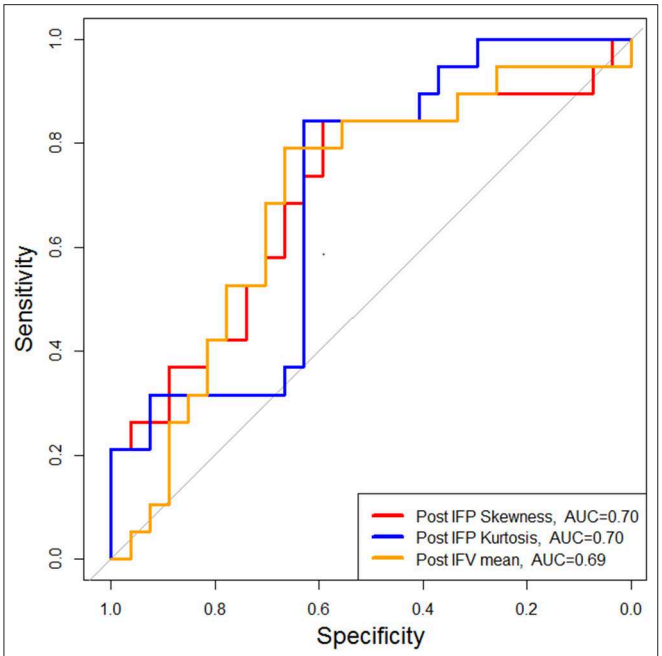

FIGURE 2 | Patients with OR showed significantly lower mean IFP skewness and kurtosis and higher mean IFV within 12 weeks post-SRS compared with patients with non-OR (either SD or PD). OR, objective response; SD, stable disease; PD, progressive disease.

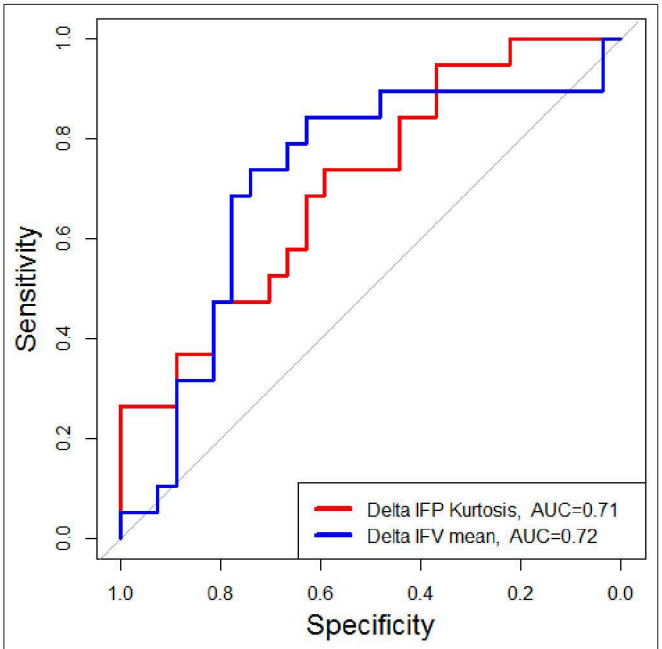

FIGURE 3 | Patients with OR showed significantly greater pre-SRS to post-SRS (Δ) declines in mean IFP kurtosis and greater increases in mean IFV within 12 weeks post-SRS compared with patients with non-OR (either SD or PD). OR, objective response; SD, stable disease; PD, progressive disease.

parameters to predict outcomes in cervical cancer (49). Utilizing histogram analysis, we showed a difference in the distribution of IFP in patients who experienced OR vs. non-OR. Similar to prior studies in cervical cancer (17, 50), IFP may be a useful prognostic indicator for brain metastases. Further investigation is needed to determine whether the evaluation of metastasis microenvironments from CFM estimated IFP and IFV can be utilized to personalize therapy regimens and improve outcomes. This may be especially relevant in the context of targeted chemotherapeutic agents and immunotherapy since elevated intratumoral IFP can prevent adequate penetration of intravenous drugs.

Boucher et al. (51) reported direct WIN measurements of IFP in rodent models, and from 11 human primary brain tumors during intracranial brain surgery. The rodent brain tumor mean IFP in $n = 4$ small F98 gliomas ($V_{mean} = 10 \pm 2.5$ mm^3) was 1.2 + 0.33 kPa. In 10 of the 11 human cases, IFP ranged from 0.066 to 0.4 kPa; in one astrocytoma, IFP was found to be 1.2 kPa. The estimates of IFP in our CFM are consistent with the measured results in the small-scale rodent tumors. Similar results were found in measurements of IFP in preclinical study by Navalitloha et al. (52) on rat gliomas.

A strength of our study is the inclusion of only NSCLC brain metastases undergoing single modality locoregional therapy with SRS. This allows for the relative control of potential confounders, including heterogeneous tumor histologies and variable baseline treatment effects from non-ablative modalities like WBRT. Additionally, the majority of our patients were followed until death, providing a clearer understanding of individual lesion outcomes.

As a retrospective investigation limited to BMs of a single, albeit common, histopathology, our results cannot be generalized to the treatment of BMs with SRS more broadly. With respect to our fluid model, the parameter values for hydraulic conductivity, vessel permeability, effective pressure, and microvascular surface area need to be verified experimentally to increase the simulation accuracy. Furthermore, the lack of confirmatory direct lung cancer brain metastasis pressure measurements within our cohort, for example, via the WIN approach, precludes the comparison of our derived IFP and IFV estimations against a gold standard.

In conclusion, this study shows that IFP and IFV parameters in lung cancer brain metastases derived from DCE-MRI within 12 weeks of SRS can predict long-term local tumor control. These results suggest that IFP and IFV represent promising imaging biomarkers that can non-invasively characterize global tissue physiology in lung cancer brain metastases. Further investigation is needed to validate these results for other brain metastasis histologies and to assess the use of these non-invasive biomarkers to guide personalized treatment regimens that target the tumor microenvironment.

DATA AVAILABILITY STATEMENT

The datasets generated for this study will not be made publicly available The source data contain inherent protected health information. Requests to access the data are directable to the corresponding author.

ETHICS STATEMENT

The studies involving human participants were reviewed and approved by Memorial Sloan Kettering Cancer Center Institutional Review Board. Written informed consent for participation was not required for this study in accordance with the national legislation and the institutional requirements.

AUTHOR CONTRIBUTIONS

VH, AS-D, and EL conceived the idea. NS, VH, EL, RP, and AS-D collected and analyzed data and wrote the manuscript. All authors discussed results and made substantive changes to the final manuscript.

FUNDING

This study was supported by National Institutes of Health/National Cancer Institute (Cancer Center Support Grant P30 CA008748).

SUPPLEMENTARY MATERIAL

The Supplementary Material for this article can be found online at: https://www.frontiersin.org/articles/10.3389/fneur.2020.00402/full#supplementary-material

REFERENCES

1. Davis FG, Dolecek TA, McCarthy BJ, Villano JL. Toward determining the lifetime occurrence of metastatic brain tumors estimated from 2007 United States cancer incidence data. *Neuro-Oncol.* (2012) 14:1171–77. doi: 10.1093/neuonc/nos152
2. Ostrom QT, Gittleman H, Farah P, Ondracek A, Chen Y, Wolinsky Y, et al. CBTRUS statistical report: primary brain and central nervous system tumors diagnosed in the United States in 2006-2010. *Neuro-Oncol.* (2013) 15:ii1–56. doi: 10.1093/neuonc/not151
3. Gavrilovic IT, Posner JB. Brain metastases: epidemiology and pathophysiology. *J Neurooncol.* (2005) 75:5–14. doi: 10.1007/s11060-004-8093-6
4. Schiff D, Arrillaga I, Wen PY (editors). *Cancer Neurology in Clinical Practice*. Cham: Springer International Publishing (2018). p. 3–10. doi: 10.1007/978-3-319-57901-6
5. Aoyama H, Shirato H, Tago M, Nakagawa K, Toyoda T, Hatano K, et al. Stereotactic radiosurgery plus whole-brain radiation therapy vs stereotactic radiosurgery alone for treatment of brain metastases: a randomized controlled trial. *JAMA.* (2006) 295:2483–91. doi: 10.1001/jama.295.21.2483
6. Sahgal A, Aoyama H, Kocher M, Neupane B, Collette S, Tago M, et al. Phase 3 trials of stereotactic radiosurgery with or without whole-brain radiation therapy for 1 to 4 brain metastases: individual patient data meta-analysis. *Int J Radiat Oncol Biol Phys.* (2015) 91:710–7. doi: 10.1016/j.ijrobp.2014.10.024
7. Brown PD, Jaeckle K, Ballman KV, Farace E, Cerhan JH, Anderson SK, et al. Effect of radiosurgery alone vs radiosurgery with whole brain radiation therapy on cognitive function in patients with 1 to 3 brain metastases. *JAMA.* (2016) 316:401–9. doi: 10.1001/jama.2016.9839
8. Lippitz B, Lindquist C, Paddick I, Peterson D, O'Neill K, Beaney R. Stereotactic radiosurgery in the treatment of brain metastases: the current evidence. *Cancer Treat Rev.* (2014) 40:48–59. doi: 10.1016/j.ctrv.2013.05.002
9. Patel TR, McHugh BJ, Bi WL, Minja FJ, Knisely JPS, Chiang VL. A comprehensive review of MR imaging changes following radiosurgery to 500 brain metastases. *Am J Neuroradiol.* (2011) 32:1885–92. doi: 10.3174/ajnr.A2668
10. Tofts PS, Kermode AG. Measurement of the blood-brain barrier permeability and leakage space using dynamic MR imaging. 1. fundamental concepts. *Magn Reson Med.* (1991) 17:357–67. doi: 10.1002/mrm.1910170208
11. Zahra MA, Hollingsworth KG, Sala E, Lomas DJ, Tan LT. Dynamic contrast-enhanced MRI as a predictor of tumour response to radiotherapy. *Lancet Oncol.* (2007) 8:63–74. doi: 10.1016/S1470-2045(06)71012-9
12. Baronzio G, Parmar G, Baronzio M. Overview of methods for overcoming hindrance to drug delivery to tumors, with special attention to tumor interstitial fluid. *Front Oncol.* (2015) 5:165. doi: 10.3389/fonc.2015.00165
13. Jain RK. Transport of molecules in the tumor interstitium: a Review. *Cancer Res.* (1987) 47:3039–51.
14. Boucher Y, Leunig M, Jain RK. Tumor angiogenesis and interstitial hypertension. *Cancer Res.* (1996) 56:4264–6.
15. Jain RK, Martin JD, Stylianopoulos T. The role of mechanical forces in tumor growth and therapy. *Annu Rev Biomed Eng.* (2014) 16:321–46. doi: 10.1146/annurev-bioeng-071813-105259
16. Ewing JR, Nagaraja TN, Aryal MP, Keenan KA, Elmghirbi R, Bagher-Ebadian H, et al. Peritumoral tissue compression is predictive of exudate flux in a rat model of cerebral tumor: an MRI study in an embedded tumor. *NMR Biomed.* (2015) 28:1557–69. doi: 10.1002/nbm.3418
17. Yeo S-G, Kim J-S, Cho M-J, Kim K-H, Kim J-S. Interstitial fluid pressure as a prognostic factor in cervical cancer following radiation therapy. *Clin Cancer Res.* (2009) 15:6201–7. doi: 10.1158/1078-0432.CCR-09-0560
18. Fyles A, Milosevic M, Pintilie M, Syed A, Levin W, Manchul L, et al. Long-term performance of interstial fluid pressure and hypoxia as prognostic factors in cervix cancer. *Radiother Oncol.* (2006) 80:132–7. doi: 10.1016/j.radonc.2006.07.014
19. Soltani M, Chen P. Numerical modeling of fluid flow in solid tumors. *PLoS ONE.* (2011) 6:e20344. doi: 10.1371/journal.pone.0020344
20. Magdoom KN, Pishko GL, Rice L, Pampo C, Siemann DW, Sarntinoranont M. MRI-based computational model of heterogeneous tracer transport following local infusion into a mouse hind limb tumor. *PLoS ONE.* (2014) 9:e89594. doi: 10.1371/journal.pone.0089594
21. Bhandari A, Bansal A, Singh A, Sinha N. Perfusion kinetics in human brain tumor with DCE-MRI derived model and CFD analysis. *J Biomech.* (2017) 59:80–9. doi: 10.1016/j.jbiomech.2017.05.017
22. Taunk NK, Oh JH, Shukla-Dave A, Beal K, Vachha B, Holodny A, et al. Early posttreatment assessment of MRI perfusion biomarkers can predict long-term response of lung cancer brain metastases to stereotactic radiosurgery. *Neuro-Oncol.* (2018) 20:567–75. doi: 10.1093/neuonc/nox159
23. Jackson A, O'Connor JPB, Parker GJM, Jayson GC. Imaging tumor vascular heterogeneity and angiogenesis using dynamic contrast-enhanced magnetic resonance imaging. *Clin Cancer Res.* (2007) 13:3449–59. doi: 10.1158/1078-0432.CCR-07-0238
24. Tofts PS, Brix G, Buckley DL, Evelhoch JL, Henderson E, Knopp MV, et al. Estimating kinetic parameters from dynamic contrast-enhanced T(1)-weighted MRI of a diffusable tracer: standardized quantities and symbols. *J Magn Reson Imaging.* (1999) 10:223–32. doi: 10.1002/(SICI)1522-2586(199909)10:3<223::AID-JMRI2>3.0.CO;2-S
25. Bagher-Ebadian H, Jain R, Nejad-Davarani SP, Mikkelsen T, Lu M, Jiang Q, et al. Model selection for DCE-T1 studies in glioblastoma. *Magn Reson Med.* (2012) 68:241–51. doi: 10.1002/mrm.23211
26. Cramer SP, Larsson HB. Accurate determination of blood-brain barrier permeability using dynamic contrast-enhanced T1-weighted MRI: a simulation and *in vivo* study on healthy subjects and multiple sclerosis patients. *J Cereb Blood Flow Metab.* (2014) 34:1655–65. doi: 10.1038/jcbfm.2014.126

27. Yushkevich PA, Piven J, Hazlett HC, Smith RG, Ho S, Gee JC, et al. User-guided 3D active contour segmentation of anatomical structures: significantly improved efficiency and reliability. *NeuroImage.* (2006) 31:1116–28. doi: 10.1016/j.neuroimage.2006.01.015
28. Dullien FAL. *Porous Media: Fluid Transport and Pore Structure /F. A. L. Dullien*. New York, NY: Academic Press (1979). doi: 10.1016/B978-0-12-223650-1.50008-5
29. Yao W, Li Y, Ding G. Interstitial fluid flow: the mechanical environment of cells and foundation of meridians. *Evid Based Complement Altern Med.* (2012) 2012:853516. doi: 10.1155/2012/853516
30. Pishko GL, Astary GW, Mareci TH, Sarntinoranont M. Sensitivity analysis of an image-based solid tumor computational model with heterogeneous vasculature and porosity. *Ann Biomed Eng.* (2011) 39:2360–73. doi: 10.1007/s10439-011-0349-7
31. Smith JH, Humphrey JAC. Interstitial transport and transvascular fluid exchange during infusion into brain and tumor tissue. *Microvasc Res.* (2007) 73:58–73. doi: 10.1016/j.mvr.2006.07.001
32. Bhandari A, Bansal A, Singh A, Sinha N. Transport of liposome encapsulated drugs in voxelized computational model of human brain tumors. *IEEE Trans NanoBiosci.* (2017) 16:634–44. doi: 10.1109/TNB.2017.2737038
33. Bhandari A, Bansal A, Singh A, Gupta RK, Sinha N. Comparison of transport of chemotherapeutic drugs in voxelized heterogeneous model of human brain tumor. *Microvasc Res.* (2019) 124:76–90. doi: 10.1016/j.mvr.2019.03.003
34. Bhandari A, Bansal A, Jain R, Singh A, Sinha N. Effect of tumor volume on drug delivery in heterogeneous vasculature of human brain tumors. *J Eng Sci Med Diagn Ther.* (2019) 2:021004. doi: 10.1115/1.4042195
35. Tools for NIfTI and ANALYZE image - File Exchange - MATLAB Central. Available online at: https://www.mathworks.com/matlabcentral/fileexchange/8797 (accessed November 22, 2019).
36. Swabb EA, Wei J, Gullino PM. Diffusion and convection in normal and neoplastic tissues. *Cancer Res.* (1974) 34:2814–22.
37. Netti PA, Berk DA, Swartz MA, Grodzinsky AJ, Jain RK. Role of extracellular matrix assembly in interstitial transport in solid tumors. *Cancer Res.* (2000) 60:2497–2503.
38. Paulson OB, Hertz MM, Bolwig TG, Lassen NA. Filtration and diffusion of water across the blood-brain barrier in man. *Microvasc Res.* (1977) 13:113–23. doi: 10.1016/0026-2862(77)90120-0
39. Arifin DY, Lee KYT, Wang C-H. Chemotherapeutic drug transport to brain tumor. *J Controlled Release.* (2009) 137:203–10. doi: 10.1016/j.jconrel.2009.04.013
40. Lin NU, Lee EQ, Aoyama H, Barani IJ, Barboriak DP, Baumert BG, et al. Response assessment criteria for brain metastases: proposal from the RANO group. *Lancet Oncol.* (2015) 16:e270–8. doi: 10.1016/S1470-2045(15)70057-4
41. Heldin C-H, Rubin K, Pietras K, Östman A. High interstitial fluid pressure — an obstacle in cancer therapy. *Nat Rev Cancer.* (2004) 4:806–13. doi: 10.1038/nrc1456
42. O'Connor MM, Mayberg MR. Effects of radiation on cerebral vasculature: a review. *Neurosurgery.* (2000) 46:138–51. doi: 10.1093/neurosurgery/46.1.138
43. Song CW, Kim M-S, Cho LC, Dusenbery K, Sperduto PW. Radiobiological basis of SBRT and SRS. *Int J Clin Oncol.* (2014) 19:570–8. doi: 10.1007/s10147-014-0717-z
44. Lucas J, Mack WJ. Effects of ionizing radiation on cerebral vasculature. *World Neurosurg.* (2014) 81:490–1. doi: 10.1016/j.wneu.2014.01.006
45. de Lussanet QG, Backes WH, Griffioen AW, Padhani AR, Baeten CI, van Baardwijk A, et al. Dynamic contrast-enhanced magnetic resonance imaging of radiation therapy-induced microcirculation changes in rectal cancer. *Int J Radiat Oncol.* (2005) 63:1309–15. doi: 10.1016/j.ijrobp.2005.04.052
46. Salnikov AV, Iversen VV, Koisti M, Sundberg C, Johansson L, Stuhr LB, et al. Lowering of tumor interstitial fluid pressure specifically augments efficacy of chemotherapy. *FASEB J.* (2003) 17:1756–8. doi: 10.1096/fj.02-1201fje
47. Shields JD, Fleury ME, Yong C, Tomei AA, Randolph GJ, Swartz MA. Autologous chemotaxis as a mechanism of tumor cell homing to lymphatics via interstitial flow and autocrine CCR7 signaling. *Cancer Cell.* (2007) 11:526–38. doi: 10.1016/j.ccr.2007.04.020
48. Mumprecht V, Detmar M. Lymphangiogenesis and cancer metastasis. *J Cell Mol Med.* (2009) 13:1405–16. doi: 10.1111/j.1582-4934.2009.00834.x
49. Simonsen TG, Lund KV, Hompland T, Kristensen GB, Rofstad EK. DCE-MRI-derived measures of tumor hypoxia and interstitial fluid pressure predict outcomes in cervical carcinoma. *Int J Radiat Oncol Biol Phys.* (2018) 102:1193–201. doi: 10.1016/j.ijrobp.2018.04.035
50. Haider MA, Sitartchouk I, Roberts TPL, Fyles A, Hashmi AT, Milosevic M. Correlations between dynamic contrast-enhanced magnetic resonance imaging-derived measures of tumor microvasculature and interstitial fluid pressure in patients with cervical cancer. *J Magn Reson Imaging JMRI.* (2007) 25:153–9. doi: 10.1002/jmri.20795
51. Boucher Y, Salehi H, Witwer B, Harsh GR, Jain RK. Interstitial fluid pressure in intracranial tumours in patients and in rodents. *Br J Cancer.* (1997) 75:829–36. doi: 10.1038/bjc.1997.148
52. Navalitloha Y, Schwartz ES, Groothuis EN, Allen CV, Levy RM, Groothuis DR. Therapeutic implications of tumor interstitial fluid pressure in subcutaneous RG-2 tumors. *Neuro-Oncol.* (2006) 8:227–33. doi: 10.1215/15228517-2006-007

Conflict of Interest: The authors declare that the research was conducted in the absence of any commercial or financial relationships that could be construed as a potential conflict of interest.

The handling editor is currently organizing a Research Topic with one of the authors BV.

frontiers in Neurology

ORIGINAL RESEARCH
published: 29 May 2020
doi: 10.3389/fneur.2020.00444

Biomarkers of Seizure Activity in Patients With Intracranial Metastases and Gliomas: A Wide Range Study of Correlated Regions of Interest

Piyush Kalakoti[1†], *Alicia Edwards*[1†], *Christopher Ferrier*[1], *Kanika Sharma*[2], *Trong Huynh*[3,4], *Christina Ledbetter*[1], *Eduardo Gonzalez-Toledo*[5], *Anil Nanda*[3,4] *and Hai Sun*[3,4*]

[1] Department of Neurosurgery, Louisiana State University Health Science Center, Shreveport, LA, United States, [2] Department of Neurology, University of Iowa Hospitals and Clinics, Iowa City, IA, United States, [3] Department of Neurosurgery, Robert Wood Johnson Medical School, New Brunswick, NJ, United States, [4] Department of Neurosurgery, Rutgers University, Newark, NJ, United States, [5] Neuroradiology, Department of Radiology, Louisiana State University Health Science Center, Shreveport, LA, United States

OPEN ACCESS

Edited by:
Behroze Adi Vachha, Cornell University, United States

Reviewed by:
Prachi Dubey, Houston Methodist Hospital, United States
Maria Borja Angulo, New York University, United States

***Correspondence:**
Hai Sun
hs925@rwjms.rutgers.edu

[†]*These authors have contributed equally to this work and are co-primary authors*

Specialty section:
This article was submitted to Applied Neuroimaging, a section of the journal Frontiers in Neurology

Received: *30 November 2019*
Accepted: *27 April 2020*
Published: *29 May 2020*

Citation:
Kalakoti P, Edwards A, Ferrier C, Sharma K, Huynh T, Ledbetter C, Gonzalez-Toledo E, Nanda A and Sun H (2020) Biomarkers of Seizure Activity in Patients With Intracranial Metastases and Gliomas: A Wide Range Study of Correlated Regions of Interest. Front. Neurol. 11:444. doi: 10.3389/fneur.2020.00444

Introduction: Studies quantifying cortical metrics in brain tumor patients who present with seizures are limited. The current investigation assesses morphometric/volumetric differences across a wide range of anatomical regions, including temporal and extra-temporal, in patients with gliomas and intracranial metastases (IMs) presenting with seizures that could serve as a biomarker in the identification of seizure expression and serve as a neuronal target for mitigation.

Methods: In a retrospective design, the MR sequences of ninety-two tumor patients [55% gliomas; 45% IM] and 34 controls were subjected to sophisticated morphometric and volumetric assessments using BrainSuite and MATLAB modules. We examined 103 regions of interests (ROIs) across eight distinct cortical categories of interests (COI) [gray matter, white matter; total volume, CSF; cortical areas: inner, mid, pial; cortical thickness]. The primary endpoint was quantifying and identifying ROIs with significant differences in z-scores based upon the presence of seizures. Feature selection employing neighborhood component analysis (NCA) determined the ROI within each COI having the highest significance/weight in the differentiation of seizure vs. non-seizure patients harboring brain tumor.

Results: Overall, the mean age of the cohort was 58.0 ± 12.8 years, and 45% were women. The prevalence of seizures in tumor patients was 28%. Forty-two ROIs across the eight pre-defined COIs had significant differences in z-scores between tumor patients presenting with and without seizures. The NCA feature selection noted the volume of pars-orbitalis and right middle temporal gyrus to have the highest weight in differentiating tumor patients based on seizures for three distinct COIs [GM, total volume, and CSF volume] and white matter, respectively. Left-sided transverse temporal gyrus, left precuneus, left transverse temporal, and left supramarginal gyrus were associated with having the highest weight in the differentiation of seizure vs. non-seizure in tumor patients for morphometrics relating to cortical areas in the pial, inner and mid regions and cortical thickness, respectively.

Conclusion: Our study elucidates potential biomarkers for seizure targeting in patients with gliomas and IMs based upon morphometric and volumetric assessments. Amongst the widespread brain regions examined in our cohort, pars orbitalis, supramarginal and temporal gyrus (middle, transverse), and the pre-cuneus contribute a maximal potential for differentiation of seizure patients from non-seizure.

Keywords: gliomas, intracranial metastases, seizures, pars orbitalis, supramarginal gyrus, pre-cuneus, brainsuite, temporal plus epilepsy

INTRODUCTION

Seizures are a common neurological symptom that can be provoked by toxins, head trauma, electrolyte imbalances, brain hemorrhage, and/or tumors (1). Among brain tumor patients, seizures are often the only presenting clinical symptom, and its incidence varies across different tumor histopathology (2–5). The presence of seizures in tumor patients impacts the quality of life and is associated with worse outcomes following surgical resection (4, 5). Low-grade gliomas (LGGs) tend to have a higher estimated incidence of seizures, ranging from 60–75% (6–11), compared to high-grade gliomas (HGGs) [25–60%] (12–14) or intracranial metastases (IM) [20–35%] (15, 16). The variation in seizure incidence is primarily linked to tumor size, location (8), and possibly to the tumoral and peritumoral microstructure. A comprehensive understanding of these microarchitectural variations can potentially aid our ability to predict seizures and subsequently serve for implementing treatments to prevent seizures in tumor patients before its onset. In the contemporary era of cost-containment ushered by the introduction of bundled payments, such efforts could improve the value in neurosurgical healthcare delivery in tumor patients with seizures.

Studies have characterized the anatomical locations of HGGs to areas with a high ratio of gray and white matter volume, while the LGGs tend to have a preferential bias toward the secondary functional regions of the brain (17, 18). Our recent investigation characterized the peritumoral differences in fractional anisotropy (FA) and mean diffusivity (MD) values estimated from diffusion tensor imaging (DTI) in patients with HGGs and IM (19, 20). The higher FA and lower MD of HGGs in the peritumoral region were linked to a greater extent of infiltration of glioma upon the surrounding parenchyma (19). Traditional understanding of epileptogenic focus is related to structures in the temporal lobe. However, contemporary scientific advancements have established the specific anatomical basis of temporal-plus (TP+) epilepsy (21, 22). This new understanding has led researchers to scan outside the temporal lobe, toward neighboring regions for epileptogenic focus. Occipital, insular, or orbitofrontal areas are often considered for resection in addition to sections of the temporal lobe. Yet, limited literature exists on the etiological basis of extra-temporal involvement for seizure development (22). Although patients with brain tumors have not been directly linked to TP+ epilepsy, many tumor patients experience at least one seizure or develop multiple seizures even when the lesion is outside the temporal lobe. Therefore, investigating regions outside of the temporal lobe in brain tumor patients with seizures can be essential for future research.

Previously, our research team identified voxel-based metrics associated with a regional and global disruption in resting-state functional connectivity that may elucidate the epileptogenic focus and guide resection of cerebral cavernous malformations in patients with focal epilepsy (23). Despite single-institutional studies and observational cohorts utilizing administrative databases having identified the impact of seizures on short and long-term outcomes in patients undergoing intracranial tumor resection (4, 5, 24–27), meaningful clinical literature quantifying morphometric or volumetric analysis in tumor patients with seizures are limited. In the current investigation, we performed volumetric assessments to examine a wide range of anatomical regions [>100 regions of interests (ROIs)] across eight distinct cortical areas in patients with gliomas and IMs to elucidate the differences in cortical volume on the epileptogenicity of brain tumor. The primary objectives of the study are: (1) To quantify the normalized cortical volume estimates across predefined ROIs in tumor patients with and without seizures with respect to normal controls; and (2) To identify pertinent regions that express a significant contribution to differentiate seizure and non-seizure patients based upon volumetric distinctions. To achieve these objectives, we subjected the MR sequence images for tumor patients and controls to a battery of sophisticated brain-segmentation processing tools employing relevant BrainSuite and MATLAB modules. The study hypothesizes that the identification of significant volumetric differences across distinct ROIs in tumor patients could serve as possible biomarkers for predicting patients with the seizure disorder resulted from having brain tumors.

MATERIALS AND METHODS

Study Protocol and Patient Population

In this retrospective design, adult patients (>18 years of age) with IM and gliomas that underwent surgical resection at the University Health/Louisiana State University Health Sciences Center (LSUHSC), Shreveport between January 2011 and June 2016 were identified. The preoperative surgical decision-making was not influenced by morphometric/volumetric imaging analysis, as performed in the current investigation, using a combination of BrainSuite and MATLAB custom designed modules; rather was guided by the consensus of a multi-disciplinary team of physicians in the institutional Tumor Board

tailored upon patient's clinical characteristics and traditional neuroimaging modalities/scans. The study was approved by The LSUHSC Institutional Review before study initiation. Inclusion criteria applied for selection of patients that were surgically managed for their tumor pathology included: (1) confirmatory histopathological diagnoses, (2) complete MR sequences [1.5 Tesla; GE Medical Systems, Milwaukee, WI, USA] without evidence of movement artifacts. Image acquisition included T1-weighted Magnetization Prepared Rapid Acquisition with Gradient Echo (MPRAGE) sequences, diffusion tensor imaging (DTI), and 3-dimensional sagittal FLAIR sequences. Patients with a previous history of radiotherapy, chemotherapy, or neurosurgical intervention and those with multiple intracranial tumors (>2) were excluded. A review of medical records was conducted on eligible patients for the extraction of pertinent data on demographics (age, gender, race) and clinical characteristics. The latter included the presence of seizure at presentation, tumor-specific data including laterality, location, histology, and primaries for patients with IM. In addition to medical chart review, electroencephalogram (EEG) findings were used for seizure confirmation.

Controls

Thirty-four healthy controls matched for age [range: 19–79 years] and gender [15 women] were included and served as a comparison group. All control subjects were free of any neurological diseases and had no prior history of any neurological diseases. Image acquisition and processing for the control subjects was performed in a manner like that of the eligible patients.

Morphometric/Volumetric Analysis

For image processing, T1-MPRAGE sequences of all eligible patients (n = 102) and controls (n = 34) were subjected to the inbuilt automated cortical surface extraction processing in the BrainSuite software (version 18a; http://brainsuite.org/). This allows for stripping the skull from the MR sequences and initiates brain segmentation (**Figure 1**). Anatomical information from both the cortical surface models in the predefined atlas (BrainSuiteAtlas1) of BrainSuite and the volumetric estimates computed from stripped T1-MPRAGE images are utilized for co-registration between the patient imaging and the atlas (28–31). To compute relevant morphometric/volumetric data, partial tissue fraction volume was utilized along with co-registration, which yielded a single output file for each patient/control. The parcellation yielded volumes (or morphometrics) across 103 regions of interest (ROIs) using the Collin27 atlas within eight different cortical surface categories of interest (COIs): mean cortical thickness (mm), gray matter (GM) volume (mm^3), cerebrospinal fluid volume (CSF) (mm^3), white matter (WM) volume (mm^3), total volume (mm^3), mid cortical area (mm^2), inner cortical area (mm^2), and pial cortical area (mm^2). (**Figure 1**) The total volume was the summation of WM and GM volume. Out of the 102 patients deemed eligible using the study

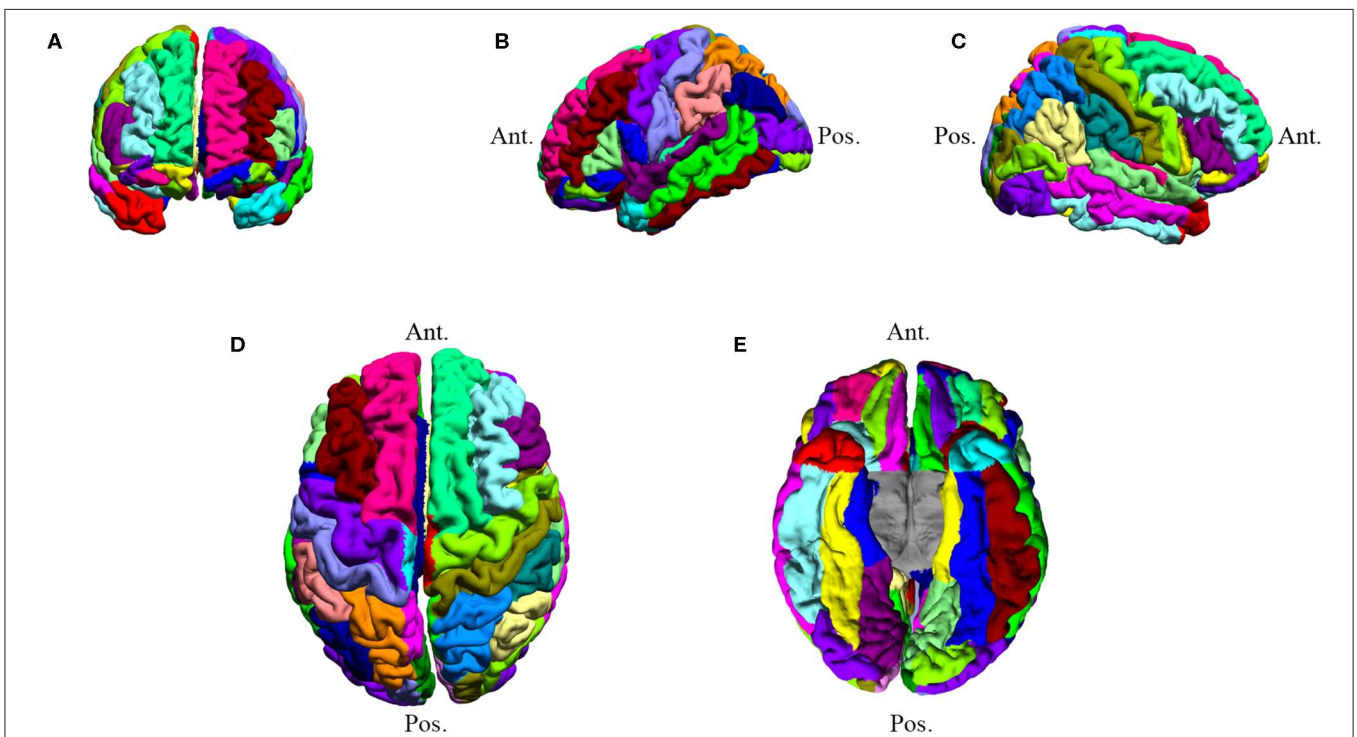

FIGURE 1 | Subject DT007: BrainSuite processed MR image. The image underwent brain segmentation to determine COI values. DT007 was a 57-year-old male with a high-grade glioblastoma and presented with seizures. Colors are used to distinguish ROIs. **(A)** Anterior coronal view **(B)** Left hemisphere view **(C)** Right hemisphere view **(D)** Superior axial view **(E)** Inferior axial view.

criteria, ten were excluded with mutual consensus following a two-step independent review [A.E. and C.F.] owing to processing and segmentation errors encountered in BrainSuite.

Volume Normalization and Z-Score Derivation

To minimize bias arising from variation in volume across patients due to differences in brain sizes/volume, whole-brain normalization was performed as a function of percent-volume for every ROI across the four cortical COIs [GM, CSF, WM, and total volume]. Quantified estimates of raw volume for ROIs were normalized in relation to individual patient/controls overall ROI. This was performed by computing percent-volume of each ROI by dividing individual ROI raw volume with summation of volumes across all ROIs for respective COIs factored by two (to accommodate both hemispheres). Following normalization, z-scores were computed for individual ROIs across all COIs. For COI's signifying area morphometrics [cortical areas: inner, mid, pial] or thickness [cortex], z-scores were computed from raw values for cortical areas and thickness, respectively. Prior to estimating z-scores, tumor patients were grouped based upon the presence of seizures, within each COI, in alignment with the study objective. Z-scores derivation for each ROI was performed using the following formula:

$$\mathrm{z-score} = \frac{Patient\ ROI\ Value\ -\ Control\ ROI\ \mu}{Control\ ROI\ \sigma}$$

To exclude aberrant z-score values affecting estimates, the mean and standard deviation (SD) for each ROI within the seizure and non-seizure COI's were calculated. ROI values beyond three SD (top/bottom 0.135%) on either end of the z-score spectrum were excluded.

Primary Outcome Measures

The primary outcome measures were: (1) mean z-score estimates for brain tumor patients with and without seizures and (2) ROI's associated with significant differences across z-score estimates between the two patient groups.

Statistical Analysis

Categorical variables were expressed as a function of frequency and proportion while values of quantitative variables were reported as mean ± standard deviation (SD). The differences in categorical variables across tumor patients [gliomas, IM] and control were analyzed using Pearson's χ^2 test of proportion or Fisher Exact test (32) as appropriate. The norm for analyzing differences in quantitative values across groups was based upon testing for Gaussian distribution. For analyzing differences across 2 groups [gliomas vs. IM; gliomas vs. controls; IM vs. controls], an independent-sample t-test or non-parametric Mann-Whitney *U*-test were utilized. For assessing differences in mean estimates across 3 groups [gliomas, IM and controls], one-way analysis of variance (ANOVA) or the non-parametric Kruskal-Wallis tests was employed.

The ROI's within individual COI's demonstrating significant one-tailed differences in z-scores were subjected to further analysis for feature weight determination within the seizure and non-seizure group using the MATLAB's Statistics and Machine Learning Toolbox. Serial iterations using the neighborhood component analysis (NCA) feature selection was utilized to determine the factor having the most weight in the classification algorithm's attempt to label each tumor patient based on the presence of seizure (vs. non-seizure) based on z-scores from the relevant COIs. To perform this, the cohort of tumor patients was split into a testing set ($n = 66$) and a training set ($n = 26$). Patients in both sets were assigned class labels as either seizure or non-seizure. More specifically, feature weights were computed using the MATLAB function for predictors and responses in which the predictors were the ROIs for every patient in each COI that was significant, and the response was the subject's seizure classification (coding for non-seizure = 0; seizure as 1). NCA was used to determine the patterns that classified each patient as either seizure or non-seizure and determined the component (ROI) that had the most weight on this classification by taking out each component iteratively until a maximum prediction accuracy was achieved (**Tables S3**, **S4**).

All statistical analyses were performed using SPSS version 25.0 (IBM Corp., NY), R Foundation for Statistical Computing (64-bit; version 3.3.3) and MATLAB. Unless otherwise stated (**Tables S1**, **S2**), all reported statistical estimates are derived from a 2-tailed significance set at a 5% alpha value.

RESULTS

Overall, 92 patients with brain tumors were included in the study. The mean age of the cohort was 58.0 ± 12.8 years, and 45% were women. Of these, ∼55% ($n = 51$) had a low/high grade glioma while 45% ($n = 41$) had IM. In patients with gliomas and IMs, no statistical differences was noted in terms of age (56 vs. 60 years; $p = 0.145$), gender (women: 37 vs. 54%; $p = 0.116$), tumor laterality (right: 43.1 vs. 39%; $p = 0.690$) or location; however racial differences were observed with a higher proportion of whites presenting with gliomas compared to IMs (75 vs. 53%; $p = 0.029$). The overall prevalence of seizure in our cohort was 28%, with no statistical differences noted across patients with glioma and IMs (37 vs. 22%; $p = 0.228$). Nearly 86% ($n = 44$) of glioma patients had an HGG vs. 14% ($n = 7$) with LGG. In HGGs, astrocytomas (WHO Grade III or IV) constituted the majority of the cohort ($n = 43$; 84%). In patients with IMs, most had primary cancer in the lung ($n = 29$; 71%), usually of the poorly-differentiated subtype of the non-small cell lung cancer (NSCLC). This was followed by breast cancer ($n = 7$; 17.1%), lymphoma ($n = 2$; 4.9%) and one each (2.9%) for metastatic melanoma, endometrial cancer, and renal cell carcinoma (**Table 1**). An overview of demographics and clinical characteristics of patients and controls is presented in **Table 1**.

A group of 34 gender-matched controls (44% women; 56% men; age range: 19–79 years) were included for comparison. Comparing controls to patients with glioma ($p = 0.527$) or IMs ($p = 0.411$), no gender differences were noted.

Z-Score Estimates Across ROI's

Using one-tailed significance testing, forty-two ROIs among eight categories of interest (COIs) were identified to have significant

TABLE 1 | Demographics and clinical characteristics of patients with brain tumors (gliomas and IM) with respect to controls.

Characteristics	Gliomas	IM	Total	*P* value	Controls	*P* value
	***N* = 51**	***N* = 41**	***N* = 92**		***N* = 34**	
Age, years						
Mean ± SD	56.3 ± 14.5	60.1± 10.2	58.0 ± 12.8	0.145	28.6 ± 10.7	**<0.001**
Median (IQR)	58 (25)	60 (10)	59 (14)		26 (7)	
Range	26-83	34-83	26-83		19-79	
Gender, n (%)						
Male	32 (62.7)	19 (46.3)	51 (55.4)	0.116	19 (55.9)	0.290
Female	19 (37.3)	22 (53.7)	41 (44.6)		15 (44.1)	
Race, *n* (%)						
Whites	38 (74.5)	21 (52.5)	59 (64.1)	**0.029**	-	-
African-Americans	12 (23.5)	19 (47.5)	31 (33.7)	**0.017**	-	-
Unknown	1 (2.0)	0 (0.0)	1 (1.1)	1.000†	-	-
Tumor Laterality, *n* (%)						
Right	22 (43.1)	16 (39.0)	38 (41.3)	0.690	-	-
Left	27 (52.9)	17 (41.5)	44 (47.8)	0.273	-	-
Corpus callosum	1 (2.0)	0 (0)	1 (1.1)	1.000†	-	-
Intraventricular‡	1 (2.0)	0 (0)	1 (1.1)	1.000†	-	-
Bilateral	0 (0)	8 (19.5)	8 (8.7)	**0.001†**	-	-
Tumor Location, *n* (%)						
Midline	5 (9.8)	1 (2.4)	6 (6.5)	0.220†	-	-
Temporal	17 (33.3)	9 (22.0)	26 (28.3)	0.228	-	-
Extra-temporal	29 (56.9)	29 (70.7)	58 (63.0)	0.171	-	-
Midline + Extra-temporal	0 (0)	(4.9)	2 (2.2)	0.196†	-	-
Tumor Histology, *n* (%)						
High-grade gliomas	**44 (86.2)**	-		-	-	-
Astrocytoma	43 (84.2)	-		-	-	-
Oligodendroglioma	1 (2.0)	-		-	-	-
Low-grade gliomas	**7 (13.8)**	-		-	-	-
Astrocytoma	3 (5.9)	-		-	-	-
Oligodendroglioma	3 (5.9)	-		-	-	-
Oligo-astrocytoma	1 (2.0)	-		-	-	-
Primary Cancer, *n* (%)						
Lung		29 (70.7)		-	-	-
Breast		7 (17.1)		-	-	-
Lymphoma		2 (4.9)		-	-	-
Melanoma		1 (2.4)		-	-	-
Endometrial adenocarcinoma		1 (2.4)		-	-	-
Renal cell		1 (2.4)		-	-	-
Seizures, *n* (%)	19 (37.3)	9 (21.9)	26 (28.3)	0.228	-	-

† Fisher exact test; ‡ Included few patients with midline tumors.
The bold P-values depict significant statistical differences across the groups at Type I error set at 5%.

differences in z-score estimates. Spatial orientation of these potential ROIs that differ based upon normalized volume [GM. WM, total volume and CSF], area [cortical: inner, mid and pial] and cortical thickness across COIs are depicted in **Figure 2**. The mean z-score estimates for these ROIs across individual COI's depicting one-tailed significance are plotted in a dot-diagram for seizure vs. non-seizure (**Figures 3A–H**). Also, the quantified z-score estimates across tumor patients' groups upon the presence of seizure are tabulated (**Tables S1**, **S2**).

Volumetric Morphometric Assessments

The filtering of ROI's significant on one-tailed significance was performed by assessments using two-tailed testing for GM, WM, Total, and CSF volume. The two-tailed significance testing formed the primary basis for identifying true differences across seizure and non-seizure patients and presented in **Tables 2**, **3** for volumetric and morphometric (area and thickness) differences across different ROIs for the 8 COIs, respectively.

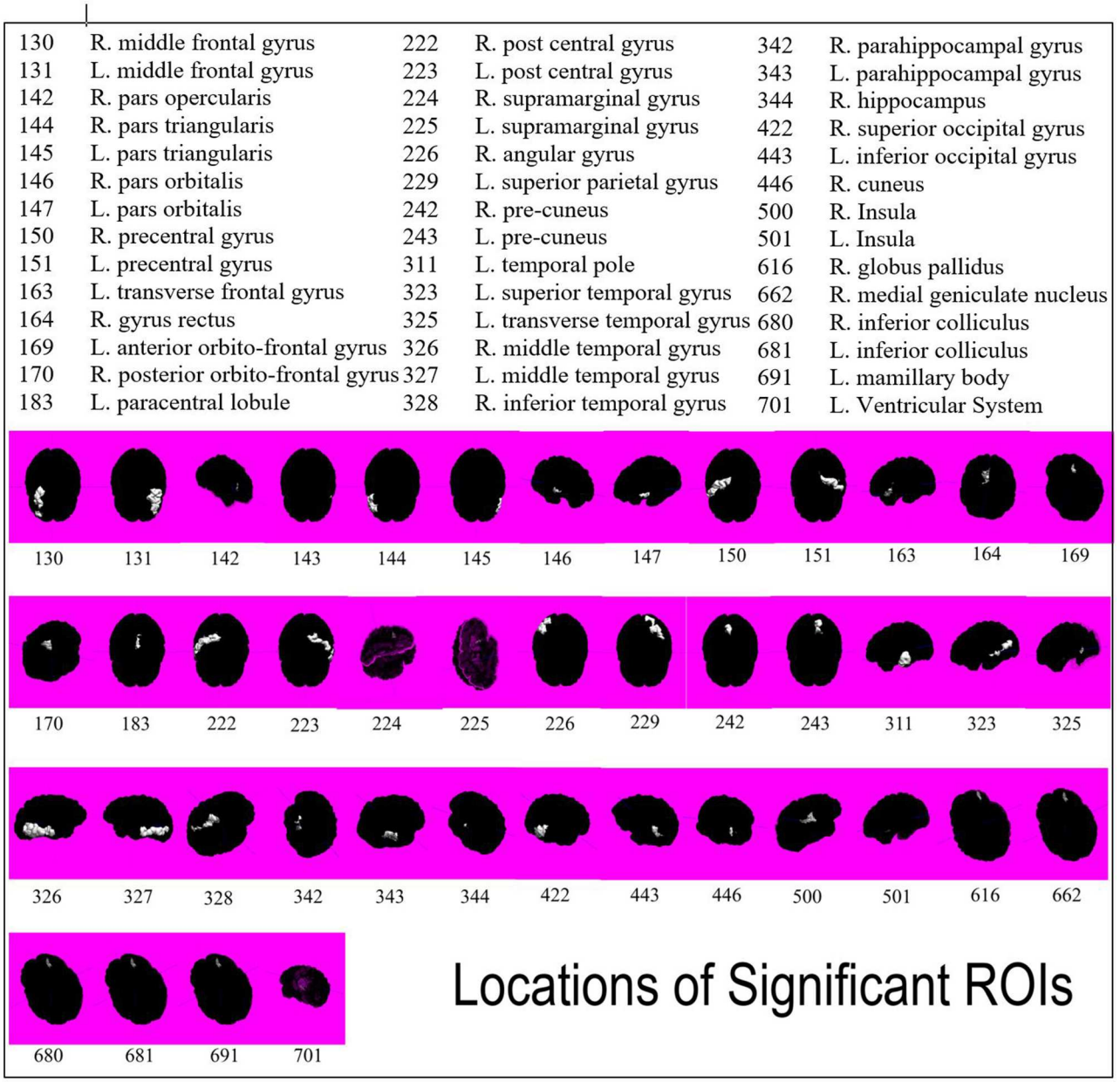

FIGURE 2 | Spatial representation of all forty-two ROIs found to be significant in differentiating seizure and non-seizure brain tumor patients. ROIs are indicated by white highlight and numbers are associated by key.

Feature Selection: Neighborhood Component Analysis

Using feature selection, the ROIs with the most influence on differentiating the seizure and non-seizure groups in tumor patients was found for all eight COIs (**Figure S1**). The NCA analysis demonstrated the normalized volume of right-sided pars orbitalis across three COIs, viz. GM, total volume and CSF volume, had the most weight in differentiating tumor patients with seizure from non-seizures. Analysis of the COI involving the WM, right-sided middle temporal gyrus was noted to have the most weight in distinguishing the presence of seizures from non-seizures.

Left-sided transverse temporal gyrus, left precuneus, left transverse temporal, and left supramarginal gyrus were associated with having the highest weight in the differentiation of seizure vs. non-seizure in tumor patients for morphometrics relating to cortical areas in the pial, inner and mid regions and cortical thickness, respectively.

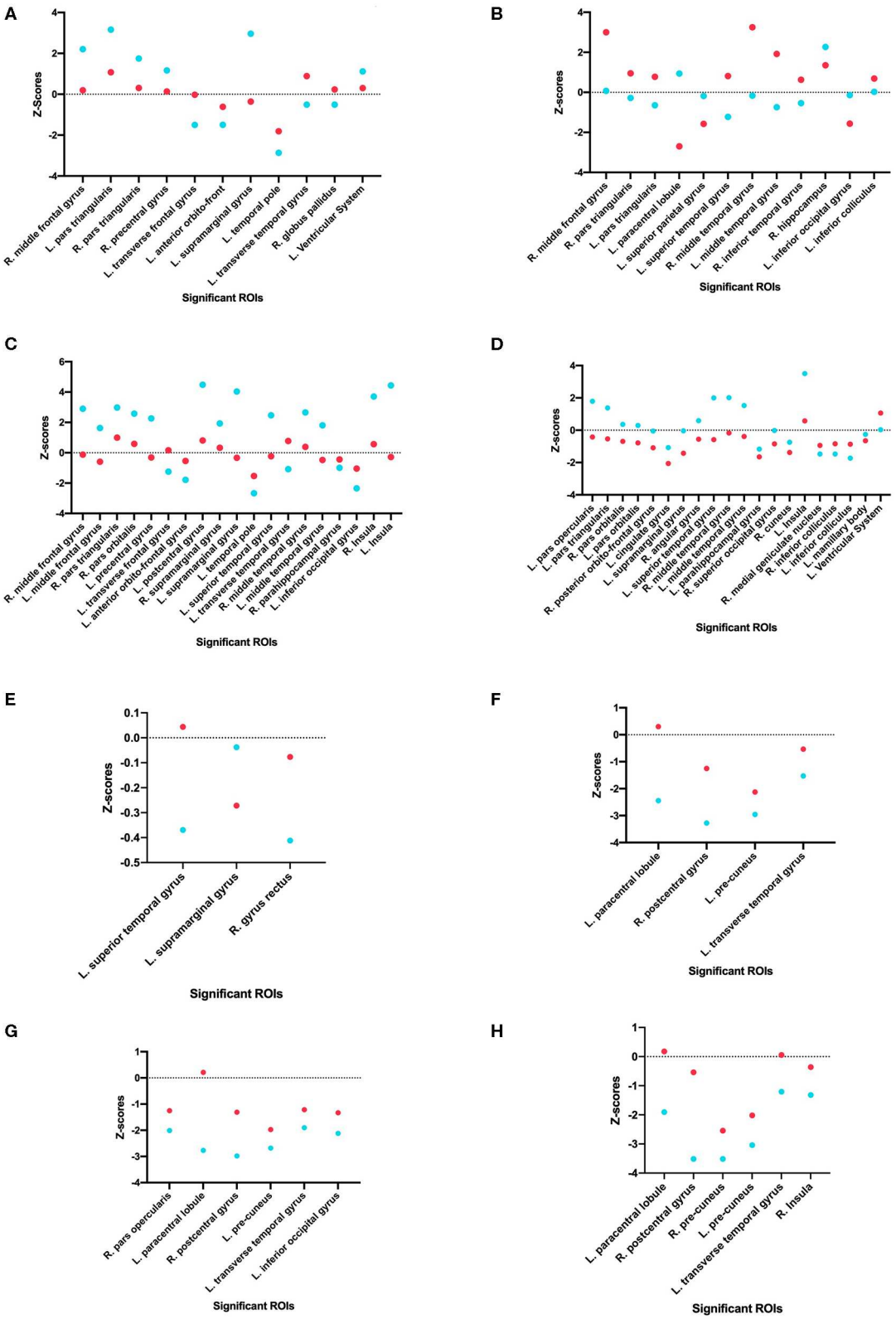

FIGURE 3 | Comparison of seizure and non-seizure subject groups, in terms of z-scores, for each significant ROI among the eight different categories of interest. The points with a more positive value indicate a raw score that is higher than the control, while points with a more negative value indicate a raw score that is lower than the control. Each graph indicates a different COI: **(A)** Gray matter volume, **(B)** White matter volume, **(C)** Total matter volume, **(D)** CSF volume, **(E)** Cortical thickness, **(F)** Mid cortical area, **(G)** Inner cortical area, and **(H)** Pial cortical area.

TABLE 2 | Significant differences in the mean z-scores in tumor patients with seizure vs. non-seizure across all volumetric COIs using two-tailed significance.

Significant ROI's	Gray matter			White matter			Total volume			CSF volume		
	Seizure	Non-seizure	*P* value (2-tailed)	Seizure	Non-seizure	*P* value (2-tailed)	seizure	Non-seizure	*P* value (2-tailed)	seizure	Non-seizure	*P* value (2-tailed)
R. middle frontal gyrus	-	-	-	3.00	0.07	**0.019**	2.90	−0.12	**0.011**	-	-	-
L. pars opercularis	-	-	-	-	-	-	-	-	-	1.79	−0.42	**0.022**
L. pars triangularis	-	-	-	-	-	-	-	-	-	1.38	−0.54	**0.001**
R. pars orbitalis	**1.75**	**0.31**	**0.094**	-	-	-	**2.58**	**0.59**	**0.055**	**0.36**	**−0.69**	**0.009**
L. pars orbitalis	-	-	-	0.77	−0.64	**0.042**	-	-	-	0.29	−0.78	**0.003**
L. transverse frontal gyrus	−1.50	−0.02	**0.010**	-	-	-	−1.25	0.16	**0.017**	-	-	-
R. posterior orbito-frontal gyrus	-	-	-	-	-	-	-	-	-	−0.05	−1.09	**0.048**
L. paracentral lobule	-	-	-	−2.70	0.94	**0.040**	-	-	-	-	-	-
L. post-central gyrus	-	-	-	-	-	-	4.48	0.81	**0.017**	-	-	-
L. supramarginal gyrus	2.96	−0.36	**0.001**	-	-	-	4.04	−0.33	**0.002**	-	-	-
L. superior temporal gyrus	-	-	-	0.81	−1.23	**0.013**	2.47	−0.23	**0.013**	1.999	−0.583	**0.001**
L. transverse temporal gyrus	-	-	-	-	-	-	−1.08	0.77	**0.017**	-	-	-
R. middle temporal gyrus	-	-	-	**3.25**	**−0.17**	**0.008**	-	-	-	2.01	−0.17	**0.008**
L. middle temporal gyrus	-	-	-	1.92	−0.74	**0.008**	-	-	-	1.53	−0.39	**0.024**
L. inferior occipital gyrus	-	-	-	1.56	−0.14	**0.040**	-	-	-	-	-	-
L. Insula	-	-	-	-	-	-	4.43	0.01	**0.047**	3.51	0.58	**0.014**
L. inferior colliculus	-	-	-	-	-	-	-	-	-	−1.73	−0.87	**0.010**
L. Ventricular System	1.12	0.30	**0.016**	-	-	-	-	-	-	-	-	-

Yellow highlighted values represent the ROI in respective COI to have the highest weight in the NCA. The bold P-values depict significant statistical differences across the groups at Type I error set at 5%.

TABLE 3 | Mean differences in z-scores across Cortical Thickness and Cortical Area zones (mid, inner, and pial) across tumor patients with and without seizures using two-tailed significance.

Significant ROI's	Cortical thickness			Mid cortical area			Inner cortical area			Pial cortical area		
	Seizure	Non-seizure	*P* value (2-tailed)	Seizure	Non-seizure	*P* value (2-tailed)	Seizure	Non-seizure	*P* value (2-tailed)	Seizure	Non-seizure	*P* value (2-tailed)
L. paracentral lobule	-	-	-	-	-	-	−2.77	0.21	0.022	-	-	-
R. post-central gyrus	-	-	-	-	-	-	−2.98	−1.31	0.047	-	-	-
L. supramarginal gyrus	**0.33**	**−0.13**	**0.055**	-	-	-	-	-	-	**-**	-	-
L. pre-cuneus	-	-	-	-	-	-	**−2.68**	**−1.97**	**0.069**	-	-	-
L. superior temporal gyrus	−0.41	0.09	**0.020**	-	-	-	-	-	-	-	-	**-**
L. transverse temporal gyrus	-	-	-	**−1.53**	**−0.53**	**0.007**	-	-	-	**−1.21**	**0.06**	**0.005**

Yellow highlighted values represent the ROI in respective COI to have the highest weight in the NCA.
The bold P-values depict significant statistical differences across the groups at Type I error set at 5%.

DISCUSSION

In this study, we utilized image processing techniques to analyze MR sequences of patients with low/high-grade gliomas and IMs, as well as a healthy group of controls. By categorizing tumor patients into two groups, seizure and non-seizure, we employed multiple metrics to differentiate the two groups across eight predefined COIs in the brain: gray matter volume, white matter volume, total matter volume, CSF volume, cortical thickness, middle cortical area, inner cortical area, and pial cortical area.

The study findings suggest significant difference in z-scores in tumor patients with seizure vs. those without seizures across several temporal and extra-temporal regions. Most consistent extratemporal areas that demonstrated significant differences in z-scores across seizure vs. non-seizure patients were right pars orbitalis, left supramarginal gyrus, left transverse gyrus, right-middle frontal gyrus and left paracentral lobule. Right-sided pars orbitalis, the rostral portion of the inferior frontal gyrus, has been implicated in high-frequency oscillations during focal neocortical seizures, especially in patients with drug-resistant epilepsy (33). The paracentral lobule, spanning over the fronto-parietal lobe, has been termed an "independent pro-epileptogenic factor" in relation to primary brain tumors due to the high volume of neurons in the structure and its association with the primary motor cortex (34). These results support the claim that the frontal lobe influences epileptogenesis progression, especially among tumor patients of all types and locations (34). Specifically, ictal spikes in the paracentral lobule from the non-dominant hemisphere are characterized by sexual sensations affecting the genitalia (35). Unfortunately, given the scope of the current study, we could not explore the relationship between tumor location and seizure semiology. Other frontal lobe structures that are known to be associated with epileptic loci, significant in our analysis, include middle frontal gyrus, pars opercularis and pars triangularis. Another pertinent ROI, the supramarginal gyrus, has been implicated in TP+ epilepsy syndromes both in patients with and without tumors (22), and differed significantly across tumor patients with seizures vs. those without seizure activity. While it is not surprising regarding the association of temporal structures (middle and superior temporal gyrus, transverse temporal gyrus) in epilepsy, studies have shown that temporal lobe epilepsy might be due to the dysfunction of GABA-B receptors (2, 36).

Our second method of determining which ROIs had the most weight in predicting whether a patient would present with seizures was Neighborhood Component Analysis (NCA) Feature Selection. NCA was used to determine the patterns that classified each subject as either seizure or non-seizure and determined the component (ROI) that had the most weight on this classification by taking out each component iteratively until a maximum prediction accuracy was achieved. This method determined that the ROIs—L. supramarginal gyrus and L. transverse temporal gyrus, along with three other ROIs—appeared again as an accurate classifier as to whether the patient was in the seizure or non-seizure groups. The COIs that these ROIs appeared in were Cortical Thickness (L. supramarginal gyrus) and Mid Cortical Area (L. transverse temporal gyrus). The reappearance of these ROIs' significance supports the claim that they have an important role in differentiating seizure and non-seizure patients. In addition to these regions of interest, the R. pars orbitalis was found to have the most feature weight in three categories of interest: gray matter volume, total volume, and CSF volume. Because of this unexpected finding, as this region of interest is not normally associated with seizure activity, it provides an opportunity for further research on this subject to confirm or deny any suspicions.

Although it is beneficial to elucidate ROI's associated with seizure development in tumor patients, the authors acknowledge that tumor location alone cannot definitively predict seizures. Although temporal lobe tumors have higher proponderence for developing seizures but not all such tumors result in seizures. Pathological predisposition for seizures in tumors arising from the temporal area can be explained from dual reasoning: hippocampal sclerosis and/or co-existent focal cortical dysplasia in temporal or extratemporal structures. On the contrary, the authors believe that such associations for extra-temporal tumors are harder to deduce. Compared to deep-seated or infratentorial tumors, superficially located tumors are more likely to be seizure prone due to its proximity to the neuronal cell bodies and thereby increasing the likelihood of cortical irritation (37, 38). Further, the literature suggests that epileptogenicity of frontal or parietal lobe tumors is second to that of temporal lobe tumors followed by occipital lobe lesions which are considered least epileptogenic (37, 38). The identified extra-temporal ROIs in our study can explain the association of fronto-parietal epilepsies. In relation to the occurrence of intraoperative seizures in tumor patients undergoing awake craniotomy, Gonen et al. concluded that tumors localized in the supplementary motor area (SMA) had higher incidence (OR: 11.36; $p < 0.002$) compared to non-SMA frontal, temporal, or parietal regions (39). The authors opine that the existing knowledge linking an association of tumor location with seizure propensity is derived from limited observational studies, and that a systematic review/meta-analysis using larger, granular, homogenous cohorts from the published literature is appreciable for strengthening such association.

STUDY LIMITATIONS

Despite the merit of the current investigation, pertinent limitations governing the study need to be addressed. First, the heterogeneity in tumor types (subgroups of gliomas and IMs) and relatively smaller sample sizes within each group limit generalization of our findings owing to suboptimal power for subgroup analysis for tumor histology. Second, the study did not account for seizure semiology and/or localization of the epileptogenic zone with tumor location. However, given the focus of the investigation, quantifying and contrasting z-scores for ROIs across seizure and non-seizure brains would not be impacted due to this limitation. Regarding the study design, the retrospective, observational nature of our investigation fails to establish a causal relationship between the differences in the ROI's due to epileptogenic loci or a result of seizure spread, which could serve as a future direction for research on the topic. As the study was not powered enough, the lack of predictive parameters (e.g., sensitivity, specificity) limits validation of the ROIs for seizure prediction. Despite these limitations, the utility

of the current investigation lies in the widespread brain areas that were examined to assess differences across scans of tumor patients with and without seizures. Discovering these ROIs in connection with differentiating seizure and non-seizure brain tumor patients has provided a foundation for more extensive research on this subject. With a larger cohort of patients, we suspect that among these significant regions found in this study, a smaller variety of ROIs will become solidified and provide a more specific connection to seizures, brain tumors, and the volume of structures in the brain.

CONCLUSION

Our study elucidates potential morphological biomarkers for seizure targeting in patients with gliomas and IMs based upon morphometric and volumetric assessments. Amongst the widespread brain regions examined in our cohort, pars orbitalis, supramarginal andtemporal gyrus (middle, transverse), and the precuneus contribute a maximal potential for differentiation of seizure patients from non-seizure. The significance of these regions of interest using a *t*-test as well as feature selection, supports the claim that these areas are connected to tumoral seizures. In the future, gathering a larger cohort that specifies in a smaller variety of tumor types will be beneficial to this specific field of interest.

DATA AVAILABILITY STATEMENT

Datasets are available on request due to privacy/ethical restrictions. Relevant data has been posted/provided in the online **Supplementary Material**.

ETHICS STATEMENT

The studies involving human participants were reviewed and approved by Louisiana State University, Shreveport. Written informed consent for participation was not required for this study in accordance with the national legislation and the institutional requirements.

AUTHOR CONTRIBUTIONS

HS, PK, AE, and CL contributed to study conceptualization and research design. AE and CF performed data acquisition/collection. AE, PK, CF, and KS performed data processing (analysis), statistical analysis, and interpretation. PK, AE, CF, and KS drafted the article. PK, KS, TH, and HS critically revised the article. All authors have read and approved the final version of the manuscript. CL, EG-T, AN, and HS provided administrative/technical/material support. Study supervision involved HS, CL, PK, and AE.

FUNDING

HS is supported by the United States Department of Defense (DOD), Congressional Directed Medical Research Program (CDMRP) grant #W81XWH-18-1-0655.

SUPPLEMENTARY MATERIAL

The Supplementary Material for this article can be found online at: https://www.frontiersin.org/articles/10.3389/fneur.2020.00444/full#supplementary-material

REFERENCES

1. Huff JS, Murr N. *Seizure*. Treasure Island, FL: StatPearls (2019).
2. Englot DJ, Chang EF, Vecht CJ. Epilepsy and brain tumors. *Handb Clin Neurol.* (2016) 134:267–85. doi: 10.1016/B978-0-12-802997-8.00016-5
3. Vecht CJ, Kerkhof M, Duran-Pena A. Seizure prognosis in brain tumors: new insights and evidence-based management. *Oncologist.* (2014) 19:751–9. doi: 10.1634/theoncologist.2014-0060
4. Bekelis K, Kalakoti P, Nanda A, Missios S. A predictive model of unfavorable outcomes after benign intracranial tumor resection. *World Neurosurg.* (2015) 84:82–9. doi: 10.1016/j.wneu.2015.02.032
5. Missios S, Kalakoti P, Nanda A, Bekelis K. Craniotomy for glioma resection: a predictive model. *World Neurosurg.* (2015) 83:957–64. doi: 10.1016/j.wneu.2015.04.052
6. Pignatti F, van den Bent M, Curran D, Debruyne C, Sylvester R, Therasse P, et al. Prognostic factors for survival in adult patients with cerebral low-grade glioma. *J Clin Oncol.* (2002) 20:2076–84. doi: 10.1200/JCO.2002.08.121
7. Chang EF, Potts MB, Keles GE, Lamborn KR, Chang SM, Barbaro NM, et al. Seizure characteristics and control following resection in 332 patients with low-grade gliomas. *J Neurosurg.* (2008) 108:227–35. doi: 10.3171/JNS/2008/108/2/0227
8. Lee JW, Wen PY, Hurwitz S, Black P, Kesari S, Drappatz J, et al. Morphological characteristics of brain tumors causing seizures. *Arch Neurol.* (2010) 67:336–42. doi: 10.1001/archneurol.2010.2
9. You G, Sha ZY, Yan W, Zhang W, Wang YZ, Li SW, et al. Seizure characteristics and outcomes in 508 Chinese adult patients undergoing primary resection of low-grade gliomas: a clinicopathological study. *Neuro Oncol.* (2012) 14:230–41. doi: 10.1093/neuonc/nor205
10. Iuchi T, Hasegawa Y, Kawasaki K, Sakaida T. Epilepsy in patients with gliomas: incidence and control of seizures. *J Clin Neurosci.* (2015) 22:87–91. doi: 10.1016/j.jocn.2014.05.036
11. Recht L, Glantz M. Neoplastic diseases. In: Engel JJ, Pedley T, editors. *Epilepsy: A Comprehensive Textbook*. New York, NY: Lippincott, Williams, and Wilkins (2008). p. 2637–42.
12. van Breemen MS, Wilms EB, Vecht CJ. Epilepsy in patients with brain tumours: epidemiology, mechanisms, and management. *Lancet Neurol.* (2007) 6:421–30. doi: 10.1016/S1474-4422(07)70103-5
13. Chaichana KL, Parker SL, Olivi A, Quinones-Hinojosa A. Long-term seizure outcomes in adult patients undergoing primary resection of malignant brain astrocytomas. Clinical article. *J Neurosurg.* (2009) 111:282–92. doi: 10.3171/2009.2.JNS081132
14. Sizoo EM, Braam L, Postma TJ, Pasman HR, Heimans JJ, Klein M, et al. Symptoms and problems in the end-of-life phase of high-grade glioma patients. *Neuro Oncol.* (2010) 12:1162–6. doi: 10.1093/neuonc/nop045
15. Lynam LM, Lyons MK, Drazkowski JF, Sirven JI, Noe KH, Zimmerman RS, et al. Frequency of seizures in patients with newly diagnosed brain tumors: a retrospective review. *Clin Neurol Neurosurg.* (2007) 109:634–8. doi: 10.1016/j.clineuro.2007.05.017
16. Avila E. Tumor associated epilepsy. In: Lichtor T, editor. *Clinical Management and Evolving Novel Therapeutic Strategies for Patients with Brain Tumors*. New York, NY: InTech. (2013) 211–24. doi: 10.5772/55491
17. Duffau H, Capelle L. Preferential brain locations of low-grade gliomas. *Cancer.* (2004) 100:2622–6. doi: 10.1002/cncr.20297

18. Larjavaara S, Mantyla R, Salminen T, Haapasalo H, Raitanen J, Jaaskelainen J, et al. Incidence of gliomas by anatomic location. *Neuro Oncol.* (2007) 9:319–25. doi: 10.1215/15228517-2007-016
19. Holly KS, Barker BJ, Murcia D, Bennett R, Kalakoti P, Ledbetter C, et al. High-grade gliomas exhibit higher peritumoral fractional anisotropy and lower mean diffusivity than intracranial metastases. *Front Surg.* (2017) 4:18. doi: 10.3389/fsurg.2017.00018
20. Holly KS, Fitz-Gerald JS, Barker BJ, Murcia D, Daggett R, Ledbetter C, et al. Differentiation of high-grade glioma and intracranial metastasis using volumetric diffusion tensor imaging tractography. *World Neurosurg.* (2018) 120:e131–e41. doi: 10.1016/j.wneu.2018.07.230
21. Andrade-Machado R, Benjumea-Cuartas V. Temporal plus epilepsy: Anatomo-electroclinical subtypes. *Iran J Neurol.* (2016) 15:153–63.
22. Jobst BC. Temporal Plus Epilepsy: Epileptic Territory Beyond the Temporal Lobes. *Epilepsy Curr.* (2016) 16:305–7. doi: 10.5698/1535-7511-16.5.305
23. D'Cruz J, Hefner M, Ledbetter C, Frilot C, Howard B, Zhu P, et al. Focal epilepsy caused by single cerebral cavernous malformation (CCM) is associated with regional and global resting state functional connectivity (FC) disruption. *Neuroimage Clin.* (2019) 24:102072. doi: 10.1016/j.nicl.2019.102072
24. Al-Dorzi HM, Alruwaita AA, Marae BO, Alraddadi BS, Tamim HM, Ferayan A, et al. Incidence, risk factors and outcomes of seizures occurring after craniotomy for primary brain tumor resection. *Neurosciences (Riyadh).* (2017) 22:107–13. doi: 10.17712/nsj.2017.2.20160570
25. Hwang SL, Lieu AS, Kuo TH, Lin CL, Chang CZ, Huang TY, et al. Preoperative and postoperative seizures in patients with astrocytic tumours: analysis of incidence and influencing factors. *J Clin Neurosci.* (2001) 8:426–9. doi: 10.1054/jocn.2000.0825
26. Hwang SL, Lin CL, Lee KS, Lieu AS, Kuo TH, Chang CZ, et al. Factors influencing seizures in adult patients with supratentorial astrocytic tumors. *Acta Neurochir (Wien).* (2004) 146:589–94: discussion 94. doi: 10.1007/s00701-004-0266-8
27. Telfeian AE, Philips MF, Crino PB, Judy KD. Postoperative epilepsy in patients undergoing craniotomy for glioblastoma multiforme. *J Exp Clin Cancer Res.* (2001) 20:5–10.
28. BDP: *Distortion Correction and Co-registration.* (2019). Available online at: http://brainsuite.org/processing/diffusion/distortion-correction-and-co-registration/ (accessed June 18, 2019).
29. Shattuck DW, Leahy RM. BrainSuite: an automated cortical surface identification tool. *Med Image Anal.* (2002) 6:129–42. doi: 10.1016/S1361-8415(02)00054-3
30. Pantazis D, Joshi A, Jiang J, Shattuck DW, Bernstein LE, Damasio H, et al. Comparison of landmark-based and automatic methods for cortical surface registration. *Neuroimage.* (2010) 49:2479–93. doi: 10.1016/j.neuroimage.2009.09.027
31. Joshi AA, Shattuck DW, Leahy RM. A method for automated cortical surface registration and labeling. In: Dawant B, Christensen G, Fitzpatrick JM, Rueckert D, editors. *Biomedical Image Registration*. Berlin Heidelberg: Springer (2012). p. 180–9. doi: 10.1007/978-3-642-31340-0_19
32. Fisher RA. On the interpretation of chi square from contingency tables, and the calculation of P. *J R Stat Soc.* (1922) 85:87–94. doi: 10.2307/2340521
33. Jirsch JD, Urrestarazu E, LeVan P, Olivier A, Dubeau F, Gotman J. High-frequency oscillations during human focal seizures. *Brain.* (2006) 129(Pt 6):1593–608. doi: 10.1093/brain/awl085
34. Akeret K, Serra C, Rafi O, Staartjes VE, Fierstra J, Bellut D, et al. Anatomical features of primary brain tumors affect seizure risk and semiology. *Neuroimage Clin.* (2019) 22:101688. doi: 10.1016/j.nicl.2019.101688
35. Mascia A, Di Gennaro G, Esposito V, Grammaldo LG, Meldolesi GN, Giampa T, et al. Genital and sexual manifestations in drug-resistant partial epilepsy. *Seizure.* (2005) 14:133–8. doi: 10.1016/j.seizure.2004.12.002
36. Kahlenberg CA, Fadul CE, Roberts DW, Thadani VM, Bujarski KA, Scott RC, et al. Seizure prognosis of patients with low-grade tumors. *Seizure.* (2012) 21:540–5. doi: 10.1016/j.seizure.2012.05.014
37. Shamji MF, Fric-Shamji EC, Benoit BG. Brain tumors and epilepsy: pathophysiology of peritumoral changes. *Neurosurg Rev.* (2009) 32:275–84; discussion 84–6. doi: 10.1007/s10143-009-0191-7
38. Sweet JA, Hdeib AM, Sloan A, Miller JP. Depths and grids in brain tumors: implantation strategies, techniques, and complications. *Epilepsia.* (2013) 54(Suppl 9):66–71. doi: 10.1111/epi.12447
39. Gonen T, Grossman R, Sitt R, Nossek E, Yanaki R, Cagnano E, et al. Tumor location and IDH1 mutation may predict intraoperative seizures during awake craniotomy. *J Neurosurg.* (2014) 121:1133–8. doi: 10.3171/2014.7.JNS132657

Conflict of Interest: The authors declare that the research was conducted in the absence of any commercial or financial relationships that could be construed as a potential conflict of interest.

frontiers in Neurology

REVIEW
published: 21 August 2020
doi: 10.3389/fneur.2020.00801

A Radiation Oncology Approach to Brain Metastases

*N. Ari Wijetunga and T. Jonathan Yang**

Department of Radiation Oncology, Memorial Sloan-Kettering Cancer Center, New York, NY, United States

Brain metastases are a significant contributor to morbidity and mortality. The incidence of brain metastases is increasing as a result of increased time for metastasis development in the setting of improved systemic therapy and extracranial disease control and improved detection by MRI. Radiotherapy is an essential treatment modality for brain metastases in both the definitive and post-surgical adjuvant treatment contexts, and radiation oncologists rely heavily on diagnostic neuroimaging to guide treatment. Insight into the aspects of diagnostic neuroimaging that radiation oncologists rely on for clinical decision-making, radiation treatment planning, and assessment of treatment response or complications can help guide radiologists when constructing their neuroimaging reports in the context of brain metastases.

Keywords: brain metastases, radiation oncology, radiology, radiotherapy, palliation, MRI, neuroimaging

OPEN ACCESS

Edited by:
Susie Y. Huang,
Massachusetts General Hospital,
Harvard Medical School,
United States

Reviewed by:
Filippo Alongi,
University of Brescia, Italy
Jennifer Soun,
University of California, Irvine,
United States

****Correspondence:***
T. Jonathan Yang
yangt@mskcc.org

Specialty section:
This article was submitted to Applied Neuroimaging, a section of the journal Frontiers in Neurology

Received: *28 November 2019*
Accepted: *26 June 2020*
Published: *21 August 2020*

Citation:
Wijetunga NA and Yang TJ (2020) A Radiation Oncology Approach to Brain Metastases. Front. Neurol. 11:801. doi: 10.3389/fneur.2020.00801

INTRODUCTION

Brain metastases occur in as many as 25% of patients with cancer and are a significant contributor to morbidity and mortality (1). They are estimated to be symptomatic in 60–75% of patients (2) and can be associated with headaches, seizures, syncope, focal neurological deficits, gait disturbances, cognitive dysfunction, nausea, vomiting, cranial nerve dysfunction, cerebellar symptoms, and speech disturbances (3). Brain metastases arise most commonly from lung, breast, colorectal, melanoma, and renal cell primaries (4). At presentation, ∼60% of patients have multiple lesions (5). There are an estimated 200,000 incident brain metastases per year, and the incidence is increasing (6) as a result of increased time for metastasis development because of improved systemic therapy and extracranial disease control and improved detection by MRI (1, 4).

Radiation therapy (RT) plays an essential role in the management of brain metastases. The first report of the palliative benefit of whole brain radiotherapy (WBRT) was a case series by Chao et al. from Memorial Hospital (now Memorial Sloan Kettering) in 1954 that demonstrated 24 of 38 patients benefiting from WBRT (7). Several subsequent trials found that post-surgical WBRT improved overall survival, local control, and functional independence relative to WBRT alone, and RT became the standard adjuvant post-surgical treatment for brain metastases (8, 9). More recently, targeted stereotactic radiosurgery (SRS) is an increasingly useful tool for treating brain metastases while minimizing off-target brain irradiation-associated neurocognitive decline (10). When added to WBRT, SRS was demonstrated to improve overall survival in patients with a single, unresectable brain metastasis compared with WBRT alone (11). This was followed by a practice-changing trial showing that SRS with WBRT reserved for treatment failure or disease progression had equivalent overall survival compared with upfront SRS and WBRT in patients with less than five brain metastases (12). Finally, SRS without WBRT was non-inferior in treating 5–10 brain metastases when compared with 2–4 brain metastases (13). Consequently, SRS is now the favored treatment for limited brain metastases for most solid tumor histologies, defined as the number of

metastases where SRS is as effective as WBRT with more cognitive protection, whereas WBRT is used to target extensive brain disease, though it is worth noting that the National Comprehensive Cancer Network (NCCN) guidelines allow for SRS to be used for both limited and extensive brain disease (14).

In both the definitive and post-surgical adjuvant treatment contexts, radiation oncologists rely heavily on diagnostic neuroimaging to decide on a treatment course and for treatment planning. Given the panoply of features that radiologists can address when constructing their reports, there are key observations that may help to guide RT. In the following article, we will provide an overview of the radiation oncology approach to brain metastases to provide insight into specific information that may be relevant to our discipline. First, we will review the aspects of diagnostic neuroimaging that radiation oncologists rely on for clinical decision-making. Then, we will provide an overview of radiation treatment planning. Lastly, we will describe how radiation oncologists use diagnostic neuroimaging to assess treatment response, treatment-related complications, and disease recurrence.

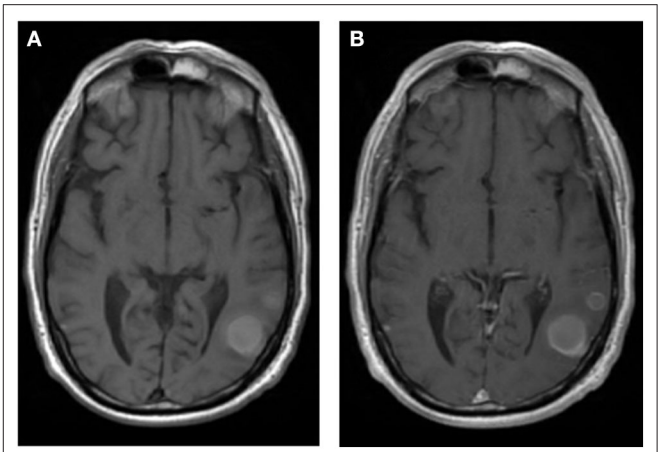

FIGURE 1 | A patient with metastatic melanoma treated with stereotactic radiosurgery (27 Gy in 3 fractions) demonstrating lesion enhancement without contrast. **(A)** T1 pre-contrast sequence demonstrating that the melanin within the tumor tends to enhance. **(B)** T1 post-contrast sequence.

Diagnostic Imaging Considerations

Brain metastases tend to occur at specific sites within the brain, and their distribution can vary by histology. For example, brain metastases are often located at the gray–white matter junction, the subarachnoid space, and the interfaces of major arterial vascular territories (15). Within the brain parenchyma, most brain metastases (up to 80%) occur in the cerebral hemispheres, whereas ∼17% occur in the cerebellum and 3% in the basal ganglia (16). Within the cerebrum, metastases tend to occur in the frontal and parietal lobes more often than in the temporal and occipital lobes (16). Uterine, prostate, and gastrointestinal cancers tend to metastasize to the posterior fossa (17).

When patients present with symptoms related to intracranial disease, CT imaging is often obtained, and it can provide initial insight into the presence of large metastases, mass effect, herniation, and hydrocephalus. Thus, CT imaging can indicate when a surgical emergency exists for which delaying care to plan RT would be inappropriate. However, CT is not the primary method for identifying and planning RT for brain metastases. Although the sensitivity of CT can be improved with contrast, CT has low sensitivity for small brain metastases relative to contrast MRI, the current gold standard for visualizing brain metastases (18, 19). Radiation oncologists typically only use CT for lesion visualization and treatment planning when MRI is contraindicated.

There are several characteristics of brain metastases that can distinguish them from primary malignancies, as well as from non-cancer abnormalities on MRI imaging. The T1 pre-contrast sequence has limited utility in visualizing most brain parenchymal metastases because brain parenchymal metastases tend to be iso-intense. However, this sequence is useful in visualizing melanoma metastases, which are T1-weighted pre-contrast hyperintense because of the presence of melanin (**Figure 1**) (20). Also, the presence of T1-weighted pre-contrast hyperintensity may indicate a hemorrhage, and lung, melanoma, choriocarcinoma, renal cell carcinoma, and thyroid carcinoma metastases are more likely to hemorrhage compared with other histologies (21). Other MR sequences such as susceptibility-weighted imaging (SWI) or gradient echo (GRE) can also detect hemorrhage and calcifications (22). The T1-weighted post-contrast sequence is essential for visualizing brain metastases. Because secondary malignancies in the brain violate the blood–brain barrier and have vasculature representative of their parent tumors (23), brain metastases generally enhance on T1-weighted post-contrast imaging, tending to appear as bright, well-demarcated, spherical masses. The center of the mass is often contrast-devoid, resulting in a rim of enhancement. Cystic metastases may appear hyperintense within the tumor on a T2-weighted sequence, whereas mucinous tumors may be T2 hypointense (24). The T2-weighted fluid-attenuated inversion recovery (FLAIR) MR sequence allows the visualization of

TABLE 1 | Summary of brain metastases imaging findings.

MRI sequence	Typical findings for brain metastases
T1 pre-contrast	Iso-intense with brain parenchyma (hemorrhage and melanoma can appear hyperintense)
T1 post-contrast	Enhancing
T1-weighted post-contrast spoiled GRE	Enhancing
T2	Variable intensity
T2 FLAIR	Hyperintense peritumoral edema
DWI	Peritumoral edema with elevated ADC compared with primary brain tumors
DTI	Anisotropy measures are lower in contrast enhancing tumor relative to primary brain tumors
SWI/GRE	Hypointense with intratumoral hemorrhage
DCE/DSC	Elevated rCBV
Spectroscopy	Choline peak within tumor and no elevation in peritumoral edema Lipid peak associated with necrosis NAA decreased

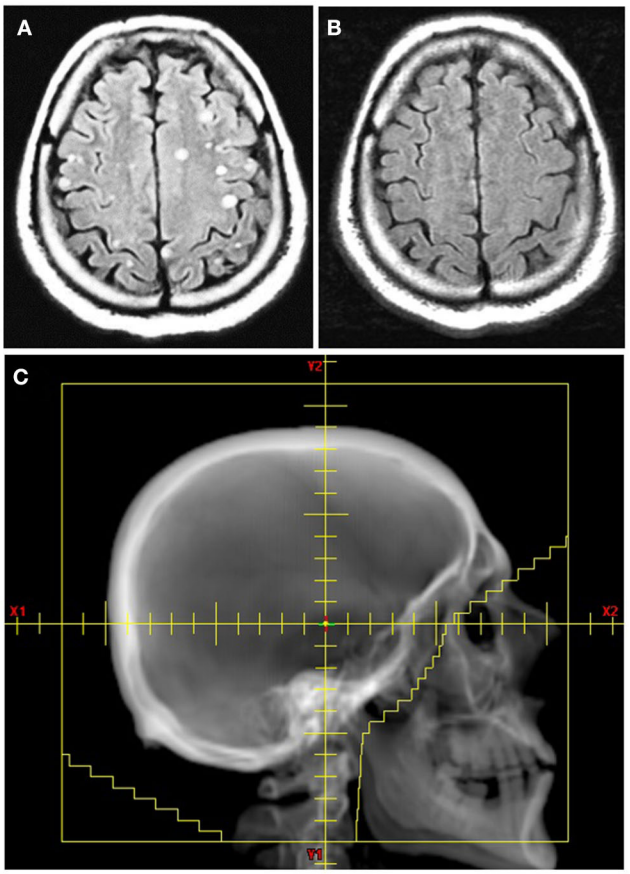

FIGURE 2 | Whole brain radiation therapy (WBRT) for a patient with non-small cell lung cancer with multiple brain metastases. **(A)** T2 FLAIR axial image before WBRT. **(B)** T2 FLAIR axial image 6 months after WBRT with 30 Gy in 10 fractions. **(C)** Radiation field for WBRT defined using the skull anatomy.

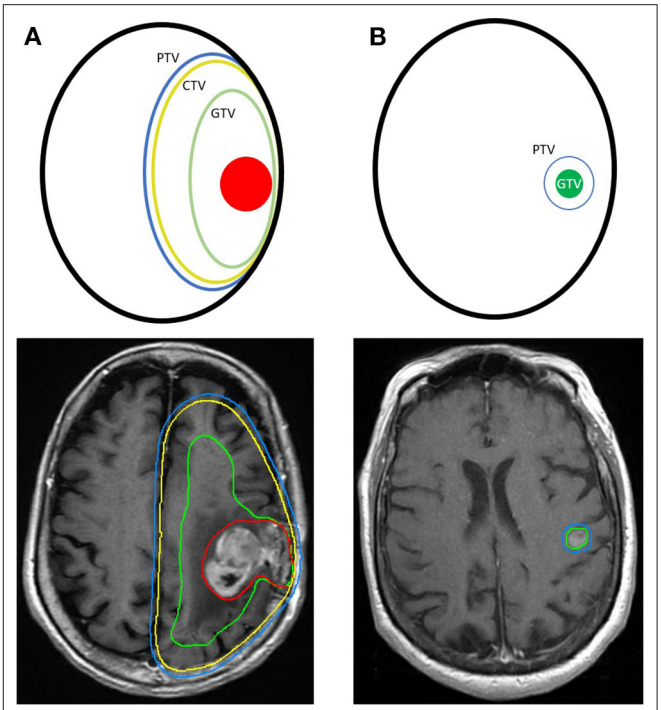

FIGURE 3 | Comparison of the radiation planning treatment volumes for a primary malignancy and stereotactic radiosurgery (SRS) for a brain metastasis. **(A)** A primary glioblastoma multiforme with a GTV, *green*, encompassing the gross tumor, *red*, and edema. A CTV, *yellow*, and PTV, *blue*, are shown as concentric expansions from the GTV. **(B)** A metastatic brain lesion treated with SRS and a GTV, *green*, with a PTV, *blue*. No CTV is required because of low risk of tumor invasion into the brain parenchyma.

peritumoral edema. Diffusion-weighted imaging (DWI) is an area of interest because metastases and gliomas have different apparent diffusion coefficients (ADCs) compared with normal brain matter, although there is considerable overlap between the ADCs of primary brain tumors, metastases, edema, and non-tumoral lesions (25). DWI can potentially distinguish gliomas from brain metastases because the mean minimum ADC within the vasogenic edema of metastases was found to be higher than that of the infiltrative edema of gliomas (26). Conversely, in dynamic contrast-enhanced (DCE) perfusion MR imaging, the relative cerebral blood volume (rCBV) of peritumoral edema for gliomas tends to be significantly greater than that of brain metastases (27). The typical MRI findings for brain metastases are summarized in **Table 1**.

Primary brain malignancies and non-cancer abnormalities have specific characteristics on diagnostic imaging that allow for their identification relative to brain metastases. Both gliomas and brain metastases tend to have low signal on T1-weighted sequences and high signal on T2-weighted sequences, making it difficult to distinguish between gliomas and brain metastases on this basis. However, gliomas tend to form expansile masses that conform to the barriers of the lobe or deep nuclear structures, whereas brain metastases are well demarcated. Because most brain metastases are contrast enhancing, enhancement can also aid in distinguishing gliomas from brain metastases depending on glioma grade. Approximately 70% of high-grade gliomas are contrast enhancing, whereas only 20% of low-grade gliomas are (28). Like gliomas, non-cancer brain abnormalities visible on imaging, including infarcts, demyelinating plaques, abscesses, hematomas, necrosis, and encephalitis, may also be confused with metastases (29). These entities can demonstrate contrast enhancement, perilesional edema, mass effect, and central necrosis. Acute infarcts can appear as masses with contrast enhancement on CT, like brain metastases; however, infarcts show evolving changes over time on repeat MRIs. T1-weighted and T2-weighted MRI sequences are less useful in the acute setting because they show abnormalities in <50% of acute infarct cases, whereas techniques like perfusion imaging and DWI can show differences within minutes of symptom onset (30). In the subacute and chronic settings, infarcted brain is associated with high extracellular fluid content and increased T2-weighted MRI signal. Abscesses are difficult to distinguish from brain metastases, appearing as round lesions with associated edema and ring-like peripheral contrast enhancement (31). DWI can

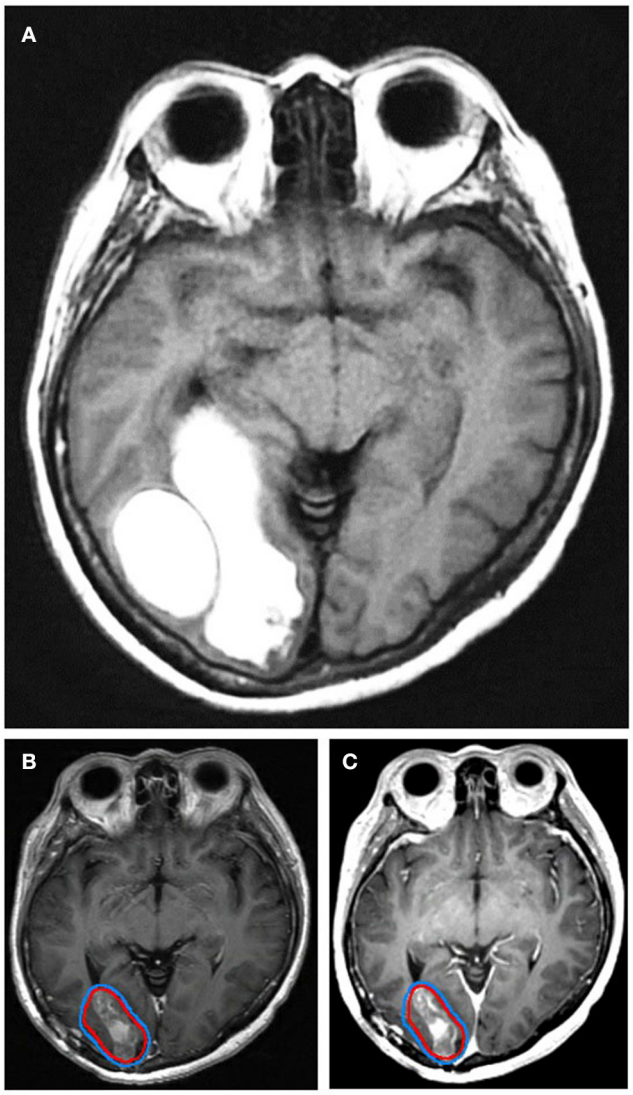

FIGURE 4 | A patient with a non-small cell lung cancer metastasis shown **(A)** preoperatively, **(B)** postoperatively on T1-post weighted MRI, and **(C)** on 3D brain volume (BRAVO) MRI. The postoperative cavity is contoured as the GTV, *red*, with an expansion to the PTV, *blue*. The patient was treated with stereotactic radiosurgery and 27 Gy in 3 fractions.

help to distinguish abscesses and tumors because abscesses have restricted diffusion in their center from the high cellularity and viscosity of pus relative to brain metastases, although mucinous and highly cellular brain metastases may also have central restricted diffusion (32). Necrosis can be the result of a malignancy or a side effect from radiation (see Post-radiation evaluation). It is considered a hallmark of high-grade gliomas, like glioblastoma multiforme, whereas it is relatively uncommon in the setting of a small, treatment-naive brain metastasis. Both necrosis and tumor can appear T2 hyperintense and contrast enhancing, so conventional MRI may fail to distinguish them (33). However, recent advances in MRI have shown a potential for differentiating necrosis from tumors, such as MR spectroscopy and amide proton transfer (APT) MR. APT MR can detect the amide protons of low-concentration mobile proteins and peptides in the cytoplasm of necrotic cells, thus differentiating necrosis from brain tumors (34).

TABLE 2 | Typical point dose constraints for organs at risk.

Organ	Total dose (Gy)
Brainstem	55
Cochlea	50
Cord	50
Lacrimal gland	40
Lens	10
Optic chiasm	54
Optic nerve	54
Pituitary	60
Retina	45

Radiation Planning and Treatment Considerations

According to the NCCN guidelines, the type and timing of RT for brain metastases depends on the clinical scenario, including the number and volume of metastases, the dose and fractionation of planned radiation, systemic treatment options, and the anticipated benefit of surgical resection (35). If a brain metastasis is >2 cm, or if the patient is acutely symptomatic from the brain metastasis, they may be referred for surgery before RT (36). The benefit of surgical resection depends on the need for tissue diagnosis, the size and location of the lesion, and the institutional experience. As SRS is a treatment option for limited brain metastases (13), at our institution, SRS is the preferred treatment method for limited brain metastases when patients have new or stable systemic disease and have additional systemic treatment options. In the setting of multiple brain metastases, the NCCN recommends SRS over WBRT if the patient has a good performance status, radioresitant histology, or low overall tumor volume. When 116 radiation oncologists were surveyed for the "maximum number of brain metastases [they] would commonly treat with upfront SRS without offering WBRT," 40.4% indicated 1–4, 42.1% indicated 5–10, 14% indicated 10–20, and 3.5% did not have a limit (37). Furthermore, when asked what other factors influenced this decision, the location and histology of the metastases mattered the most. In a similar survey, the average cutoff for switching from SRS to WBRT was 8.1 brain metastases for central nervous system (CNS) specialists with a high clinical volume compared with 4.9 brain metastases for CNS specialists with a low clinical volume (38). An example of a WBRT plan for a patient with numerous brain metastases as well as the response to the treatment is shown in **Figure 2**.

The first step in planning RT is a CT (also known as a radiation simulation) with the patient in the treatment position and appropriate immobilization devices, such as a rigid, custom-made thermoplastic mask and headrest. Using the planning

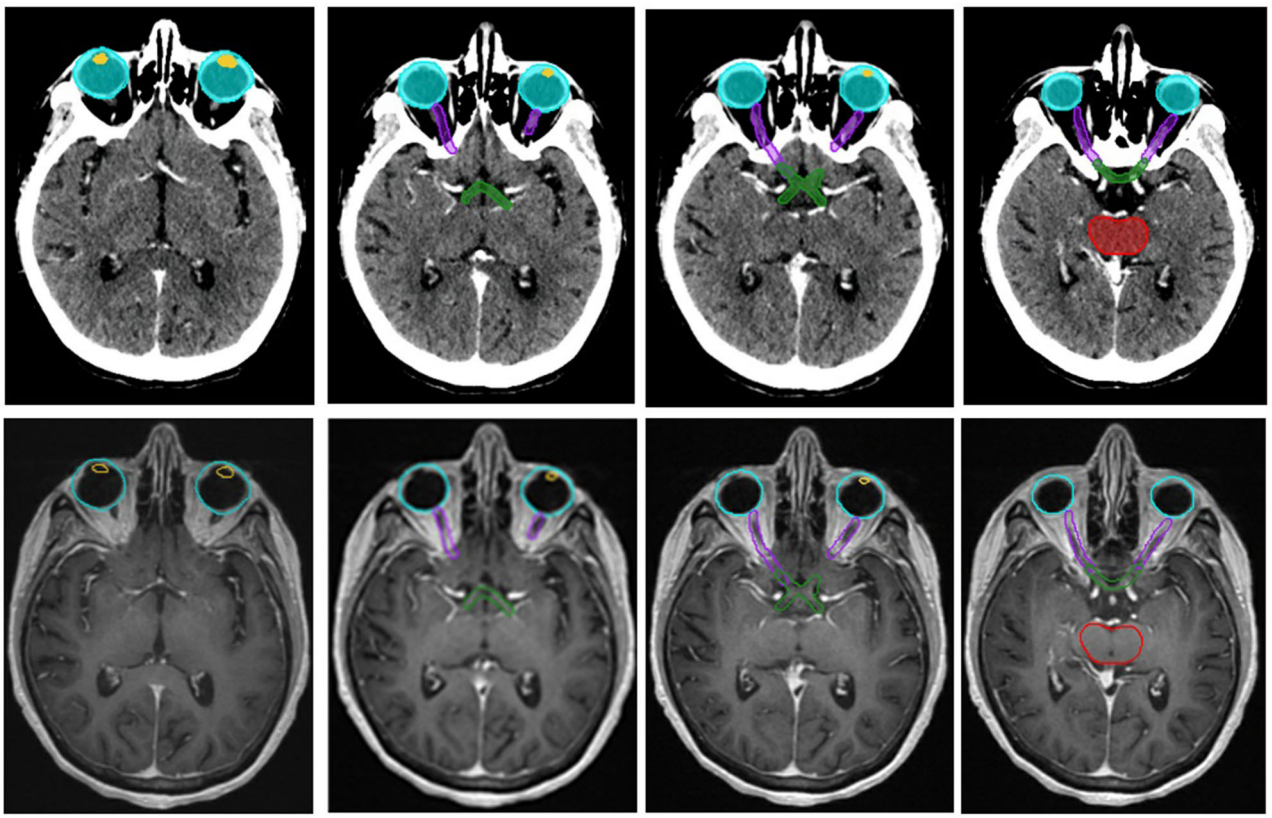

FIGURE 5 | Organs at risk (OARs) defined on a planning CT and corresponding T2-weighted MR images. The included OARs are the lenses, *yellow*, the eyes, *aqua*, the optic nerves, *purple*, the optic chiasm, *green*, and the brain stem, *red*.

CT in conjunction with MRI, radiation oncologists define the radiation treatment area primarily using three target volumes. The gross tumor volume (GTV) encompasses all visible disease. The clinical target volume (CTV) includes the GTV, but it also accounts for subclinical disease spread. The CTV is often an expansion beyond the GTV that respects anatomical borders and can include areas at risk for microscopic disease (e.g., including involved cranial nerves in the case of observed neurotropism). However, for metastatic lesions to the brain, the expansion from GTV to CTV is usually 0 mm as there is no expected subclinical extension of disease. Finally, the planning target volume (PTV) is an expansion on the CTV that accounts for daily setup uncertainties (39). Modern RT techniques include positioning devices specifically designed for neuroradiation and onboard imaging (daily 2D and 3D imaging) that allows for high accuracy of treatment and results in minimal patient setup uncertainties, thus allowing the PTV margin to be as small as 0–2 mm. An example of GTV, CTV, and PTV volumes for a typical brain metastasis SRS case compared with a primary malignancy case can be seen in **Figure 3**. In the postoperative setting, the T1 post-contrast image from the postoperative MRI is used to define a GTV as enhancing disease. If there is no enhancing disease, the postoperative cavity is contoured as a CTV. An expansion is made to the PTV directly from a GTV, in the case of residual tumor, or from CTV, in the case of gross resection, using a margin of 2–3 mm. An example of a postoperative SRS case can be seen in **Figure 4**.

In planning RT for brain metastases, radiation oncologists typically request an MRI with contrast and 1-mm slice thickness for optimal visualization of the metastases. Ideally, the patient will be immobilized during the MR with the same mask that is used for the planning CT, which will allow for near-perfect registration of the two imaging studies for contouring and treatment planning. For WBRT, no fusion is typically needed, as the anatomical borders of the brain will determine the borders of the treatment fields. However, MRI fusion is required for hippocampal-sparing WBRT, a technique associated with memory preservation and improved quality of life, to ensure the lack of visible metastases in the bilateral hippocampal regions and for accurate contouring (40). For SRS planning, the T1-weighted post-contrast sequence is generally able to visualize the metastases. A T1-weighted post-contrast spoiled GRE sequence, known for high spatial resolution to display anatomical structures of both normal brain and tumors (41) and to detect small brain metastases (42), is also often requested. These two MR sequences are fused to the planning CT, and a GTV is contoured encompassing the visible lesion with a 0–2 mm expansion to PTV.

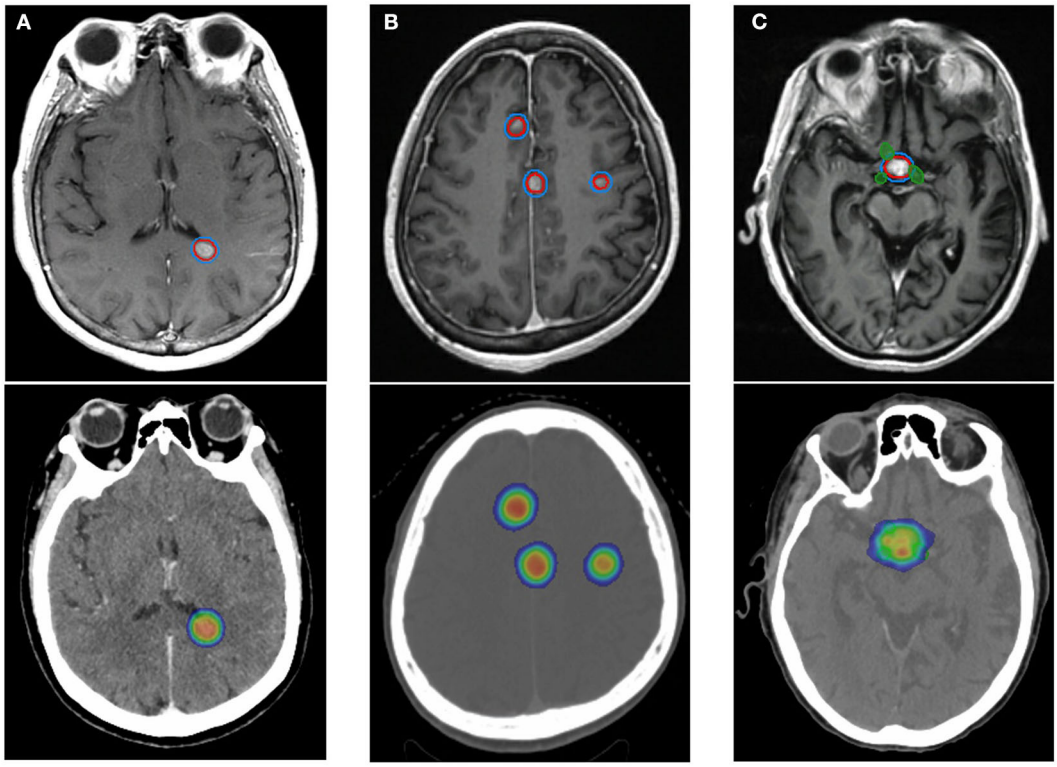

FIGURE 6 | The planning target volumes and corresponding radiation plan for three patients using stereotactic radiosurgery and altered fractionation depending on number and location of metastases relative to organs at risk. **(A)** A patient with a single brain metastasis treated with 21 Gy in 1 fraction. No organs at risk fall within the treatment fields. **(B)** A patient with multiple brain metastases, each treated with 27 Gy in 3 fractions. The lesions are close to one another and are located at the midline. **(C)** A patient with a single brain metastasis overlying the optic chiasm, *green*, treated with 30 Gy in 5 fractions. GTV, *red*. PTV, *blue*. The radiation dose gradient depicts 10 Gy as *blue* and >100% of prescribed dose as *orange*.

To safely deliver radiation to the brain, it is important to note the proximity of a tumor to organs at risk (OARs). The doses to OARs are constrained according to empirically derived limits and can vary by institution and study group. Whether the mean radiation dose to the organ or the maximum point dose to the organ is constrained during radiation planning depends on whether the organ functions serially (such as the brainstem), in parallel (such as the brain parenchyma), or both. The common OARs that are constrained in the head are the lens, eyes, lacrimal glands, optic nerves, optic chiasm, cochlea, pituitary, and brainstem (**Table 2**). Each structure is carefully contoured during treatment planning so that toxicities are limited (**Figure 5**). The proximity of a tumor to an OAR will alter a planned dose and fractionation so that dose limits are not exceeded, and patients are spared risk of toxicity (**Figure 6**). MR imaging can detect toxicity to OARs after RT. For example, decreased white matter fiber integrity in the para-hippocampal cingulum after brain irradiation demonstrated by MR diffusion tensor imaging (DTI) is thought to relate to late cognitive decline (43).

Post-radiation Evaluation

Patients are usually evaluated every 2–3 months for 1–2 years after RT with high-resolution MRI to determine treatment response and are followed by interval scans every 4–6 months thereafter. The Response Assessment in Neuro-Oncology group defined treatment response using criteria that include T1 gadolinium enhancing disease, T2 and FLAIR changes, the appearance of new lesions, corticosteroid requirement, and clinical status. Evaluation of treatment response can be complicated by several factors, including radiation inflammation, radionecrosis, and recurrence of the tumor (44). Post-radiation changes to tumors and normal tissue vary over time and are typically observed as acute (during or immediately following RT), subacute (within 3 months of RT), or late (months to years after RT). Acute-onset encephalopathy related to RT may not have associated imaging findings but will likely have associated symptoms that will prompt neuroimaging, such as headache, nausea, vomiting, fever, altered mental status, worsening neurologic symptoms, and increased intracranial pressure. It is estimated that ∼5% of patients receiving SRS to the brain will present with acute neurotoxicity (45), and MRI can show varying amounts of edema. Depending on the imaging findings and the severity of symptoms, high-dose steroids can often improve the acute effects of brain irradiation, and, occasionally, surgery is warranted. Subacute radiation effects include increased inflammation, which may cause a tumor

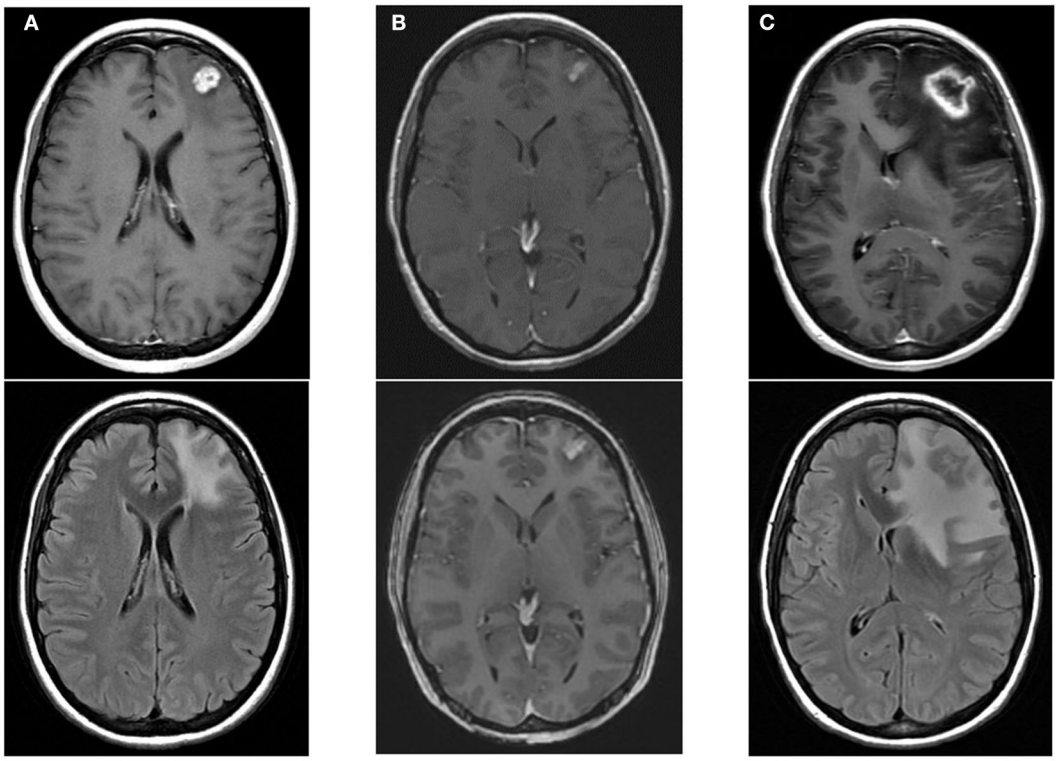

FIGURE 7 | An example of radiation necrosis after stereotactic radiosurgery with 21 Gy in 1 fraction with upper images showing T1-post contrast and the lower images showing edema. **(A)** Pre-radiotherapy scans showing a left frontal metastasis. **(B)** 2 months post-RT scans showing contraction of the treated metastasis with some effacement of the ventricles. **(C)** 6 months post-RT peripheral enhancement of treated metastasis with a necrotic center and associated edema, ultimately requiring surgical intervention.

to appear larger on MRI than it was before radiation. In addition, some chemotherapies, such as temozolomide, can cause pseudoprogression in the subacute context, making irradiated brain lesions look like they have progressed on MRI when they have not (46). If a patient with suspected pseudoprogression is asymptomatic, they are typically monitored with follow-up MRI to rule out genuine disease progression. Late changes after radiation include stabilization or contraction of the observed lesion if there has been treatment response. MR SWI sequences can show microbleeds after radiation that increase in frequency over time (47). In the subacute to late setting, potentially symptomatic radiation necrosis can also occur, with mass effect and neurologic dysfunction.

Radiation oncologists often rely on MRI to identify radiation necrosis. Radiation necrosis is hypothesized to be related to vascular injury and glial and white matter damage, as well as effects on the fibrinolytic enzyme system and immune mechanisms (48). The volume of irradiated brain increases the risk of this serious complication (49, 50). In a study of 206 patients with 310 brain metastases treated with SRS, radiation necrosis was observed in 24% of treated lesions, and roughly half were asymptomatic, unlikely to have been detected in the absence of MRI (49). Moreover, in autopsy studies of patients who underwent SRS for brain metastases, necrosis was noted as early as 3 weeks after treatment (51). Some indications of radiation necrosis that are noted on MRI are conversion from non-enhancing to enhancing lesions, new periventricular enhancement, and soap-bubble or Swiss cheese enhancement (48). To correctly distinguish necrosis from tumor recurrence, it is likely that multiple MRI sequences will be needed (52). There is some evidence that the DTI anisotropy ratio of a contrast-enhanced lesion is significantly lower in patients with radiation necrosis than in those with recurrent tumor, and facilitated diffusion favors radiation necrosis (53). MR spectroscopy, which can interrogate the chemical content of a volume of tissue may be useful in differentiating radiation necrosis from disease recurrence. Because necrotic tissue and treated tumor should have different metabolic profiles, identifying metabolic spectra can differentiate necrosis and treatment response (54). There is also some evidence of elevated lipid levels in necrotic brain tissue that may be detectable on MR spectroscopy (55). As tumors are generally more metabolically active than necrotic tissue, fluorine-18 fluorodeoxyglucose (FDG) PET-CT activity can also help distinguish progression relative to radiation injury, though it is not as predictive as perfusion imaging (56). An example of radiation necrosis after SRS is shown in **Figure 7**.

A recurrent brain metastasis can be obscured by post-treatment inflammation and radionecrosis, so it is important to

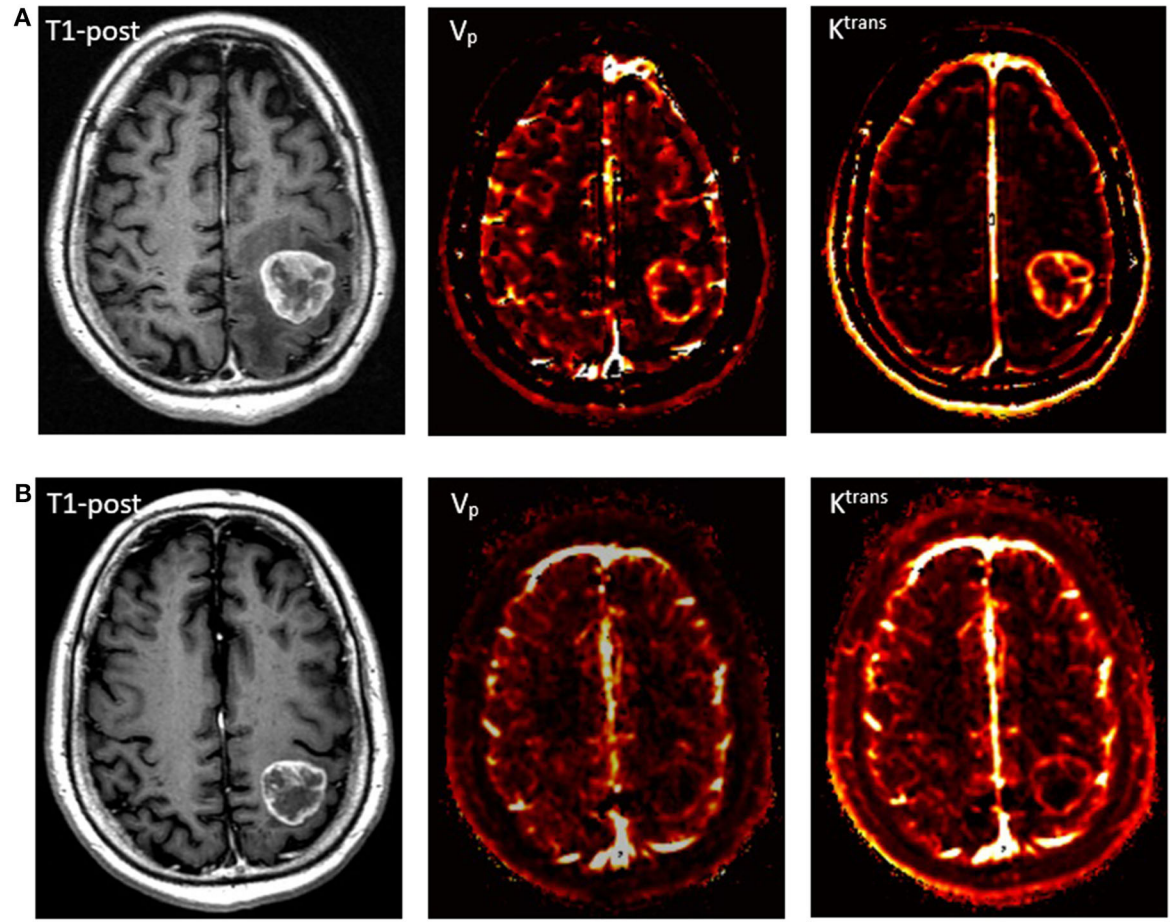

FIGURE 8 | Perfusion imaging of a patient with metastatic squamous cell carcinoma. **(A)** A pre-treatment T1-post contrast MRI with corresponding V_p and K^{trans} perfusion imaging demonstrating increased signal. **(B)** 2-month follow-up scan after receiving SRS with 27 Gy in 3 fractions showing slight contraction of the mass on T1-post MRI and marked decrease in perfusion.

carefully rule out these side effects during follow-up imaging. Because DCE MRI can provide insight into tumor vascularity and hemodynamics, plasma volume (V_p) and the volume transfer coefficient (K^{trans}) can aid in deciphering brain metastasis recurrence during post-treatment diagnostic imaging. These MR sequences use a two-compartment kinetic model, where contrast is initially assumed to be within the blood plasma volume and, over time, it leaks into the interstitial space. V_p approximates tumor vascularity, and K^{trans} is proportional to the accumulation of contrast in the interstitial space, where it can indicate increased permeability. In contrast to gliomas that can produce molecules such as VEGF that disrupt the blood–brain barrier (57), metastatic disease generally does not affect the surrounding vascularity of the brain. Therefore, an increase in V_p after radiation, when the V_p signal was previously noted to nadir, is correlated with tumor recurrence (56). Elevated K^{trans} signal has also been associated with tumor recurrence compared with treatment-induced necrosis (58), and the combination of V_p and K^{trans} signals together can further improve sensitivity and specificity (56). An example of post-RT perfusion imaging is shown in **Figure 8**. Dynamic susceptibility contrast (DSC) MRI has similar perfusion parameters to DCE MRI, such as rCBV, but it is not preferred over DCE MRI because of worse spatial resolution and more artifacts (59). Like V_p and K^{trans}, elevated rCBV is shown to indicate recurrent metastatic tumors after brain SRS (60). As is the case with radionecrosis, in MR spectroscopy, the metabolic spectra of enhancing edema may be able to differentiate tumor recurrence. For example, *N*-acetyl aspartate (NAA) is suppressed and choline is elevated in both high-grade primary malignancies and secondary brain tumors; however, only the edema associated with primary tumors tends to have a relative increase in choline (61).

CONCLUSION

In the USA, radiation oncology split from diagnostic radiology training in 1969, as it was recognized that radiation oncology training should be specialized to accommodate increasing cancer detection, new imaging modalities, and improved radiation delivery. Because radiation oncologists often do not receive formal diagnostic radiology training, they are instead expected to partner with diagnostic radiologists, who can provide important

insight to guide clinical decision-making. As Sarah Donaldson, a former president of the Radiologic Society of North America and radiation oncologist, wrote, "[Radiation oncologists] need to see and measure tumors in every dimension, understand how tumors move, their heterogeneity, their blood supply, and their molecular pathways. More than ever before in the history of radiology, radiation oncologists have an intensely strong interrelationship that already aligns radiologists as partners." (62) Though there have been numerous advances in imaging, including MRI with DWI, DTI, SWI/GRE, DCE/DSC, MR spectroscopy, and APT MR, these methods are not always incorporated into clinical decision-making by radiation oncologists. Thus, the close partnership between radiologists and radiation oncologists will allow these exciting technologies to become commonplace in radiation oncology clinical practice and, ultimately, lead to earlier brain metastases detection, improved radiotherapy treatment planning, more accurate treatment delivery, and optimal post-therapy monitoring.

AUTHOR CONTRIBUTIONS

NW and TY both evaluated the scientific literature and wrote the review together. Both authors contributed to the article and approved the submitted version.

FUNDING

Funding support for this study was provided by the National Institute of Health (NIH), NIH-NCI U54CA137788/U54CA132378.

REFERENCES

1. Gavrilovic I, Posner J. Brain metastases: epidemiology and pathophysiology. *J Neurooncol*. (2005) 75:5–14. doi: 10.1007/s11060-004-8093-6
2. Soffietti R, Cornu P, Delattre JY, Grant R, Graus F, Grisold W, et al. EFNS Guidelines on diagnosis and treatment of brain metastases: report of an EFNS Task Force. *Eur J Neurol*. (2006) 13:674–81. doi: 10.1111/j.1468-1331.2006.01506.x
3. Chang E, Lo S. Diagnosis and management of central nervous system metastases from breast cancer. *Oncologist*. (2003) 8:398–410. doi: 10.1634/theoncologist.8-5-398
4. Barnholtz-Sloan JS, Sloan AE, Davis FG, Vigneau FD, Lai P, Sawaya RE. Incidence proportions of brain metastases in patients diagnosed (1973 to 2001) in the Metropolitan Detroit Cancer Surveillance System. *J Clin Oncol*. (2004) 22:2865–72. doi: 10.1200/JCO.2004.12.149
5. DeAngelis L. Management of brain metastases. *Cancer Investig*. (1994) 12:156–65. doi: 10.3109/07357909409024871
6. Schouten LJ, Rutten J, Huveneers HA, Twijnstra A. Incidence of brain metastases in a cohort of patients with carcinoma of the breast, colon, kidney, and lung and melanoma. *Cancer*. (2002) 94:2698–705. doi: 10.1002/cncr.10541
7. Chao J, Phillips R, Nickson JJ. Roentgen-ray therapy of cerebral metastases. *Cancer*. (1954) 7:682–9. doi: 10.1002/1097-0142(195407)7:4<682::AID-CNCR2820070409>3.0.CO;2-S
8. Patchell R, Tibbs PA, Regine WF, Dempsey RJ, Mohiuddin M, Kryscio RJ, et al. Postoperative radiotherapy in the treatment of single metastases to the brain: a randomized trial. *JAMA*. (1998) 280:1485–9. doi: 10.1001/jama.280.17.1485
9. Noordijk EM, Vecht CJ, Haaxma-Reiche H, Padberg GW, Voormolen JH, Hoekstra FH, et al. The choice of treat-ment of single brain metastasis should be based on extracranial tumoractivity and age. *Int J Radiat Oncol Biol Phys*. (1994) 29:711–7. doi: 10.1016/0360-3016(94)90558-4
10. Shinde A, Akhavan D, Sedrak M, Glaser S, Amini A. Shifting paradigms: whole brain radiation therapy versus stereotactic radiosurgery for brain metastases. *CNS Oncol*. (2019) 8:1. doi: 10.2217/cns-2018-0016
11. Andrews DW, Scott CB, Sperduto PW, Flanders AE, Gaspar LE, Schell MC, et al. Whole brain radiation therapy with or without stereotactic radiosurgery boost for patients with one to three brain metastases: phase III results of the RTOG 9508 randomised trial. *Lancet*. (2004) 363:1665–72. doi: 10.1016/S0140-6736(04)16250-8
12. Aoyama H, Shirato H, Tago M, Nakagawa K, Toyoda T, Hatano K, et al. Stereotactic radiosurgery plus whole-brain radiation therapy vs stereotactic radiosurgery alone for treatment of brain metastases: a randomized controlled trial. *JAMA*. (2006) 295:2483–91. doi: 10.1001/jama.295.21.2483
13. Yamamoto M, Serizawa T, Shuto T, Akabane A, Higuchi Y, Kawagishi J, et al. Stereotactic radiosurgery for patients with multiple brain metastases (JLGK0901): a multi-institutional prospective observational study. *Lancet Oncol*. (2014) 15:387–95. doi: 10.1016/S1470-2045(14)70061-0
14. National Comprehensive Cancer Network Clinic Practice Guidelines in Oncology. *Central Nervous System Cancers* (Version 3.2019) (2019). Available online at: https://www.nccn.org/professionals/physician_gls/pdf/cns.pdf (accessed November 23, 2019).
15. Cha S. Update on brain tumor imaging: from anatomy to physiology. *Am J Neuroradiol*. (2006) 27:475–87. Available online at: http://www.ajnr.org/content/27/3/475.long
16. Hwang T, Close T, Grego J, Brannon W, Gonzales F. Predilection of brain metastasis in gray and white matter junction and vascular border zones. *Cancer*. (1996) 77:1551–5. doi: 10.1002/(SICI)1097-0142(19960415)77:8<1551::AID-CNCR19>3.0.CO;2-Z
17. Delattre JY, Krol G, Thaler HT, Posner JB. Distribution of brain metastases. *Arch Neurol*. (1988) 45:741–4. doi: 10.1001/archneur.1988.00520310047016
18. Graif M, Bydder GM, Steiner RE, Niendorf P, Thomas DG, Young IR. Contrast-enhanced MR imaging of malignant brain tumors. *AJNR*. (1985) 6:855–62.
19. Sze G, Milano E, Johnson C, Heier L. Detection of brain metastases: comparison of contrast-enhanced MR with unenhanced MR and enhanced CT. *Am J Neuroradiol*. (1990) 11:785–91.
20. Isiklar I, Leeds NE, Fuller GN, Kumar AJ. Intracranial metastatic melanoma: correlation between MR imaging characteristics and melanin content. *Am J Roentgenol*. (1995) 165:1503–12. doi: 10.2214/ajr.165.6.7484597
21. Fink KR, Fink JR. Imaging of brain metastases. *Surg Neurol Int*. (2013) 4:S209–19. doi: 10.4103/2152-7806.111298
22. Wycliffe ND, Choe J, Holshouser B, Oyoyo UE, Haacke EM, Kido DK. Reliability in detection of hemorrhage in acute stroke by a new three-dimensional gradient recalled echo susceptibility-weighted imaging technique compared to computed tomography: a retrospective study. *J Magn Reson Imaging*. (2004) 20:372–7. doi: 10.1002/jmri.20130
23. Long DM. Capillary ultrastructure in human metastatic brain tumors. *J Neurosurg*. (1979) 51:53–8. doi: 10.3171/jns.1979.51.1.0053
24. Oshiro S, Tsugu H, Komatsu F, Abe H, Ohmura T, Sakamoto S, et al. Metastatic adenocarcinoma in the brain: magnetic resonance imaging with pathological correlations to mucin content. *Anticancer Res*. (2008) 28:407–13. Available online at: http://ar.iiarjournals.org/content/28/1B/407.long
25. Maier SE, Sun Y, Mulkern RV. Diffusion imaging of brain tumors. *NMR Biomed*. (2010) 23:849–64. doi: 10.1002/nbm.1544
26. Lee EJ, terBrugge K, Mikulis D, Choi DS, Bae JM, Lee SK, et al. Diagnostic value of peritumoral minimum apparent diffusion coefficient for differentiation of glioblastoma multiforme from solitary metastatic lesions. *Am J Roentgenol*. (2011) 196:71–6. doi: 10.2214/AJR.10.4752
27. Law M, Cha S, Knopp EA, Johnson G, Arnett J, Litt AW. High-grade gliomas and solitary metastases: differentiation by using

perfusion and proton spectroscopic MR imaging. *Radiology*. (2002) 222:715–21. doi: 10.1148/radiol.2223010558
28. Silverman C, Marks JE. Prognostic significance of contrast enhancement in low-grade astrocytomas of the adult cerebrum. *Radiology*. (1982) 139:211–3. doi: 10.1148/radiology.139.1.7208924
29. Stadnik TW, Demaerel P, Luypaert RR, Chaskis C, Van Rompaey KL, Michotte A, et al. Imaging tutorial: differential diagnosis of bright lesions on diffusion-weighted MR images. *Radiographics*. (2003) 23:e7. doi: 10.1148/rg.e7
30. Kidwell CS, Villablanca JP, Saver JL. Advances in neuroimaging of acute stroke. *Curr Atheroscler Rep*. (2000) 2:126–35. doi: 10.1007/s11883-000-0107-z
31. Huisman TA. Tumor-like lesions of the brain. *Cancer Imaging*. (2009) 9A:S10. doi: 10.1102/1470-7330.2009.9003
32. Schaefer PW. Applications of DWI in clinical neurology. *J Neurol Sci*. (2001) 186:S25–35. doi: 10.1016/S0022-510X(01)00488-9
33. Dooms GC, Hecht S, Brant-Zawadzki M, Berthiaume Y, Norman D, Newton TH. Brain radiation lesions: MR imaging. *Radiology*. (1986) 158:149–55. doi: 10.1148/radiology.158.1.3940373
34. Zhou J, Tryggestad E, Wen Z, Lal B, Zhou T, Grossman R, et al. Differentiation between glioma and radiation necrosis using molecular magnetic resonance imaging of endogenous proteins and peptides. *Nat Med*. (2011) 17:130. doi: 10.1038/nm.2268
35. National Comprehensive Cancer Network Clinic Practice Guidelines in Oncology. *Central Nervous System Cancers* (Version 3.2019) (2019). Available online at: https://www.nccn.org/professionals/physician_gls/pdf/cns.pdf (accessed November 23, 2019).
36. Ewend MG, Morris DE, Carey LA, Ladha AM, Brem S. Guidelines for the initial management of metastatic brain tumors: role of surgery, radiosurgery, and radiation therapy. *J Natl Compr Cancer Netw*. (2008) 6:505–14. doi: 10.6004/jnccn.2008.0038
37. Blomain ES, Kim H, Garg S, Bhamidipati D, Guo J, Kalchman I, et al. Stereotactic radiosurgery practice patterns for brain metastases in the United States: a national survey. *J Radiat Oncol*. (2018) 7:241–6. doi: 10.1007/s13566-018-0353-8
38. Sandler KA, Shaverdian N, Cook RR, Kishan AU, King CR, Yang I, et al. Treatment trends for patients with brain metastases: does practice reflect the data? *Cancer*. (2017) 123:2274–82. doi: 10.1002/cncr.30607
39. Purdy JA. Current ICRU definitions of volumes: limitations and future directions. *Semin Radiat Oncol*. (2004) 14:27–40. doi: 10.1053/j.semradonc.2003.12.002
40. Gondi V, Tomé WA, Mehta MP. Why avoid the hippocampus? A comprehensive review. *Radiother Oncol*. (2010) 97:370–6. doi: 10.1016/j.radonc.2010.09.013
41. Hou BL, Hu J. MRI and MRS of human brain tumors. *Tumor Biomark Discov*. (2009) 520:297–314. doi: 10.1007/978-1-60327-811-9_21
42. Nagai A, Shibamoto Y, Mori Y, Hashizume C, Hagiwara M, Kobayashi T. Increases in the number of brain metastases detected at frame-fixed, thin-slice MRI for gamma knife surgery planning. *Neuro Oncol.* (2010) 12:1187–92. doi: 10.1093/neuonc/noq084
43. Chapman CH, Nagesh V, Sundgren PC, Buchtel H, Chenevert TL, Junck L, et al. Diffusion tensor imaging of normal-appearing white matter as biomarker for radiation-induced late delayed cognitive decline. *Int J Radiat Oncol Biol Phys*. (2012) 82:2033–40. doi: 10.1016/j.ijrobp.2011.01.068
44. Lin NU, Lee EQ, Aoyama H, Barani IJ, Barboriak DP, Baumert BG, et al. Response assessment criteria for brain metastases: proposal from the RANO group. *lancet Oncol.* (2015) 16:e270–e278. doi: 10.1016/S1470-2045(15)70057-4
45. Shaw EG, Coffey RJ, Dinapoli RP. Neurotoxicity of radiosurgery. *Semin Radiat Oncol*. (2005) 5:235–45. doi: 10.1016/S1053-4296(05)80022-0
46. Brandes AA, Tosoni A, Spagnolli F, Frezza G, Leonardi M, Calbucci F, et al. Disease progression or pseudoprogression after concomitant radiochemotherapy treatment: pitfalls in neurooncology. *Neuro Oncol.* (2008) 10:361–7. doi: 10.1215/15228517-2008-008
47. Bian W, Hess CP, Chang SM, Nelson SJ, Lupo JM. Susceptibility-weighted MR imaging of radiation therapy-induced cerebral microbleeds in patients with glioma: a comparison between 3T and 7T. *Neuroradiology*. (2014) 56:91–6. doi: 10.1007/s00234-013-1297-8
48. Kumar AJ, Leeds NE, Fuller GN, Van Tassel P, Maor MH, Sawaya RE, et al. Malignant gliomas: MR imaging spectrum of radiation therapy- and chemotherapy-induced necrosis of the brain after treatment. *Radiology*. (2000) 217:377–84. doi: 10.1148/radiology.217.2.r00nv36377
49. Minniti G, Clarke E, Lanzetta G, Osti MF, Trasimeni G, Bozzao A, et al. Stereotactic radiosurgery for brain metastases: analysis of outcome and risk of brain radionecrosis. *Radiat Oncol*. (2001) 6:48. doi: 10.1186/1748-717X-6-48
50. Blonigen BJ, Steinmetz RD, Levin L, Lamba MA, Warnick RE, Breneman JC. Irradiated volume as a predictor of brain radionecrosis after linear accelerator stereotactic radiosurgery. *Int J Radiat Oncol Biol Phys*. (2010) 77:996–1001. doi: 10.1016/j.ijrobp.2009.06.006
51. Koike Y, Hosoda H, Ishiwata Y, Sakata K, Hidaka K. Effect of radiosurgery using Leksell gamma unit on metastatic brain tumor—autopsy case report. *Neurol Med Chir*. (1994) 34:534–7. doi: 10.2176/nmc.34.534
52. Mullins ME, Barest GD, Schaefer PW, Hochberg FH, Gonzalez RG, Lev MH. Radiation necrosis versus glioma recurrence: conventional MR imaging clues to diagnosis. *Am J Neuroradiol*. (2005) 26:1967–72. Available online at: http://www.ajnr.org/content/26/8/1967.long
53. Shah R, Vattoth S, Jacob R, Manzil FF, O'Malley JP, Borghei P, et al. Radiation necrosis in the brain: imaging features and differentiation from tumor recurrence. *Radiographics*. (2012) 32:1343–59. doi: 10.1148/rg.325125002
54. Chiang IC, Kuo YT, Lu CY, Yeung KW, Lin WC, Sheu FO, et al. Distinction between high-grade gliomas and solitary metastases using peritumoral 3-T magnetic resonance spectroscopy, diffusion, and perfusion imagings. *Neuroradiology*. (2004) 46:619–27. doi: 10.1007/s00234-004-1246-7
55. Kuesel AC, Sutherland GR, Halliday W, Smith IC. 1H MRS of high grade astrocytomas: mobile lipid accumulation in necrotic tissue. *NMR Biomed*. (1994) 7:149–55. doi: 10.1002/nbm.1940070308
56. Hatzoglou V, Yang TJ, Omuro A, Gavrilovic I, Ulaner G, Rubel J, et al. A prospective trial of dynamic contrast-enhanced MRI perfusion and fluorine-18 FDG PET-CT in differentiating brain tumor progression from radiation injury after cranial irradiation. *Neuro Oncol*. (2015) 18:873–80. doi: 10.1093/neuonc/nov301
57. Hardee MR, Zagzag D. Mechanisms of glioma-associated neovascularization. *Am J Pathol*. (2012) 181:1126–41. doi: 10.1016/j.ajpath.2012.06.030
58. Jain R, Narang J, Sundgren PM, Hearshen D, Saksena S, Rock JP, et al. Treatment induced necrosis versus recurrent/progressing brain tumor: going beyond the boundaries of conventional morphologic imaging. *J Neuro Oncol*. (2010) 100:17–29. doi: 10.1007/s11060-010-0139-3
59. Salama GR, Heier LA, Patel P, Ramakrishna R, Magge R, Tsiouris AJ. Diffusion weighted/tensor imaging, functional MRi and Perfusion weighted imaging in glioblastoma—foundations and future." *Front Neurol*. (2018) 8:660. doi: 10.3389/fneur.2017.00660
60. Barajas RF, Chang JS, Sneed PK, Segal MR, McDermott MW, Cha S. Distinguishing recurrent intra-axial metastatic tumor from radiation necrosis following gamma knife radiosurgery using dynamic susceptibility-weighted contrast-enhanced perfusion MR imaging. *Am J Neuroradiol*. (2009) 30:367–72. doi: 10.3174/ajnr.A1362
61. Falini A, Calabrese G, Origgi D, Lipari S, Triulzi F, Losa M, et al. Proton magnetic resonance spectroscopy and intracranial tumours: clinical perspectives. *J Neurol*. (1996) 243:706–14. doi: 10.1007/BF00873976
62. Donaldson SS. The power of partnerships: a message for all radiologists. *Radiology*. (2014) 271:315–9. doi: 10.1148/radiol.14140272

Conflict of Interest: The authors declare that the research was conducted in the absence of any commercial or financial relationships that could be construed as a potential conflict of interest.

frontiers in Neurology

BRIEF RESEARCH REPORT
published: 27 October 2020
doi: 10.3389/fneur.2020.587327

Accelerated Post-contrast Wave-CAIPI T1 SPACE Achieves Equivalent Diagnostic Performance Compared With Standard T1 SPACE for the Detection of Brain Metastases in Clinical 3T MRI

Augusto Lio M. Goncalves Filho[1,2,3]*, *John Conklin*[1,2,3], *Maria Gabriela F. Longo*[1,2,3], *Stephen F. Cauley*[1,2,3], *Daniel Polak*[2,4], *Wei Liu*[5], *Daniel N. Splitthoff*[4], *Wei-Ching Lo*[6], *John E. Kirsch*[1,2,3], *Kawin Setsompop*[1,2,3,7], *Pamela W. Schaefer*[1,3], *Susie Y. Huang*[1,2,3,7] *and Otto Rapalino*[1,3]

[1] Department of Radiology, Massachusetts General Hospital, Boston, MA, United States, [2] Athinoula A. Martinos Center for Biomedical Imaging, Charlestown, MA, United States, [3] Harvard Medical School, Boston, MA, United States, [4] Siemens Healthcare GmbH, Erlangen, Germany, [5] Siemens Shenzhen Magnetic Resonance Ltd., Shenzhen, China, [6] Siemens Medical Solutions, Boston, MA, United States, [7] Harvard-MIT Division of Health Sciences and Technology, Cambridge, MA, United States

Background and Purpose: Brain magnetic resonance imaging (MRI) examinations using high-resolution 3D post-contrast sequences offer increased sensitivity for the detection of metastases in the central nervous system but are usually long exams. We evaluated whether the diagnostic performance of a highly accelerated Wave-controlled aliasing in parallel imaging (Wave-CAIPI) post-contrast 3D T1 SPACE sequence was non-inferior to the standard high-resolution 3D T1 SPACE sequence for the evaluation of brain metastases.

Materials and Methods: Thirty-three patients undergoing evaluation for brain metastases were prospectively evaluated with a standard post-contrast 3D T1 SPACE sequence and an optimized Wave-CAIPI 3D T1 SPACE sequence, which was three times faster than the standard sequence. Two blinded neuroradiologists performed a head-to-head comparison to evaluate the visualization of pathology, perception of artifacts, and the overall diagnostic quality. Wave–CAIPI post-contrast T1 SPACE was tested for non-inferiority relative to standard T1 SPACE using a 15% non-inferiority margin.

Results: Wave–CAIPI post-contrast T1 SPACE was non-inferior to the standard T1 SPACE for visualization of enhancing lesions ($P < 0.01$) and offered equivalent diagnostic quality performance and only marginally higher background noise compared to the standard sequence.

OPEN ACCESS

Edited by:
Tarik F. Massoud, Stanford University, United States

Reviewed by:
Bo Gao, Affiliated Hospital of Guizhou Medical University, China
Fulvio Zaccagna, University of Toronto, Canada

***Correspondence:**
Augusto Lio M. Goncalves Filho
afilho@mgh.harvard.edu

Specialty section:
This article was submitted to Applied Neuroimaging, a section of the journal Frontiers in Neurology

Received: *25 July 2020*
Accepted: *30 September 2020*
Published: *27 October 2020*

Citation:
Goncalves Filho ALM, Conklin J, Longo MGF, Cauley SF, Polak D, Liu W, Splitthoff DN, Lo W-C, Kirsch JE, Setsompop K, Schaefer PW, Huang SY and Rapalino O (2020) Accelerated Post-contrast Wave-CAIPI T1 SPACE Achieves Equivalent Diagnostic Performance Compared With Standard T1 SPACE for the Detection of Brain Metastases in Clinical 3T MRI. Front. Neurol. 11:587327. doi: 10.3389/fneur.2020.587327

Conclusions: Our findings suggest that Wave-CAIPI post-contrast T1 SPACE provides equivalent visualization of pathology and overall diagnostic quality with three times reduced scan time compared to the standard 3D T1 SPACE.

Keywords: brain, metastases, magnetic resonance imaging, parallel imaging, Wave-CAIPI, post-contrast, high-resolution, 3D

INTRODUCTION

Brain metastases are the most common tumors of the central nervous system (CNS) (1). However, their true incidence is probably underestimated as they may be asymptomatic in 60–70% of cases (2), or even some are overlooked in severely ill patients. Nevertheless, the current advancements in immunotherapeutic agents and improved local stereotactic radiosurgery demonstrate the importance of early surveillance for brain metastases. If CNS metastases are recognized earlier, when patients still have a good performance status, they can benefit from more aggressive treatment strategies (3). Certain malignancies are more frequently associated with brain metastases, including cancers of the lung, breast, skin (melanoma), colon, kidney, pancreas, testes, ovary, and cervix (1, 2, 4). Moreover, melanomas have the highest preference to metastasize to the brain (∼50%) (5).

Brain magnetic resonance imaging (MRI) provides high sensitivity for non-invasive diagnosis of intracranial metastases. It allows for a detailed evaluation of the different compartments of the CNS, including the skull, brain parenchyma, ependymal surface, leptomeninges, and pachymeninges. The intrinsic superior soft-tissue contrast and the multiplanar capability of MR imaging increase the sensitivity for the screening of secondary tumor implants. Metastases typically enhance after administering gadolinium contrast material due to the absence of the blood-tumor barrier (6). Contrast-enhanced MRI is considered the preferred modality for the evaluation of metastatic disease and is superior to other modalities such as computed tomography in detecting metastases from systemic melanoma or breast cancer (6).

There is much debate regarding which post-contrast T1-weighted pulse sequence is the best. The preference may vary according to the available field strength and other limitations in hardware and software resources at different sites. 3 Tesla (3T) MRI offers better signal-to-noise ratio and produces higher contrast between tumor and normal brain tissue than at 1.5T (7). Magnetization prepared 3D gradient recalled echo pulse sequences, that include MPRAGE, IR-SPGR, and BRAVO, are T1-weighted sequences that show excellent anatomical depiction and are widely available in clinical protocols. In fact, they are considered a pillar sequence in the standardized brain tumor protocol for gliomas (8) and in the minimum requirements for brain imaging recommended by the Response Assessment in Neuro-Oncology–Brain Metastases working group (9). However, gradient recalled echo (GRE)-based pulse sequences show brighter white matter signal and may potentially diminish the conspicuity of enhancing lesions due to the reduced contrast ratio (5). Conversely, Spin-Echo (SE)-based sequences offer increased contrast in enhancing lesions and better flow suppression, facilitating the distinction of cortical subcentimeter enhancing metastases from vessels that might otherwise appear as bright dots in GRE-based sequences (5).

The introduction of optimized 3D fast/turbo SE imaging, such as sampling perfection with application-optimized contrasts using different flip angle evolutions (SPACE), offers a robust and flexible approach for 3D SE-based imaging with the benefits of optimal contrast depiction and the added advantage of multiplanar reformatted viewing for evaluating tumor within the complex brain anatomy (10). A meta-analysis by Suh et al. (11) included studies that compared the detectability of brain metastases using SE or GRE contrast-enhanced sequences and found that 3D SE images using 1 mm thick slices are preferred for detecting brain metastases in 3T scans, notably for the detection of small lesions (11). Thus, the ideal recommended contrast-enhanced pulse sequence suggested in the most recent consensus publication on a standardized protocol for brain metastases imaging (5) favors the 3D SE-based sequence (SPACE) over the GRE-based pulse sequence (MPRAGE).

Several advanced MR techniques, including proton MR spectroscopy, diffusion, and perfusion imaging, increase the precision of tumor characterization and support the distinction of metastases from other entities. Hence, MR brain protocols for the evaluation of neoplasms often consist of multiple standard and advanced sequences that result in a prolonged scanning time, which may contribute to motion artifacts (12) and patient anxiety (13). The introduction of a new encoding technology that can accelerate the scan time of high-resolution sequences could facilitate broader application of the advantages of 3D SE-based MRI, such as SPACE (14). Wave-controlled aliasing in parallel imaging (Wave-CAIPI) is an advanced technique that combines a corkscrew gradient trajectory with CAIPI shifts in the ky and kz directions to efficiently encode k-space and evenly spread the voxel aliasing in all dimensions, taking full advantage of the 3D coil sensitivity information to provide highly accelerated parallel imaging with negligible artifact and signal-to-noise ratio penalties (15). Wave-CAIPI is an advanced parallel imaging encoding technique that has been demonstrated to achieve highly accelerated structural imaging with negligible noise amplification using standard scanner hardware (16).

The goal of this study was to compare a highly accelerated Wave-CAIPI post-contrast 3D T1 SPACE sequence (Wave-T1 SPACE) with the commonly used standard high-resolution 3D T1 SPACE sequence for routine clinical brain imaging at 3T. We hypothesized that Wave-T1 SPACE is non-inferior to the standard sequence with equivalent

TABLE 1 | Demographic information and clinical diagnoses of participants.

Oncologic cases (*N* = 33)	
Age (mean ± SD, year)	58.2 ± 13.5
Sex (%)	
Male	12 (36%)
Female	21 (64%)
Systemic diagnosis (%)	
Melanoma	12 (36%)
Lung cancer	8 (24%)
Gastrointestinal cancer	5 (15%)
Breast cancer	4 (12%)
Lymphoma	1 (3%)
Thyroid cancer	1 (3%)
Biliary cancer	1 (3%)
Sarcoma	1 (3%)

diagnostic quality and an estimated three-fold reduction of acquisition time.

METHOD

Selection of Participants and Study Design

With Institutional Review Board (IRB) approval, 33 patients undergoing clinical brain MRI with and without contrast for the evaluation of brain metastases at a single institution were consecutively enrolled. Adult patients (age > 18 years) were scanned on a 3T MRI scanner (MAGNETOM Prisma, Siemens Healthcare, Erlangen, Germany) using a commercially available 20- or 32-channel receiver coil array. The study was Health Insurance Portability and Accountability Act compliant. The need for informed consent was waived by the institution's IRB since all MRI exams were acquired as part of the standard care of the enrolled individuals, without significant added time to each exam (i.e., <2 min of additional imaging per case). Instead, patients were provided with an information sheet describing the scope of the research study and could opt out prior to the start of the scan. All participants had a prior confirmed diagnosis of systemic tumor and came for MRI evaluation, in both inpatient and outpatient settings, in search of intracranial metastases or to evaluate previously diagnosed metastatic disease. Distribution of the study subjects and detailed systemic oncologic diagnoses are demonstrated in **Table 1**.

MRI Protocol

The accelerated post-contrast Wave-T1 SPACE was embedded in the standard contrast enhanced brain MRI protocol for oncologic evaluation. Each scan included a standard post-contrast T1 SPACE sequence and Wave-T1 SPACE sequence. Gadolinium-enhanced images were obtained after intravenous administration of standard dose of 0.2 ml/kg (0.1 mmol/kg) of gadoterate meglumine (Dotarem®, Guerbet; Paris, France) at a flow rate of ∼2 ml/s. Twenty-four studies were performed with the standard post-contrast T1 SPACE sequence acquired before Wave-T1 SPACE, and 9 studies were performed with the sequence order inverted, acquiring Wave-T1 SPACE before the standard T1 SPACE, to control for potential differences related to the order of acquisition.

TABLE 2 | Pulse sequence acquisition parameters.

	Standard T1-SPACE	**Wave-T1 SPACE**
Acquisition parameters		
FOV read (mm)	230	256
Matrix size	256 × 256	256 × 256
Slice thickness (mm)	0.9	1.0
TR/TE (ms)	700/11	700/12
Flip angle (degree)	120	120
Echo train length	38	43
Acceleration factor *R*	GRAPPA, *R* = 4	Wave-CAIPI, *R* = 9
Scan time	4 min 19 s	1 min 40 s

Wave-CAIPI Post-contrast T1 SPACE Sequence and Reconstruction

Wave-T1 SPACE was implemented using a prototype single slab 3D fast spin echo SPACE sequence (15). On-line reconstruction was performed using an autocalibrated procedure in which the true gradient trajectory is estimated during the reconstruction without the need for additional calibration scans. This allowed for simultaneous estimation of the parallel imaging reconstruction and the true k-space trajectory (17), with a reconstruction time of ∼60 s. We matched the main pulse sequence parameters that contribute to T1-weighted contrast (i.e., TR, TE, and flip angle) between the Wave-T1 SPACE and standard T1 SPACE sequences. The standard T1-SPACE sequence used in our institution's routine clinical protocol employs the default vendor reconstruction filter, which introduces a small degree of spatial smoothing. To provide comparable effective spatial resolution using the prototype Wave-T1 SPACE sequence, a slightly larger isotropic voxel size was used (0.9 vs. 1.0 mm). This resulted in visually comparable effective spatial resolution as evaluated by the study neuroradiologists. Additional sequence parameters are shown in **Table 2**.

Image Evaluation

Two neuroradiologists (O.R and S.Y.H.) with 18 and 8 years of experience, respectively, independently reviewed all images in a blinded and randomized fashion. A pre-determined 5-point grading scale was used to compare Wave-T1 SPACE with the standard T1 SPACE, following the scales set for previously published clinical validation studies of Wave-CAIPI sequences (18) and adapted for the evaluation of enhancing lesions. After the DICOM datasets had been anonymized, reviewers evaluated only the post-contrast images on an independent workstation and were allowed to adjust the window width and level settings for each image series for optimal viewing.

Reviewers underwent several head-to-head analysis sessions in which they evaluated the detection of pathological enhancement in common locations for metastatic seeding (parenchymal, leptomeningeal, dural, and ependymal), the

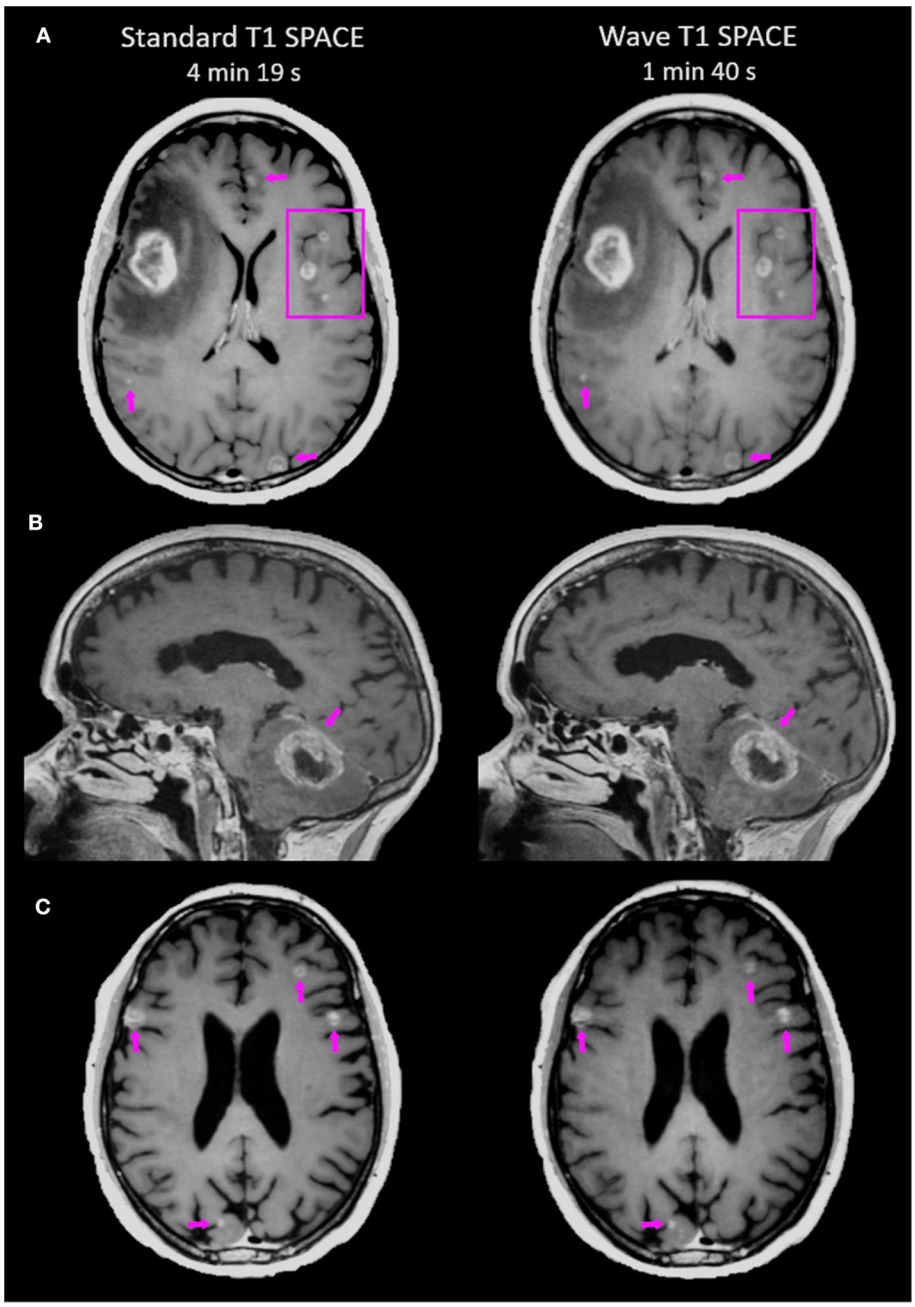

FIGURE 1 | Representative images comparing the post-contrast Standard T1 SPACE and Wave-T1 SPACE sequences. **(A)** A 25-year-old female with metastatic melanoma presenting a large mass in the right frontal lobe. Other smaller scattered enhancing metastases are visualized in both hemispheres (arrows and box). **(B)** Infratentorial intraparenchymal metastasis in a 76-year-old female with a history of melanoma. There is also abnormal dural enhancement on the overlying tentorium (arrow). **(C)** Multiple cortical/subcortical metastases in a 54-year-old man with lung cancer are equally visualized in both sequences (arrows).

presence of artifacts related to motion or background image noise, and the overall diagnostic quality. The screen position of the sequences and the order of the cases were randomized.

All cases were rated for each feature within the 5-point grading scale, where positive numbers favored the sequence on the right and negative numbers favored the sequence on the left side of the screen (**Supplementary Table 1**). Disagreements between readers were adjudicated by a third neuroradiologist (P.W.S.) with over 20 years of experience.

Statistical Analysis

We tested for non-inferiority of Wave-T1 SPACE compared to standard T1 SPACE in the head-to-head analysis. A non-inferiority margin (Δ) of 15% was chosen as part of a larger,

systematic evaluation of Wave-T1 SPACE for post-contrast imaging, with the null hypothesis (H_0) that the proportion of cases where standard T1 SPACE was preferred over Wave-T1 SPACE was >15% (19). We used the Z statistic to calculate the probability of the standard sequence being preferred over the Wave-T1 SPACE sequence in more than 15% of cases ($H_0 > \Delta$), with a type 1 error rate (α) of 0.05. Other descriptive data were summarized by the calculation of means and standard deviations. We also calculated the upper bound of the 95% confidence interval for the proportion of cases where standard T1 SPACE was preferred over Wave-T1 SPACE, i.e., the critical value, $P_{critical}$. The interrater agreement was reported using the quadratically weighted Cohen κ to disproportionately penalize larger disagreements. The agreement of categorical variables was interpreted according to Landis and Koch (20). All statistical calculations were performed using R version 3.6.3.

RESULTS

All the 33 oncologic cases were successfully acquired and evaluated. In the head-to-head comparison, abnormal enhancement concerning for metastases was detected in 20 cases (60%) (**Figure 1**). Of the 20 cases that showed abnormal enhancement, 15 (75%) had parenchymal enhancement, 10 (50%) had dural enhancement, 10 (50%) had leptomeningeal enhancement, and 2 (10%) had ependymal enhancement, with 11 showing more than one type of enhancing lesion. Interrater agreement ranged from moderate to substantial ($\kappa = 0.40$ for visualization of enhancing lesions, 0.52 for artifacts, 0.68 for diagnostic quality). The results of the head-to-head comparison and the non-inferiority testing are shown in **Figure 2**. Wave-T1 SPACE was non-inferior to standard T1 SPACE for delineating enhancing pathology with most cases being rated as equivalent by reviewers (19 of 20 cases, 98%). In one case (1 of 20 cases, 2%), Wave-T1 SPACE was preferred over the standard sequence. From the complete cohort, most cases (65%) were considered equivalent for evaluation of the general perception of artifacts, in 18 cases (55%) for noise level and 25 cases (76%) for motion. In only two cases (3%), the Wave-T1 SPACE was preferred over the standard sequence for perception of artifacts. The standard sequence was preferred over Wave-T1 SPACE for presenting less background noise in 14 cases (42%) and in 7 cases (21%) for fewer motion artifacts, but this difference did not affect the visualization of underlying structures nor obscured any

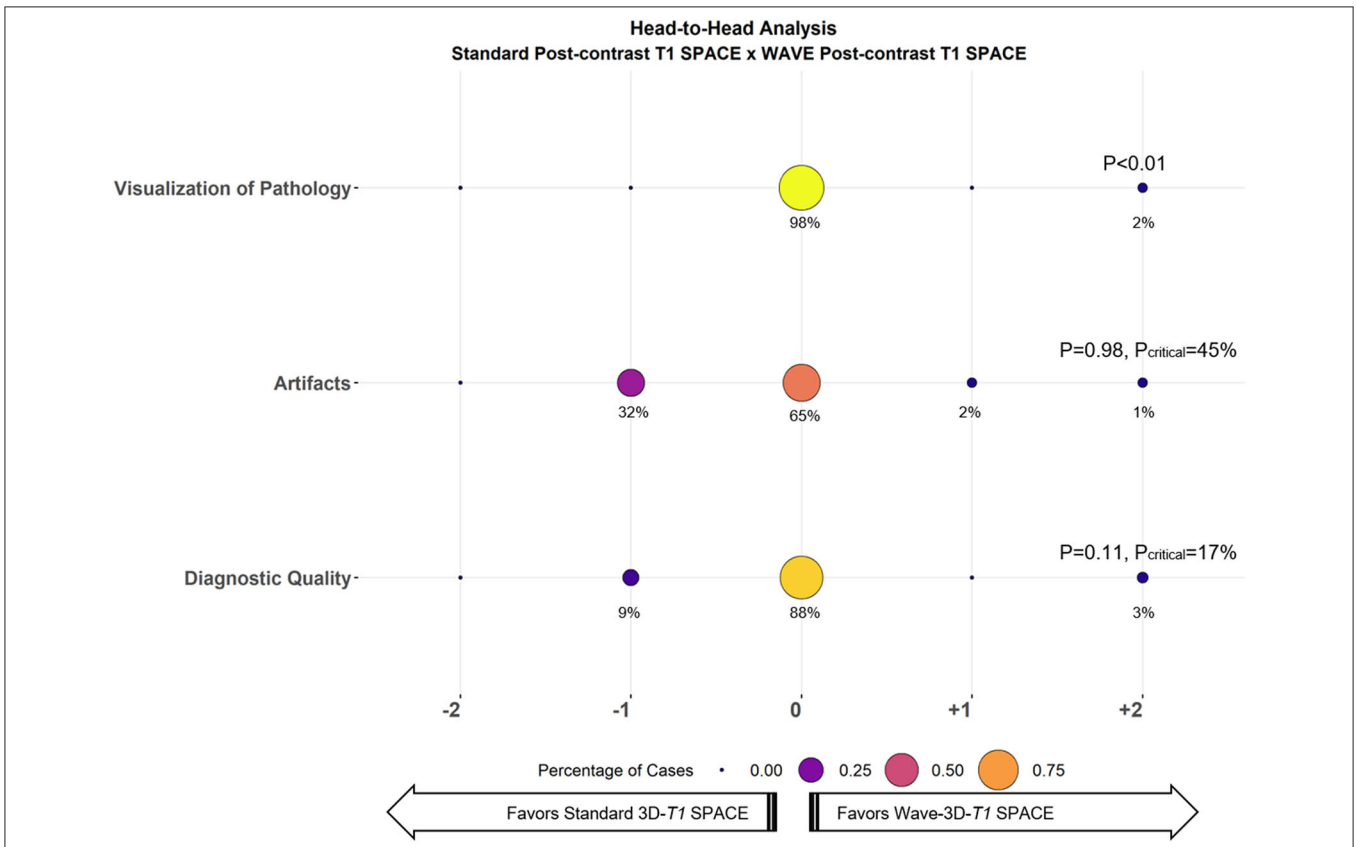

FIGURE 2 | Balloon plot showing the results of the head-to-head comparison of Standard T1 SPACE and Wave-T1 SPACE for visualization of pathology (i.e., enhancing lesions), artifacts, and diagnostic quality. Each circle's size and color represent the percentage of cases assigned a given score from a total of 33 cases. The percentage of cases receiving a given score is indicated below each circle. A zero-score indicates equivalency, negative scores (left) favor Standard T1 SPACE, and positive scores (right) favor Wave-T1 SPACE. The critical value ($P_{critical}$) is also provided, corresponding to the upper bound of the 95% confidence interval for the proportion of cases in which Standard T1 SPACE was preferred.

small lesions. The overall diagnostic quality was considered equivalent in 88% of the sample (29 cases, of 33). In three cases (9%), the standard sequence was preferred without affecting the final clinical diagnosis. In one case (3%), Wave-T1 SPACE was preferred to the extent that it would affect the final clinical diagnosis, due to the presence of extensive motion artifact on the standard sequence. To better validate the comparison of Wave-T1 SPACE with the standard sequence, we also performed additional sub analyses by coil channel, by order of acquisition, and expanded the evaluation of visualization of enhancement by each compartment (parenchymal, leptomeningeal, dural, and ependymal). The results showed that Wave-T1 SPACE provided equivalent visualization of enhancing pathology independently of the number of channels in the coil array and the order of acquisition (**Supplementary Figures 1–5**). However, given the larger number of independent coil elements in the 32-channel coil, we observed an improvement in the image signal-to-noise ratio (SNR) and noise amplification (g-factor), which translated in a better performance of the diagnostic quality in this subset of cases.

DISCUSSION

This study compared the performance of highly accelerated 3D Wave-T1 SPACE to the standard 3D T1 SPACE sequence in the visualization and diagnostic evaluation of brain metastases. Wave-T1 SPACE showed equivalent diagnostic performance for delineating enhancing metastases and was three times faster than the standard sequence. Wave-T1 SPACE images were slightly noisier compared to the standard sequence, but this difference did not interfere with the final diagnosis. Our findings suggest that Wave-T1 SPACE could replace standard T1 SPACE for the evaluation of brain metastases, as the advantages of lesion detection of the thin slice 3D SE-based pulse sequence are preserved and the gains in saved acquisition time would improve patient comfort and utilization of MR resources. The decreased scan time of Wave-CAIPI may overcome the slight underperformance in image quality from slightly greater noise, likely due to the high intrinsic contrast-to-noise ratio of the 3D SE-based pulse sequence for enhancing lesions.

The savings in acquisition time without loss of clinically important information can provide synergistic benefits with the combined use of accelerated sequences that shorten the overall exam time and may improve utilization of MR resources, particularly in motion-prone populations. The Wave-CAIPI encoding approach has been applied to other imaging sequences providing complementary contrasts such as susceptibility weighted imaging (18, 21) and structural MPRAGE (without IV contrast administration) (22). Combining multiple Wave-CAIPI based 3D acquisitions could synergistically further reduce acquisition times and increase patient throughput, to the benefit of the patients and their providers.

Our study has several limitations. First, we have a relatively small sample size due to the proof-of-concept design within the specific indication of contrast-enhanced imaging for the evaluation of brain metastases. Other relevant limitations involve the heterogeneity of the multiple primary tumors and differences in tumor biology among participants. Nevertheless, our findings show a clear trend in the benefits of reduced scan time with preserved sensitivity for lesion detection, suggesting that these findings might be generalized to many tumor types. The small sample size probably underpowered the non-inferiority test, and the results could be considered as the basis for replicating these findings in a larger tumor-specific future study.

Second, we observed slightly greater artifacts with Wave-T1-SPACE than Standard-T1-SPACE (standard sequence preferred in 32%, Wave sequence preferred in 3%, no preference in 65%). Artifacts in 3D SE-based sequences, including SPACE, arise through a variety of mechanisms. Because it can be difficult for the radiologist to be certain of the mechanism of a given artifact, we grouped the different causes of artifact in a single category. Possible explanations for the increased artifacts observed in Wave-T1 SPACE include interactions between the Wave-CAIPI approach and motion/flow-related artifacts (possibly exacerbated by high vascular signal in the presence of gadolinium contrast), the free induction decay (10) and other 3D SE related artifacts, or imperfections in the Wave-CAIPI acquisition and reconstruction procedure itself. Although these factors did not result in the obscuration of any enhancing lesions and did not alter the radiologists' overall assessment of diagnostic quality, further evaluation of the underlying causes (and strategies for artifact mitigation) is warranted before a more general application of Wave-T1-SPACE in a clinical setting.

Third, although we did our best to balance the order of acquisition for the post-contrast standard and Wave-T1 SPACE sequences to control for potential differences in the conspicuity of enhancing lesions related to the time elapsed between contrast injection and image acquisition, more studies had standard T1 SPACE acquired before Wave-T1 SPACE (24 vs. 9). Despite this imbalance, 98% of the cases were rated as equivalent for visualization of enhancing lesions, attesting to the minimal contribution of acquisition order to the overall degree of enhancement on either sequence, as supported by the head-to-head analysis results as well as qualitative assessment of the images by all three raters.

Finally, the selection of a suitable non-inferiority margin for imaging studies is often challenging. Our selection was informed by a review of similar imaging-based non-inferiority studies and consensus among our group of neuroradiologists that the new sequence could be considered non-inferior if the standard sequence were preferred in fewer than 15% of cases. Since this threshold is essentially subjective, we also reported the critical value (P_{critical}), equivalent to the upper bound on a 95% confidence interval for the proportion of cases in which the standard sequence was preferred. Lastly, although readers were blinded to the acquisition protocol, some aspects of the images might have allowed the readers to identify the pulse sequence being evaluated, which could introduce bias. We sought to minimize this possibility by matching the most important

parameters that determine image quality and image contrast (including TR, TE, and flip angle) between acquisitions.

CONCLUSION

In conclusion, we show that contrast-enhanced Wave-CAIPI 3D T1 SPACE provides equivalent visualization of enhancing lesions and overall diagnostic quality for evaluating brain metastases with three times reduction in scan time compared to standard 3D T1 SPACE. The clinical application of the Wave-CAIPI approach may facilitate more efficient utilization of MR resources without loss of clinically valuable information, which can be especially beneficial to motion-prone patients with brain metastases. The present study offers several opportunities for future study, including the mechanisms and appearance of Wave-T1 SPACE artifacts, and supports the promise and continued evaluation of post-contrast Wave-T1 SPACE for routine use in clinical practice and clinical trials.

DATA AVAILABILITY STATEMENT

The raw data supporting the conclusions of this article will be made available by the authors, without undue reservation.

ETHICS STATEMENT

The studies involving human participants were reviewed and approved by Mass General Brigham Institutional Review Boards. Written informed consent for participation was not required for this study in accordance with the national legislation and the institutional requirements.

AUTHOR CONTRIBUTIONS

AG wrote the first draft of the manuscript, organized the database, and performed the statistical analysis. AG, JC, ML, PS, SH, and OR contributed to the conceptualization and design of the study, as well as to the interpretation of the data. SC, DP, WL, DS, W-CL, JK, and KS contributed to technical expertise on the acquisition and reconstruction of the data. All authors contributed to manuscript revision and review and approved the submitted version.

FUNDING

The authors declare that this study received funding from Siemens Healthineers. The funder was not involved in the study design, collection, analysis, interpretation of data, the writing of this article or the decision to submit it for publication.

SUPPLEMENTARY MATERIAL

The Supplementary Material for this article can be found online at: https://www.frontiersin.org/articles/10.3389/fneur.2020.587327/full#supplementary-material

REFERENCES

1. Gavrilovic IT, Posner JB. Brain metastases: epidemiology and pathophysiology. *J Neurooncol*. (2005) 75:5–14. doi: 10.1007/s11060-004-8093-6
2. Soffietti R, Cornu P, Delattre JY, Grant R, Graus F, Grisold W, et al. EFNS guidelines on diagnosis and treatment of brain metastases: report of an EFNS task force. *Eur J Neurol*. (2006) 13:674–81. doi: 10.1111/j.1468-1331.2006.01506.x
3. Sperduto PW, Kased N, Roberge D, Xu Z, Shanley R, Luo X, et al. Summary report on the graded prognostic assessment: an accurate and facile diagnosis-specific tool to estimate survival for patients with brain metastases. *J Clin Oncol*. (2012) 30:419–25. doi: 10.1200/JCO.2011.38.0527
4. Fink K, Fink J. Imaging of brain metastases. *Surg Neurol Int*. (2013) 4(Suppl. 4):209–19. doi: 10.4103/2152-7806.111298
5. Kaufmann TJ, Smits M, Boxerman J, Huang R, Barboriak DP, Weller M, et al. Consensus recommendations for a standardized brain tumor imaging protocol for clinical trials in brain metastases. *Neuro Oncol*. (2020) 22:757–72. doi: 10.1093/neuonc/noaa030
6. Deike-Hofmann K, Thünemann D, Breckwoldt MO, Schwarz D, Radbruch A, Enk A, et al. Sensitivity of different MRI sequences in the early detection of melanoma brain metastases. *PLoS ONE*. (2018) 13:e0193946. doi: 10.1371/journal.pone.0193946
7. Nöbauer-Huhmann IM, Ba-Ssalamah A, Mlynarik V, Barth M, Schöggl A, Heimberger K, et al. Magnetic resonance imaging contrast enhancement of brain tumors at 3 tesla versus 1.5 tesla. *Invest Radiol*. (2002) 37:114–9. doi: 10.1097/00004424-200203000-00003
8. Ellingson BM, Bendszus M, Boxerman J, Barboriak D, Erickson BJ, Smits M, et al. Consensus recommendations for a standardized brain tumor imaging protocol in clinical trials. *Neuro Oncol*. (2015) 17:1188–98. doi: 10.1093/neuonc/nov095
9. Lin NU, Lee EQ, Aoyama H, Barani IJ, Barboriak DP, Baumert BG, et al. Response assessment criteria for brain metastases: proposal from the RANO group. *Lancet Oncol*. (2015) 16:e270–8. doi: 10.1016/S1470-2045(15)70057-4
10. Mugler JP. Optimized three-dimensional fast-spin-echo MRI. *J Magn Reson Imaging*. (2014) 39:745–67. doi: 10.1002/jmri.24542
11. Suh CH, Jung SC, Kim KW, Pyo J. The detectability of brain metastases using contrast-enhanced spin-echo or gradient-echo images: a systematic review and meta-analysis. *J Neurooncol*. (2016) 129:363–71. doi: 10.1007/s11060-016-2185-y
12. Havsteen I, Ohlhues A, Madsen KH, Nybing JD, Christensen H, Christensen A. Are movement artifacts in magnetic resonance imaging a real problem?-a narrative review. *Front Neurol*. (2017) 8:232. doi: 10.3389/fneur.2017.00232
13. Munn Z, Pearson A, Jordan Z, Murphy F, Pilkington D, Anderson A. Patient anxiety and satisfaction in a magnetic resonance imaging department: initial results from an action research study. *J Med Imaging Radiat Sci*. (2015) 46:23–9. doi: 10.1016/j.jmir.2014.07.006
14. Setsompop K, Feinberg DA, Polimeni JR. Rapid brain MRI acquisition techniques at ultra-high fields. *NMR Biomed*. (2016) 29:1198–221. doi: 10.1002/nbm.3478
15. Bilgic B, Gagoski BA, Cauley SF, Fan AP, Polimeni JR, Grant PE, et al. Wave-CAIPI for highly accelerated 3D imaging. *Magn Reson Med*. (2015) 73:2152–62. doi: 10.1002/mrm.25347
16. Polak D, Cauley S, Huang SY, Longo MG, Conklin J, Bilgic B, et al. Highly-accelerated volumetric brain examination using optimized wave-CAIPI encoding. *J Magn Reson Imaging*. (2019) 50:961–74. doi: 10.1002/jmri.26678
17. Cauley SF, Setsompop K, Bilgic B, Bhat H, Gagoski B, Wald LL. Autocalibrated wave-CAIPI reconstruction; Joint optimization of k-space trajectory and parallel imaging reconstruction. *Magn Reson Med*. (2017) 78:1093–9. doi: 10.1002/mrm.26499

18. Conklin J, Longo MGF, Cauley SF, Setsompop K, González RG, Schaefer PW, et al. Validation of highly accelerated WAVE-CAIPI SWI compared with conventional SWI and T2*-weighted gradient recalled-echo for routine clinical brain MRI at 3T. *Am J Neuroradiol*. (2019) 40:2073–80. doi: 10.3174/ajnr.A6295
19. Ahn S, Park SH, Lee KH. How to demonstrate similarity by using noninferiority and equivalence statistical testing in radiology research. *Radiology*. (2013) 267:328–38. doi: 10.1148/radiol.12120725
20. Landis JR, Koch GG. The measurement of observer agreement for categorical data. *Biometrics*. (1977) 33:159. doi: 10.2307/2529310
21. Chung MS, Lee EJ, Kim S, Kim SO, Byun JS. Wave-CAIPI susceptibility-weighted imaging achieves diagnostic performance comparable to conventional susceptibility-weighted imaging in half the scan time. *Eur Radiol*. (2020) 30:2182–90. doi: 10.1007/s00330-019-06574-1
22. Longo MGF, Conklin J, Cauley SF, Setsompop K, Tian Q, Polak D, et al. Evaluation of ultrafast wave-CAIPI MPRAGE for visual grading and automated measurement of brain tissue volume. *Am J Neuroradiol*. (2020) 41:1388–96. doi: 10.3174/ajnr.A6703

Conflict of Interest: DP, WL, DS, and W-CL were employed by the company Siemens Healthineers.

The remaining authors declare that the research was conducted in the absence of any commercial or financial relationships that could be construed as a potential conflict of interest.

The handling editor is currently organizing a Research Topic with one of the authors SH.

Advantages of publishing in Frontiers

OPEN ACCESS
Articles are free to read for greatest visibility and readership

FAST PUBLICATION
Around 90 days from submission to decision

HIGH QUALITY PEER-REVIEW
Rigorous, collaborative, and constructive peer-review

TRANSPARENT PEER-REVIEW
Editors and reviewers acknowledged by name on published articles

Frontiers
Avenue du Tribunal-Fédéral 34
1005 Lausanne | Switzerland

Visit us: www.frontiersin.org
Contact us: frontiersin.org/about/contact

REPRODUCIBILITY OF RESEARCH
Support open data and methods to enhance research reproducibility

DIGITAL PUBLISHING
Articles designed for optimal readership across devices

FOLLOW US
@frontiersin

IMPACT METRICS
Advanced article metrics track visibility across digital media

EXTENSIVE PROMOTION
Marketing and promotion of impactful research

LOOP RESEARCH NETWORK
Our network increases your article's readership